



**HAL**  
open science

# Optimization of physical chemistry of the Pt/Ru/PbZrTiO<sub>3</sub> interface for future high capacitance density devices

Ibrahima Gueye

► **To cite this version:**

Ibrahima Gueye. Optimization of physical chemistry of the Pt/Ru/PbZrTiO<sub>3</sub> interface for future high capacitance density devices. Micro and nanotechnologies/Microelectronics. Université Grenoble Alpes, 2017. English. NNT : 2017GREAT119 . tel-02127036

**HAL Id: tel-02127036**

**<https://theses.hal.science/tel-02127036>**

Submitted on 13 May 2019

**HAL** is a multi-disciplinary open access archive for the deposit and dissemination of scientific research documents, whether they are published or not. The documents may come from teaching and research institutions in France or abroad, or from public or private research centers.

L'archive ouverte pluridisciplinaire **HAL**, est destinée au dépôt et à la diffusion de documents scientifiques de niveau recherche, publiés ou non, émanant des établissements d'enseignement et de recherche français ou étrangers, des laboratoires publics ou privés.

## THÈSE

Pour obtenir le grade de

### DOCTEUR DE L'UNIVERSITÉ DE GRENOBLE

Spécialité : **Nano Electronique et Nano Technologies**

Arrêté ministériel : 7 août 2006

Présentée par

**Ibrahima GUEYE**

Thèse dirigée par **Nick BARRETT**

préparée au sein **Laboratoire d'électronique et de technologie de l'information**

et de **L'Ecole Doctorale d'Electronique, Electrotechnique, Automatique, Télécommunications (EEATS)**

## **Optimization of physical chemistry of the Pt/Ru/PbZrTiO<sub>3</sub> interface for future high capacitance density devices**

Thèse soutenue publiquement le **13/11/2017**,  
devant le jury composé de :

**Mr, Christophe Vallée**

Professeur, université Grenoble-Alpes , Président

**Mr, Brice Gautier**

Professeur, Institut National des Sciences Appliquées de Lyon , Rapporteur

**Mr, Lucian Pintilie**

Directeur de recherche, National Institute of Materials Physics Bucharest,  
Rapporteur

**Mme, Nathalie Lemée-Le Calvez**

Hdr, Université de Picardie Jules Verne, Amiens, Examinatrice

**Mr, Olivier Renault**

Ingénieur chercheur, CEA-Grenoble, Examineur

**Mr, Nick Barrett**

Chercheur sénior, CEA-Saclay, Directeur de thèse

**Mr, Gwenaël Le Rhun**

Ingénieur chercheur, CEA-Grenoble , Invité



---

	<b>7</b>
<b>ACKNOWLEDGEMENTS</b>	<b>8</b>
<b>ABSTRACT</b>	<b>10</b>
<b>RESUME</b>	<b>12</b>
<b>PREFACE</b>	<b>15</b>
Bibliography . . . . .	23
<b>1 METAL/INSULATOR/METAL BASED ON Pb(Zr<sub>0.52</sub>Ti<sub>0.48</sub>)O<sub>3</sub> THIN FILMS</b>	<b>24</b>
1.1 Overview of Metal-Insulator-Metal . . . . .	25
1.1.1 Electrical Parameters in Capacitors . . . . .	25
1.2 Dielectric Materials Investigations . . . . .	26
1.2.1 Polarizability in Dielectric Materials . . . . .	27
1.2.2 Ferroelectricity in Dielectric Materials . . . . .	29
1.3 Lead Zirconate Titanate Pb(Zr,Ti)O <sub>3</sub> . . . . .	31
1.4 Schottky Model of Metal/Semiconductor Contact . . . . .	35
1.5 Conclusion . . . . .	38
Bibliography . . . . .	39
<b>2 EXPERIMENTAL METHODS</b>	<b>43</b>
2.1 Capacitor Deposition . . . . .	44
2.1.1 Bottom Electrode Deposition on the Silicon Substrate . . . . .	44
2.1.2 PZT Deposition . . . . .	45
2.1.3 Top Electrodes . . . . .	48
2.1.4 Post Metallization Annealing Conditions . . . . .	49
2.2 X-rays Diffraction . . . . .	50
2.3 Overview of Electronic Microscopes . . . . .	51
2.4 Characterizations of Surface and Interface . . . . .	52
2.4.1 Basic Principles of Photoemission . . . . .	52

2.4.2	Experimental Set-up of XPS . . . . .	62
2.4.3	Synchrotron Beamline . . . . .	66
2.5	Conclusion . . . . .	72
	Bibliography . . . . .	73
<b>3</b>	<b>ELECTRICAL RESPONSE OF Pt/Ru/PZT/Pt CAPACITOR</b>	<b>78</b>
3.1	Electrical Measurement Processes . . . . .	78
3.1.1	Capacitance Density and Loss Tangent . . . . .	79
3.1.2	Breakdown Voltage (Field) Measurement . . . . .	81
3.2	Pb Excess and Post Metallization Annealing Effects . . . . .	84
3.2.1	Dielectric Constant and Loss Tangent . . . . .	85
3.2.2	Breakdown Field . . . . .	89
3.3	Conclusion . . . . .	90
	Bibliography . . . . .	92
<b>4</b>	<b>SURFACE CHEMISTRY IN Pb PRECURSOR-RICH Pb(Zr<sub>0.52</sub>Ti<sub>0.48</sub>)O<sub>3</sub> SOL-GEL THIN FILMS</b>	<b>96</b>
4.1	Pb(Zr <sub>0.52</sub> Ti <sub>0.48</sub> )O <sub>3</sub> Surface with 30 % Pb Excess . . . . .	97
4.2	X-ray Photoelectron Spectroscopy . . . . .	98
4.3	Investigations of Surface Chemistry . . . . .	100
4.3.1	XPS Measurement at Normal Emission . . . . .	101
4.3.2	Angle dependent XPS investigations . . . . .	103
4.3.3	Depth Profile by Ion Beam Etching . . . . .	104
4.3.4	X-ray Diffraction Analysis . . . . .	107
4.3.5	Discussion . . . . .	108
4.4	Nanostructures as a Function of the Pb Excess . . . . .	112
4.4.1	Scanning Electron Microscopy . . . . .	112
4.4.2	X-ray Photoelectron Spectroscopy . . . . .	113
4.4.3	X-ray Diffraction . . . . .	115
4.4.4	Discussion . . . . .	116
4.5	Conclusion . . . . .	118
	Bibliography . . . . .	119
<b>5</b>	<b>Pt/Ru/PbZr<sub>0.52</sub>Ti<sub>0.48</sub>O<sub>3</sub> INTERFACES</b>	<b>125</b>
5.1	Hard X-ray Photoelectron Spectroscopy . . . . .	126
5.2	PZT Bare with 10 % of Pb Excess . . . . .	126
5.3	Investigations of Pt/Ru/PZT10 Interfaces . . . . .	130
5.3.1	Survey of Buried Interface of Pt/Ru/PZT10 . . . . .	130
5.3.2	Dielectric Constant and Polarization of Pt/Ru/PZT/Pt . . . . .	131
5.3.3	Bias Correction After HAXPES Measurements . . . . .	134
5.3.4	Background Subtraction . . . . .	135
5.3.5	Analysis on <i>Operando</i> HAXPES Data Based on PZT10 . . . . .	136
5.4	Interface Analysis of Pb Excess Content in PZT . . . . .	140
5.4.1	Pt/Ru/PZT30/Pt Electrical Measurements . . . . .	140
5.4.2	Analysis on <i>Operando</i> HAXPES Data Based on PZT30 . . . . .	142
5.5	Post Metallization Annealing of Pt/Ru/PZT10 Interface . . . . .	144
5.5.1	Electrical Characterization After PMA . . . . .	145

5.5.2 Ru and Pt Chemical State Before and After PMA . . . . .	145
5.5.3 Analysis on <i>Operando</i> HAXPES Data Based on PZT10 After PMA .	147
5.6 Conclusion . . . . .	150
Bibliography . . . . .	152
<b>SUMMARY AND OUTLOOK</b>	<b>157</b>



---

I would like to dedicate my thesis

to

my grand father

***EL HADJI BABACAR GUEYE.***

Death changes everything! Time changes nothing ...

I still miss the sound of your voice, the wisdom in your advice, the stories of your life and just being in your presence. So No, time changes nothing, I miss you as much today as I did the day you are gone.

All my life I will keep with me memories of us two, and how lucky I have been to have a ***MAME*** smile like you.

Love!

---

# ACKNOWLEDGEMENTS

After a long period of intense learning for me, this note of thanks is the finishing touch on my Ph.D. study. This thesis has had a big impact on me, not only in the scientific arena, but also on a personal level. I would like to express the deepest appreciation to the people who have supported and helped me so much throughout this period.

First and foremost, I would like to express my sincere gratitude to my advisor Dr. Nick BARRETT from the Service of Condensed Matter (SPEC) in the IRAMIS institute of the French Atomic Energy Commission (CEA). He has been continuous support of my Ph.D. study and related research, for his patience, motivation, and immense knowledge. His guidance helped me in all the time of research and writing of this thesis. You definitely provided me with the tools that I needed to choose the right direction and successfully complete my dissertation. I could not have imagined having a better advisor and mentor for my Ph.D. study.

I would like to offer my special thanks to my major associate advisors Dr. Olivier RENAULT and Dr. Gwenaël LE RHUN for their valuable guidance and an inspiration in many academic & technological ways. You supported me greatly and were always willing to help me during the most difficult times. You definitely provided me with the tools that I needed to choose the right direction and successfully complete my thesis. I am particularly grateful for the scientific and moral assistance given by Prof. Emmanuel DEFAY.

Besides my advisor, I would like to thank Prof. Brice GAUTIER and Dr. Lucian PINTILIE for being part of my Generals committee and accepting the position of thesis reviewers. Also thank you for their insightful comments and encouragement, but also for the hard question which incited me to widen my research from various perspectives. I would like to express the deepest appreciation to the other members of my thesis defense committee, Prof. Christophe VALLÉE, Dr. Nathalie LEMÉE-LE CALVEZ and once again Dr. Nick BARRETT, Dr. Olivier RENAULT and Dr. Gwenaël LE RHUN for their advice and comments.

My sincere thanks also goes to Stéphane FANGET who provided me an opportunity to join their team as Ph.D. student, and who gave access to the laboratory and research facilities. Without the precious support of Laboratoire de Composants Micro-Actionneur (LCMA) it would not be possible to conduct this research. I would also like to express my gratitude to LETI for their financial support.

I am particularly grateful for the assistance given by Christel DIEPPEDALE, Clémence BONNARD and Marjolaine ALLAIN for the preparation and deposition of samples. Bruno REIG gives me constructive comments and warm encouragement, Thank you. I wish to thank Christine COURTOIS and Beatrice ROSTAND for their support and help during my stay at LETI. I have greatly benefited from Veronika KOVACOVA and Marie BOUSQUET, thank you for your help!

My real thanks also goes to Mrs Jumana Boussey from doctoral school for Electronics,

---

Power Systems, Automatic Control and Signal Processing (EEATS)

I thank the Platform for Nano-characterization and Platform for electrical measurements. Advice and comments given by Anass, Eugénie, Eric, Nicolas and David have been a great help in my experiences. I thank Patrice GERGAUD and Nicolas VAXELAIRE. I am particularly grateful for the technical assistance given by Irène PHENG, Patrick BRUNET-MANQUAT, Jennifer GUILLAUME and Henri BLANC for preparation and testing of samples.

Thank you Thierry CHEVOLLEAU and all members of the Upstream Technological Platform for their help during the lithography and etching process.

I thank SOLEIL for provision of synchrotron radiation facilities and all members of GALAXIES beamline. Special thanks also to Denis CEOLIN and Jean-Pascal RUEFF, without their help, our HAXPES operando project would not have materialized.

A special acknowledgement goes to my officemates of many years, Luca, Marc, Thomas, Romain, Olivier, Geoffroy, Guillaume, Marie, Jaroslaw, Maxime, Federico, Rémy, Adrien, Gabrielle and Hadley for our long discussion at lunch time, afterwork and the outings around Grenoble, especially its beautiful mountains and lakes. Thanks to Luca and Marc for teaching me how to ski.

A big thank you to my friends Bilal and Sandrine who has always supported me during these three years. A big thank you to my friend Sylla for her support and help before and during the thesis defense. Thank you, Agnes for having accompanied, supported and helped me during the last straight line of my thesis

Last but not the least, I would like to thank all my African family: my parents, my brothers, my sisters my aunt, my uncle and my cousin, for supporting me spiritually throughout this thesis and my life in general.

Thank you very much, everyone!

---

# ABSTRACT

The growing need for the integration of an increasing number of functions into the new generation of portable devices contributes to overcrowding of printed circuit boards. In this context, the miniaturization of discrete components is imperative to maintain a manageable size of the printed circuit boards. Decoupling capacitors are one of the most important such discrete components. Miniaturization requires an increase of capacitance density, involving the integration of high-density capacitors. The success of such integration relies on the use of both high dielectric permittivity materials and a suitable stacking architecture. Lead zirconate titanate (PZT) in decoupling multiple metal-insulator-metal (multi-MIM) stacks is a good candidate for the new generation of integrated capacitors. The multi-MIM technology consists in stacking two or more PZT film-based MIM structures connected in parallel in order to increase the density of the capacitance without any effective surface area change. Device performance is heavily affected by the quality of the interface with the electrodes, so it is important to engineer interface chemistry which does not degrade the multi-MIM performance.

This thesis, supported by the French "**Programme de l'économie numérique des investissements d'Avenir**" addresses two aspects of development aiming to improve the quality of the Pt/Ru/PZT interfaces: the first one concerns the optimization of Pb excess content in the PZT film, while the second one investigates the Post Metallization Annealing (PMA) done after deposition of electrode/PZT multilayer.

The first part of the thesis presents the capacitance density analysis performed on Pt/Ru/PZT/Pt capacitors as a function of Pb excess in the sol-gel precursor solution (10, 15, 20 and 30 % of excess Pb for PZT10, PZT15, PZT20 and PZT30, respectively). Pb excess compensates the lead evaporation during calcination.

An increase of Pb excess from 10 to 20 % leads to an increase of the maximum dielectric constant of 8.8 %, a decrease of the loss tangent from 4.36 to 3.08 % and breakdown field from 1.68 to 1.26 MV/cm. PMA favors the enhancement of the maximum of dielectric constant by 7.5 %, and the breakdown field increases to 0.5 MV/cm.

The influence of the surface chemistry is studied as a function of Pb precursor excess. X-ray photoelectron spectroscopy demonstrates that low level of Pb excess leads to the presence of a  $ZrO_x$  surface phase in the form of nanostructures. Higher Pb precursor content allows the PZT synthesis to proceed to its end-point, fully consuming the  $ZrO_2$  precursor and eliminating the low dielectric constant  $ZrO_x$  surface phase.

We have then studied the Pt/Ru/PZT interface as a function of Pb excess and PMA. TEM cross-sectional analysis shows that the crystalline  $ZrO_x$  nanostructures are still present at the electrode interface, constituting a dielectric layer which contributes to defining capacitor performance. Operando hard X-ray photoelectron spectroscopy (HAXPES) analysis using synchrotron radiation highlights a polarization-dependent electronic response, most probably due to imperfect screening of the depolarizing field at the Pt/Ru/PZT10 interface. Furthermore, a new component ( $PbO_x$ ) is observed at the Pt/Ru/PZT30 due to the high

---

Pb excess. This component seems to induce a reduction in breakdown field and capacitance density. Finally, PMA on the PZT10 suggests the creation of interface  $\text{ZrRuO}_x$  and  $\text{PbRuO}_x$  which could be at the origin of the improvement of electrical responses of PZT capacitors after PMA.

In conclusion, this thesis has provided valuable information and methodology on the correlation between surface and interface physical chemistry of PZT and Pt/Ru/PZT and electric characteristics of PZT based MIM capacitors.

---

# RESUME

Le besoin croissant d'intégration de nouvelles fonctions dans les futures générations de dispositifs portables contribue au surpeuplement des circuits imprimés. Dans ce contexte, la miniaturisation des composants discrets est impérative pour compenser l'augmentation de leur nombre et pour garder la taille des cartes de circuit imprimé gérable. L'un des composants les plus courants de ce type est le condensateur, qui peut être utilisé pour découpler une partie d'un réseau électrique d'un autre. Cependant, la miniaturisation des condensateurs nécessite une augmentation de leur densité de capacité, impliquant l'intégration de condensateurs haute densité. Le succès d'une telle intégration repose sur l'utilisation à la fois de matériaux à haute constante diélectrique et d'une architecture d'empilement. Dans ce contexte, les couches de titanate-zirconate de plomb (PZT) combinées aux piles multi-MIM sont de bons candidats pour la nouvelle génération de condensateurs. La technologie multi-MIM consiste à empiler deux ou plusieurs structures MIM en parallèle afin d'augmenter la densité de la capacité sans modification effective de la surface. Avec la géométrie multi-MIM, la performance de l'appareil est fortement affectée par la qualité de l'interface Métal/PZT, il est donc important d'élaborer une chimie d'interface qui ne dégrade pas les performances des multi-MIM.

Cette thèse soutenue par le projet français " **Programme de l'économie numérique des investissements d'Avenir** " vise deux axes de développement pour améliorer de la qualité des interfaces Pt/Ru/PZT: la première concerne l'optimisation du contenu de Pb en excès dans la couche de PZT, tandis que le second étudie les effets du recuit de post métallisation (PMA).

La première partie de la thèse est dédiée aux analyses de densité de capacité réalisées sur les condensateurs Pt/Ru/PZT/Pt en fonction de l'excès de précurseur du Pb dans les couches de PZT déposées par voie sol-gel (10, 15, 20 et 30 % de Pb respectivement pour PZT10, PZT15, PZT20 et PZT30).

Nous montrons qu'une augmentation de l'excès de Pb de 10 à 20 % entraîne une augmentation de la constante diélectrique maximale (environ 8,8 %), ainsi qu'une diminution de la tangente de perte (de 4,36 à 3,08 %) et du champ de claquage (de 1,68 à 1,26 MV/cm). La PMA favorise l'augmentation du maximum de constant diélectrique (jusqu'à 7,5 %) et le champ de claquage augmente de 0.5 MV/cm.

Ensuite, l'influence de la chimie de surface des PZT est étudiée en fonction de l'excès de précurseur de Pb. Cet excès de Pb permet de compenser l'évaporation du plomb pendant le traitement thermique successif. En utilisant la spectroscopie de photoélectrons par rayons X (XPS), nous montrons la présence d'une phase de surface  $ZrO_X$ . Les faibles niveaux d'excès de Pb conduisent à la formation de nanostructures  $ZrO_X$  à la surface de la couche de PZT. Un taux plus élevé en Pb favorise la disparition totale nanostructures  $ZrO_X$  en surface.

Enfin, nous avons sondé l'interface Pt/Ru/PZT en fonction de l'excès de Pb et de la PMA. La microscopie électronique en transmission (TEM) montre que les nanostructures de  $ZrO_X$  sont présentes à l'interface du Ru/PZT10. Les nanostructures cristallines  $ZrO_X$

---

pourraient former une couche non ferroélectrique et ainsi affecter la densité de capacité. L'analyse en mode operando (sous polarisation in situ) par XPS haute-énergie montre une réponse électronique dépendant de la polarisation appliquée, probablement grâce à l'écrantage imparfait du champ dépolarisant à l'interface Pt/Ru/PZT10. En outre, une nouvelle phase ( $\text{PbO}_x$ ) est observée au niveau Pt/Ru/PZT30, probablement liée à la quantité de Pb en excès dans le PZT30. Cette phase semble induire la diminution du champ de claquage et la densité de capacité observée au niveau du Pt/Ru/PZT30/Pt. Enfin, PMA sur le Pt/Ru/PZT10 montre la création d'alliage à base de  $\text{ZrRuO}_x$  et  $\text{PbRuO}_x$  qui pourrait être à l'origine de l'amélioration des réponses électriques des condensateurs PZT après PMA.



---

# PREFACE

Driven by major technological progresses in the microelectronics, the market of portable equipments, especially smartphones, has experienced a rapid growth. Smartphones are now the most demanded electronic devices with an increase of about 200 million sales each year. With almost a total of 1.5 billion units sold in 2015, forecasts show that market will reach around 2 billion units in 2019 [1]. This situation stems from the fact that smartphone manufacturing technology has entered in a phase of sufficient maturity. In fact, smartphones now include multiple and varied functions such as internet browsing, data downloading, Global Positioning System (GPS), photography and even contactless payment.

However, the growth needs for integrating various functions (diversification) in portable equipments contributes generally to the overcrowding on printed circuit boards (PCB) through the increase of the number of discrete components and the downscaling process. Furthermore, this unrestrained race of miniaturization associated to these electronic devices responds to a consequence of Moore law called "More Moore" which planned to double the number of transistors in an integrated circuit every 18 months. This miniaturization therefore allows an increase of performance and a diversification ("More Than Moore") of functionalities. In fact, by reducing the size of components, the freed up space makes it possible to integrate new functionalities in the chip.

In fact, when the Discrete Surface Mount Devices (SMD) are encapsulated in individual packages in order to ensure several tasks, they can occupy a significant place at the PCB due to components count and interconnections as shown in Figure 1(a). However, in order to respond to the miniaturization and diversification aspects, new technologies called Integrated Passive Devices (IPD), which are much more compact than discrete components, are developed. The use of IPD technology to optimize space in microchips (by replacing SMD and reducing interconnections) can allow to achieve the set objectives as it can be seen Figure 1(b). Among the various components directly integrated in order to increase the possible functionalities of electronic chip, we will focus on Metal-Insulator-Metal (MIM) capacitors, which are by far the most used.

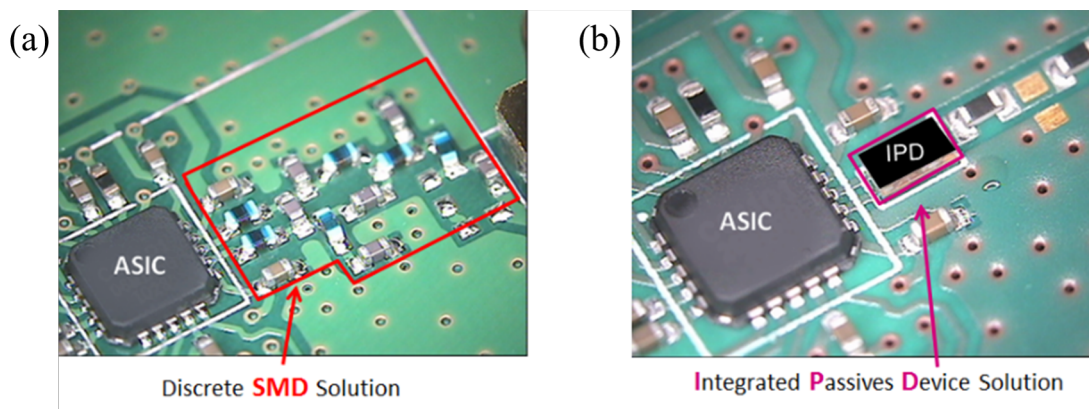


Figure 1: Illustration of the occupancy rate of components (a) discrete Surface Mount Devices (SMD) on a (PCB) and (b) Integrated Passive Devices (IPD) on a PCB [2]

## Metal-Insulator-Metal Integration

MIM capacitors are essential components in many areas of microelectronic technologies. They are easily embeddable onto a PCB or integrated circuits as illustrated in Figure 2. Furthermore, the important use of MIM structures is related to the fact that capacitors can play various roles in microelectronic devices.

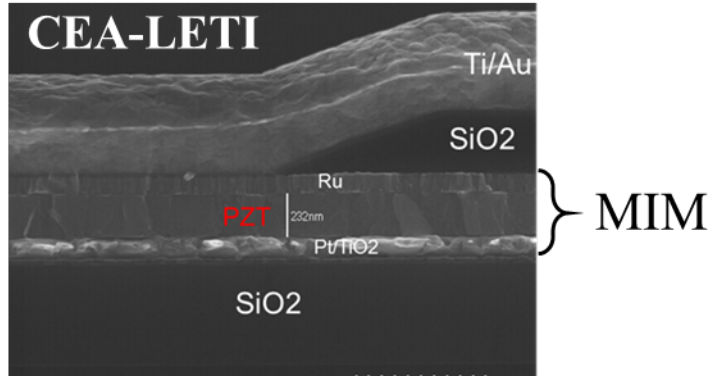


Figure 2: Planar Ru/PZT/Pt capacitor manufactured at CEA-LETI

The main functions of capacitors in a mobile phone circuit concern mainly the decoupling, filtering and coupling of signals, as illustrated below:

### Decoupling Capacitors

The most widespread application of MIM capacitors is to decouple a system, such as an integrated circuit, from the quick voltage change within the power supply. These capacitors have the function of separating parasitic signals on the voltage supplies between two blocks. They are connected in parallel with the supply circuit. The sinusoidal components are removed by filtering and only the DC voltage is recovered across the capacitors. For a decoupling capacitor, a high capacitance density and breakdown voltage (field) are required.

### Filtering Capacitors

The second most common function is the filtering of signals from undesired frequencies. By modulating the reactance of the capacitor which is inversely related to the frequency, it is possible to increase or decrease the impedance of the circuit (filter) at certain frequencies. There are various model of filters used in electronic circuits, such as LPF (Low Pass Filter), HPF (high Pass Filter) and BPF (Band Pass Filter).

### Coupling Capacitors

These capacitors have the reverse function of decoupling capacitors. Coupling capacitors are used to eliminate the DC component of the signal and only the sinusoidal components are kept. They are mounted in series in the circuit. The specifications are a high density and a good frequency resistance in order to preserve the spectral component of the signal.

In many of these applications, capacitors occupy a large fraction of the chip area. Additionally, the capacitance density required in a mobile phone circuit is on the order of

several hundreds of nanofarads per square millimeter. Therefore, capacitors with higher capacitance density are very attractive. Several approaches have been used to improve the capacitance density. The capacitance density can be mainly improved by modifying the architecture of capacitors and increase relative dielectric constant of the insulator used in Metal-Insulator-Metal structures.

## Multiple and 3D Trench MIM Capacitors

In a Planar MIM architecture (Figure 2), the reduction of the insulator thickness allows to increase the capacitance density. However, this option has drawbacks because the breakdown voltage (field) decreases with the reduction of the insulator thickness [3].

However, other alternatives are possible to increase the capacitance density without modifying the thickness. In fact, in order to increase the capacitance density of capacitors, two principal architectures are developed: stacked metal-insulators-metal (Multiple-MIM or Multi-MIM) or three-dimensional (3D) structures as illustrated in Figure 3 (a) and Figure 3 (b) respectively. The fabrication of Multi-MIM and 3D structures has drawn great interests mainly at the research and development level in materials science and engineering.

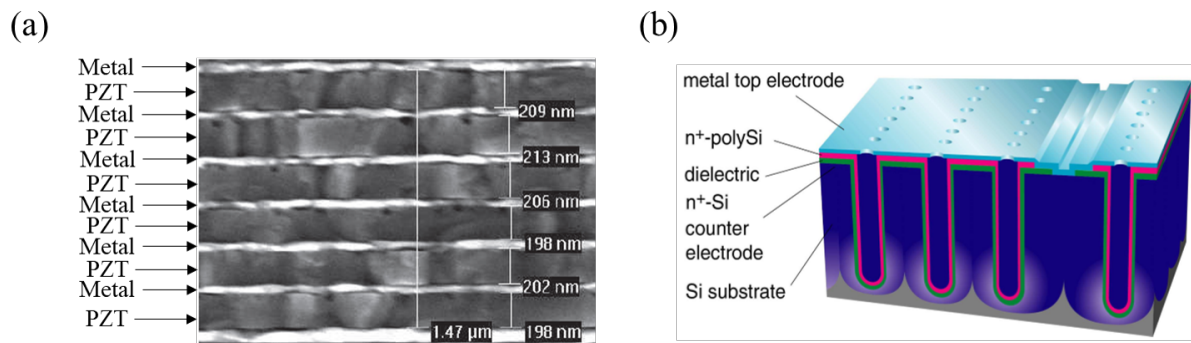


Figure 3: Metal-Insulator-Metal (MIM) technologies (a) Multiple-MIM (Multi-MIM) based PZT oxide [4] and (b) 3D trench MIM capacitor

Multi-MIM technology consists of two or more MIM structures to increase the capacitance density without increasing the effective area occupied by the capacitor as illustrated in Figure 3 (a). Furthermore, capacitors that are based on three-dimensional structures offer increased capacitance densities for the same area occupied on smaller footprint via modifying the geometry of the devices. Indeed, the idea of the trench structure (or 3D) is to increase the surface area developed by creating holes in the substrate or in the interconnection levels. Thus, the walls of the holes are then filled by a bottom electrode, an insulator and a top electrode as illustrated in Figure 3 (b).

## Dielectric Materials Used in MIM Technology

Beyond the modification of the architecture, the optimization of the capacitance density of MIM capacitors can be obtained by the modification of the insulator used. Indeed, scientists have explored various dielectric materials in order to increase the permittivity value

while retaining certain other electrical characteristics such as the breakdown field. Figure 4 presents a non-exhaustive classification of dielectric materials as a function of their relative dielectric constant values.

Historically, a lot of research has been conducted to develop new materials that could replace silicon oxide ( $\text{SiO}_2$ ). Indeed, the first dielectric used in microelectronics have been produced by thermal oxidation of silicon [5]. Although the insulator obtained  $\text{SiO}_2$  is reliable, robust and chemically stable, it now has considerable limitations. One of these limitations is the high level of current leakage due to the reduction in the thickness of the oxide from generation to generation.

Thus, from the simple  $\text{SiO}_2$  initially used in Metal Oxide Semiconductor (MOS) transistors, different categories of dielectrics are now available.

**Low-k** with values of relative dielectric constants lower than 10 is used as inter or intra-level insulators to reduce propagation delay and interferences along interconnections.

**Medium-k** mainly composed of binary materials with values of relative dielectric constants between 15 and 50 ( $\text{HfO}_2$ ,  $\text{ZrO}_2$ ,  $\text{Ta}_2\text{O}_5, \dots$ ) is used as gate dielectrics of MOS transistors or for linear MIM capacitors.

**High-k** includes mainly the ternary materials from the family of perovskites with values of relative dielectric constants greater than 100 as  $\text{PbTiO}_3$ ,  $\text{SrTiO}_3$ ,  $\text{BaTiO}_3$ ,  $\text{PbZrTiO}_3$  and  $\text{BaSrTiO}_3$ . This group is rather intended for Micro Electro Mechanical Systems or non-linear MIM capacitors.

In addition to the high value of relative dielectric constant, the second main criterion for thin selection of dielectrics in MIM technology concerns the breakdown voltage (field) characteristic. The breakdown voltage is defined as the maximum permissible voltage across the capacitor as we will discuss below.

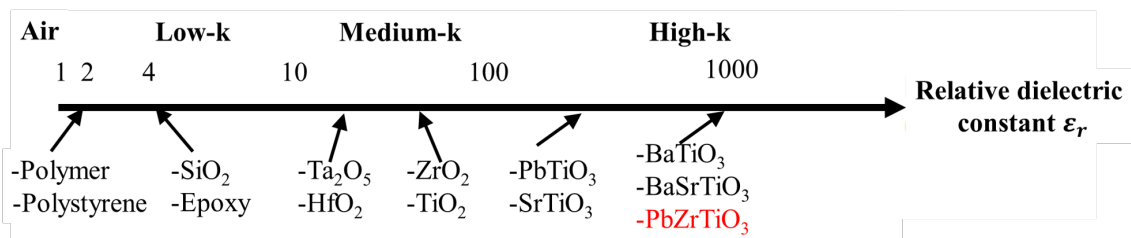


Figure 4: Classification of dielectric materials as a function of relative dielectric constant values

## Advantages of PZT Material in Microelectronic Devices

The development of mobile equipments requires the use of higher and higher capacitance densities. Materials with a high dielectric constant (high-k) are the best candidate to be incorporated into MIM structures. High-k materials provide an optimized dielectric constant

and breakdown field. From the literature review proposed by McPherson *et al.* [6], it is possible to establish a "universal" relationship describing the breakdown field as a function of the dielectric constant. More precisely, the breakdown field decreases when the value of the dielectric constant increases as shown in Figure 5. The problem of selecting the appropriate material therefore lies in the trade off between breakdown field and dielectric constant.

However, recent published results show that better optimization of manufacturing and integration processes could improve electrical performance. Indeed, Bouyssou *et al.* [7] mentions a "new" PZT (red square in Figure 5) whose breakdown field is higher than the one of the PZT (blue square in Figure 5) aligned on the green line. Despite the best dielectric constant values reported for the PZT, the associated breakdown fields reach more than 2 MV/cm (red square). These breakdown field values fully meet the specifications imposed for applications in the mobile phone circuits. According to these promising results of the PZT materials, our choice for the optimization of MIM structures is naturally focused on it. The choice of PZT gives the highest dielectric constant together with relatively high breakdown field.

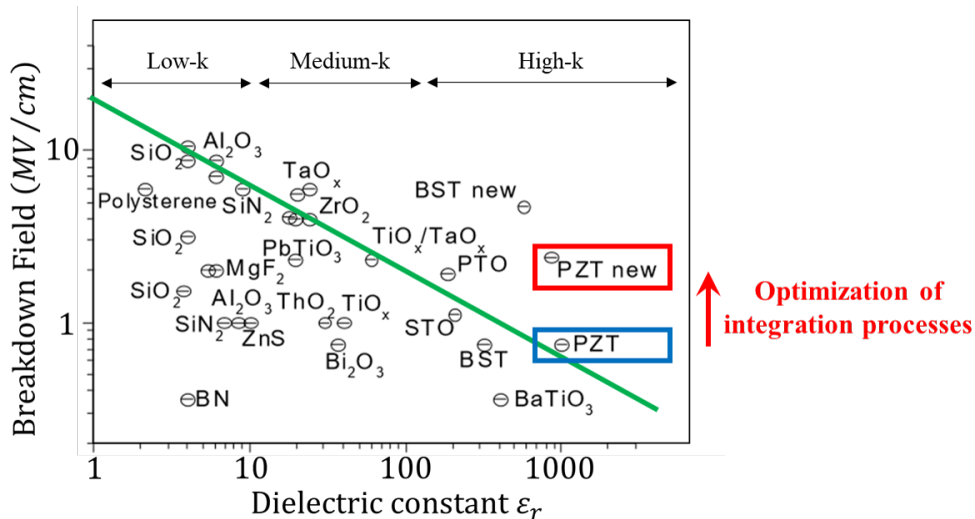


Figure 5: Illustration of the universal law of the breakdown field values as the function of dielectric constants [6]. The green line (universal law) is a fit through the data of the best samples. One more recent data point (red square) is added by Bouyssou *et al.* [7] and indicates an improvement of breakdown field values of PZT (blue square)

## Challenge of PZT Thin Film Integration

This thesis is part of a project supported by the French "**Programme de l'économie numérique des investissements d'Avenir**" aiming at developing a new generation of decoupling capacitors, based on Multi-MIM technology. This new technology allows to get an enhancement of capacitance density and breakdown voltage. The Multi-MIM technology developed at CEA-LETI consists of two or more lead zirconate titanate (PZT) based MIM structures connected in parallel in order to increase the capacitance density without any effective surface area change as described by Klee *et al.* [4]. Starting from the experience

accumulated over the past years on PZT technology at CEA-LETI, two axes of development have been identified to optimize PZT capacitors performances:

The first one concerns the interface electrode/PZT, which can control the adhesion issues in Multi-MIM capacitors as demonstrated with the investigation of Multi-MIM capacitors at CEA-LETI as seen in Figure 6. In fact, the use of Ru interlayer between Pt and PZT interfaces ensures better adhesion and avoid the delamination (or creation of cavity) observed in case of Pt/PZT interface (Figure 6 (a)). Additionally, electrode/PZT interfaces are known to play a major role on the performances of capacitors such as polarization switching, dielectric permittivity, breakdown voltage, fatigue, reliability [8, 9, 10]. However, results presented in Figure 6 (b) show that Pt/Ru electrodes seem to be required for enhancing the integration technology of Multi-MIM capacitor. From this investigation, we used during this thesis an interfacial layer of Ru between the Pt and PZT layers.

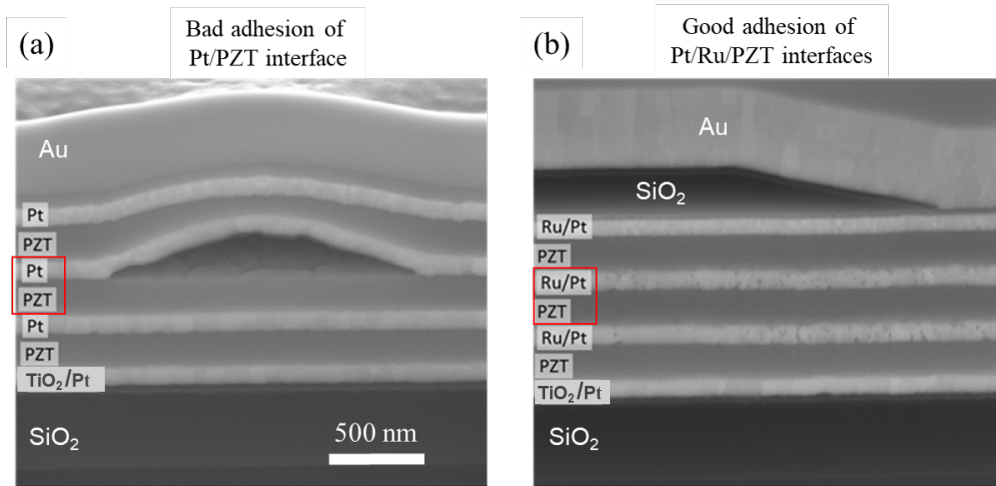


Figure 6: Investigation of adhesion issues in the Multi-MIM based on PZT thin film (CEA-LETI)

The second one concerns the stoichiometry of Pb content in the PZT film. Song [11] reported in Figure 7 (a), the relationship between the deposition temperature and the relative amount of Pb in a PZT thin film with the composition of 0.52 and 0.48 for Zr and Ti content. Indeed, the volatility of Pb at high temperature makes the control of Pb composition difficult, which is crucial for PZT properties. However, in order to adjust the Pb rate in the PZT layer, some amount of Pb excess is added in PZT precursors solution.

Further, this amount of Pb excess content in precursors solution to compensate the high volatility of Pb during the successive thermal treatments might also act on the microstructures of PZT layers or on the electric responses of thin film PZT-based capacitors. Indeed, the investigation performed by Arai *et al.* [12] (presented in Figure 7 (b)) on a similar perovskite  $(\text{Pb}(\text{Mg}_{1/3}\text{Nb}_{2/3})\text{O}_3\text{PbTiO}_3)$  (PMN-PT) thin films) demonstrates that the dielectric constant and the dielectric loss response on the excess lead content in the PZT precursor solution. According to these results, the control of the Pb excess used in the precursors solution during the deposition process due to the high volatility of Pb seems to be necessary.

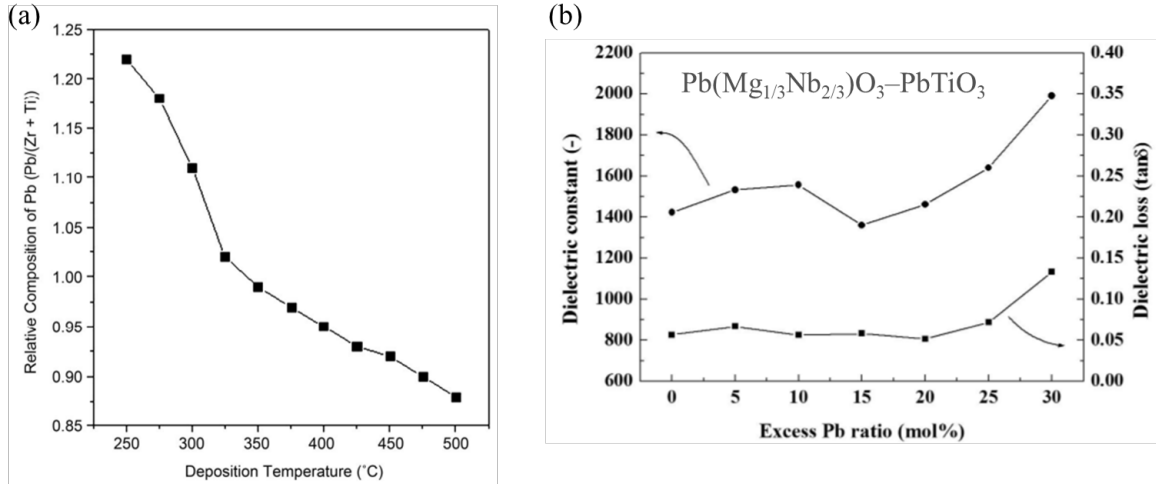


Figure 7: (a) The amount of Pb with the various deposition temperatures and (b) Dielectric constants and dielectric loss for  $\text{Pb}(\text{Mg}_{1/3}\text{Nb}_{2/3})\text{O}_3\text{-PbTiO}_3$  (PMN-PT) thin films on LSCO/CeO<sub>2</sub>/YSZ/Si at room temperature and 1 kHz as a function of the lead content

## Objectives and Plan

Elucidate all Pb excess content effects and interface contributions in a single step by directly using a Multi-MIM structure is beyond the scope of this thesis research. However, the goal of this thesis Consists to understand the properties of Metal/PZT/metal structures.

The general objective of this thesis is to understand the role of the interface and the effect of Pb precursor excess and post-metallization annealing (PMA) on the performances of simple PZT-based MIM capacitors. To this end, the work was partitioned into two interdependent fields of activity: on the one hand, deposition and electrical characterization; on the other hand, physico-chemical characterization. For this reason, the work was performed within two research laboratories (CEA-LETI): the Laboratory of micro-actuator components (LCMA) and the platform for nanocharacterization (PFNC). Photoelectron spectroscopy was mainly used to investigate the PZT surface chemistry, the Pt/Ru/PZT interfaces chemistry and the electronic structure. Correlations with electrical properties such as the capacitance, the loss tangent and the breakdown field (voltage) are drawn.

This thesis manuscript consists of five different chapters:

**Chapter 1** introduces the theoretical background related to this thesis. First, the metal-insulator-metal capacitors characteristic and their main properties required in the microelectronic application are described. Then, the ferroelectric and dielectric material properties are presented with focus on PZT. In the last section, the review of some impact of surface and interface state on capacitor performance is detailed.

**Chapter 2** presents the deposition process and characterization techniques used in this work. The first part is dedicated to the description of top and bottom electrodes and PZT material elaboration, by sputtering and sol-gel techniques, respectively. Following

that, the microstructural (X-ray diffraction) and structural (electronic microscopies) tools for analyzing the bulk and the surface of PZT thin film are described. The next section is devoted entirely to the physical principles of photoelectron spectroscopy, which are used to study the physico-chemical properties of PZT thin layers and PZT-based capacitors. This part also points to the importance of using hard X-ray produced by synchrotron radiation, as opposed to softer, laboratory X-rays for studying buried interfaces. Finally, we describe the XPS analyzer, synchrotron equipment and HAXPES *operando* protocol.

**Chapter 3** describes the results of electrical measurements relative to both the Pb excess and post metallization annealing effect on the MIM structure based on PZT thin films. First, we describe both electrical setups and theoretical aspects used for performing the measurements of the capacitance density, the loss tangent and the breakdown voltage. Then, we present and discuss the electrical properties regarding the Pb excess content and the effect of the thermal treatment after top electrodes deposition (post metallization annealing).

**Chapter 4** highlights first the surface chemistry dependence of Pb excess amount in the sol-gel precursors and the surface properties of PZT thin films. Pb excess ranging from 10 % to 30 % is studied during this chapter. Surface-sensitive tools such as X-ray photoelectron spectroscopy and scanning electron microscopy are used to study both the chemistry and the morphology of PZT thin film surfaces. We also perform X-ray diffraction measurements for understanding the texture modification as a function of Pb excess in the PZT films synthesized by sol-gel method. The results obtained in this chapter have been correlated with the electrical characterization presented in chapter 3.

**Chapter 5** is dedicated to the study of the Pt/Ru/PZT interface in a Pt/Ru/PZT/Pt-/TiO<sub>2</sub>/SiO<sub>2</sub>/Si stack, carried out with Hard X-ray photoelectron spectroscopy (HAXPES) under in-situ bias (*operando* conditions). This chapter is divided into four parts. First, we have analyzed the PZT bare with 10 % of Lead excess content. Following that, the interface of Pt/Ru/PZT stack with 10 % of Lead excess has been probed under bias voltage using the HAXPES. The last two sections describe the chemistry and the electronic structure of the Pt/Ru/PZT stacks depending on the effect of higher Pb excess and the thermal treatment under voltage.

**This manuscript ends with the general conclusion followed by perspectives for future work.**

## Bibliography

- [1] Mobile phone forecast from 2015 to 2019. <http://www.ccsinsight.com/>.
- [2] Integrated Passive Components (IPC's). <https://en.wikipedia.org/>.
- [3] P Jain and E. J. Rymaszewski. Embedded thin film capacitors-theoretical limits. *IEEE Transactions on Advanced Packaging*, 25(3):454–458, 2002.
- [4] M. Klee, H. Boots, B. Kumar, C. Van Heesch, R. Mauczok, W. Keur, M. De Wild, H. Van Esch, L. Roest, K. Reimann, L. Van Leuken, O. Wunnicke, J. Zhao, G. Schmitz, M. Mienkina, M. Mleczko, and M. Tiggelman. Ferroelectric and piezoelectric thin films and their applications for integrated capacitors, piezoelectric ultrasound transducers and piezoelectric switches. *IOP Conference Series: Materials Science and Engineering*, 8:012008, 2010.
- [5] T. H. Yeh. Thermal Oxidation of Silicon. *Journal of Applied Physics*, 33(9):2849, 1962.
- [6] P Jain and E.J. Rymaszewski. Embedded thin film capacitors-theoretical limits. *IEEE Transactions on Advanced Packaging*, (3):454–458.
- [7] E. Bouyssou, G. Guégan, S. Bruyère, R. Pezzani, L. Berneux, L. Dantas De Morais, J. P. Rebrassé, C. Anceau, and C. Nopper. Extended reliability study of high density PZT capacitors: Intrinsic lifetime determination and wafer level screening strategy. pages 433–438. IEEE, 2007.
- [8] J. F. Scott. *Ferroelectric Memories*, volume 3 of *Springer Series in Advanced Microelectronics*. Springer Berlin Heidelberg, 2000.
- [9] F. Chen, R. Schafranek, A. Wachau, S. Zhukov, J. Glaum, T. Granzow, H. von Seggern, and A. Klein. Barrier heights, polarization switching, and electrical fatigue in  $\text{Pb}(\text{Zr},\text{Ti})\text{O}_3$  ceramics with different electrodes. *Journal of Applied Physics*, 108(10):104106, 2010.
- [10] X. J. Lou. Polarization fatigue in ferroelectric thin films and related materials. *Journal of Applied Physics*, 105(2):024101, 2009.
- [11] H. W. Song. The Effect of Deposition Temperature of  $\text{Pb}(\text{Zr},\text{Ti})\text{O}_3$ ;(PZT)Thin Films with Thicknesses of around 100 nm on the Piezoelectric Response for Nano Storage Applications. *World Journal of Condensed Matter Physics*, 02(02):51–56, 2012.
- [12] T Arai, T Ohno, T Matsuda, N Sakamoto, N Wakiya, and H Suzuki. Synthesis and electrical properties of  $\text{Pb}(\text{Mg}_{1/3}\text{Nb}_{2/3})\text{O}_3$ - $\text{PbTiO}_3$  epitaxial thin films on Si wafers using chemical solution deposition. *Thin Solid Films*, 603:97–102, 2016.

# Chapter 1

## METAL/INSULATOR/METAL BASED ON Pb(Zr<sub>0.52</sub>Ti<sub>0.48</sub>)O<sub>3</sub> THIN FILMS

### Contents

<b>1.1</b>	<b>Overview of Metal-Insulator-Metal</b>	<b>25</b>
1.1.1	Electrical Parameters in Capacitors	25
<b>1.2</b>	<b>Dielectric Materials Investigations</b>	<b>26</b>
1.2.1	Polarizability in Dielectric Materials	27
1.2.2	Ferroelectricity in Dielectric Materials	29
<b>1.3</b>	<b>Lead Zirconate Titanate Pb(Zr,Ti)O<sub>3</sub></b>	<b>31</b>
<b>1.4</b>	<b>Schottky Model of Metal/Semiconductor Contact</b>	<b>35</b>
<b>1.5</b>	<b>Conclusion</b>	<b>38</b>
	<b>Bibliography</b>	<b>39</b>

The main purpose of this chapter is to introduce some characteristics related to the Metal-Insulator-Metal (MIM) capacitors based on the ferroelectric Pb(Zr<sub>0.52</sub>Ti<sub>0.48</sub>)O<sub>3</sub> thin films. For this goal, the chapter will be divided into four sections.

First section is dedicated to both the presentation of fundamental properties of the parallel plate capacitor and the definition of major properties required in microelectronic applications.

The second part is consecrated to the investigation of the polarizability and ferroelectricity properties of the dielectric materials. This second part also exposes the main advantages of integrating the PZT material in microelectronic devices.

The third section deals with the crystallographic characteristics of the Lead zirconate titanate called PZT for Pb(Zr<sub>0.52</sub>Ti<sub>0.48</sub>)O<sub>3</sub> and the p-type semiconductor behavior of the PZT thin films.

In the last section, the major impact of the surface of PZT and the contact metal/PZT on the electrical performances of capacitors is detailed.

## 1.1 Overview of Metal-Insulator-Metal

A capacitor is a passive electronic component that store energy in the form of an electrostatic field. Basically, a capacitor device consists of two conducting plates separated by an insulator like vacuum, air or dielectric materials. Physically, the capacity to store an electric charge for a given potential difference  $\Delta V$  between the conductor plates represents the capacitance  $C$ . In other words, capacitance is how much charge a capacitor can hold per voltage (i.e., how many coulombs per volt (C/V) or Farad (F)).

In the case of a parallel plate capacitor as shown schematically in Figure 1.1, the capacitance  $C$  is directly proportional to the surface of the plates  $A$  and is inversely proportional to the thickness of insulator  $d$ . Capacitance also depends on the dielectric constant  $\epsilon_r$  of the insulator [1], as defined by Equation 1.1:

$$C = \frac{\epsilon_r \epsilon_0 A}{d} \quad (1.1)$$

Here  $\epsilon_0$  is the vacuum permittivity ( $\epsilon_0 = 8.854 \times 10^{-12}$  F/m). The dielectric constant (symbol  $\epsilon_r$ ) is the ratio of the permittivity of an insulator medium to the permittivity of free space. The permittivity expresses the ability of an insulator medium to polarize in response to an applied electric field.

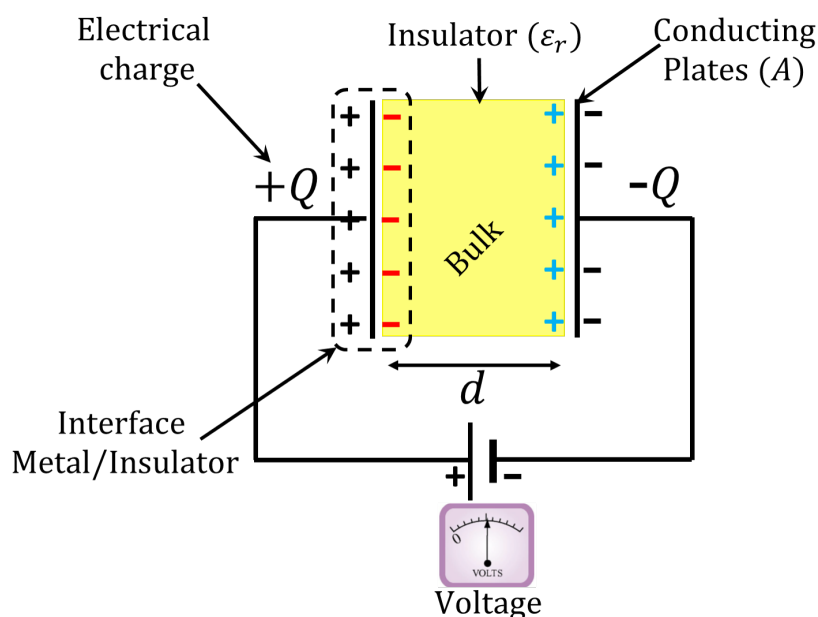


Figure 1.1: Parallel plate capacitor with insulator inserted between the parallel plates. (+ and -) represent the sign of the conducting plates charge  $Q$ , (+ and -) represent the sign of charge  $Q$  stored in the insulator.  $A$ ,  $d$  and  $\epsilon_r$  represent respectively the surface conducting plate, the thickness and dielectric constant of insulator.

### 1.1.1 Electrical Parameters in Capacitors

The improvement of device performances requires the control of some decisive characteristics of MIM such as:

- Surface capacitance: Miniaturization is required to increase the capacitance density ( $nF/mm^2$ ) in order to optimize the space occupied on the printed circuit boards. The necessity to increase the capacitance density promotes the use of new high-permittivity materials. For example, using PZT allows to achieve a capacitance density values up to  $50 nF/mm^2$  [2, 3].

- Loss tangent: it is defined as the quantity used to indicate the energy loss characteristic of a material. This function characterizes the relation between the energy lost per cycle and the energy stored per cycle in the Metal-Insulator-Metal structure as defined by the expression in Equation 1.2:

$$\tan\delta = \frac{\varepsilon''(f)}{\varepsilon'(f)} \quad (1.2)$$

Here,  $\varepsilon'$  represents the part of relative permittivity that increases capacitance,  $\varepsilon''$  represents the loss and  $f$  the frequency. With a very good dielectric material, the loss tangent tends towards zero (for the thin film PZT a loss tangent  $< 4 \%$  is often required) [4, 5].

- Breakdown Field (Voltage): The breakdown field is the maximum permissible electric field through the insulator prior to the destruction of MIM capacitors. Therefore, it is an important electrical characteristic for assessing the intrinsic quality of an insulator. Applications using capacitor with dielectric usually require high breakdown field (typically 2-3 MV/cm). Benhadjala *et al.* [6, 7] have reported breakdown field values between 1.67 and 2.5 MV/cm on PZT and PZT doped with Manganese and Niobium.

Thus, optimization of all these physical properties requires a better understanding of insulator and capacitor used. In this context, we will now discuss on the properties of dielectric materials used in MIM capacitors.

## 1.2 Dielectric Materials Investigations

In crystal or polycrystalline materials with a specific symmetry of the unit cell, the displacement or the orientation of atoms can involve ferroelectric, piezoelectric or pyroelectric effects. On the basis of the symmetry elements of translational position and orientation, there are 230 space groups. Ignoring translational repetition, these 230 groups break down into 32 classes, known as the 32 point groups. The 32 point groups can be classified according to their properties [8, 9] as illustrated schematically in Figure 1.2.

First, it can be seen that 11 of them are centrosymmetric, i.e. they have a center of symmetry implying that they cannot present polar properties. Among centrosymmetric classes, certain electromechanical effects can also appear.

Out of the 21 non-centrosymmetric classes, one displays no piezoelectric effect because the movement of the charges during mechanical solicitation does not induce the appearance of a dipole.

Therefore, 20 present piezoelectric properties, which result in coupling electric field and mechanical stress like Quartz  $\alpha$  ( $\text{SiO}_2$ ) material. Thus, polarization can be induced in a material by the application of an external stress. In this case, we talk of direct piezoelectric effect. Similarly, a material may deform when an electric field is applied; it is the conversed piezoelectric effect.

Within these piezoelectric crystals, 10 present both spontaneously polarized and preferential direction of the polarization called polar axis. These classes are named pyroelectric because their polarization amplitude changes with temperature. It is the case of aluminium nitride (AlN) and zinc oxide (ZnO).

Finally, among pyroelectric crystals, we can distinguish the ferroelectric ones for which the polar axis is mobile in the crystal lattice under external electric field. It is possible to reverse the direction of the polarization when the applied electric field is sufficiently strong. Perovskite materials like  $\text{BaTiO}_3$  or  $\text{Pb}(\text{Zr,Ti})\text{O}_3$  and the Ilmenite family, including Lithium Niobate and Tantalate ( $\text{LiNbO}_3$ ,  $\text{LiTaO}_3$ ), are ferroelectric materials [9].

In the next part, we will describe dielectric and ferroelectric properties through simplified examples.

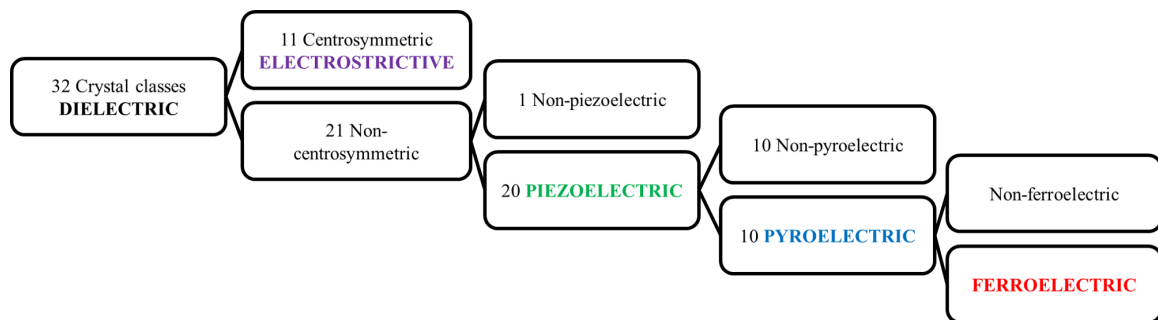


Figure 1.2: Classification of crystals according to their piezoelectric, pyroelectric, ferroelectric and electrostrictive properties [8]

### 1.2.1 Polarizability in Dielectric Materials

Polarizability is the result of displacement and orientation of charges under the effect of the electric field.

More the entities considered are massive, more their mobility is reduced. Also, time required for the movement under electric field is longer. Thus, the duration of polarization establishment defined by a time constant can therefore be associated with each type of displacement mechanism in the dielectric [8, 10].

Basically, all these situations derive from the fundamental principle that, except in vacuum, no system is able to respond instantly to an external stimulation (electrical, optical, etc.). Thus, the response of a ferroelectric dielectric material to electric stimulation is always time (frequency) dependent.

Indeed, under a sinusoidal electric field:  $\vec{E} = \vec{E}_0 \cdot e^{i(2\pi f)t}$ , the polarization ( $\vec{P} = \vec{P}_0 \cdot e^{i((2\pi f)t - \delta)}$ ) displays a delay  $\delta$  (depending on the frequency  $f$ ). Thus, the electric induction  $\vec{D} = \varepsilon_0 \cdot \varepsilon_r \cdot \vec{E}$  will be necessarily sinusoidal with the same delay  $\delta$  as illustrated by Equation 1.3:

$$\vec{D} = \vec{D}_0 \cdot e^{i((2\pi f)t - \delta)} = \varepsilon_0 \cdot \varepsilon_r^* \cdot \vec{E} \quad (1.3)$$

It follows that, for a linearly homogeneous isotropic material, the permittivity is a complex quantity. It is related to the frequency  $f$  as seen in Equation 1.4:

$$\varepsilon_r^*(f) = \varepsilon_r(f=0) \cdot e^{i\delta} = \varepsilon'(f) + i\varepsilon''(f) \quad (1.4)$$

$$\begin{cases} \varepsilon'(f) = \varepsilon_r(f=0) \cdot \cos\delta \\ \varepsilon''(f) = \varepsilon_r(f=0) \cdot \sin\delta \end{cases} \quad (1.5)$$

The  $\varepsilon'$  is the relative dielectric constant,  $\varepsilon''$  the dielectric losses (Equation 1.5). The frequency, as shown in Figure 1.3, is an important parameter which can be used to separate the different contributions of the polarization.

Given the establishment of the external electric field, electronic polarization is due to the displacement of the electron cloud with respect to the nucleus. Electronic polarization dominates in the visible and ultraviolet ranges (from  $10^{14}$  to  $10^{16}$  Hz). Without exception, electronic polarization is present in all dielectric materials.

The atomic (or ionic) polarization related to the displacements of the ions with respect to each other is established more slowly than the electronic polarization. It occurs at frequencies between  $10^{11}$  to  $10^{14}$  Hz.

Under the effect of an external electric field, materials with permanent dipole moments tend to line up. This results in a polarization called polarization by orientation (or dipolar polarization). It occurs at frequencies between  $10^6$  to  $10^{10}$  Hz.

Hopping polarization attributed to jumps of the carriers between two sites occurs at frequencies between  $10^2$  to  $10^6$  Hz.

Interfacial polarization results from the local accumulation of charge carriers due to migration phenomena around defects such as impurities, vacancies, grain boundaries, space charge at interfaces, etc. This polarization is characterized by rather long establishment time. It occurs at frequencies between 0.01 to 100 Hz.

Further, we can introduce the loss tangent  $\delta$ , which is commonly used because it allows to easily compare the ratio of the imaginary and real parts of the dielectric constant giving

access directly to the delay  $\delta$ . In other words, it represents the ratio of the energy dissipated into the dielectric on the accumulated energy [11].

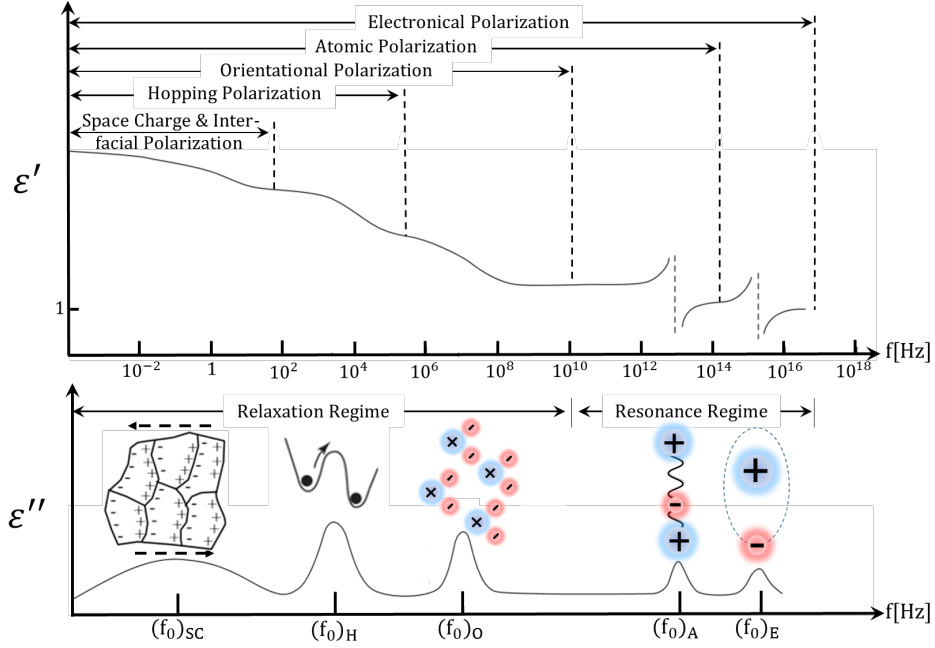


Figure 1.3: Relative permittivity (dielectric constant and loss factor) as a function of frequency [8]

### 1.2.2 Ferroelectricity in Dielectric Materials

Ferroelectricity was first discovered in Rochelle salt in 1920 [12]. It is present in mono or poly-crystalline materials [13]. Ferroelectricity is a property which arises from the asymmetry of certain crystals like Lead Zirconate Titanate below Curie temperature  $T_C$ . Ferroelectricity occurs due to a phase transition from a paraelectric phase characterized by a higher symmetry (cubic in the case of PZT) to a ferroelectric phase characterized by a lower symmetry (e.g. tetragonal). The phase transition in PZT involves, primarily, permanent ion displacements from their equilibrium positions in the paraelectric cubic phase. These displacements lead to the temperature dependent of spontaneous polarization, characteristic to pyroelectrics. The ferroelectrics have the additional property that the spontaneous polarization can be reversed by the application of a suitable external electric field.

Under the application of an electric field, positive and negative charges of a polarizable material move in the opposite direction, creating a dissymmetry responsible for an electric dipole moment  $\vec{P}_i$  in each unit cell as illustrated in Figure 1.4. Ferroelectric materials present a displacement of atoms which remains after removing the applied electric field. This is the state of remanent polarization. By considering the polarization as an order parameter, the behavior of ferroelectric can be modeled by the Landau-Ginzburg-Devonshire theory which is based on the free energy  $F$  [14]. Furthermore, on the macroscopic scale, the electric field applied over the entire volume  $V$  of the dielectric with a presence of all electric dipole

moment  $\vec{P}_i$  in each unit cell induces a macroscopic polarization. The polarization vector  $\vec{P}$  is therefore defined by Equation 1.6:

$$\vec{P} = \sum \vec{P}_i / dV \quad (1.6)$$

Below the Curie temperature  $T_C$  and without external electric field, a spontaneous polarization ( $P_s$ ) develops along at least two symmetries which determine directions. In order to minimize the depolarizing field  $\vec{E}_d$  energy which results from uncompensated polarization charges at the interface, the ferroelectric material tends to create several volume with uniform polarization called domain ferroelectric. This phenomenon constitutes the most natural means by which the system has recourse to remain ferroelectric and minimize its electrostatic.

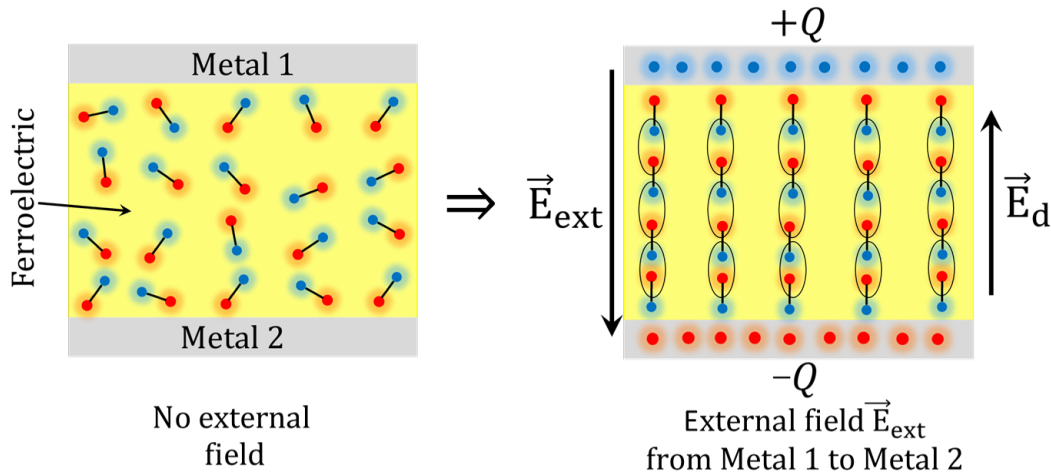


Figure 1.4: Illustration of the alignment of the dipoles in a dielectric under the effect of the applied electric field ( $+\delta \bullet - \bullet - \delta$ )

Now, when the external electric field is initially increased from zero value, the polarization increases as more dipoles are lined up along the electric field direction. When the electric field is strong enough, all dipoles are lined up with the electric field, so the material is in a saturation state  $P_{sat+}$  as illustrated in Figure 1.5. If the applied electric field decreases from the saturation point, the polarization also decreases. However, when the external electric field reaches zero, the polarization does not reach zero. The polarization at the zero electric field is called the remanent polarization  $P_{r+}$  ( $P_{r-}$ ). When the direction of the electric field is reversed, the polarization decreases. When the reverse electric field reaches a certain value, called the coercive field  $E_{C-}$  ( $E_{C+}$ ), the polarization becomes null. By further increasing the electric field in this reverse direction, the reverse saturation  $P_{sat-}$  ( $P_{sat+}$ ) can be reached. When the electric field is decreased from this saturation point  $P_{sat-}$ , the sequence just reverses itself and above  $E_{C+}$ , the polarization can switch towards  $P_{sat+}$ .

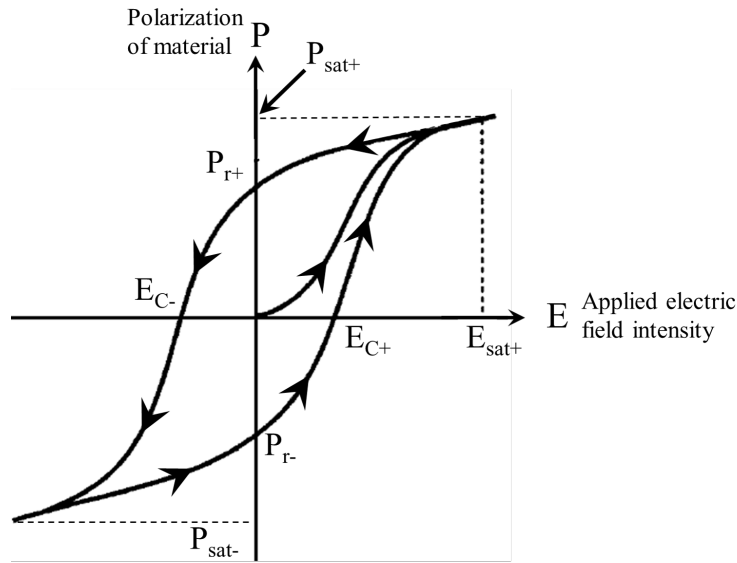


Figure 1.5: Typical ferroelectric hysteresis cycle showing saturation polarization  $P_{sat\pm}$ , remanent polarization  $P_{r\pm}$  and the coercive field  $E_{c\pm}$  [9]

Finally, for ferroelectric dielectric materials, the variation of the dielectric constant (permittivity) and loss tangent with bias voltage present a butterfly curve characteristic due to the high non-linear nature as shown with PZT thin film in Figure 1.6.

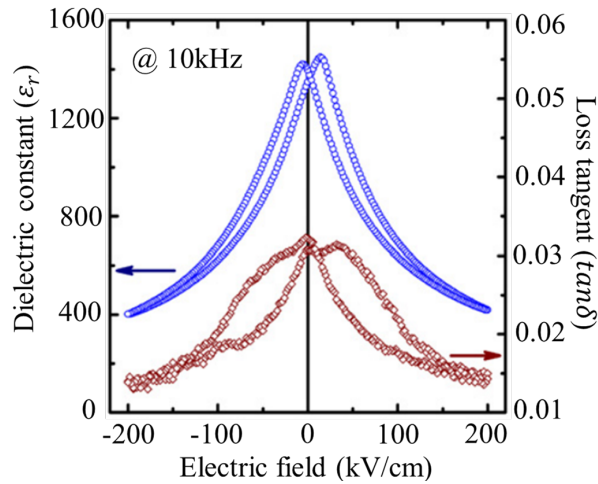


Figure 1.6: Variation of the dielectric constant and loss tangent with electric field (bias voltage) (The thickness of PZT film is  $1 \mu m$ ) [15]

### 1.3 Lead Zirconate Titanate $Pb(Zr,Ti)O_3$

Lead zirconate titanate  $Pb(Zr,Ti)O_3$  (PZT) crystallizes in a perovskite structure [9]. The general formula for perovskite-type oxide is  $ABO_3$ . The unit cell is nearly cubic where



and  $495^\circ C$  for PZO, PZT (with  $Zr/Ti=0.52/0.48$ ) and PTO respectively. Below the  $T_C$ , the structure depends on the percentage of Ti ( $x$ ) in the solution and the temperature. These distortions of the ideal unit cell can be: the tilting of the oxygen octahedra, the displacements of the cations ( $Pb^{2+}$ ,  $Ti^{4+}$  and  $Zr^{4+}$ ) or the distortion of the octahedra. Thus, as can be remarked in Figure 1.8 (a), these modifications lead to the change from paraelectric order to ferroelectric order with presence of tetragonal, rhombohedral or orthorhombic phase.

At room temperature, the lattice parameters of  $PbZrO_3$  in the orthorhombic phase are  $a=5.886 \text{ \AA}$ ,  $b=11.749 \text{ \AA}$  and  $c=8.248 \text{ \AA}$  [20] whereas  $PbTiO_3$  in the tetragonal ferroelectric phase are  $a=b=3.904 \text{ \AA}$ ,  $c=4.152 \text{ \AA}$  [21].

Furthermore, when  $x$  is between 0.45 and 0.5 as shown in Figure 1.8 (b), dielectric and piezoelectric responses of the PZT become optimal as presented in Figure 1.9. This zone is named Morphotropic Phase Boundary (MPB) [22, 23]. The word morphotropic is used to designate an abrupt structure change of a solid solution with the variation in composition. With diffraction measurements, it has been long believed that this phase is simply a mixture of tetragonal and rhombohedral phases [24]. In 2000, however, Noheda *et al.* showed the presence of a monoclinic phase in this area of the phase diagram by using high resolution Synchrotron X-ray diffraction [25]. The presence of this monoclinic phase could be at the origin of high dielectric constants and piezoelectric coefficients properties of PZT in this particular morphotropic zone. It may act as a bridge between the tetragonal and rhombohedral phases [26].

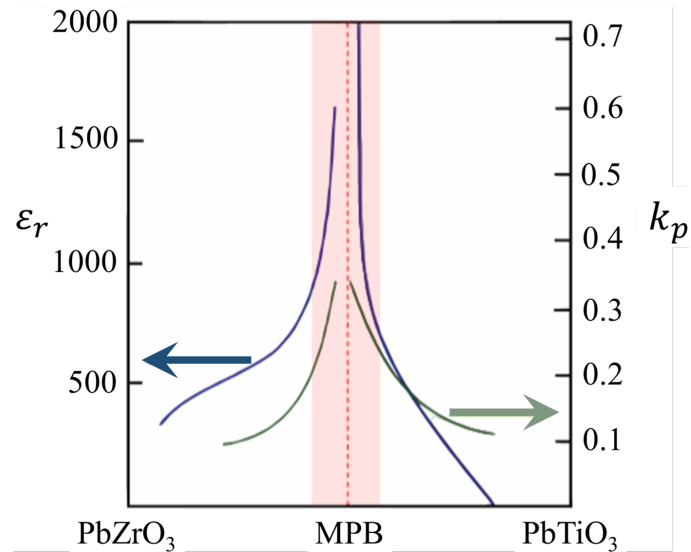


Figure 1.9: Dielectric constant (blue lines) and electromechanical coupling coefficient (green lines) of PZT depending on the zirconium and titanium ratio. Image adapted from Carter and Norton [27]

### • PZT p-Type Semiconductor

Ferroelectric materials like PZT have been previously regarded as an insulator. This approach has been successful to explain the phase transition and ferroelectric switching. Ferroelectric performances of perovskites ( $ABO_3$ ) can be strongly attributed to the nature of

chemical bonds [28]. Basically, chemical bonds of all perovskites were rather considered to be ionic [29]. Recently, ferroelectricity in perovskites has been shown to be quite directly related to the nature of the chemical bonds. First, Cohen gave an origin of the difference of ferroelectric behavior between the  $BaTiO_3$  (BTO) and the  $PbTiO_3$  (PTO) [30]. In fact, with BTO, the Ba-O bond is purely ionic, while in PTO the Pb-O bond is strongly hybridized (the bond is partially covalent) [28]. Furthermore, the Pb-O bonds in tetragonal  $PbTiO_3$  show rather strong covalency, while those in cubic  $PbTiO_3$  are ionic. From these results, we can say that the type of bond constitutes a key factor on the ferroelectric properties of a perovskite materials.

Chen *et al.* [31] explain that the different ferroelectric behaviors of  $ATiO_3$  perovskites are closely related to charges on A and A-O interaction. They also provide that Pb bonds to O mainly with its 6p AOs whereas Ba atoms link to oxygen atoms through the ns-2s bonding. Finally, they show that the bond order of Pb-O is larger than (between 3 and 4 times more) that of Ba-O, indicating that Pb-O is more covalent than Ba-O. Miyazawa *et al.* [32] describe that the Born effective charge (defined as the change of polarization associated to a specific atomic displacement) of Ba is not enhanced as much as that of Pb because Ba has no covalent bond with nearest oxygen ions. In fact, Born effective charge gives the importance of the hybridization or the polarization of an atom and thus play a central role in the study of Coulomb effects. Ghosez *et al.* [33] demonstrate that the covalence effect tend to increase the amplitude of the Born effective charge. Additionally, Born effective charges data from Zhong *et al.* are respectively 3.9 and 2.7 for Pb and Ba [34]. All these previous results are confirmed by the comparison of the ionic states between Pb and Ba effectuated by Kuroiwa *et al.* [35], which give a lower estimation of 1.1 for Pb and a high value of 1.9 for Ba. Globally, these calculations have highlighted that the degree of covalence is higher in Pb-based ferroelectric perovskites than in  $BaTiO_3$ .

Furthermore, this ferroelectric approach fails totally in describing the transport mechanisms or other properties that involve internal mobile charges. In fact, many works [36, 37] regard ferroelectrics as wide bandgap semiconductors, making it easy to adapt well founded theories for semiconductors. However, how to include the semiconductivity is still a difficult problem when analyzing experimental data. Simplified models based on semiconductivity may ignore important effects or limit the range of parameters.

Pintilie *et al.* [28] explain that the Pb-based materials should be regarded rather as a semiconductor than an insulator with a specification on the fact that of their electronic properties might be influenced by the ferroelectric polarization. This assertion have been supported by the analysis performed on the capacitance and hysteresis data of the PZT thin film. Indeed, results of capacitance and hysteresis are coherently explained using a model based on the conventional metal-semiconductor Schottky contact in which the effect of the ferroelectric polarization on band-bending was also considered.

For ferroelectric perovskite oxides such as PZT, three mobile charge carrier participate in conduction: electrons, holes and oxygen vacancies by far the most mobile ionic species. Basically, acceptor dopants increase the concentration of holes and therefore promote the p-type conductivity. Donor dopants increase the concentration of electrons and therefore promote the n-type conductivity.

In the case of PZT film with band gap values in the range of 3.2 - 3.9 eV range (depending

on the Zr/Ti ratio), the conduction type is still the subject of debate, with arguments both for p and n type conduction. In fact, PZTs should be p-type according to the defect chemistry, but often they are regarded as an n-type semiconductor due to a higher mobility of the electrons.

According to Yarmarkin *et al.* [38] and Smyth [39], a variation of the semiconductor type within the film thickness has been considered. Due to the oxygen vacancy accumulation, an n-type layer is supposed to occur at the surface whereas the bulk remains p type. Scott[40] stated that in all ferroelectric thin-film capacitors, the conduction was predominantly due to electrons injected from the cathode, not due to holes (the p-type character of the film). It also pointed out that n-type perovskite ferroelectric films could be formed when samples were deposited in reducing atmospheres. When oxygen is lost in the form of neutral O<sub>2</sub>, it leaves behind electrons, thus the vacancies turn out to be donors. In appearance, n-type perovskite has a darker outlook compared to p-type.

Work of Stolichnov *et al.* [41] on Pt/PZT/Pt capacitors showed that the conduction is supported by holes. Wouters *et al.* [42] also found that the hole barrier is smaller than the electron barrier in their study on Pt/PZT/Pt capacitors.

Following above description, it is important to recall the features of Schottky contact based on the metal/semiconductor (p and n type) model.

## 1.4 Schottky Model of Metal/Semiconductor Contact

When metal and semiconductor (SC) materials are contacted such as to form an interface, the Fermi level of both materials at thermodynamic equilibrium are equal. Thus, the barrier height  $\Phi_B$  between the metal and the semiconductor after contact is given by Equation 1.7 [9]:

$$\Phi_B = \Phi_M - \chi \quad (1.7)$$

Here  $\chi$  is the electron affinity of the semiconductor which represents the difference energy between the conduction band of the semiconductor and the vacuum level.  $\Phi_M$  indicates the work function of the metal i.e. the difference between the Fermi level of the metal and the vacuum level. From the relation giving in Equation 1.7, three kind of contact can be obtained depending on the metal used and the semiconductor. The contacts can be neutral, ohmic (conducting) or rectifying (blocking for one polarity, conducting for the opposite polarity as illustrated in Figure 1.10.

Figure 1.10 (a) presents an ohmic contact for electrons and a rectifying (blocking) contact for holes. In fact, with  $\Phi_M < \Phi_{SC}$  electrons in the metal can encounter the least barrier to their flow into the semiconductor. The electrons are injected into the semiconductor near the interface. Thus, an electric field  $E_i$  oriented from the metal towards the semiconductor develops, preventing further migration of electrons from the metal. This interface electric field is described by an energy variation (or band bending) towards lower energies at the level of depletion layer width  $W$ . Here  $E_{CBm}$  is the Conduction Band minimum,  $E_{VBM}$  Valance Band Maximum, ( $h^+$ ) is the hole, ( $e^-$ ) is electron and  $E_F$  is the Fermi level. The reverse situation  $\Phi_M > \Phi_{SC}$  can be observed in Figure 1.10 (b) which presents an ohmic

contact for holes and a rectifying (blocking) contact for electrons. The two types of carriers cannot flow in the same direction when a certain external voltage is applied on the sample.

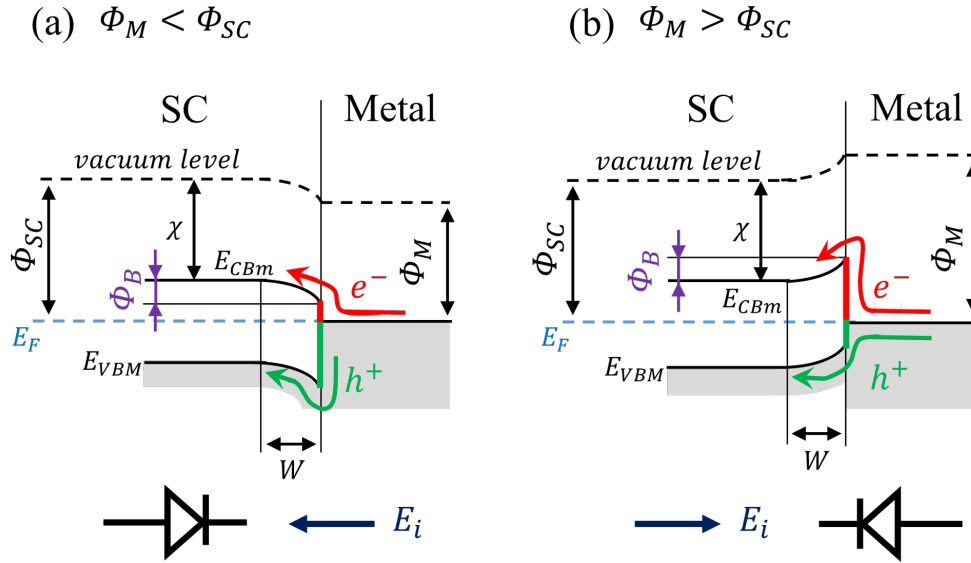


Figure 1.10: Schematics of band bending occurring at a metal/semiconductor interface [43]. The work function of the metal is lower (a) or higher (b) than that of the semiconductor. In the first case, the contact is ohmic for electrons and rectifying for holes. In the second case, the contact is rectifying for electrons and ohmic for holes. Schottky models of the metal-semiconductor  $\Phi_M < \Phi_{SC}$  with barriers width  $W$ . ( $h^+$ ) is the hole and ( $e^-$ ) is electron,  $E_F$  is the Fermi level

Furthermore with the presence of the depletion layer width  $W$ , the PZT thin film is assumed to be divided into a layer depleted of charge, and an interior region of p-type side. The space charge region  $W$ , can be treated as a voltage dependent parallel plate capacitor, with capacitance. In fact, the depleted regions may present a capacitance, which are serial connected to the capacitance of the bulk material if both metal-semiconductor interfaces behave as Schottky contact and therefore may impact on the measured capacitance of MIM structures.

By assuming that the ferroelectrics such as PZT are wide-gap p-type semiconductors and by adapting the theories for metal-semiconductor rectifying contacts to the metal-ferroelectric contact, Pintilie and Alexe [44] gave the specific capacitance  $C$  of the depleted region when an infinite sheet of surface charge ( $A$ ) is used in the depletion approximation (Equation 1.8):

$$C = \frac{\epsilon_0 \epsilon_{st}}{W} = \sqrt{\frac{q \epsilon_0 \epsilon_{st} N_{eff}}{2(V + V'_{bi})}} \quad (1.8)$$

Where,  $N_{eff}$  is the effective charge density in the depleted layer,  $V$  voltage bias,  $V'_{bi}$  the apparent built-in potential.

Thus, the presence of apparent built-in potential  $V_{bi}'$  will lead to the appearance of different values at the two interfaces of a MFM structure, even in the case of perfectly symmetric electrodes. This implies different band bendings at the two electrodes. Additionally, this serial capacitor can modify the total capacitance of MFM capacitor.

• **Interfacial Layer Effects at the Level of Metal-Dielectric Interface**

We have studied an ideal contact between the metal/semiconductor and the possible effect due to the depleted region. However, band bendings will be always affected by the presence of interfacial layer which often induces the additional effect and will tend to modify the result. Interface effects can be induced by the interface ionized (defect) states, thin oxide layers yielding to additional junctions or adsorbed molecules etc.

Apostol *et al.* showed that the band bending of Au/PZT [45] and Cu/PZT [46] are untimely linked to the surface polarization. They demonstrated that the band bending at the electrode interface depends on the polarization orientation. Pintilie *et al.* showed that the polarization charges control the height of potential barriers at the electrode interfaces in the case of Pb(Zr,Ti)O<sub>3</sub> and BaTiO<sub>3</sub> epitaxial films [47]. Bardeen highlighted the importance of interface states in determining the barrier height [48]. Saravanan *et al.* [49] described that the surface states (which will participate to the interface formation) can emerge from chemical and physical imperfections. The use of high resolution transmission electron microscopy for probing the atomic structure of the interface SrRuO<sub>3</sub>/Pb(Zr<sub>0.2</sub>Ti<sub>0.8</sub>)O<sub>3</sub> [50] has showed a reduction of atomic displacements at the interface due to the effect of the interfacial layer which leads to the reduction of the spontaneous polarization.

Furthermore, in PZT films, except the pyrochlore phase [51, 52], which is the most known undesired phase at the surface of the PZT thin film, others authors suggested also the presence of the secondary phase base on the fluorite [53], ZrO<sub>2</sub> [54], PbO [55, 56, 57]. These secondary phases can thus behave as a dead layer [58] at the metal-semiconductor interface and induce a modification of the characteristics at the interface.

In fact, the dead layer is often used in the serial capacitor model to explain the thickness dependence of the dielectric permittivity. Indeed, from the point of view of the dielectric performances, MIM capacitors can be impacted by the presence of interfacial layer (or dead layer with a low dielectric constant) at the level of metal/dielectric interfaces. This additional dead layer induces a capacitance  $C_{interface}$  in series with the  $C_{high-k}$  from the dielectric [59, 60]. The total capacitance  $C_{tot}$  formed by these two layers is determined by the following relation (Equation 1.9):

$$\frac{1}{C_{tot}} = \sum_i \left( \frac{1}{C_i} \right) = \frac{1}{C_{high-k}} + \frac{1}{C_{interface}} = \frac{1}{A \cdot \epsilon_0} \left[ \frac{d_{high-k}}{\epsilon_{high-k}} + \frac{d_{interface}}{\epsilon_{interface}} \right] \quad (1.9)$$

Here  $A$  is the surface plate,  $\epsilon_0$  is the vacuum permittivity,  $d_{high-k}$  and  $d_{interface}$  are respectively the thickness of high-k material and dead layer at interface metal/high-k. From a purely capacitive point of view, the interface layer will dominate the value of total capacitance presented in Equation 1.9 if the thickness of structure decrease. Thus, the control of the presence of these secondary phases at the surface of PZT layer constitutes a real lever in order to broad and improve our knowledge on the electrode/PZT interface properties of capacitor devices.

## **1.5 Conclusion**

In this chapter, we have presented some of the basic properties of Metal-Insulator-Metal structure followed by the presentation of crystalline materials and their properties. A large part of this chapter has been devoted to the description of PZT near the morphotropic phase boundary. Additionally, this chapter have pointed out the importance of both the PZT surface and the electrode/PZT interface in the performance of MIM. Given the impact of the surface states in the real interface metal/semiconductor, this thesis will try to understand the surface (and interface) PZT characteristics by associating the structural, microstructural and physicochemical analyses as well as the electrical performances. Before presenting the electrical response relative to the Pb excess and the post-annealing, in the next chapter, we will first present the different stages of the deposition and the characterization of the PZT based metal/insulator/metal heterostructure and the principles of the main techniques used to characterize the surface and interface chemistry and structure.

## Bibliography

- [1] C. R. Robertson. *Fundamental Electrical and Electronic Principles*. Elsevier Ltd, 3rd edition, 2008.
- [2] Ibrahima Gueye, Gwenaél Le Rhun, Olivier Renault, Emmanuel Defay, and Nicholas Barrett. Electrical response of Pt/Ru/PbZr<sub>0.52</sub>Ti<sub>0.48</sub>O<sub>3</sub>/Pt capacitor as function of lead precursor excess. *Applied Physics Letters*, 111(22):222902, nov 2017.
- [3] Yole. Thin film pzt for semiconductor: Application trends technology update (feram, ipds and mems). *Yole Développement SA*, 2013.
- [4] V. Koval, C. Alemany, J. Brianin, and H. Bruncková. Dielectric Properties and Phase Transition Behavior of xPMN-(1-x)PZT Ceramic Systems. *Journal of Electroceramics*, 10:19–29, 2003.
- [5] X. Chen, H. Fan, and S. Ke. Low-temperature synthesis of (Pb,La)(Zr,Ti)O<sub>3</sub> thick film on Ti substrates by the hydrothermal method using oxide precursors. *Applied Physics Letters*, 88(1):012901, 2006.
- [6] W. Benhadjala, G. Le Rhun, C Dieppedale, F. Sonnerat, J. Guillaume, C. Bonnard, P. Renaux, H. Sibuet, C. Billard, P. Gardes, and P. Poveda. Sol-gel doped-PZT thin films for integrated tunable capacitors. *International Symposium on Microelectronics*, 2015(1):000256–000261, 2015.
- [7] W. Benhadjala, F. Sonnerat, J. Guillaume, C. Dieppedale, P. Renaux, G. Le Rhun, H. Sibuet, and C. Billard. Highly tunable Mn-doped PZT thin films for integrated RF devices. *Additional Conferences (Device Packaging, HiTEC, HiTEN, & CICMT)*, 2015(DPC):002095–002127, 2015.
- [8] K. C. Kao. *DIELECTRIC PHENOMENA IN SOLIDS With Emphasis on Physical Concepts of Electronic Processes*. Academic Press, 2004.
- [9] E. Defay. *Integration of Ferroelectric and Piezoelectric Thin Films*. John Wiley & Sons, Inc, 2011.
- [10] C. Kittel. *Introduction to Solid State Physics, EIGHTH EDITION*. John Wiley & Sons, Inc, 2005.
- [11] C. Huber. *Synthèse et caractérisation de nouveaux matériaux ferroélectriques accordables pour applications hyperfréquences*. . PhD thesis, 2003.
- [12] J. Valasek. Piezo-Electric and Allied Phenomena in Rochelle Salt. *Physical Review*, 17(4):475–481, 1921.
- [13] K. M. Rabe, C. H. Ahn, and J. M. Triscone. *Physics of Ferroelectrics A Modern Perspective*, volume 105 of *Topics in Applied Physics*. Springer Berlin Heidelberg, 2007.
- [14] C. Kittel. *Introduction to Solid State Physics 7th Edition*. 2010.
- [15] M. D. Nguyen, H. Nazeer, M. Dekkers, D. H. A. Blank, and G. Rijnders. Optimized electrode coverage of membrane actuators based on epitaxial PZT thin films. *Smart Materials and Structures*, 22(8):085013, 2013.

- [16] R. W. Schwartz. Chemical solution deposition of perovskite thin films. *Chemistry of Materials*, 9(11):2325–2340, 1997.
- [17] F. Cordero, F. Trequattrini, F. Craciun, and C. Galassi. Octahedral tilting, monoclinic phase and the phase diagram of PZT. *Journal of Physics: Condensed Matter*, 23(41):415901, 2011.
- [18] B. Jaffe, W. R. Cook, and H. Jaffe. Solid solutions of  $\text{Pb}(\text{Ti}, \text{Zr}, \text{Sn}, \text{Hf})\text{O}_3$ . In *Piezoelectric Ceramics*, pages 135–183. Elsevier, 1971.
- [19] B. Noheda and D. E. Cox. Bridging phases at the morphotropic boundaries of lead oxide solid solutions. *Phase Transitions*, 79(1-2):5–20, 2006.
- [20] L. B. Kong, J. Ma, W. Zhu, and O. K. Tan. Preparation and characterization of lead zirconate ceramics from high-energy ball milled powder. *Materials Letters*, 49(2):96–101, 2001.
- [21] K. Iijima, Y. Tomita, R. Takayama, and I. Ueda. Preparation of c-axis oriented  $\text{PbTiO}_3$  thin films and their crystallographic, dielectric, and pyroelectric properties. *Journal of Applied Physics*, 60(1):361–367, 1986.
- [22] V.A. Isupov. Comments on the paper X-ray study of the PZT solid solutions near the morphotropic phase transition. *Solid State Communications*, 17(11), 1975.
- [23] S. K. Mishra, D. Pandey, and A. P. Singh. Effect of phase coexistence at morphotropic phase boundary on the properties of  $\text{Pb}(\text{Zr}_x\text{Ti}_{1-x})\text{O}_3$  ceramics. *Applied Physics Letters*, 69(12):1707–1709, 1996.
- [24] B. Noheda, J. A. Gonzalo, L. E. Cross, R. Guo, S. E. Park, D. E. Cox, and G. Shirane. Tetragonal-to-monoclinic phase transition in a ferroelectric perovskite: The structure of  $\text{PbZr}_{0.52}\text{Ti}_{0.48}\text{O}_3$ . *Physical Review B*, 61(13):8687–8695, 2000.
- [25] B. Noheda, D. E. Cox, G. Shirane, R. Guo, B. Jones, and L. E. Cross. Stability of the monoclinic phase in the ferroelectric perovskite  $\text{PbZr}_{1-x}\text{Ti}_x\text{O}_3$ . *Physical Review B*, 63(1):014103, 2000.
- [26] Z. Wu and H. Krakauer. First-principles calculations of piezoelectricity and polarization rotation in  $\text{Pb}(\text{Zr}_{0.5}\text{Ti}_{0.5})\text{O}_3$ . *Physical Review B*, 68(1):014112, 2003.
- [27] C. B. Carter and M. G. Norton. *Ceramic Materials: Science and Engineering*. Springer New York, 2007.
- [28] L. Pintilie, M. Lisca, and M. Alexe. Epitaxial-quality PZT: Insulator or semiconductor? *Journal of Optoelectronics and Advanced Materials*, 8:7–12, 2006.
- [29] M. E. Lines and A. M. Glass. *Principles and Applications of Ferroelectrics and Related Materials*. Oxford, Clarendon Press, 1977, 1977.
- [30] R. E. Cohen. Origin of ferroelectricity in perovskite oxides. *Nature*, 358(6382):136–138, 1992.
- [31] Z. X. Chen, Y. Chen, and Y. S. Jiang. Comparative study of  $\text{ABO}_3$  perovskite compounds. 1.  $\text{ATiO}_3$  ( $A = \text{Ca}, \text{Sr}, \text{Ba}, \text{and Pb}$ ) perovskites. *Journal of Physical Chemistry B*, 106(39), 2002.
- [32] H. Miyazawa, F. Ishii, E. Natori, T. Shimoda, and T. Oguchi. Contribution of Pb to Ferroelectricity in Perovskite-Type Oxides. *Ferroelectrics*, 301(1):49–53, 2004.

- 
- [33] Ph. Ghosez, J.-P. Michenaud, and X. Gonze. Dynamical atomic charges: The case of  $\text{ABO}_3$  compounds. *Physical Review B*, 58(10):6224–6240, 1998.
- [34] W. Zhong, R. D. King-Smith, and D. Vanderbilt. Giant LO-TO splittings in perovskite ferroelectrics. *Physical Review Letters*, 72(22):3618–3621, 1994.
- [35] Y. Kuroiwa, S. Aoyagi, A. Sawada, J. Harada, E. Nishibori, M. Takata, and M. Sakata. Evidence for Pb-O Covalency in Tetragonal  $\text{PbTiO}_3$ . *Physical Review Letters*, 87(21):217601, 2001.
- [36] J. Robertson. Band offsets of wide-band-gap oxides and implications for future electronic devices. *Journal of Vacuum Science Technology B, Nanotechnology and Microelectronics: Materials, Processing, Measurement, and Phenomena* 18, 1785, 2000.
- [37] W. Doolittle, G. Namkoong, A. G. Carver, and A. S. Brown. Challenges and potential payoff for crystalline oxides in wide bandgap semiconductor technology. *Solid. State. Electron.* 47 (12), 2143, 2003.
- [38] V. K. Yarmarkin, B. M. Goltsman, M. M. Kazanin, and V. V. Lemanov. Barrier photovoltaic effects in PZT ferroelectric thin films. *Phys. Solid State* 42 (3), 522, 2000.
- [39] D. M. Smyth. Defect structure in perovskite titanates. *Curr. Opin. Solid State Mater. Sci.* 1 (5), 692, 1996.
- [40] J. F. Scott. Ferroelectric Memories. *Springer Series in Advanced Microelectronics, (Springer Berlin Heidelberg, Berlin, Heidelberg)*, Vol. 3, 2000.
- [41] I. Stolichnov, A. K. Tagantsev, E. L. Colla, and N. Setter. Cold-field-emission test of the fatigued state of  $\text{Pb}(\text{Zr}_x\text{Ti}_{1-x})\text{O}_3$  films. *Appl. Phys. Lett.* 73 (10), 1361, 1998.
- [42] D. J. Wouters, G. J. Willems, and H. E. Maes. Electrical conductivity in ferroelectric thin films. *Microelectron. Eng.* 29 (1-4), 249, 1995.
- [43] C. S. S. R. Kumar. *Surface Science Tools for Nanomaterials Characterization*. Springer Berlin Heidelberg, 2015.
- [44] L. Pintilie and M. Alexe. Metal-ferroelectric-metal heterostructures with Schottky contacts. I. Influence of the ferroelectric properties. *Journal of Applied Physics*, 98(12), 2005.
- [45] N. G. Apostol, L. E. Stoflea, G. A. Lungu, C. Chirila, L. Trupina, R. F. Negrea, C. Ghica, L. Pintilie, and C. M. Teodorescu. Charge transfer and band bending at  $\text{Au}/\text{Pb}(\text{Zr}_{0.2}\text{Ti}_{0.8})\text{O}_3$  interfaces investigated by photoelectron spectroscopy. *Applied Surface Science*, 273:415–425, 2013.
- [46] L. E. Stoflea, N. G. Apostol, C. Chirila, L. Trupina, R. Negrea, L. Pintilie, and C. M. Teodorescu. Schottky barrier versus surface ferroelectric depolarization at  $\text{Cu}/\text{Pb}(\text{Zr},\text{Ti})\text{O}_3$  interfaces. *Journal of Materials Science*, 49(9):3337–3351, 2014.
- [47] I. Pintilie, C. M. Teodorescu, C. Ghica, C. Chirila, A. G. Boni, L. Hrib, I. Pasuk, R. Negrea, N. Apostol, and L. Pintilie. Polarization-Control of the Potential Barrier at the Electrode Interfaces in Epitaxial Ferroelectric Thin Films. *ACS Applied Materials & Interfaces*, 6(4):2929–2939, 2014.
- [48] J. Bardeen. Surface states and rectification at a metal semi-conductor contact. *Physical Review*, 71(10):717–727, 1947.

- [49] K. V. Saravanan and Raju K. C. J. Understanding the influence of surface chemical states on the dielectric tunability of sputtered  $Ba_{0.5}Sr_{0.5}TiO_3$  thin films. *Materials Research Express*, 1(1), 2014.
- [50] C. Jia, V. Nagarajan, J. He, L. Houben, T. Zhao, R. Ramesh, K. Urban, and R. Waser. Unit-cell scale mapping of ferroelectricity and tetragonality in epitaxial ultrathin ferroelectric films. *Nature Materials*, 6(1):64–69, 2007.
- [51] L. A. Bursill and K. G. Brooks. Crystallization of solgel derived leadzirconatetitanate thin films in argon and oxygen atmospheres. *Journal of Applied Physics*, 75(9), 1994.
- [52] M.A. Subramanian, G. Aravamudan, and G.V. Subba Rao. Oxide pyrochlores A review. *Progress in Solid State Chemistry*, 15(2), 1983.
- [53] A. D. Polli, F. F. Lange, and C. G. Levi. Metastability of the Fluorite, Pyrochlore, and Perovskite Structures in the  $PbO - ZrO_2 - TiO_2$  System. *Journal of the American Ceramic Society*, 83(4):873–881, 2004.
- [54] A. Etin, G. E. Shter, G. S. Grader, and G. M. Reisner. Interrelation of ferroelectricity, morphology, and thickness in sol-gel derived  $PbZr_xTi_{1-x}O_3$  films. *Journal of the American Ceramic Society*, 90(1), 2007.
- [55] J. Wang, J.M. Xue, D.M. Wan, and B.K. Gan. Mechanically Activating Nucleation and Growth of Complex Perovskites. *Journal of Solid State Chemistry*, 154(2):321–328, 2000.
- [56] P. Muralt. PZT thin films for microsensors and actuators: Where do we stand? *IEEE Transactions on Ultrasonics, Ferroelectrics and Frequency Control*, 47(4), 2000.
- [57] I. M. Reaney, K. Brooks, R. Klissurska, C. Pawlaczyk, and N. Setter. Use of Transmission Electron Microscopy for the Characterization of Rapid Thermally Annealed, SolutionGel, Lead Zirconate Titanate Films. *Journal of the American Ceramic Society*, 77(5), 1994.
- [58] M. Stengel, D. Vanderbilt, and N. A. Spaldin. Enhancement of ferroelectricity at metaloxide interfaces. *Nature Materials*, 8(5):392–397, 2009.
- [59] K. Amanuma, T. Mori, T. Hase, T. Sakuma, A. Ochi, and Y. Miyasaka. Ferroelectric Properties of Sol-Gel Derived  $Pb(Zr, Ti)O_3$  Thin Films. *Japanese Journal of Applied Physics*, 32(Part 1, No. 9B):4150–4153, 1993.
- [60] M. Stengel and N. A. Spaldin. Origin of the dielectric dead layer in nanoscale capacitors. *Nature*, 443(7112):679–682, 2006.

# Chapter 2

## EXPERIMENTAL METHODS

### Contents

<b>2.1</b>	<b>Capacitor Deposition</b>	<b>44</b>
2.1.1	Bottom Electrode Deposition on the Silicon Substrate	44
2.1.2	PZT Deposition	45
2.1.3	Top Electrodes	48
2.1.4	Post Metallization Annealing Conditions	49
<b>2.2</b>	<b>X-rays Diffraction</b>	<b>50</b>
<b>2.3</b>	<b>Overview of Electronic Microscopes</b>	<b>51</b>
<b>2.4</b>	<b>Characterizations of Surface and Interface</b>	<b>52</b>
2.4.1	Basic Principles of Photoemission	52
2.4.2	Experimental Set-up of XPS	62
2.4.3	Synchrotron Beamline	66
<b>2.5</b>	<b>Conclusion</b>	<b>72</b>
	<b>Bibliography</b>	<b>73</b>

The second chapter divided into four sections is consecrated to the presentation of experimental methods used to elaborate and investigate the capacitors based on the PZT ferroelectric.

In the first section, we will present the different steps of fabrication of Pt/Ru/PZT/Pt/TiO<sub>2</sub>/-SiO<sub>2</sub> stacks on the silicon wafer. In order to achieve this goal, we will proceed first the bottom electrode fabrication, followed by the PZT thin film elaboration and finally the top electrode deposition. The second section will be entirely consecrated to the detail of X-ray diffraction and Grazing Incidence X-ray diffraction tools mainly used to characterize the texture of PZT thin films. The third chapter will be dedicated to the electron microscopy study, which is used to investigate the surface and interface morphology. Finally, photoelectron spectroscopy used to characterize both the surface and interface of capacitors based on the PZT thin film will be largely addressed. To finish, we will first establish the basic principles of photoelectron, followed by the presentation of the X-ray photoelectron spectroscopy and Hard X-ray photoelectron spectroscopy tools used to study the physicochemical surface and the interface of Metal/PZT.

## 2.1 Capacitor Deposition

In order to select an appropriate deposition technology for a specific application, several criteria have to be considered such as applications or material characteristics [1]. Thus, the procedure of Pt/Ru/PZT/substrates deposition used in this PhD is splitted into three parts which are the manufacture of Pt/TiO<sub>2</sub>/SiO<sub>2</sub> on the silicon (Si) substrate then the deposition of the PZT by sol-gel method and finally the deposition of top electrode materials by sputtering.

### 2.1.1 Bottom Electrode Deposition on the Silicon Substrate

Silicon is the basic material used for manufacturing almost all electronic devices. Silicon is more abundant, cheaper, stronger and presents a larger band-gap allowing it the ability to operate at quite high temperature. However, it is not possible to grow PZT directly on silicon because of interfacial reactions and Pb diffusion into the silicon at elevated temperatures ( $> 500^{\circ}\text{C}$ ). Thus the choice of the bottom electrode is crucial for the growth and the properties of the PZT. Several electrodes such as LaNiO<sub>3</sub> [2], RuO<sub>2</sub> [3], SrRuO<sub>3</sub> [4] or iridium and iridium oxide [5] have been studied. However, the most commonly used bottom electrode to grow PZT is platinum (Pt) [6, 7] because it is chemically inert at elevated temperatures under oxidizing atmosphere (does not oxidize easily) and presents low resistivity. With Pb based materials, the Platinum displays lattice matching, chemical robustness and temperature stability. The standard substrate used for PZT deposition is Pt/TiO<sub>2</sub>/SiO<sub>2</sub>/Si heterostructures [8] as described in Figure 2.1. The manufacturing steps before depositing PZT on the 200 mm diameter (8 inches) 750  $\mu\text{m}$  thick standard Si (100) wafer will be described in the following part.

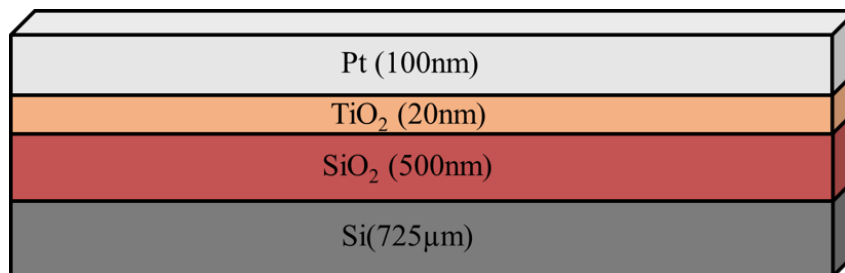


Figure 2.1: Schematic Pt/TiO<sub>2</sub>/SiO<sub>2</sub>/Si substrates

First, the silicon wafers are cleaned using a standard RCA cleaning process [9] in order to remove any organic, particle and metallic contamination which may be present on the surface. After cleaning, a layer of SiO<sub>2</sub> [10] serving as a passivation is thermally grown. This step is carried out at temperature of  $1050^{\circ}\text{C}$  in a conventional furnace (Tempress) in the presence of oxygen and water vapor. The cooling is carried out under inert atmosphere (N<sub>2</sub>). Furthermore, temperatures employed for the crystallization of PZT are greater than  $500^{\circ}\text{C}$  (temperature at which the perovskite phase starts to form). At this temperature, there is a significant risk of diffusion of Pb from the PZT layer down to the substrate because Pt does not constitute a good diffusion barrier. In order to prevent the diffusion effect of Pb down to the Si substrate, a barrier layer, such as the TiO<sub>2</sub> is deposited between the platinum and the SiO<sub>2</sub> layers.

Further, the adhesion of platinum or any metal on SiO<sub>2</sub> is low [11]. This situation induces the use of a suitable adhesion layer between the platinum and the SiO<sub>2</sub>. Lots of materials

such as zirconium, tantalum and their oxides [12, 13, 14] are tested but  $\text{TiO}_2$  (addition to the role of diffusion barrier) is the material most frequently used as adhesion layer [15]. The deposition of 10 nm of titanium by sputtering is performed at  $350^\circ\text{C}$  under argon. The wafer is then annealed at  $750^\circ\text{C}$  under  $\text{O}_2$  to form around 20 nm of  $\text{TiO}_2$ . The layer is shown in orange in Figure 2.1.

Pt (100 nm) layer is then deposited at  $450^\circ\text{C}$ . This temperature promotes the (111) Pt orientation and tensile stress in the Pt film. The tensile stress is caused by the differences in thermal expansion coefficients of the Pt film and the Si substrate [16]. In case of lower deposition temperature, for example  $25^\circ\text{C}$ , both (111) and (100) orientations occur. According to Cuff *et al.* [17], Pt deposited at  $25^\circ\text{C}$  undergoes a small compressive stress and when the deposition temperature rises, Pt stress becomes more tensile [17]. The Pt orientation used to be a crucial point, because it defined the orientation of PZT [18]. Nowadays, this issue has been overcome with the single crystallized PZT layer acting as a seed layer. The latter guarantees the (100) orientation of the entire PZT film (with 10 % Pb excess) fabricated in CEA-LETI cleanrooms. In this thesis, platinum layer was deposited at  $450^\circ\text{C}$ .

### 2.1.2 PZT Deposition

Sol-gel method is one of the most employed method in the microelectronics industry for growing PZT films [19, 20, 21]. The sol-gel process has the advantage of being easy to implement at the foundry [21, 22]. In addition, this method easily allows to adjust the proportions of the different constituents of PZT solution. The PZT solution used in this study is produced by Mitsubishi Materials Corporation from Japan. The solvent made of 1-butanol [ $\text{C}_4\text{H}_9\text{OH}$ ] and propylene glycol [ $\text{CH}_3\text{CH}(\text{OH})\text{CH}_2\text{OH}$ ] allows to stabilize the solution over time and control the rheological properties of the sol [23]. The PZT precursors used are lead acetate trihydrate [ $\text{Pb}(\text{CH}_3\text{CO}_2)_2 \cdot 3\text{H}_2\text{O}$ ], titanium tetra-iso-propoxide [ $\text{Ti}(\text{i-OC}_3\text{H}_7)_4$ ] and zirconium tetra-nbutoxide [ $\text{Zr}(\text{n-OC}_4\text{H}_9)_4$ ]. This metal-organic solution has a very specific composition, in order to achieve the desired morphotropic composition of the PZT, which is 52 % of Zr and 48 % of Ti [24]. Note that during this research work, different proportion of lead acetate is added to the solution (Pb excess from 10 % to 30 %) in order to compensate the amount of Pb lost. These loss of Pb are mainly caused not only by the evaporation of Pb during the annealings but also the diffusion of the Pb at Pt/ $\text{TiO}_2$  interface. The sol-gel method [25] used during this work to deposit four layers thick PZT film is described hereafter:

**Sol-Gel Deposition Process:** During this work, 220 nm thick PZT films were formed by stacking four layers of 55 nm each. The deposition process by sol-gel [26] is illustrated in Figure 2.2. The first layer (55 nm), which serves as a seed layer is deposited by spin coating, drying, calcination (with  $n=1$ ) and crystallization. Following that, the spin coating, drying and calcination steps are again performed three times ( $n=3$ ) in order to deposit the second, third and fourth layers. Finally, a re-crystallization step is performed after calcination of the fourth layer.

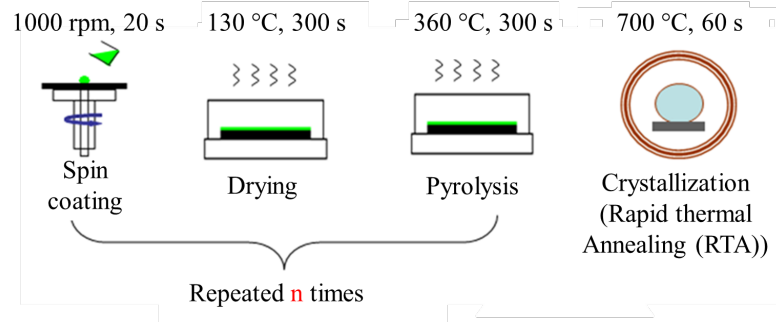


Figure 2.2: Sol-gel process flow used for PZT (4 layers of 55 nm) deposition

**Spin Coating:** The purpose of this step is to coat uniformly the wet solution containing the precursors on the wafer (Pt/TiO<sub>2</sub>/SiO<sub>2</sub>/Si) as presented in Figure 2.3. First, a known volume of precursors is dispensed on the surface of the substrates by using a pipette or pipettor and the plate is then rotated. In contact with the water present in air, sol is hydrolyzed to form a gel on the surface of the wafer. Further, the thickness of a unit layer of PZT depends on centrifugal conditions. The parameters affecting the thickness are the rotation speed, the acceleration and the rotation time. The typical spin coating parameters are set to 1000 rpm (revolution per minute) with 1500 rpm/s acceleration for 20s spin coating duration for our PZT layers.

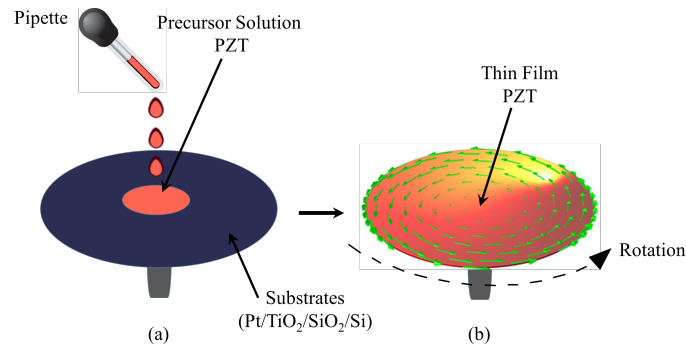


Figure 2.3: Coating processes of a solvent on a substrate by spin coating (a) First, the substrate is coated with the solution containing the precursors dissolved in a solvent by using a pipette (b) The substrate is rotated at high speed and the majority of the excess solution is flung off the side by the centrifugal force as shown by the arrows. Further, the centripetal force combined with the surface tension of the solution pulls the precursors coating into an even covering.

**Drying and Calcination:** The purpose of these steps is to obtain a dry amorphous layer without any organic compounds. These two steps are achieved on hotplates. The drying is done at 130°C for 5 minutes. During this step, the remaining solvent in the gel is evaporated. The calcination is operated at 360°C. During calcination, the remaining organic compounds are eliminated. This step is critical because it is accomplished at a temperature at which

the PbO can evaporate ( $T > 300^\circ\text{C}$ ). This may lead to Pb deficiencies and can impact the ferroelectric properties of the film, or even prevent crystallization into a perovskite phase.

**Crystallization:** This step is carried out in a Rapid Thermal Annealing (RTA) furnace. After calcination, the PZT is still in the amorphous state. To crystallize the PZT in the perovskite phase, the wafer has to reach at least  $500^\circ\text{C}$  [1]. Infrared lights are used to heat the wafer by radiation. This type of annealing is extremely fast. During this step, the thin layer of PZT crystallizes in perovskite phase. PZT is heated at  $700^\circ\text{C}$  for 1 minute under an oxygen flow. The rise of the temperature is higher than  $10^\circ\text{C}/\text{sec}$  and have to be finely controlled in order to prevent the film from cracking. The pressure of oxygen in RTA annealing chamber is at atmosphere.

In this thesis, four 200 mm wafers of PZT thin films at the morphotropic phase boundary composition (Zr/Ti: 0.52/0.48) with 220 nm of total thickness were elaborated at the MINATEC High-Technologies Building cleanrooms at the CEA-LETI (Grenoble). Each sample is composed with four layers of 55 nm of thickness as we can see in Figure 2.4.

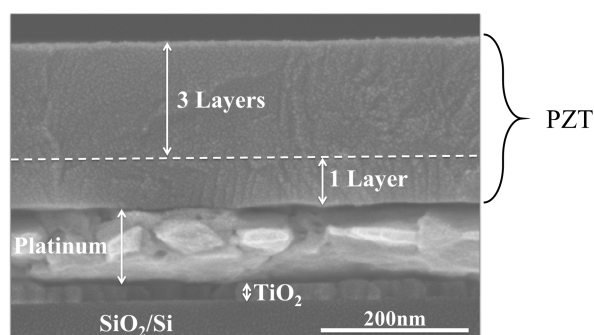


Figure 2.4: SEM cross section of PZT/Pt/TiO<sub>2</sub>/SiO<sub>2</sub>/Si stack

Different composition of Pb excess to compensate the Pb lost during calcination were used for fabricating these samples as presented schematically in Figure 2.5. Four samples, each with 2 sol-gel layers 10 % excess Pb sandwiched by two layers with 10, 15, 20 and 30 % excess Pb, hereafter referred to as PZT10, PZT15, PZT20 and PZT30 have been elaborated. This enables us to study structural microstructural and physico-chemical properties of PZT thin films depending of the Pb excess effects. The use of Pb excess only in the 1<sup>st</sup> and 4<sup>th</sup> layers of PZT film is explained by the fact that, these two layers are more exposed to a high temperature during the crystallization annealing phases (RTA). This leads to greater loss of Pb during RTA phases and therefore, we need to add an excess of Pb.

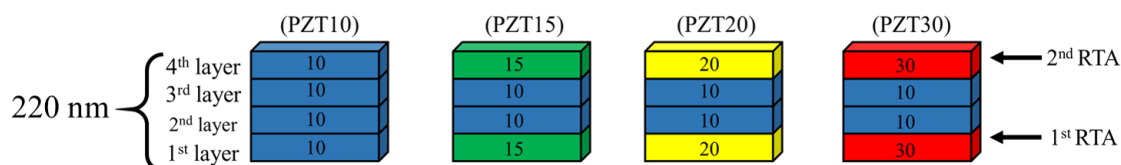


Figure 2.5: Stacking of PZT10, PZT15, PZT20 and PZT30 samples depending on the Lead excess amount contained in the first/second/third/fourth layers

### 2.1.3 Top Electrodes

In order to perform electrical characterizations (Capacitance, loss tangent and breakdown voltage) at laboratory and *operando* hard X-ray photoelectron spectroscopy (HAXPES) measurements under biasing at synchrotron beamline, the deposition of top electrodes is required. Deposition of top electrode materials are carried out by sputtering at room temperature.

For electrical characterizations, top electrodes (Pt/Ru) are made with one layer of 5 nm of Ru then followed of 100 nm of Pt as illustrated in Figure 2.6 (a.1). Following the sputtering deposition of top electrodes of Pt/Ru, PZT and Pt/Ru layers are patterned with a specific design to obtain the desired devices. This step allows to access the bottom electrode contact during electrical measurements.

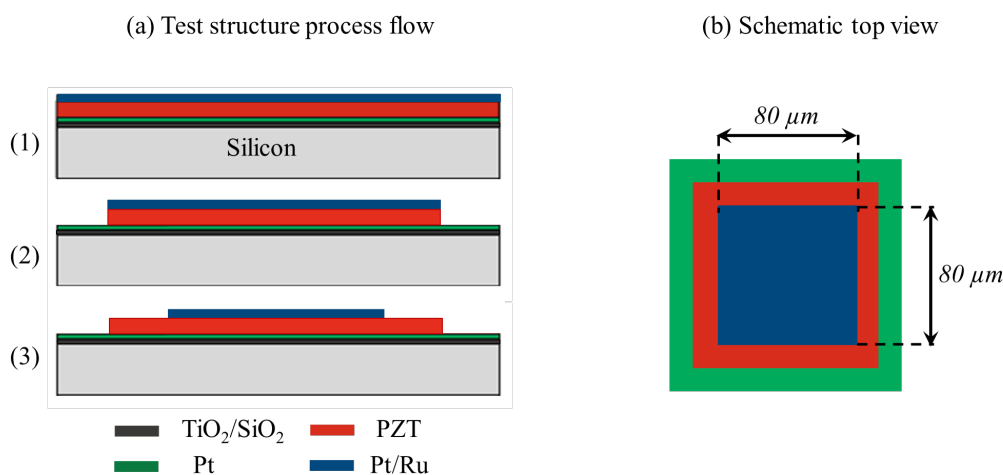


Figure 2.6: Schematic flow process of Pt/Ru/PZT/Pt stack patterning: (a.1) Pt/Ru/PZT/Pt layers (a.2) Pt/Ru and PZT etching (a.3) patterning of capacitor (BE: Bottom electrode and TE: Top electrode) and (b) top view of the schematic devices

The first step consists in removing (stripped) a part of PZT in order to obtain an access to the bottom electrode. For that, we deposit a negative photosensitive chemical resist, then, carry out a photolithography process and finally perform a dry etching by Ion beam etching (IBE) on the PZT layer until reach the Platinum layer localized underneath the PZT layer as illustrated in Figure 2.6 (a.2).

The last step of the patterning [9] is performed by depositing a positive photosensitive chemical resist on the Pt/Ru surface. The sample is then partially protected of UV light by a mask containing the desired pattern. Therefore, after insolation, the parts of the resist protected by the mask stay on the wafer after development. The parts exposed to the UV are disintegrated after development and reveal the Pt/Ru electrode. Pt/Ru electrodes is then etching down to the PZT layer. Finally the resist is removed with acetone and isopropyl alcohol (IPA) as seen in Figure 2.6 (a.3) and Figure 2.6 (b). Afterwards, capacitor with  $(80 \times 80) \mu\text{m}^2$  of area is cut from the wafer. Now the process of device fabrication is finished and MIM capacitors based on the PZT oxide are ready for testing as shown in Figure 2.6 (b).

According to the very low values of inelastic mean free paths (IMFPs) of electrons in the matter, during the *operando* HAXPES experiments, top electrodes consist of one layer of 5 nm Ru followed with thinner Pt (5 nm) layer (contrary to the thicker Pt (100 nm) used for electrical measurements) as illustrated in Figure 2.7 (a). Furthermore, even though the patterning process of contact (Pr/Ru) is the same with the ones performed in Figure 2.6, larger area contact ( $(1 \times 1)mm^2$ ) is used here for *operando* HAXPES experiments as shown in Figure 2.7 (b).

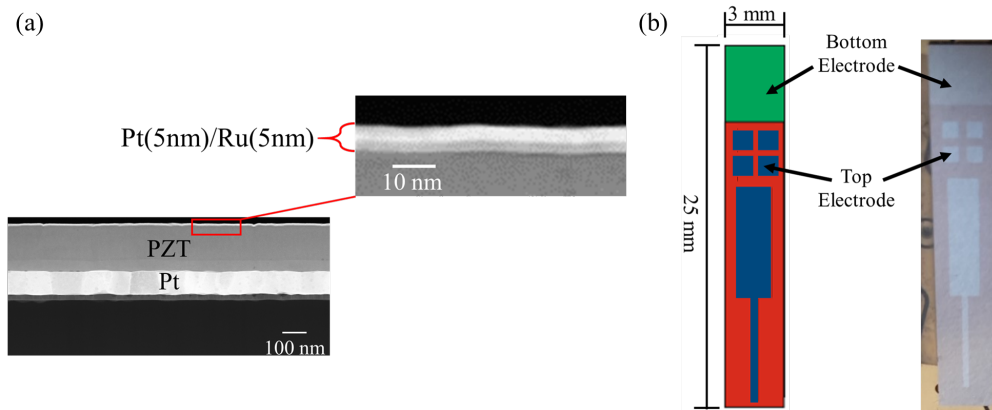


Figure 2.7: Pt/Ru/PZT/Pt (a) Cross section of the Pt/Ru/PZT/Pt stack obtained by STEM and (b) top view of the schematic and actual device

#### 2.1.4 Post Metallization Annealing Conditions

In order to investigate the post metallization annealing (PMA) effect on the capacitor based on the PZT with different Pb excess rate used in the first and fourth layers, we annealed all Pt/Ru/PZT/Pt samples. PMA were carried out at CEA-LETI with an annealing furnace as schematically illustrated in Figure 2.8 with a top and bottom heating, sample and the process tubes. In order to prevent all contamination at high temperatures, a constant flux of pre-heated  $O_2$  passes over the annealing chamber before the introduction of samples. Samples are then annealed at  $500^\circ C$  under  $O_2$  at atmospheric pressure during 30 min. This step allows to analyze the evolution of electrical performances of capacitor and the chemistry of Pt/Ru/PZT top interfaces.

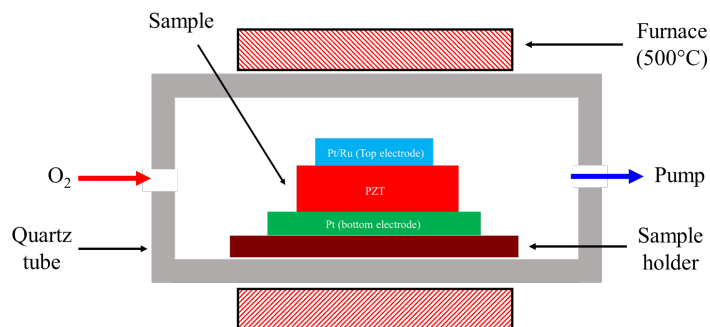


Figure 2.8: Schematic representation of the PMA furnace of Pt/Ru/PZT/Pt samples

## 2.2 X-rays Diffraction

X-ray Diffraction (XRD) is used to provide important information on the crystal orientation. Using  $\theta/2\theta$  scans, information about the growth axis perpendicular to the surface of the substrate can be determined. For this type of measurement, the incident X-ray beam is fixed while the movements of the sample ( $\theta$ ) and the detector ( $2\theta$ ) are coupled. As shown in Figure 2.9 (a), this method consists in sending an X-rays beam with an angle of incidence  $\theta$  on the surface of the sample. In this way, the planes (hkl) parallel to the surface of the substrate will be successively brought into a diffraction condition. According to the Bragg condition, the different scattered beams interfere constructively only when the angle of diffusion is equal to the angle of incidence, which results in the following Equation 2.1:

$$2d_{hkl}\sin(\theta) = n\lambda \quad (2.1)$$

Where,  $d_{hkl}$ , the distance between the planes of Miller indices hkl,  $n$  the order of the diffraction,  $\lambda$  the X-ray wavelength and  $\theta$ , the incidence angle [27]. XRD ( $\theta/2\theta$ ) measurement was performed during this PhD by using a XPER PRO MRD XL from PANALYTICAL with  $CuK_{\alpha}$  radiation ( $\lambda = 0.15405nm$ ).

Furthermore, surface texture can be obtained with Grazing Incidence X-Ray Diffraction (GIXRD) [28, 29]. It was also carried out to obtain information regarding surface crystallography. The advantage of grazing incidence lies in the possibility of controlling the penetration of X-rays into the material. It is thus possible to probe separately different depths of a material. When the incident beam is close to or below the critical angle, the total external reflection surface sensitivty is enhanced. The in-plane diffraction measurements were performed on a Smartlab Rigaku 5-circles [30], using an incidence angle ( $\alpha_i = \omega$ ) of  $0.5^{\circ}$  as can be shown in Figure 2.9 (b). The diffracted X-ray beam ( $2\theta\chi$ ) is recorded for an azimuthal range from  $15$  to  $65^{\circ}$  while keeping the angle ( $\alpha_f = \theta$ ) of  $0.5^{\circ}$  constant with respect to the sample surface.

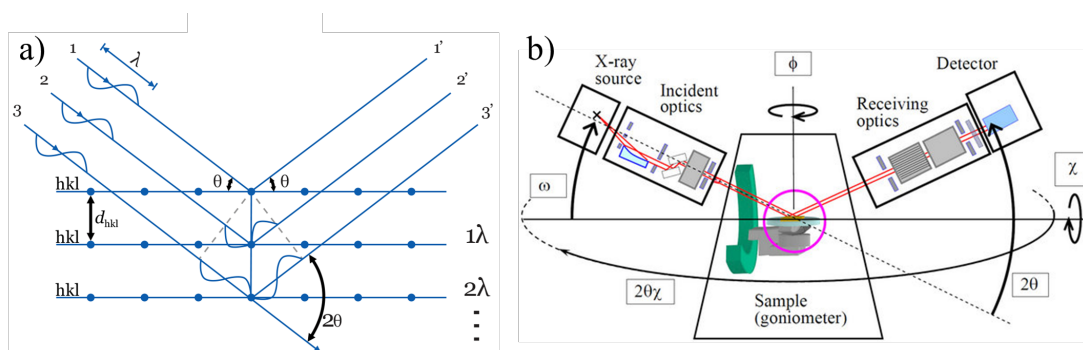


Figure 2.9: Schematic illustration X-ray diffraction in  $\theta/2\theta$  geometry with plane family (hkl), incident beam (1, 2, 3) and scattered beam (1', 2', 3') and (b) A schematic illustration of 5-circle goniometer system [30].

## 2.3 Overview of Electronic Microscopes

The main interactions exploited in electron microscopy [31], shown in Figure 2.10 (a), can be summarized in two different types of interactions [32]:

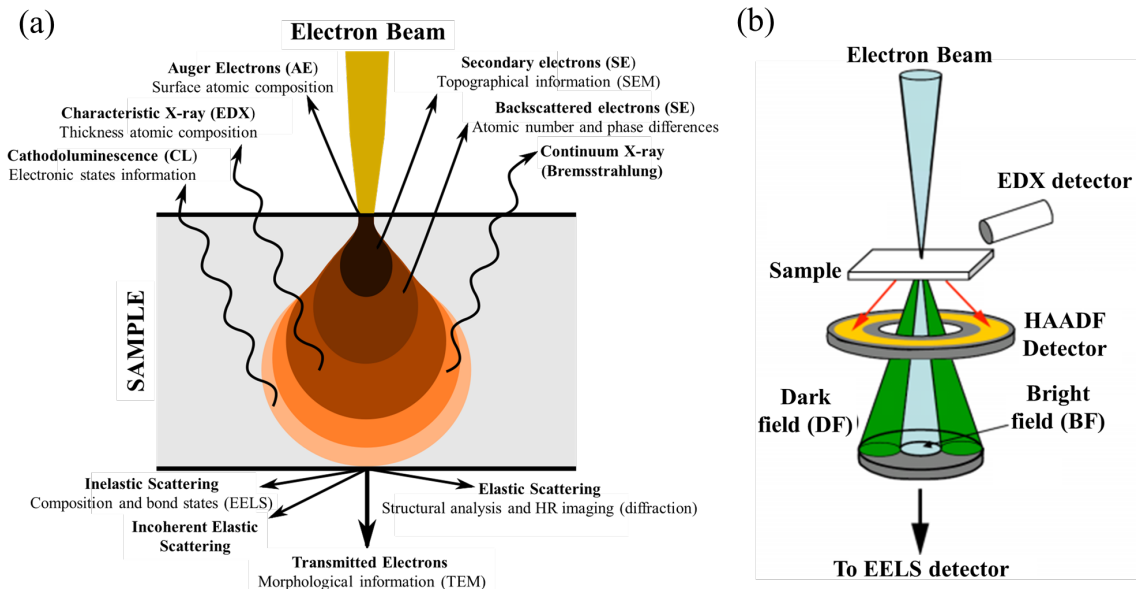


Figure 2.10: (a) schematic diagram illustrating phenomena resulting from the interaction of highly energetic electrons with matter [33] and (b) Probe configuration in a Scanning Transmission Electron Microscopy [34].

First is the elastic interaction which results in no loss of energy and leads to Rutherford scattering or back scattering and electron diffraction.

Second is the inelastic interaction where the kinetic energy of the incident electron changes and can induce the inner-shell ionization, braking radiation (Bremsstrahlung), secondary electrons, phonons, plasmons, cathodoluminescence.

Experimentally, Scanning Electron Microscopy (SEM), which is based on the secondary electrons are utilized when examining thick or bulk specimens while Transmission Electron Microscopy (TEM), which is based on the transmitted electrons used to examine a thin specimens. Further, the addition of scanning coils on the TEM can lead to the creation of a scanning TEM (STEM).

As illustrated in Figure 2.10 (b), STEM can allow to measure, Bright Field (BF: forward elastic scattered), Dark Field (DF: forward diffraction scattered), High Angle Annular Dark Field (HAADF: Rutherford scattered), Electron Energy Loss Spectroscopy (EELS:), Electron Energy Loss Spectroscopy (EELS: lost energy distribution due to inelastic scattering through the sample) and Energy Dispersive X-ray (EDX: X-rays generated from electron excitations in the sample)

During this work, Scanning Electron Microscopy is used in backscattering mode. EDX/-STEM and HAADF/STEM measurement are performed with Transmission Electron Microscopy.

## 2.4 Characterizations of Surface and Interface

Physicochemical properties of surfaces and interfaces can be substantially different from those encountered in bulk materials. Understanding the important role played by the surface and interface requires the use of specialized characterization processes. Although, methods of analyzing materials are numerous. Surface-sensitive spectroscopies, such as photoemission (Photoelectron spectroscopy (PES)), have greatly advanced physicochemical knowledge of surfaces and interfaces. PES is based on the photoelectric discovered by Hertz in 1887 [35] and explained theoretically by Einstein in 1905 in terms of quantum physics [36]. This theory allows him to obtain the Nobel Prize in 1921. According to the importance of the PES tool, in the next section, we will recall concepts and theories that describe the photoemission processes, allowing to deduce the electronic structure of a material.

### 2.4.1 Basic Principles of Photoemission

Photoemission occurs when a light beam (photon for example) with energy  $h\nu$  greater than the work function  $\Phi_W$  of the material illuminates the sample [37]. For an electron with binding energy  $E_{bin}$ , the photon with energy  $h\nu$  can cause the ejection of a photoelectron in the vacuum level with kinetic energy  $E_{kin}$ . In fact, during the process of photoionization, the ejection of an electron will result in the formation of a positive ion ( $I^+$ ). The energy required to cause the ejection of an electron is known as ionization energy or electron binding energy. Overall, ionization energy will depend on the location of the electrons in preference to the nucleus of the atom. As electrons are arranged in orbitals surrounding the atomic nucleus, the ionization energy will be higher or lower depending on whether the electrons are located in the core or valence shell. Core electrons, which are closer to the nucleus, will require more energy to be ejected. Furthermore, each chemical element has a different number of protons in the nucleus, resulting in a unique set of ionization energies for every element. Thus, from that, energy conservation allows us to write (Equation 2.2):

$$E_{kin} = h\nu - E_{bin} - \Phi_W \quad (2.2)$$

Further, experimentally the sample is electrically connected to the spectrometer. They have a common Fermi level. In this way, the kinetic energy measured is calibrated relatively to analyzer  $\Phi_{Sp}$  as seen in Figure 2.11 [37].

By using a common Fermi level, the measured kinetic energy can be obtained with Equation 2.3 and it may allow to determine the chemical elements within a sample.

$$E_{kin}^{meas} = E_{kin} - \Phi_{analyzer} = h\nu - E_{bin} - \Phi_W - (\Phi_{Sp} - \Phi_W) = h\nu - E_{bin} - \Phi_{Sp} \quad (2.3)$$

However, the previous description of photoelectric emission in Equation 2.3 can not clarify very well the different phases of the photoemission process as we will detail later with the three step model.

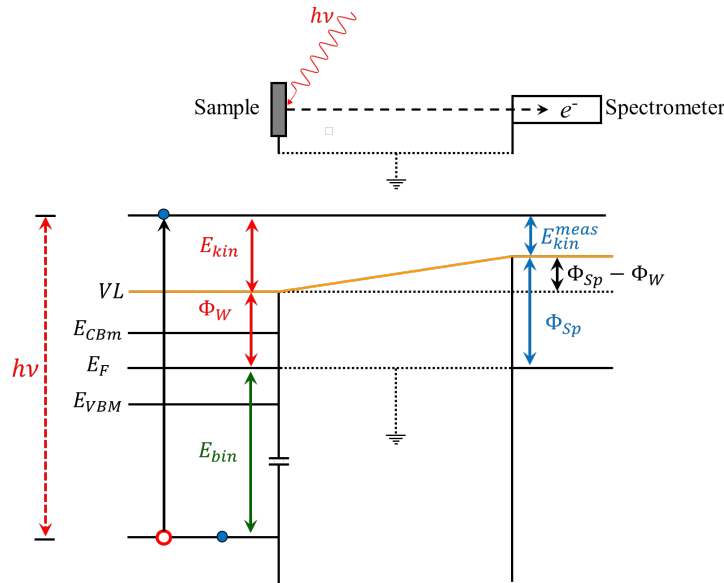


Figure 2.11: Energy level diagram from a sample to the spectrometer [38].  $VL$ : Vacuum Level,  $E_{CBM}$  Conduction Band minimum,  $E_F$  Fermi Level,  $E_{VBM}$  Valence Band Maximum, electron (blue circle) and empty orbital (red empty circle)

### Three Step Model of Photoemission Process

Although, the photoemission process is a complex quantum mechanical process taking place in a single step, Berglund and Spicer in 1964 introduced a simpler more pedagogic model allowing to describe the photoemission process in the material [39]. This approach called three step model, in which the photoemission process can be described in terms of three independent steps: (1) the probability of excitation in the bulk solid, (2) the probability of scattering of the excited electron on its path to the surface by the atoms constituting the solid, (3) the probability of transmission through the surface potential barrier into vacuum as sketched in Figure 2.12.

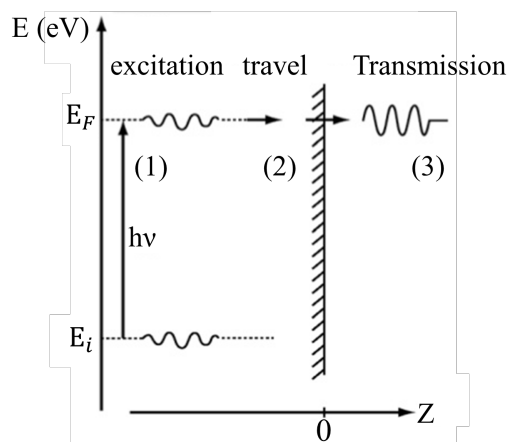


Figure 2.12: Illustration of the three-step model in PES [39].

### • Step I: Photoexcitation of the Electron in the Solid

The photoionization of the atom results from an excitation of an electron in atom by a photon with energy  $h\nu$ . This photoelectron can be localized either in valence band or the discrete core levels. The process is subject to a certain transition probability determined by the photoionization cross section ( $\sigma$ ) of the electron. This photoionization cross section is associated with the probability of interaction between the photon and the electron.

**Photoionization Cross Section ( $\sigma$ ):** Experimentally, the transition probability is often estimated using the photoionization cross section ( $\sigma$ ) of the electron. The photoionization cross section ( $\sigma$ ) depends on the type of material, the level of the electron considered and the energy of the incident photons. However, the study of the angular distribution  $\Omega$  of electrons ejected from atoms in the photoionization process is significance in the understanding of the transition probability in the solids. Thus the photoelectron angular distribution for circular polarized and unpolarized photon may be written as in Equation 2.4 [40]:

$$\frac{d\sigma_i}{d\Omega} = \frac{\sigma_i}{4\pi} \left[ 1 - \frac{\beta}{2} P_2(\cos\theta) + \left( \frac{\gamma}{2} \sin^2\theta + \delta \right) \cos\theta \right] \quad (2.4)$$

Where  $\beta$  the dipole parameter,  $\gamma$  et  $\delta$  are two nondipolar parameters,  $\theta$  is the angle between the vectors of propagation of photon and photoelectron.  $P_2$  is the second order Legendre polynomial. For instance, cross sections for elements with  $Z = 1$  to  $Z = 103$  have been calculated using the Hartree-Fock one-electron central potential and the dipole approximation [41, 42].

### • Step II: Travel of the Photoelectron to the Surface

Once that the electron is emitted, the probability for reaching the surface depends on both the material and the kinetic energy of the electron. Indeed, during transport through the sample, the electron can undergo elastic and inelastic scattering by the Coulomb potential of neighbouring atoms, which can modify its energy.

**Inelastic Mean Free Path ( $\lambda_e$ ):** It represents the average length of an electron traveled between two successive inelastic scattering events. It strongly depends on the kinetic energy of the particle and the medium in which the particle moves. A predictive model proposed by Tanuma Powell and Coll [43] presented in Equation 2.5 can be used to determine the IMFP:

$$\lambda_e = E/E_p^2 [\beta \ln(\gamma E) - (C/E) + (D/E^2)] \quad (2.5)$$

Where  $E$  is the kinetic energy of the electron considered,  $E_p$  the energy of the plasmons and  $\beta$ ,  $\gamma$ ,  $C$  and  $D$  are adjustable parameters. This relation takes into account only inelastic electron-electron interactions in atom and conduction plasmons. However, the data fit so-called universal curve shown in Figure 2.13 is a good estimation of the free path for many

materials.

Indeed, depending on the energy range used, we can increase largely the IMFP. Utilizing photons with high energies, the inelastic mean free depth of photoelectrons increase and allows to probe electronic structures depth in the bulk and buried interfaces with which conventional XPS are difficult to cope. In fact, The probing depth of lab-based XPS can be just a few angstroms according to the universal escape depth curve. However, low energy lasers or high-energy photons available from the synchrotron facility can be used to probe the bulk or interface of materials. The low-energy approach is limited by the finite number of available lasers and by the energy level excitable by the low-energy lasers (no access to the core levels). On the other hand, it is becoming easier to probe the bulk structure at the high kinetic energy side of the curve because of the development of high-energy beamlines at synchrotron facilities (tunable X-rays and high brightness can overcome the low cross section at hard X-ray energy).

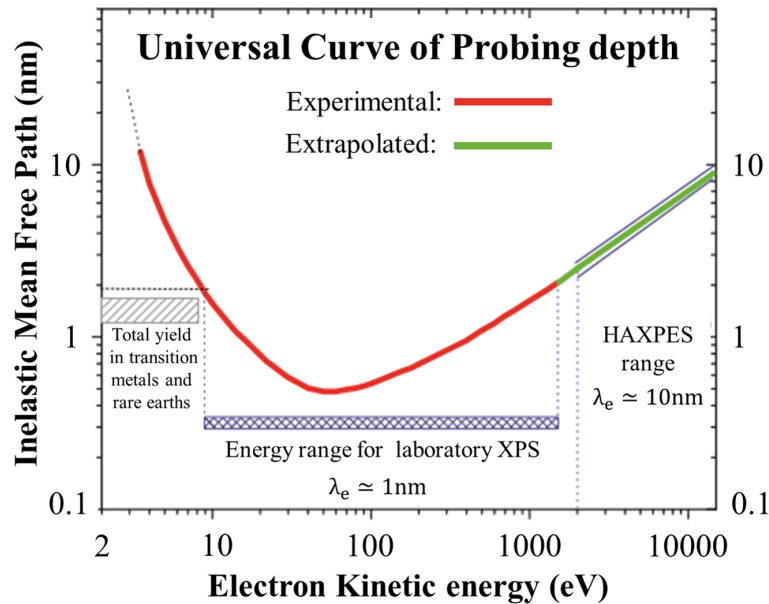


Figure 2.13: (a) Universal curve of dependence of the inelastic mean free path on the electron kinetic energy [44] [45].

### • Step III: Penetration Through the Surface and Escape Into The Vacuum

Finally, the photoelectron can only escape from the surface if its kinetic energy is sufficient to overcome the surface potential barrier of the sample  $\Phi_W$ . When this condition is fulfilled, the photoelectron can be emitted and then detected by the analyzer. The reduced residual pressure in the spectrometer ( $< 10^{-9}$  mbar) allows to minimize the additional inelastic scattering in the path of electron between the surface sample and the entrance of detector. In this context several types of photoelectrons can be distinguished as illustrated in Figure 2.14:

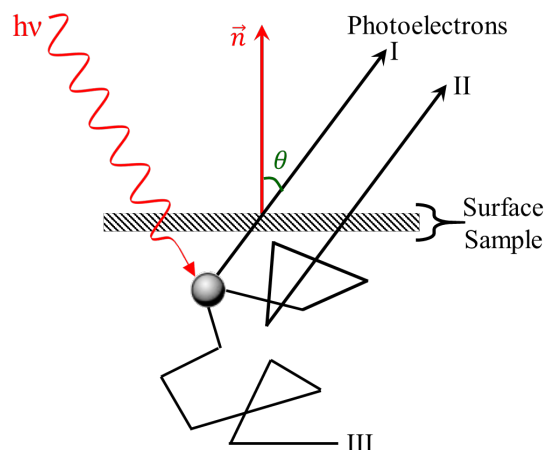


Figure 2.14: Scattering processes involved in photoemission: (I) primary electron, (II) secondary electrons and (III) reabsorbed electrons [46]

\* Electrons that have not suffered inelastic scattering are emitted with maximum kinetic energy and have the expected binding energy (case I in Figure 2.14). They are referred to as primary electrons and contribute to the intensity of main photoelectron peak. They provide chemical (from core levels) and electronic structure (from the valence band) information.

\* Due to inelastic scattering (case II in Figure 2.14), photoelectrons lose kinetic energy by exciting their surroundings and will be currently detected with a higher binding energy. Thus, kinetic energy losses may arise due to electron-phonon or electron-electron interactions which induce the presence of other peaks like satellites or plasmons. As for photoelectrons having undergone inelastic interactions, photoelectrons are still emitted but have lost electronic and chemical information. They are found in the energy-loss tail of the main photoelectric peak or in the secondary electrons background at low energy kinetic.

\* The electrons which undergo so many inelastic scattering interactions will not leave the surface of the material. They are reabsorbed and do not contribute to the photoemission signal (case III in Figure 2.14).

### (a) Angle-Dependent Studies

Degree of surface sensitivity of an electron-based technique such as XPS may be varied by collecting photoelectrons emitted at different emission angles to the surface plane. This approach may be used to perform nondestructive analysis of the variation of surface composition with depth (with chemical state specificity). The Beer-Lambert attenuation law describes how the photoelectron intensity will decrease exponentially as a function of depth into the sample. In fact, the intensity of the no-loss peak as a function of the probing depth or electron escape depth  $d$  and a take-off angle  $\theta$  (is the emission angle of the electrons acquired by the analyzer with respect to the surface normal) can thus be written in Equation 2.6:

$$I(d) = I_0 e^{-(d/\lambda_e \sin\theta)} \quad (2.6)$$

Here  $I_0$  is the intensity without attenuation. Overlayer films of thickness  $\lambda_e \sin\theta$  and  $2\lambda_e \sin\theta$  contribute respectively to 63 % and 86 % of the total signal. When the percentage of detected photoelectrons is 95 %,  $d$  is called sampling depth and is estimated to be  $3\lambda_e \sin\theta$ . This effect can be used to rapidly estimated if an element is localized at the surface or in the bulk.

According to the relation between the information depth and the take-off angle described in Equation 2.6, it is possible to tune the depth profile. In fact, to enhance the surface signal, we can decrease the angle of electron emission relative to the surface by using the angle-resolved XPS [39] as shown in Figure 2.15. Thus, by tilting the sample from near normal emission to near grazing emission provides a method for depth profiling the surface region of a solid sample.

Near normal emission produces a spectrum in which, the bulk peak dominates while the surface peak dominates in the spectrum from the grazing emission. According to Equation 2.6, when photoelectrons are collected at angles other than  $90^\circ$  with respect to the surface normal, these depths decrease by a factor of  $\sin\theta$  relative to the intensity of the bulk peak. In fact, when the take-off angle (TOA) is at  $90^\circ$ , the sample surface is perpendicular to the line of acceptance of the analyzer, and sampling depth  $d = 3\lambda_e \sin\theta$  is the maximum. Thus, By tilting the take-off angle (TOA) of  $60^\circ$  and  $30^\circ$  respectively, the sampling depth decreases from approximately 0.87 and 0.5 relatively to the sampling depth of the TOA =  $90^\circ$  [47].

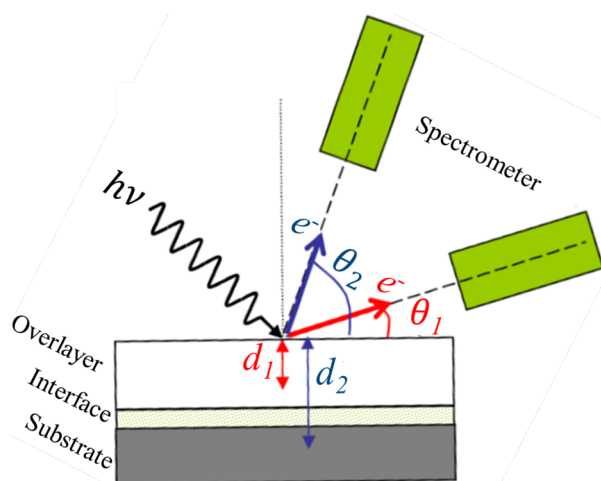


Figure 2.15: Scheme of principle of angle-resolved XPS [47]

### (b) Features of Photoelectron Spectrum

A photoemission spectrum contains informations from photoemitted electrons over a wide energy range [39]. A typical XPS spectrum as a function of kinetic energy is shown in Figure 2.16.

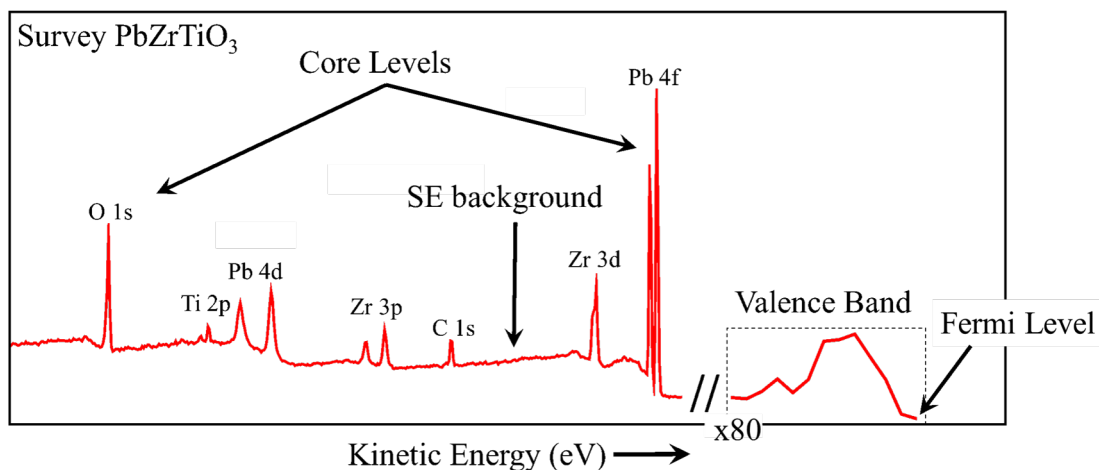


Figure 2.16: Typical photoemission spectrum with mainly two important regions: the core-level peaks (here Pb, Ti, Zr, O and carbon from the contamination) and the valence band spectrum. SE stands for Secondary Electrons

Here we briefly describe the main aspects of the XPS spectrum shown in Figure 2.16.

#### Continuous Background:

An important aspect in the interpretation of photoemission results is the continuous background (Figure 2.16). The continuous background is dominated by electrons that have undergone many inelastic scattering with their surroundings. The inelastically-scattered electrons or Secondary electrons (SE) have lost coherence with their initial state and constituted therefore a background. However, an incorrect subtraction of background can induce a misinterpretation of the recording data. Numerous background types are published but however, linear and Shirley background have been used during this thesis work [48]. For example Pb 4f and Pb 4d in Figure 2.16, Shirley background is the most sense according to the fact that, the background decreases with increasing kinetic energy.

#### Core-Level Peaks:

Core level allows to obtain valuable information of electronic structure, chemical state, local geometric structure and nature of chemical bonding of the emitting atom (Pb, Zr, Ti and O in Figure 2.16). These are rather narrow and localized levels around a nucleus. According to the fact that, each atom may have several signatures related to the environment, the understanding of characteristic of core level peaks become, therefore, essential in order to extend our knowledge on the materials.

- **Chemical Shifts:** Core-electron chemical shift represents a very powerful way of detecting different variations of the chemical environment in a complex system. In fact, even though, core electrons do not participate directly on the chemical bonding, they are sensitive to the changes in valence-level charge distributions [49, 50]. Indeed, depending to the

electronegativity of the neighbors, the core electrons of the atom will present lower or higher binding energies as described in more detail below in section 2.4.1, page 59.

• **Multiplet Splitting and Spin-Orbit Splitting:** Multiplet splitting can occur when the valence band levels are only partially occupied. In such cases, the valence electrons can couple with one another, such that, there is a net spin  $S$  and a net orbital angular momentum  $L$  on a given site. Further, when an electron is emitted from a core level, the new (N-1) electrons remaining and the partially filled valence band can be coupled. This can lead to several final states  $S_f$  and  $L_f$ . This is termed a multiplet splitting of core-level binding energies, and includes spin-orbit splitting.

### Photoemission Valence Band:

The initial states of these photoelectrons are just below the Fermi level as presented in Figure 2.16. It is these electrons that participate in the band structure. In the case of semiconductors or insulators, they participate in ionic and/or covalent bonds, often directional. In all cases, they determine the chemical, electrical and magnetic properties of the materials. Finally, valence electrons are most often studied using the UPS (Ultraviolet Photoemission Spectroscopy).

### (c) Core-Level Chemical Shifts

The interpretation of photoelectron core-level spectra in terms of binding energy shifts is an essential task in photoemission data analysis. The exact binding energy of an electron depends not only on the level from which photoemission is occurring, but also on the formal oxidation state of the atom, the local chemical and physical environment. Indeed, any change in the chemical environment generates differences in electronic and atomic potentials, which induce a change of the core level binding energy. Thus, a general relation of the core-level energy shift referenced to the Fermi level of the spectrometer  $\Delta E_B^F$  can be summarized as follows in Equation 2.7 [51]:

$$\Delta E_B^F = \Delta\varepsilon - \Delta E_R - \Delta V - \Delta\phi \quad (2.7)$$

In this simplified expression, first two terms on the right account for initial state (chemical shift  $\Delta\varepsilon$  due for example to the oxidation state of the common ion) and final state (with an extra and intra-atomic relaxation energies  $\Delta E_R$ ) contributions respectively.  $\Delta V$  is the difference in crystal field potential energy and  $\Delta\phi$  the work function correction or change surface potential.

One of the most important core level shift effect can be highlighted with the investigation of the **Surface Core Level Shift (SCLS)**. The SCLS [39, 52] is caused by the structural environment modification of the atoms at the surface with respect to the bulk.

The fact that the atoms in the first atomic layer of a solid (at the vacuum interface) must have electronic properties which are different from those of the atoms in the bulk had long been anticipated on theoretical grounds. Atoms at the surface have fewer neighbors than those in the bulk and are in an environment of lower symmetry. One might expect to find changes in band width and crystal field splitting due to the discontinuity at the surface.

Indeed, we consider three atomic environments as shown in Figure 2.17. The first one is in the bulk solid (c), the second one on the solid surface (b) and the third one is an isolated atom (a). The situation of the atom localized at the surface is situated between the situation in the bulk and the situation of isolated atom as illustrated in the diagram in Figure 2.17.

In fact, the rise to degeneracy effect induced by the reducing of the coordination is to shrink the valence band of the surface. However, the number of electrons in the valence band at the surface does not change with respect to the number of the valence band in the volume (this is the condition for maintaining charge neutrality). However, it occupies a wider energy range with the presence of energetic gap.

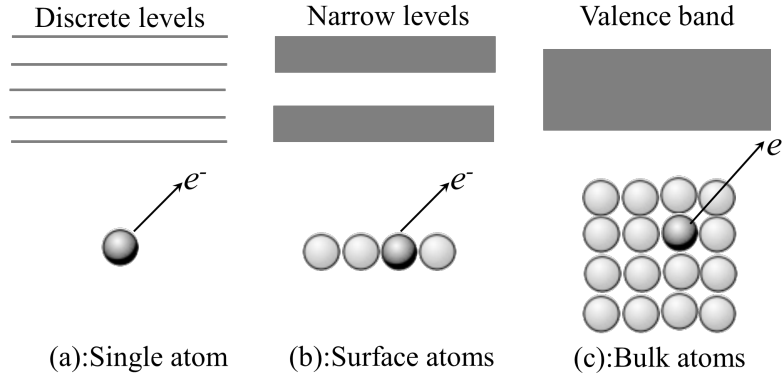


Figure 2.17: Diagram showing how the passage of the isolated atom to the solid state is accompanied by degeneracy of energy levels.

Thus, theoretical binding energy core level shift relation between the bulk atoms and the surface atoms is given by Equation 2.8:

$$\Delta_{SCLS} = [E^{Surf}(n_c - 1) - E^{Surf}(n_c)] - [E^{Bulk}(n_c - 1) - E^{Bulk}(n_c)] \quad (2.8)$$

where  $E^{Surf/Bulk}(n_c)$  is the total energy of the system considered as a function of the number of electrons  $n_c$  at the surface or in the bulk respectively [53, 54]. There are two models that can explain the physical core level displacement, the microscopic model [50] and thermodynamic model [55].

In the following, we will study the thermodynamic model that allows to describe accurately the SCLS contrary to the microscopic approach based on the Koopmans theory [56] which does not take into account the final state effects due to the screening of the core-hole.

In fact, Koopmans theorem is based on the assumption that the orbitals of the other electrons of atom remain unchanged when the photoelectron is emitted. It is consequently called the frozen-orbital approximation, and results in a final state which is not an eigenstate of the system with the photo-hole. In other words, this theorem which freezes the electron orbitals during photoemission, states that the negative of the eigenvalue of an occupied orbital from a Hartree-Fock calculation is equal to the ionization energy of the ion formed by the photoionization of the atom. However, there are limitations to Koopman's theorem. In fact, even if the photoelectron is removed in a time short compared to that characterizing

motion of the other electron, i.e. in the sudden approximation, a set of eigenstates is actually produced. The ground state of atom with the hole has the same energy as obtained if the photoelectron leaves the atom slowly enough. This process is called adiabatic description. In this limit the outer orbitals relax as the electron departs from the atom, leaving a hole in an inner shell. This relaxation lowers the energy of the final state well below that of the Koopmans state. For the isolated atom the difference between the energy of the Koopmans state and that of the fully relaxed state is called the intra-atomic relaxation energy. If the core electron is removed more rapidly, then the relaxation process will populate not only the ground state of the hole-state atom, but also those of its excited states allowed by selection rules. A sum rule shows that, in the sudden approximation the centroid of the population of these final eigenstates will coincide with Koopmans energy. The final state with lowest energy is usually the strongest and is called the main line, the rest are called shake-up satellites, because they correspond to the excited states of hole state atom. Theoretical values for the free-atom binding energies are obtained by calculating the total energy of atom both with and without the core hole. The difference corresponds to the binding energy measured in photoemission.

**Thermodynamic Model:** Thermodynamic models are based on the Equivalent Core Approximation (ECA) [57]. ECA is based on the assumption that removing one of the inner electrons is felt by the outer electrons as an increase in the nuclear charge by one unit. This approximation is justified when electrons cannot reach the inner part of the atom, and therefore, cannot make the distinction between the nuclear charge and the additional core hole. In this way it is reasonable to assume that the removal of a core electron is felt by the valence electrons as a change in the nuclear charge from  $Z$  to  $Z+1$ . [53].

From the ECA one can build up a Born-Haber cycle [55, 58]. Born-Haber cycles are used primarily as a means of calculating lattice energy (or more precisely enthalpy), which cannot otherwise be measured directly. The lattice enthalpy is the enthalpy change involved in the formation of an ionic compound from gaseous ions (an exothermic process), or sometimes defined as the energy to break the ionic compound into gaseous ions (an endothermic process). A Born-Haber cycle applies Hess's law to calculate the lattice enthalpy by comparing the standard enthalpy change of formation of the ionic compound (from the elements) to the enthalpy required to make gaseous ions from the elements.

Thus, the segregation energy for clean surfaces of material was split into two contributions. The first one is the difference of surface energy between the elements  $[Z+1]$  and  $[Z]$  and the second one is a dilution term which was neglected. In fact, Born-Haber cycle in which surface effects arise from a reduction of the cohesive energy due to the lower coordination number have been successfully used to interpret the Surface-atom core-level shifts on clean surfaces. This approach has been also generalized for adsorbate covered surfaces and it was shown that the presence of chemisorbed atoms introduces an additional contribution to SCLS (Equation 2.9).

$$\Delta_{SCLS} = -p'/p [E_{ads}(Z+1) - E_{ads}(Z)] \quad (2.9)$$

where  $E_{ads}(Z)$  is the (positive) adsorption energy of the adatoms at the surface of the  $[Z]$  crystal (here the element  $[Z+1]$  is assumed to have the same crystalline structure as

the element  $[Z]$ ),  $p$  is the number of bonds (assumed to be geometrically equivalent) of an adatom with the substrate atoms and  $p'$  is the number of bonds (also assumed to be geometrically equivalent) between the substrate atom on which the SCLS is measured and the adsorbates. In the usual cases where these bonds are not equivalent, the above formula can still be used to get an approximate value of the additional SCLS due to adsorbate(s). This formalism also yields excellent estimates of binding energies in metals. It can be readily extended to deal with the change in binding energy at the surface, as well as to relate binding energy shift in alloys to heats of solution.

Basically, the ability to discriminate between different oxidation states and chemical environments is one of the major strengths of the XPS technique. In fact, all these shifts are readily observable and interpretable in XPS spectra because this technique is of high intrinsic resolution. Furthermore, as shown in Figure 2.18, atoms of a higher positive oxidation state exhibit a higher binding energy due to the extra coulombic interaction between the photoemitted electron and the ion core. Reversely, atoms of a higher reduction state exhibit a lower binding energy.

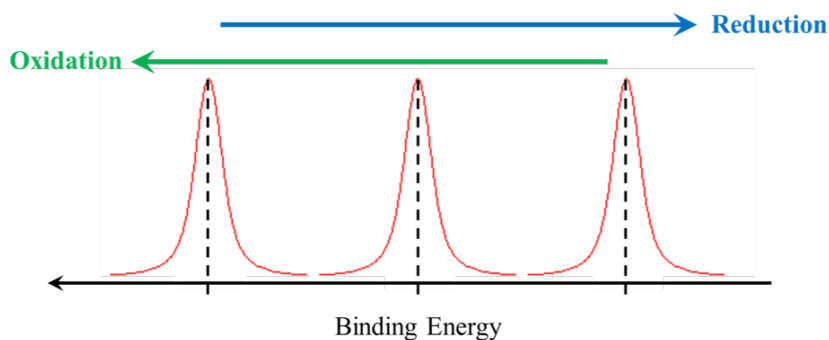


Figure 2.18: Photoelectron binding energy evolution depending on their oxidation states

#### (d) Practical Approach in the Case of Semiconductor

In addition to the binding energy shifts mentioned above, there are briefly other possible effects of binding energy shifts in the case of semiconductor material. Firstly, the variation of the Fermi level, whose position in the gap depends on the semiconductor type and level of doping. Secondly the band bending on the surface, due to the presence of a charge depletion layer to the surface of the material related to surface states in the gap. Finally, an extrinsic phenomenon linked to the illumination of the material such as the surface charge effect during analysis can act the binding energy.

### 2.4.2 Experimental Set-up of XPS

All surface studies during this thesis were carried out using ScientaOmicron Multi-probe XPS (M-XPS) illustrated in Figure 2.19. The M-XPS system [59] delivered by Scienta Omicron and installed at the Platform For Nanocharacterization of MINATEC (CEA-Grenoble, France) is designed to perform X-ray photoelectron spectroscopy (XPS), ultraviolet photoelectron spectroscopy (UPS), Angle-resolved XPS (ARXPS). The design allows an easy sample transfer between the different chambers under ultrahigh vacuum pressure ( $10^{-10}$

mbar). The airlock and a high vacuum analysis chamber are connected to the sample storage chamber. The airlock is equipped with a sample docking station for three samples and can be brought rapidly to atmospheric pressure using  $N_2$  gas in order to minimize the contamination gas upon sample insertion. The storage chamber with multi-samples carousel system is endowed with a heating stage for cleaning surface and heat-treating samples. The analysis chamber is equipped with a sample holder rotatable enabling to vary not only the take-off angle but also a monochromatic X-ray source of aluminum and a hemispherical electron energy analyzer.

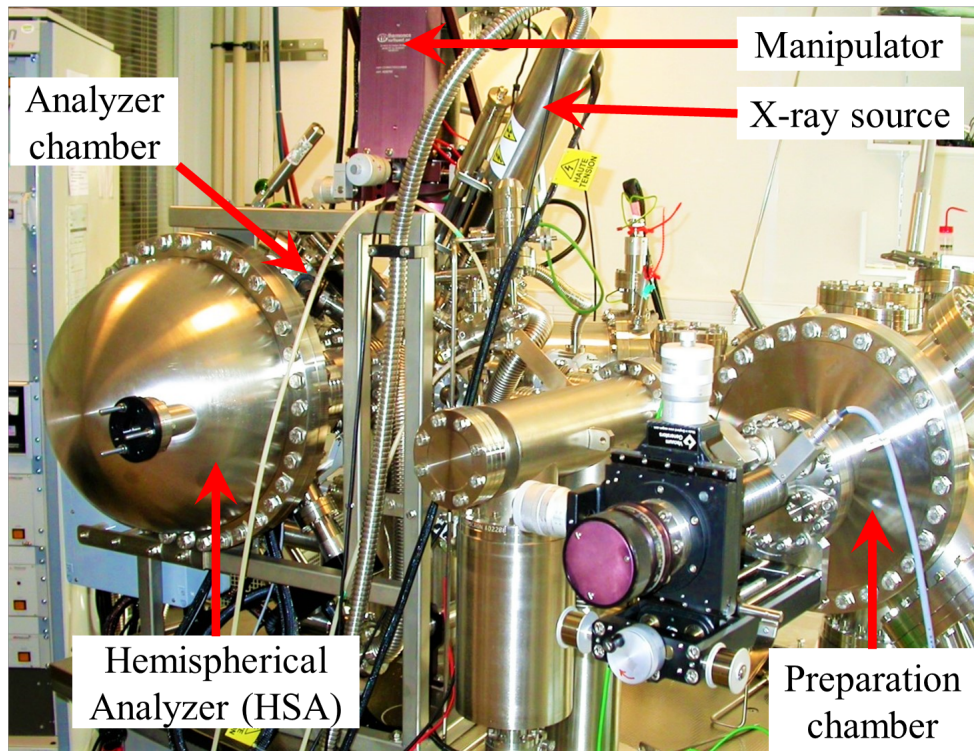


Figure 2.19: M-XPS equipment in MINATEC Nano-Characterization Centre

#### (a) Width and Shape of Core Level Photoemission Peaks:

The shape of photoemission peaks are not simply delta functions  $\delta$ . Experimentally, photoemission peaks from semiconductors or insulators are described by the Gaussian-Lorentzian (Voigt) profile due to the symmetric peak shape, while asymmetric peaks from metal materials are interpreted by the Doniach-Sunjic profile. This situation is linked to the fact that, the width and shape of photoemission peaks take into consideration several effects that will be discuss below.

One of the first contribution of the width of photoemission peak is the X-ray source. The linewidth of the X-ray line source used for the excitation is  $\Delta E_X$ . With a good energy resolution ( $\Delta E_X \simeq 250$  meV), the M-XPS is equipped with a conventional X-ray laboratory source with  $Alk_\alpha$  photon for core level excitation [60] having a line energy and width of 1486.6 eV and 0.16 eV respectively [61].

A second contribution of the width of photoemission peak is the analyzer used (hemispherical analyzer in the case of the M-XPS). A hemispherical analyzer is constituted of a multi-elements: an electrostatic input lens, a hemispherical deflector with entrance  $\omega_S$ , exit slits  $\omega_F$ , and an electron detector (i.e., a channeltron or a multi-channel detector) [61]. Basically, a hemispherical analyzer is consisted of two concentric hemispherical electrodes held at different potentials  $V = V_2 - V_1$ . In this case, the trajectory of the incoming electrons is bent into a curve as seen in Figure 2.20. Charged particles of only well-defined kinetic energy called the pass energy  $E_p$ , are able to complete their path along the median trajectory of radius  $R_0 = (R_1 + R_2)/2$  with  $R_1$  and  $R_2$  radii of the inner and outer hemisphere and emerge at the exit slit  $\omega_F$ . Particles at energies sufficiently lower or higher will hit the walls. The system acts as a narrow band pass energy filter. The bandwidth is described by Gaussian profile. The energy resolution of the analyzer  $\Delta E_A$  with an angular aperture of the analyzer  $\alpha$  can be expressed by the formula in Equation 2.10:

$$\Delta E_A = E_p \left[ \frac{\omega_F - \omega_S}{2R_0} + \alpha^2 \right] \quad ; \quad E_p = e\Delta V \left( \frac{R_1 R_2}{R_1^2 - R_2^2} \right) \quad (2.10)$$

Thus, by using a pass energy of 10 eV with an entrance slit  $(1 \times 10)$  mm<sup>2</sup>, and acceptance angle of  $\pm 3.1^\circ$  (acceptance angle is the angle under which the majority of emitted photoelectrons will be collected by analyzer and recognized by detector), the analyzer resolution  $\Delta E_A$  is 90 meV. The overall energy resolution of X-ray source and analyzer is 0.27 eV.

Finally, even though, the XPS tool has a high resolution, we can observe that in Figure 2.16 some peak line-shapes are broad and others are sharp. We can understand these differences by the consideration of the core-hole lifetime, which is very relevant in photoemission process. The core-hole lifetime  $\Delta t$  of the state which is instead a Lorentzian function can be related to intrinsic or natural line-width  $\Delta E_{LS} = 2\Gamma$  by the Heisenberg uncertainty principle as shown in Equation 2.11:

$$\Delta E_{LS} = 2\Gamma \sim \frac{h}{2\pi} \times \frac{1}{\Delta t} \quad (2.11)$$

Here  $h$  is the Planck constant, and  $\Delta t$  the core-hole lifetime. Heisenberg uncertainty principle defined that the precision with which we can define the energy of a state, depends on the lifetime of electron in this state. The shorter the lifetime, the less the certainty with which we can define the energy. In fact, if we suppose an electron in a ground state with a long lifetime and a precisely defined energy. It passes to an excited state with a short lifetime. In this case, the uncertainty principle tells us that the energy of the excited state cannot be defined precisely. It will have an inherent uncertainty in its energy and therefore a widening of the full-width-at-half-maximum of the photoemission peak.

Additionally, we can also note that, the deeper the orbital, the shorter the lifetime of the core level remaining after photoemission and the broader the peak width because of the

very large number of electrons around the hole.

Thus, the total energy resolution defined as the full-width-at-half-maximum of the peak after background subtraction can be approximated by a quadratic sum of the natural linewidth, X-ray bandwidth and analyzer resolution as illustrated in Equation 2.12 [62]:

$$\Delta E_{Tot} = \sqrt{(2\Gamma)^2 + (\Delta E_X)^2 + (\Delta E_A)^2} \quad (2.12)$$

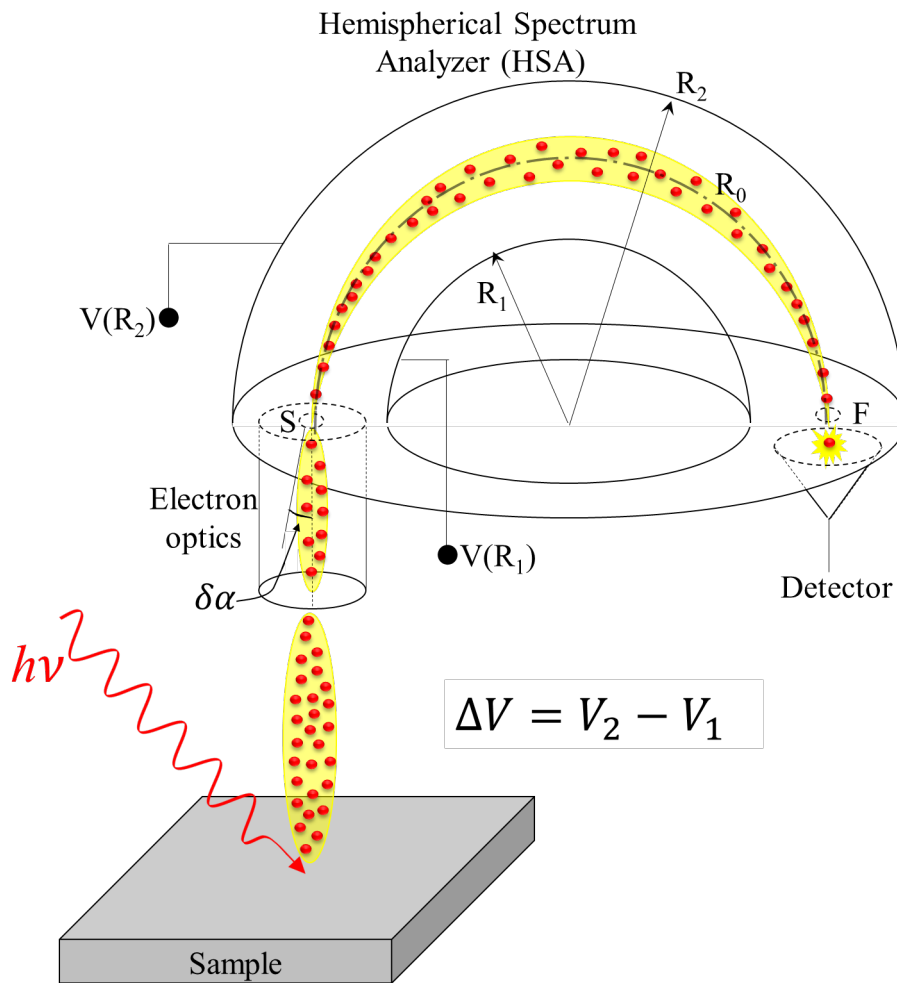


Figure 2.20: HemiSpherical Analyzer (HSA);  $S$  and  $F$  are the widths of the entrance and exit slit, respectively, and  $\alpha$  is the angular spread of the electron beam.  $R_0$ ,  $R_1$  and  $R_2$  are the radius of the median equipotential surface and the radii of the concentric hemispheres at potentials  $V_1$  and  $V_2$  and [62]

### (b) Quantification Analysis

XPS signal intensity, measured for a fixed kinetic energy  $E_k$  at a depth  $z$  from the surface, depends on several parameters as illustrated in Equation 2.13 [63].  $I_0$  is the incident photon

intensity,  $n$  is the atomic density,  $\lambda(E_k)$  is the inelastic mean free path of electrons of energy  $E_k$  in the sample.  $D(E_k)$  is the efficiency of the spectrometer detector for the electrons of energy  $E_k$ , and  $\sigma_{ph}(h\nu)$  is the photoionization cross section.  $L(\gamma)$  represents angular asymmetry of photoemission intensity from each atom and  $T(E_k)$  is the electron spectrometer transmission.  $\theta$  is the angle formed by photoelectrons escape direction and the normal to the sample.

$$I(E_{k,z}) = I_0 n \sigma_{ph}(h\nu) D(E_k) T(E_k) L(\gamma) \exp[-(z/\lambda(E_k)\cos\theta)] \quad (2.13)$$

Now, we define the atomic sensitivity factor  $S$  by:

$$S = I(E_{k,z}/n) = I_0 \sigma_{ph}(h\nu) D(E_k) T(E_k) L(\gamma) \exp[-(z/\lambda(E_k)\cos\theta)] \quad (2.14)$$

In the case where, the incident photons intensity remains constant during the experiment, we can determine the atomic concentration  $c_i$  of any element by using Equation 2.15 [37]:

$$c_i = \frac{n_i}{\sum_j n_j} = \frac{I_i/S_i}{\sum_j (I_j/S_j)} \quad (2.15)$$

This approach will provide semi-quantitative results for most situations, except where heterogeneous samples are involved, or where serious contamination layers obscure the underlying elements. During this thesis, CasaXPS software [64] was used for treatment all of the acquiring data. The transmission coefficient ( $a, b$ ) were extracted from the ScientaOmicron database.

### 2.4.3 Synchrotron Beamline

The main interest of using Hard X-rays in photoemission (HAXPES) [65] is to increase the probing depth, which allows to study deeply buried interfaces unlike to the classical XPS (limited only to the extreme surface). Synchrotron radiation used in HAXPES measurement is the electromagnetic light emitted from deviated or accelerated relativistic electrons. The main interests of using synchrotron radiation for photoemission are the tunability of the photons produced, the high photon flux and the high energy resolution that can be achieved [66, 67]. The energy range can be between infrared to hard x-rays, allowing to produce low or high kinetic energy photoelectron.

Production of photons with a synchrotron source passes through various stages as illustrated briefly below in Figure 2.21. Electrons are produced by an electron gun in the linear particle accelerator (LINAC) followed by the gain of energy from 100 MeV to 2.75 GeV in the BOOSTER RING before finally entering the STORAGE RING. The storage ring (of perimeter 354 m in the case of the SOLEIL synchrotron) is an assembly of components used to confine and maintain a high energy electron beam in a closed orbit for periods of several hours. Electrons produce synchrotron light at each successive orbital deviation for a wide

variety of experiments as illustrated in Figure 2.22. In the storage ring, electrons travel in a metal tube in which an ultra-high vacuum is maintained. Thus, there are almost no collisions to slow down the relativistic electrons into the storage ring.

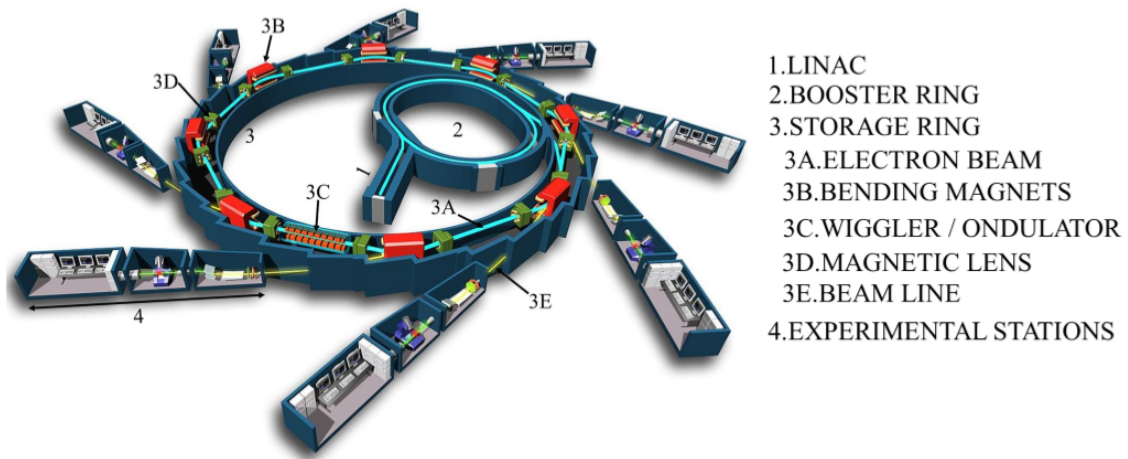


Figure 2.21: SOLEIL Synchrotron Radiation Center [68]

In the storage ring, electrons are kept on their circular path by the help of strong magnetic fields applied by the several magnetic devices. These magnets devices behave like synchrotron radiation sources as shown in Figure 2.22.

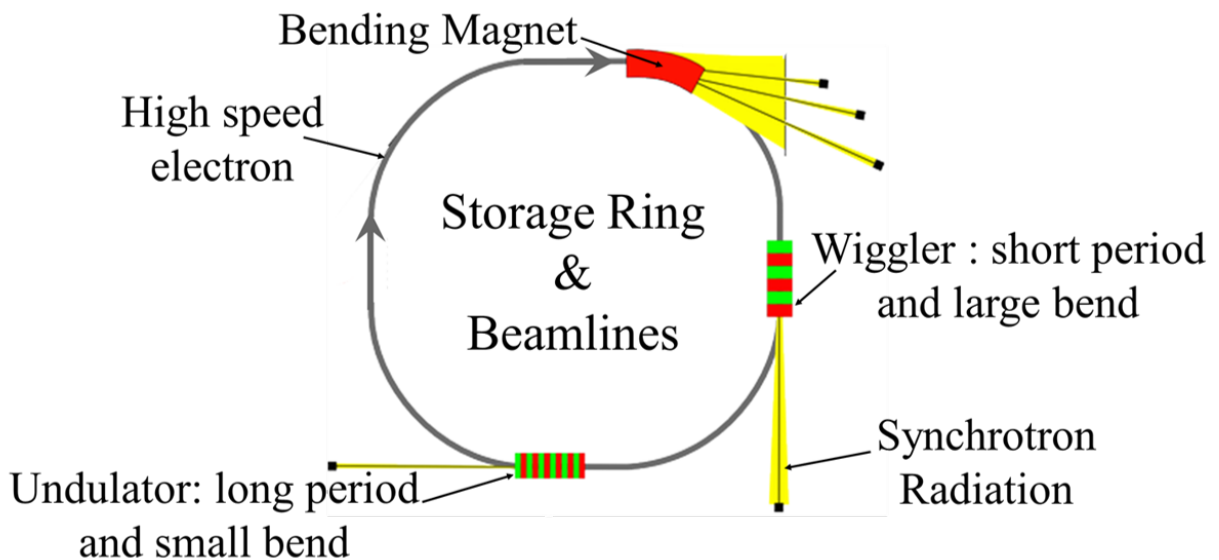


Figure 2.22: Comparative of the spectral brilliance of bending magnet and insertion devices (wiggler and undulator)[69]

The **bending magnets** are one of the sources of synchrotron light (Figure 2.22), where a narrow cone of radiation is emitted as the electrons pass the bend. Between these circular bending magnets are inserted straight sections with multi-magnet devices called insertion

devices (Wiggler and Undulator presented in Figure 2.22). A **wiggler** generates a quasi-continuum, with a flux higher than a bending magnet roughly in proportion to the number of wiggles (short period and large bend). In an **undulator**, the self-reinforcing aspect of interaction of the electron beam with the magnetic structure leads to increase a gain in brightness. The undulator allows to get also a partially coherent point source, a highly collimated, and a very highly structured energy spectrum (long period and small bend). The synchrotron light emitted by the electrons is directed to beamlines through the circular beam ports.

### (a) Undulator

The HAXPES experiments were done at the Galaxies beamline (SOLEIL synchrotron, Saint Aubin, France). Here, we describe briefly the photon source (undulator) and the beamline. The hard X-ray source during *operando* HAXPES measurements in this thesis is provided by U20 undulator with a 98 magnetic periods installed in a short straight section of the SOLEIL synchrotron. The length of each magnetic periods (N-S poles) called  $\lambda_0$  is 20mm. The maximum magnetic field at a minimum gap of 5.5mm of the U20 undulator is 0.96 Tesla [70].

Figure 2.23 (a) shows a schematic of the undulator. The magnetic pole successions force the electrons to move in a sinusoidal-like fashion around the central axis with spatial period  $\lambda_0$ . Thus each electron emits individual synchrotron radiation at each deviation. These radiation emissions will overlap and interfere with each other, sometimes constructively with narrow bands centered at the harmonics  $\lambda$ ,  $\lambda/3$ ,  $\lambda/5$  ... and sometimes destructively with  $\lambda/2$ ,  $\lambda/4$  ... As illustrated in the Figure 2.23 (b). Usually, harmonic curves or photon energy can be promoted by tuning mechanically the magnetic gap between the magnetic poles. Indeed, by changing the gap the value of the magnetic field is varied.

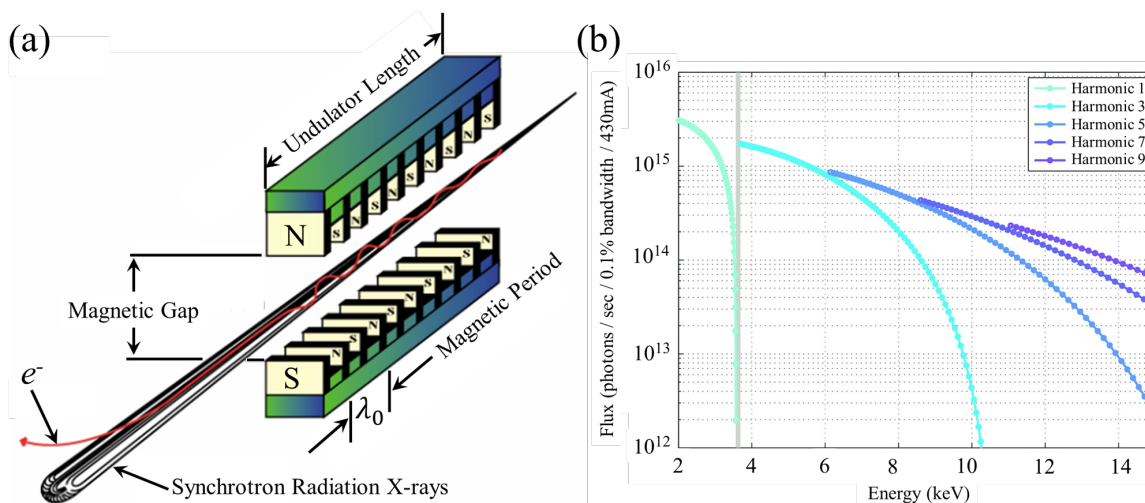


Figure 2.23: (a) Schematic description of the undulator and (b) U20 (from SOLEIL) spectral brilliance of harmonics depending on the accessible energy

To favor the 3rd harmonic with a photon energy of 6.8936 keV, we fixed the magnetic

gap to 6 mm. The radiation emitted from undulator is naturally linearly polarized because of the symmetry of the electron trajectory within each period of the insertion device.

### (b) Double Crystal Monochromator

From the undulator, the beam of light enters in the optics hutch which contains several optical devices and the Silicon (Si) double crystal monochromator (DCM). The resolution of the exit beam with desired energy is selected by a double-crystal Si liquid-nitrogen-cooled fixed-exit monochromator (DCM). The energy will be selected by performing the angle rotation (for two crystals) and translational motions (parallel and perpendicular motions for second crystal) whilst keeping the crystals parallel to one another as illustrated in Figure 2.24 (a).

During our experiment, the Si(333) reflections of the double crystal monochromator [71, 72] were used to obtain monochromatized X-ray at 6.8936 keV with a bandwidth of 150 meV as shown in the calculated energy resolution of Figure 2.24 (b).

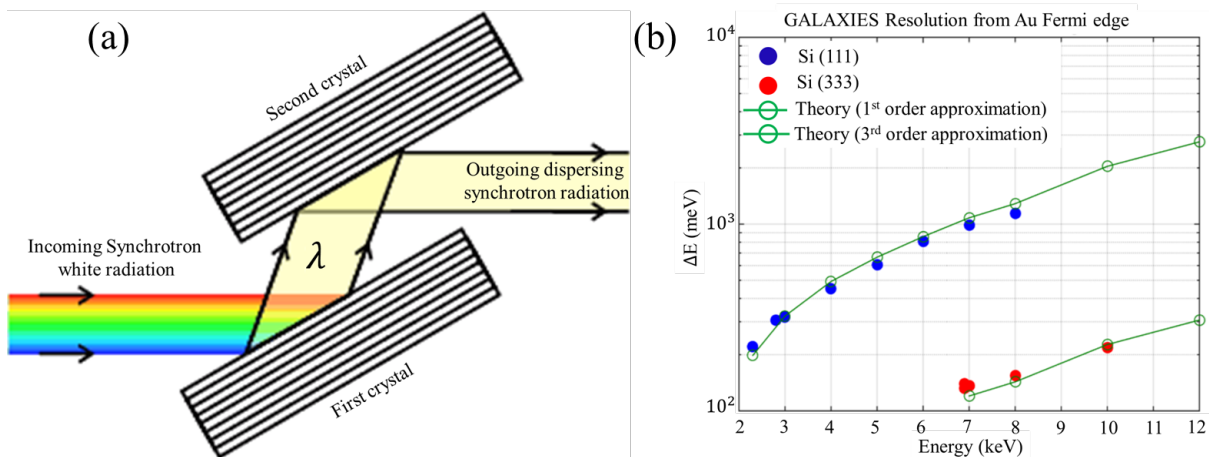


Figure 2.24: (a) Schematic description of the Double Crystal Monochromator (DCM) and (b) calculated energy resolution Si double crystal monochromator [73]

### (c) HAXPES Set-up

Finally, thanks to mirrors, photoelectrons are measured by a Scienta EW4000 hemispherical photoelectron analyzer installed on the HAXPES station illustrated in Figure 2.25. The hemispherical photoelectron analyzer provides a high transmission thanks to the  $60^\circ$  total opening angle of the lens. The instrument is optimized for the detection of electron kinetic energies up to 12 keV. The analyzer chamber is compatible with the manipulation of solid samples which are mounted on a specifically designed sample holder. The holder is attached to a fully motorized 4 axes-manipulator located on top of the chamber. The sample holder can host two sample plates that are electrically isolated from the sample holder ground.

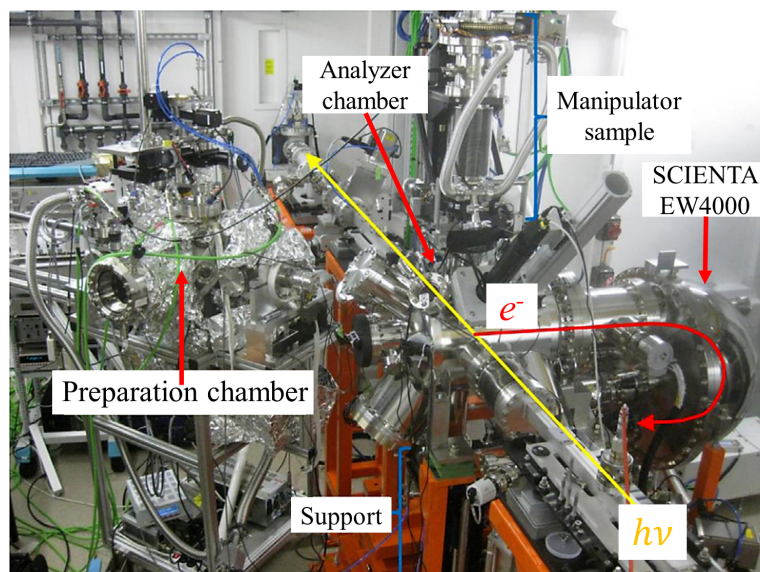


Figure 2.25: HAXPES station at the GALAXIES beamline (Synchrotron SOLEIL) with an SCIENTA EW4000 hemispherical energy analyzer [71, 74]

From the photon resolution provided by the DCM (150 meV) presented in Figure 2.24 (b) and the analyzer bandwidth (180 meV) from hemispherical analyzer (with a passing energy of 200 eV and a slit size of 400  $\mu\text{m}$ ), the total resolution for an energy of 6.8936 keV is  $\simeq 235$  meV.

#### (d) Advantages of Analysis for *Operando* HAXPES on the Metal/PZT Stacks

HAXPES *in-situ* technique provides the possibility to access to the chemical and electronic information from the bulk of capacitor devices based on the materials. It also allows to investigate the buried interfaces in layered material stacks. Additionally, with HAXPES technique, photoemission measurements can be performed without any surface cleaning procedures (with the presence of surface contamination) or extra preparations contrary to the XPS technique. However, HAXPES *in-situ* technique is often applied to materials at equilibrium, which does not allow to get a very accurate representation of interactions at the atomic scale under normal (dynamic) operating conditions.

However, for the development of future high capacitance devices, it is crucial to determine the chemical and electronic states of buried interface between the active layer and the electrodes. The use of HAXPES measurement *in-operando* situation i.e. by applying *in-situ* an electric field between the electrodes of the capacitor is a very relevant means to study the complexity of the actual devices under realistic condition. To achieve this experimental challenge, a specific protocol is implemented as described in the next section.

#### (e) Experimental Protocol for *Operando* HAXPES

Figure 2.26 shows a schematic of the sample configuration and the actual experimental measuring device employed during this PhD. Two Omicron sample plates are used on the

manipulator. One for the sample mounting and top electrode bias and a second one to contact the bottom electrode via a Cu spring contact. The sample is mounted on the Printed Circuit Board (PCB) by using a double-sided tape for UHV and the PCB is screwed onto the sample holder. The electric contacts with the top and bottom electrodes are done by wires which contacting the sample plate (for the top electrode) and a second sample plate via a Cu spring for the bottom electrode. In this way, both top and bottom electrodes are floating with respect to the experiment ground. Therefore, capacitor can be poled by using an Agilent E4980A capacitance/voltage generator and its electrical characteristics measured *in-situ*.

In Figure 2.27, we can see through the window of the analysis chamber, the sample of PZT and supports. The sample plates used for *operando* HAXPES are attached to a fully motorized 4 axes-manipulator. This device makes it possible to align the photon beam (with a beam spot of width of  $\sim (100 \times 100)\mu\text{m}^2$ ) and the surface ( $1\text{mm}^2$ ) of capacitor that will be analyzed. Angle configuration between analyzer and source is  $90^\circ$  on the HAXPES tool. We performed all measurements with a take-off angle ( $\theta$ ) of  $60^\circ$  during this beamtime.

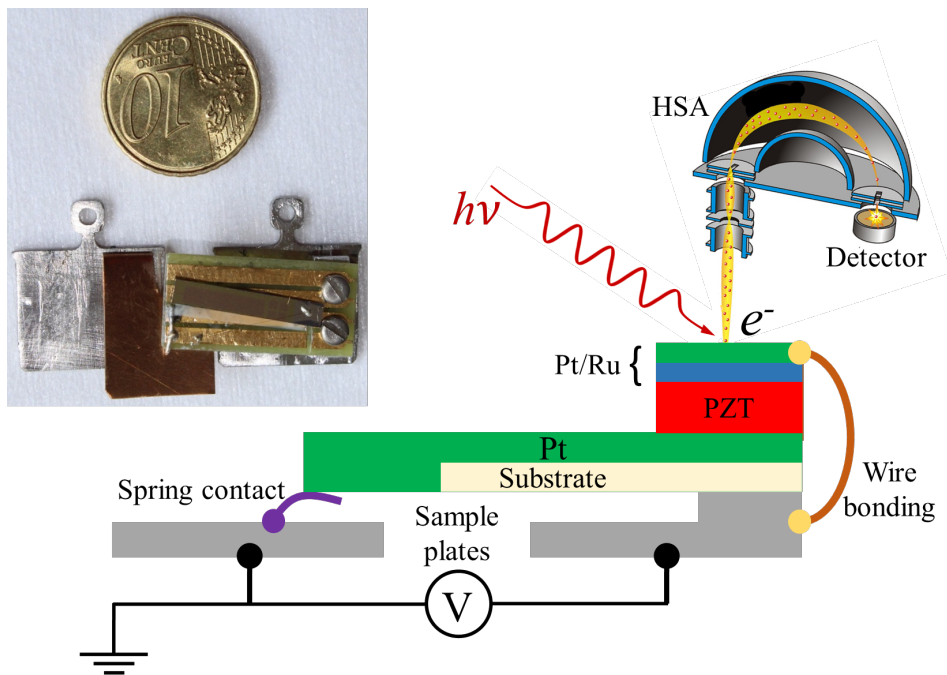


Figure 2.26: Samples geometry of the *operando* HAXPES: First, the spring contact allows to connect the bottom electrode (Platinum) of sample and the ground. The wire bonding joints second sample holder under voltage and the top electrode (Pt/Ru). This created a closed circuit which makes it possible to polarize the capacitor. Photon is focus on the center of the surface of capacitor ( $1\text{mm}^2$ ) and the electron extracted are analyzed by the hemispherical photoelectron analyzer and then detected by the detector. The inset presents the actual assembly [75]

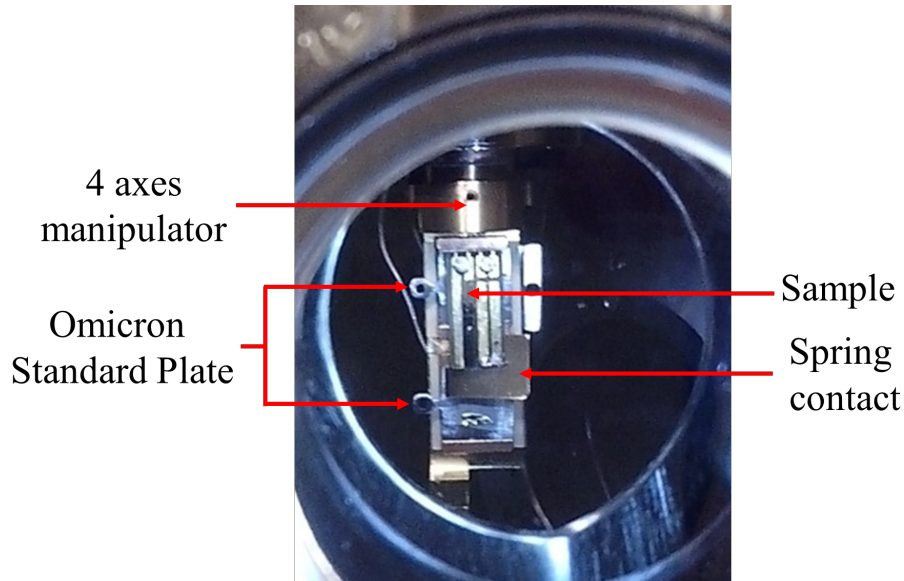


Figure 2.27: Complete assembly of electrical measurements in the analyze chamber of HAX-PES station

## 2.5 Conclusion

In this chapter, we have reviewed the processes of deposition and characterization used during this thesis work. We first presented the different phases of fabrication of our Pt/Ru/PZT/Pt/substrates structures. In particular, we focused on the sol-gel technique, which is very suitable for depositing thin films. After that, we have described the microstructural (X-ray diffraction) and structural (electronic microscopies) tools used for studying the PZT layers. We have developed and explained the functioning of photoemission spectroscopy, which is an extremely effective technique in the physico-chemical study of materials. It also largely allows to study the extreme surface of samples but also the buried interfaces of structures in stacks according to the sources of energy used. Finally, in this chapter, we have described the synchrotron beamline working and the protocol used to perform the *operando* HAXPES. In the next chapter, we will investigate the electrical performances of PZT thin film depending both on the Pb excess content in the PZT film and the post metallization annealing Pt/Ru/PZT/Pt stacks.

## Bibliography

- [1] K. Seshan. *Handbook of Thin-Film Deposition Processes and Techniques - Principles, Methods, Equipment and Applications (2nd Edition)*. William Andrew Publishing/Noyes, 2002.
- [2] M. Chen, T. Wu, and J. Wu. Effect of textured  $\text{LaNiO}_3$  electrode on the fatigue improvement of  $\text{Pb}(\text{Zr}_{0.53}\text{Ti}_{0.47})\text{O}_3$  thin films. *Applied Physics Letters*, 68(10):1430, 1996.
- [3] H.N. Al-Shareef, K.R. Bellur, O. Auciello, and A.I. Kingon. Phase evolution and annealing effects on the electrical properties of  $\text{Pb}(\text{Zr}_{0.53}\text{Ti}_{0.47})\text{O}_3$  thin films with  $\text{RuO}_2$  electrodes. *Thin Solid Films*, 256(1-2):73–79, 1995.
- [4] J. S. Cross, M. Fujiki, M. Tsukada, Y. Kotaka, and Y. Goto. Characterization of PZT capacitors with  $\text{SrRuO}_3$  electrodes. *Integrated Ferroelectrics*, 21(1-4):263–271, 1998.
- [5] H. Fujisawa, K. Kita, M. Shimizu, and H. Niu. Low-Temperature Fabrication of Ir/Pb(Zr,Ti) $\text{O}_3$ /Ir Capacitors Solely by Metalorganic Chemical Vapor Deposition. *Japanese Journal of Applied Physics*, 40(Part 1, No. 9B):5551–5553, 2001.
- [6] K. KushidaAbdelghafar, H. Miki, K. Torii, and Y. Fujisaki. Electrode induced degradation of  $\text{Pb}(\text{Zr}_x\text{Ti}_{1-x})\text{O}_3$  (PZT) polarization hysteresis characteristics in Pt/PZT/Pt ferroelectric thinfilm capacitors. *Applied Physics Letters*, 69(21):3188–3190, 1996.
- [7] R. Bruchhaus, D. Pitzer, O. Eibl, U. Scheithauer, and W. Hoesler. Investigation of Pt Bottom Electrodes for "In-Situ" Deposited  $\text{Pb}(\text{Zr,Ti})\text{O}_3$  (PZT) thin Films. *MRS Proceedings*, 243:123, 1991.
- [8] E. Simo. Thin Films on Silicon. In *Handbook of Silicon Based MEMS Materials and Technologies*, pages 124–205. Elsevier, 2015.
- [9] R. Gohdssi and L. Pinyen. *MEMS Materials and Processes Handbook*, volume 1. Springer US, 2011.
- [10] L. Pardo and J. Ricote. *Multifunctional Polycrystalline Ferroelectric Materials: Processing and Properties*. Springer Series in Materials Science. Springer Netherlands, 2011.
- [11] E. A. Kneer, Dunbar P. Birnie, J. C. Podlesny, and G. Teowee. Evolution of surface relief during firing of PZT thin films. *Ferroelectrics*, 152(1):67–72, 1994.
- [12] Y. Jeon, D. Kim, K. No, S. Kim, and J. Chung. Residual Stress Analysis of Pt Bottom Electrodes on  $\text{ZrO}_2/\text{SiO}_2/\text{Si}$  and  $\text{SiO}_2/\text{Si}$  Substrates for  $\text{Pb}(\text{ZrTi})\text{O}_3$  Thick Films. *Japanese Journal of Applied Physics*, 39(Part 1, No. 5A):2705–2709, 2000.
- [13] T. Maeder, L. Sagalowicz, and P. Muralt. Stabilized Platinum Electrodes for Ferroelectric Film Deposition using Ti, Ta and Zr Adhesion Layers. *Japanese Journal of Applied Physics*, 37(Part 1, No. 4A):2007–2012, 1998.
- [14] C.C. Mardare, E. Joanni, A.I. Mardare, J.R.A. Fernandes, C.P.M. de Sá, and P.B. Tavares. Effects of adhesion layer (Ti or Zr) and Pt deposition temperature on the properties of PZT thin films deposited by RF magnetron sputtering. *Applied Surface Science*, 243(1-4):113–124, 2005.
- [15] G. Vêlu and D. Rêmiens. Electrical properties of sputtered PZT films on stabilized platinum electrode. *Journal of the European Ceramic Society*, 19(11):2005–2013, 1999.

- [16] G. A. C. M. Spierings, G. J. M. Dormans, W. G. J. Moors, M. J. E. Ulenaers, and P. K. Larsen. Stresses in Pt/Pb(Zr,Ti)O<sub>3</sub>/Pt thinfilm stacks for integrated ferroelectric capacitors. *Journal of Applied Physics*, 78(3):1926–1933, 1995.
- [17] M. Cueff. *Micro-actionneurs piézoélectriques*. PhD thesis, 2011.
- [18] M. Cueff, M. Allain, J. Abergel, G. Le Rhun, M. Aid, E. Defay, and D. Faralli. *Influence of the crystallographic orientation of Pb(Zr,Ti)O<sub>3</sub> films on the transverse piezoelectric coefficient d<sub>31</sub>*. PhD thesis, 2011.
- [19] C. Sudhama, A. C. Campbell, P. D. Maniar, R. E. Jones, R. Moazzami, C. J. Mogab, and J. C. Lee. A model for electrical conduction in metalferroelectric-metal thin-film capacitors. *Journal of Applied Physics*, 75(2):1014–1022, 1994.
- [20] K. D. Budd, S. Y. Dey, and D. A. Payne. Sol-gel processing of PbTiO<sub>3</sub>, PbZrO<sub>3</sub>, PZT, and PLZT thin films. *British Ceramic Society Proceedings*, 36(January 1985):107–121, 1985.
- [21] Yole. Thin film pzt for semiconductor: Application trends technology update (feram, ipds and mems). *Yole Développement SA*, 2013.
- [22] U. C. Nwaogu and N. S. Tiedje. Foundry Coating Technology: A Review. *Materials Sciences and Applications*, 02(08):1143–1160, 2011.
- [23] A. Mirzaei, M. Bonyani, and S. Torkian. Synthesis and characterization of nanocrystalline PZT powders: From sol to dense ceramics. *Processing and Application of Ceramics*, 10(1):9–16, 2016.
- [24] V. Kovacova. *Study of correlations between microstructure and piezoelectric properties of PZT thin films*. PhD thesis, 2016.
- [25] L. L. Hench and J. K. West. The sol-gel process. *Chemical Reviews*, 90(1):33–72, 1990.
- [26] G. Yi, Z. Wu, and M. Sayer. Preparation of Pb(Zr,Ti)O<sub>3</sub> thin films by sol gel processing: Electrical, optical, and electrooptic properties. *Journal of Applied Physics*, 64(5):2717–2724, 1988.
- [27] C. Kittel. *Introduction to Solid State Physics 7th Edition*. 2010.
- [28] K. Vojisavljevi, G. Brankovi, T. Srekovi, A. Renik, and Z. Brankovi. Preparation of ultra-thin PZT films by a chemical solution deposition method from a polymeric citrate precursor. *Journal of the European Ceramic Society*, 30(2):485–488, 2010.
- [29] K. K. Maurya, S. K. Halder, S. Sen, A. Bose, and S. Bysakh. High resolution X-ray and electron microscopy characterization of PZT thin films prepared by RF magnetron sputtering. *Applied Surface Science*, 313:196–206, 2014.
- [30] K. Inaba, S. Kobayashi, K. Uehara, A. Okada, S. L. Reddy, and T. Endo. High Resolution X-Ray Diffraction Analyses of (La,Sr)MnO<sub>3</sub>/ZnO/Sapphire(0001) Double Heteroepitaxial Films. *Advances in Materials Physics and Chemistry*, 3(01):72–89, 2013.
- [31] FEI Company. An Introduction to Electron microscopy . Available from: <https://www.fei.com/documents/introduction-to-microscopy-document/>.
- [32] F. Krumeich. Properties of electrons, their interactions with matter and applications in electron microscopy. . Available from: <http://www.microscopy.ethz.ch/downloads/Interactions.pdf>.

- 
- [33] Wikipedia. Electron microscope. Available from: [https://en.wikipedia.org/wiki/Electron\\_microscope](https://en.wikipedia.org/wiki/Electron_microscope).
- [34] S. Utsunomiya, M. Kogawa, E. Kamiishi, and R. C. Ewing. Scanning Transmission Electron Microscopy and Related Techniques for Research on Actinide and Radionuclide Nanomaterials. In *Actinide Nanoparticle Research*, pages 33–62. Springer Berlin Heidelberg, 2011.
- [35] H. Hertz. Ueber einen Einfluss des ultravioletten Lichtes auf die elektrische Entladung. *Annalen der Physik und Chemie*, 267(8):983–1000, 1887.
- [36] A. B. Arons and M. B. Peppard. Einstein’s Proposal of the Photon Concepta Translation of the Annalen der Physik Paper of 1905. *American Journal of Physics*, 33(5):367–374, 1965.
- [37] C. C. Chusuei and D.W. Goodman. X-Ray Photoelectron Spectroscopy. In *Encyclopedia of Physical Science and Technology*, pages 921–938. Elsevier, 2003.
- [38] C. S. Fadley. Basic Concepts of X-ray Photoelectron Spectroscopy, in *Electron Spectroscopy: theory, experiments and applications*. 2, 1978.
- [39] S. Hüfner. *Photoelectron Spectroscopy*, volume 82. Springer Berlin Heidelberg, 1996.
- [40] M.B. Trzhaskovskaya, V.K. Nikulin, V.I. Nefedov, and V.G. Yarzhemsky. Non-dipole second order parameters of the photoelectron angular distribution for elements  $Z=1100$  in the photoelectron energy range 110keV. *Atomic Data and Nuclear Data Tables*, 92(2):245–304, 2006.
- [41] I.M. Band, Yu.I. Kharitonov, and M.B. Trzhaskovskaya. Photoionization cross sections and photoelectron angular distributions for x-ray line energies in the range 0.1324.509 keV targets:  $1 \leq Z \leq 100$ . *Atomic Data and Nuclear Data Tables*, 23(5):443–505, 1979.
- [42] J.J. Yeh and I. Lindau. Atomic subshell photoionization cross sections and asymmetry parameters:  $1 \leq Z \leq 103$ . *Atomic Data and Nuclear Data Tables*, 32(1):1–155, 1985.
- [43] S. Tanuma, C. J. Powell, and D. R. Penn. Calculations of electron inelastic mean free paths. II. Data for 27 elements over the 50-2000 eV range. *Surface and Interface Analysis*, 17(13):911–926, 1991.
- [44] Qunfeng Xiao, Xiaoyu Cui, Yinbo Shi, Yongfeng Hu, Tsun-Kong Sham, Hong Piao, and James McMahon.
- [45] B. Philippe, M. Hahlin, K. Edstrom, T. Gustafsson, H. Siegbahn, and H. Rensmo. Photoelectron Spectroscopy for Lithium Battery Interface Studies. *Journal of the Electrochemical Society*, 163(2):A178–A191, 2015.
- [46] J. Rault. *Structure chimique et electronique des interfaces metal/ferroelectrique en fonction de la polarisation ferroelectrique*. PhD thesis, 2013.
- [47] T. Schneider, K. Artyushkova, J. E. Fulghum, A. Broadwater, L. and Smith, and O. D. Lavrentovich. Oriented monolayers prepared from lyotropic chromonic liquid crystal. *Langmuir*, 21(6):2300–2307, 2005.
- [48] M. Repoux. Comparison of background removal methods for XPS. *Surface and Interface Analysis*, 18(7):567–570, 1992.

- [49] C. S. Fadley, S. B. M. Hagstrom, M. P. Klein, and D. A. Shirley. Chemical Effects on Core-Electron Binding Energies in Iodine and Europium. *The Journal of Chemical Physics*, 48(8):3779–3794, 1968.
- [50] M.C. Desjonqueres, D. Spanjaard, Y. Lassailly, and C. Guillot. On the origin of the variation of the binding energy shifts of core levels between surface and bulk atoms in transition metals. *Solid State Communications*, 34(10):807–810, 1980.
- [51] K.S. Kim and N. Winograd. X-ray photoelectron spectroscopic binding energy shifts due to matrix in alloys and small supported metal particles. *Chemical Physics Letters*, 30(1):91–95, 1975.
- [52] P. H. Citrin, G. K. Wertheim, and Y. Baer. Core-Level Binding Energy and Density of States from the Surface Atoms of Gold. *Physical Review Letters*, 41(20):1425–1428, 1978.
- [53] W.F. Egelhoff. Core-level binding-energy shifts at surfaces and in solids. *Surface Science Reports*, 6(6-8):253–415, 1987.
- [54] D. Spanjaard, C. Guillot, M. C. Desjonquères, G. Tréglià, and J. Lecante. Surface core level spectroscopy of transition metals: A new tool for the determination of their surface structure. *Surface Science Reports*, 5(1-2):1–85, 1985.
- [55] B. Johansson and N. Mårtensson. Core-level binding-energy shifts for the metallic elements. *Physical Review B*, 21(10):4427–4457, 1980.
- [56] Ulrich Gonser, editor. *Microscopic Methods in Metals*. Springer Berlin Heidelberg, 1986.
- [57] G. Abramovici, M. Desjonqu, and D. Spanjaard. Oxygen Induced Surface Core Level Shifts of W ( 110 ) Deduced From Surface Segregation Energies. *Journal de Physique I*, 5(110):907–916, 1995.
- [58] A. Rosengren and B. Johansson. Calculated transition-metal surface core-level binding-energy shifts. *Physical Review B*, 22(8):3706–3709, 1980.
- [59] E. Martinez, A. Herrera-Gomez, M. Allain, A. Renault, O. Faure, A. Chabli, and F. Bertin. Characterization of geometrical factors for quantitative angle-resolved photoelectron spectroscopy. *Journal of Vacuum Science & Technology A: Vacuum, Surfaces, and Films*, 30(4):040605, 2012.
- [60] S. Hofmann. *Auger- and X-Ray Photoelectron Spectroscopy in Materials Science*, volume 49 of *Springer Series in Surface Sciences*. Springer Berlin Heidelberg, 2013.
- [61] J. F. Watts and J. Wolstenholme. *An introduction of Surface Analysis and XPS*, volume 27. John Wiley & Sons, Ltd, 2003.
- [62] F. Allegretti. Characterization of Solid Surfaces and Thin Films by Photoelectron and Auger Electron Spectroscopy. *Versuch Nr. 35 Lehrstuhl E20, Raum 229 F-Praktikum in den Masterstudiengängen Physik*.
- [63] M. P. Seah. XPS reference procedure for the accurate intensity calibration of electron spectrometers? results of a BCR intercomparison co-sponsored by the VAMAS SCA TWA. *Surface and Interface Analysis*, 20(3):243–266, 1993.
- [64] Fairley, N. *CasaXPS Manual 2.3.15 Rev 1.2 Casa Software Ltd., 2009*.

- 
- [65] J. C. Woicik. *Hard X-ray Photoelectron Spectroscopy (HAXPES)*, volume 59 of *Springer Series in Surface Sciences*. Springer International Publishing, 2016.
- [66] W. Drube. Preface. *Journal of Electron Spectroscopy and Related Phenomena*, 190(PART B):125–126, 2013.
- [67] K. Siegbahn. Preface to hard X-ray photo electron spectroscopy (HAXPES). *Nuclear Instruments and Methods in Physics Research Section A: Accelerators, Spectrometers, Detectors and Associated Equipment*, 547(1):1–7, 2005.
- [68] S. Kaiser, U. Das, Y. Lu, V. Kundapur, and Tim May. Synchrotron Radiation: Applications in Diagnosis and Treatment of Malignant Brain Tumors. In *Diagnostic Techniques and Surgical Management of Brain Tumors*. InTech, 2011.
- [69] H. Kamitsubo. SPring-8 Program. *Journal of Synchrotron Radiation*, 5(3):162–167, 1998.
- [70] M.P. Level and P. Morin. SOLEIL : une source synchrotron multidisciplinaire. *Cnrs*, 2004.
- [71] J.P. Rueff, J. M. Ablett, D. Céolin, D. Prieur, Th. Moreno, V. Balédent, B. Lassalle-Kaiser, J. E. Rault, M. Simon, and A. Shukla. The GALAXIES beamline at the SOLEIL synchrotron: inelastic X-ray scattering and photoelectron spectroscopy in the hard X-ray range. 22(1):175–179, 2015.
- [72] J. M. Ablett, J.-M. Dubuisson, T. Moreno, D. Céolin, D. Prieur, E. Raimon, D. Corruble, J. Coquet, A. Lestrade, C. Bourgoïn, and J.P. Rueff. New Design Concept for a High-Resolution In-Vacuum 4-Bounce Hard X-Ray Monochromator at the GALAXIES Beamline at the SOLEIL Synchrotron. *Journal of Physics: Conference Series*, 425(5):052007, 2013.
- [73] GALAXIES Synchrotron Beamline. <https://www.synchrotron-soleil.fr/fr/lignes-de-lumiere/galaxies>.
- [74] D. Céolin, J.M. Ablett, D. Prieur, T. Moreno, J.-P. Rueff, T. Marchenko, L. Journel, R. Guillemin, B. Pilette, T. Marin, and M. Simon. Hard X-ray photoelectron spectroscopy on the GALAXIES beamline at the SOLEIL synchrotron. *Journal of Electron Spectroscopy and Related Phenomena*, 190(PART B):188–192, 2013.
- [75] I. Gueye, G. Le Rhun, O. Renault, D. Cooper, D. Ceolin, J-P. Rueff, and N. Barrett. Operando hard X-ray photoelectron spectroscopy study of the Pt/Ru/PbZr 0.52 Ti 0.48 O 3 interface. *Applied Physics Letters*, 111(3):032906, 2017.

# Chapter 3

## ELECTRICAL RESPONSE OF Pt/Ru/PZT/Pt CAPACITOR

### Contents

<b>3.1 Electrical Measurement Processes . . . . .</b>	<b>78</b>
3.1.1 Capacitance Density and Loss Tangent . . . . .	79
3.1.2 Breakdown Voltage (Field) Measurement . . . . .	81
<b>3.2 Pb Excess and Post Metallization Annealing Effects . . . . .</b>	<b>84</b>
3.2.1 Dielectric Constant and Loss Tangent . . . . .	85
3.2.2 Breakdown Field . . . . .	89
<b>3.3 Conclusion . . . . .</b>	<b>90</b>
<b>Bibliography . . . . .</b>	<b>92</b>

Properties of PZT films highly depend on the composition, particularly Zr/Ti ratio [1, 2]. PZT grown at the morphotropic phase boundary shows best electrical properties such as piezoelectric coefficients and dielectric constant [3, 4, 5]. In contrast to the Zr/Ti ratio, the lead (Pb) excess content effect has not been much addressed in the literature. We will therefore focus on the study of lead content, which is difficult to control due to volatility of the PbO during heat treatments. In fact, tuning the Pb excess precursor during the growth of PZT, in order to compensate the loss of Pb, might also play a major role in the electric properties of PZT [6]. Further, the post metallization annealing (PMA) of the whole metal-ferroelectric-metal stack might also modify electrical responses of the capacitor [7]. Thus, the thermal treatment and the Lead excess content were considered in this thesis work to optimize and to enhance the performances of PZT-based MIMs.

In this chapter, first, we will describe the experimental procedures for electrical characterization of PZT based capacitors.

Finally, electrical results (dielectric constant, loss tangent and breakdown field) from Pt/Ru/PZT/Pt capacitors depending on the rate of lead excess and the PMA will be reported and explained.

### 3.1 Electrical Measurement Processes

We detail the different electrical measurement methods used in this thesis to characterize the dielectric constant, loss tangent and breakdown voltage of Pt(100 nm)/Ru(5 nm)/PZT(220 nm)/-

Pt(100 nm)/TiO<sub>2</sub>/SiO<sub>2</sub>/Si stacks at room temperature. All capacitors studied are  $(80 \times 80)\mu\text{m}^2$  of area. Electrical measurements are carried out with a probe station (cascade) and by applying the bias on the bottom electrode with the top electrode connected to the ground. The measurement tools are monitored by a computer with the software GAMME developed at LETI [8], as shown in Figure 3.1. For breakdown voltage tests, current measurements are performed with Keithley 2400 source meter Voltage, while for the capacitance and loss tangent, it is plugged on the LCR-Meter HP4284A Agilent.

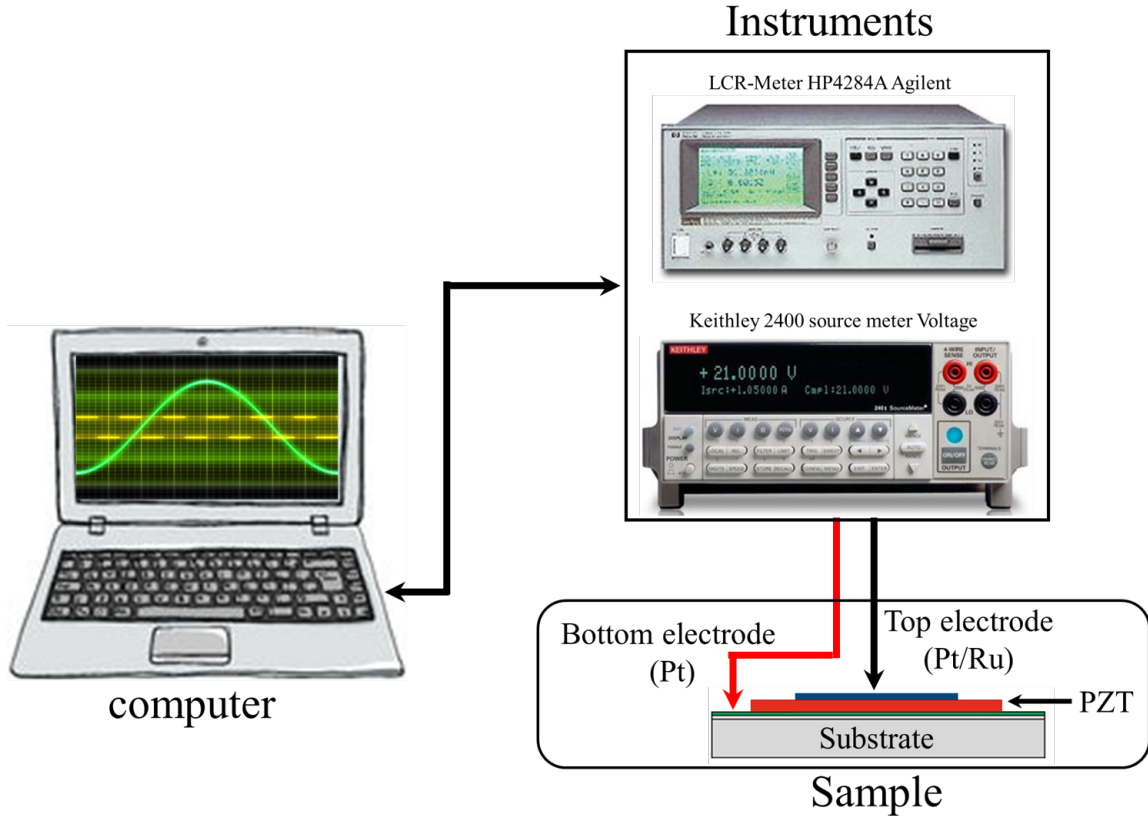


Figure 3.1: Schematic electrical measurements set up

### 3.1.1 Capacitance Density and Loss Tangent

The purpose of the capacitance-voltage measurement using impedance meters is to determine the dielectric constant and the dielectric losses of PZT samples as a function of the voltage applied. Experimentally, the properties of the actual capacitor differ from those of the ideal capacitor. Ideal capacitor is characterized by a pure capacitance denoted  $C$  (linked to the dielectric constant), which is constant and independent of the source frequency. In reality, the ideal capacitor does not exist. Indeed, with the actual capacitor, the energy losses are often present and the measured values of  $C$  always depend on the frequency. Hence, different models are used to describe the imperfections in the capacitor systems.

The most common and simplest model of a capacitor called the series-equivalent circuit model is schematically presented in Figure 3.2. With this model,  $R_s$  (which summarizes all

the resistance of metallic plates and connecting wires) represents the losses caused not only by the resistance of the electrodes but also by the electrical interconnection contributions.  $C$  is the pure capacitance of the ideal capacitor.  $R_p$  is the resistance taking into account the finite resistance of the dielectric material and is related only to leakage current but not to dielectric losses, which are included in the imaginary part of the relative permittivity. In practice, for a sufficiently insulating material, the dielectric losses are typically predominant compared to the losses through the leakage currents [9].

The predominance of  $R_p$  or  $R_s$  depends on both the capacitance value and the frequency range. At low frequencies, the parallel circuit will be the most representative while at high frequencies, it is the circuit in series that will be the most representative [10].

Moreover, knowing that the capacitance of a ferroelectric capacitor is small (usually less than  $1\mu F$ ), the contribution of the equivalent parallel resistance ( $R_p$ ) has relatively more importance than the equivalent series resistance ( $R_s$ ). Indeed, a small capacitance yields large reactance, which implies that the effect of the parallel resistance  $R_p$  has relatively more significance than that of series resistance  $R_s$ . The low value of resistance represented by  $R_s$  has negligible significance compared with the capacitive reactance. Therefore  $R_s$  can be negligible compared to  $R_p$ .

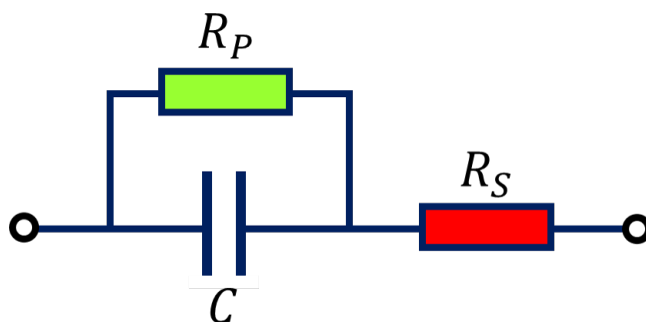


Figure 3.2: Electric equivalent circuit model of a capacitor with  $C$ ,  $R_s$  and  $R_p$  are the ideal capacitor, the serial resistance and the parallel resistance, respectively

Taking into account all these considerations, the admittance (We recall that admittance is the reverse of impedance  $Z = R + jX$  with a real part  $R$  is the resistance and the imaginary part  $X$  is the reactance ( $X = (2\pi fC)^{-1}$ )) in the equivalent parallel resistance is [11]:

$$Y = G + jB = G - j2\pi fC_p = Z^{-1} = \frac{1}{R + jX} \quad ; \quad (j^2 = -1) \quad (3.1)$$

where the real part is the conductance  $G$  and the imaginary part is the susceptance  $B$ . These components can also be expressed as a function of  $R$  and  $X$ .

$$G = R(Y) = \frac{R}{R^2 + X^2} \quad ; \quad B = I(Y) = \frac{X}{R^2 + X^2} \quad (3.2)$$

Thus, by using the real and imaginary axes projections of the complex admittance  $Y$  (phasor diagram) and the relationship between the susceptance  $B$  and capacitance  $C$ , one can determine respectively:

$$\tan\delta = R/X \quad ; \quad C_p = X / (2\pi f \cdot (R^2 + X^2)) \quad (3.3)$$

From  $C_p$ ,  $\tan\delta$  and geometric parameters of the capacitors (thickness  $d$  and surface  $A$ ), it is possible to obtain the expressions of  $\varepsilon_r'$  and  $\varepsilon_r''$

$$\varepsilon_r' = C_p \cdot d / (\varepsilon_0 \cdot A) \quad ; \quad \varepsilon_r'' = \varepsilon_r' \cdot \tan\delta \quad (3.4)$$

During this thesis, capacitance and loss tangent measurements using LCR-Meter HP4284A Agilent are performed by sweeping the bias between  $-10V$  and  $+10V$ , which superimposed an alternating signal with an amplitude of  $100mV$  and frequency at  $10kHz$ . In order to obtain reliable electric results, for each PZT (PZT10, PZT15, PZT20 and PZT30) samples, several capacitors (13 capacitors) have been studied. In the following, we will present the average result of these statistical studies.

### 3.1.2 Breakdown Voltage (Field) Measurement

Electrical shorting in FE capacitor i.e. breakdown, results in sudden and permanent damage of the dielectric. The breakdown is manifested by the formation of a conductive path between the conducting parallel plates, which causes high current flow through the dielectric. The mechanism of breakdown is a complex phenomenon. Three mechanisms of breakdown are distinguished: intrinsic or electronic breakdown, thermal breakdown and avalanche breakdown [12]. However, in the case of dielectrics obtained under carefully controlled conditions without any defects, the breakdown strength called intrinsic breakdown occurs at very high electric field. However, real dielectrics often fail under electric field stresses below intrinsic breakdown values due to the extrinsic defects, which are linked on external causes, particularly related to defects.

In real dielectrics two types of defect can be distinguished: the intrinsic defects, which are related to the specific properties of the dielectric material (vacancies, dislocations, grain boundaries) and the extrinsic defect, which are based on external causes like particles contamination during material deposition or damages caused during integration process steps like dry etching and passivation deposition.

Regarding to the intrinsic breakdown, two models have been developed to explain this mechanism. A qualitative model presented by Suñé *et al.* [13] is based on two parameters: critical number of defects and the area of unit cells. This statistical model is based on the random generation of defects into the bulk of dielectric under the influence of the applied electric field. Thus, the breakdown process starts when a critical number of defects is reached in one of the elementary cells. To locally reach this critical number of defects, a total number of defects will be created throughout the volume of the oxide leading to

the breakdown of dielectric by the creation of the conduction path between the electrodes. However, the model of Suñé is limited by the fact that it considers only the cases where the defects appear at the interface level.

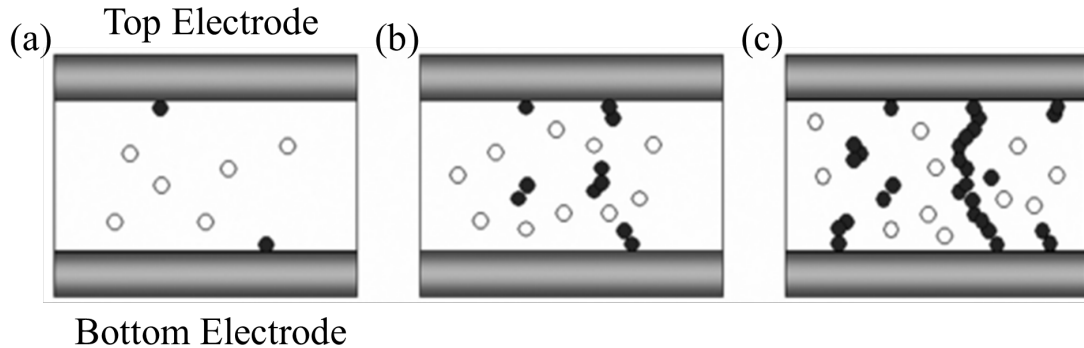


Figure 3.3: Illustration of the percolation model. (a) As a first step, the defects (empty circle) are randomly generated in the dielectric. (b) Defects overlap or come into contact with the electrodes agglomerates as referred by the black filled circle (c) Finally, the breakdown is triggered when a percolation path between the two electrodes is formed. [9]

The model proposed by Degraeve *et al.* [14] to supplement the Suñé model is based on percolation model. In the percolation model, the defects are represented by spheres with a constant radius. When electrical field is applied, the defects are created in the dielectric at random positions. As soon as the two electrodes are connected by overlapping spheres (clusters creation), a conducting path is formed for electrons and the breakdown condition is reached as illustrated in Figure 3.3. Parameters introduced in this quantitative model are the total density of defects generated in the dielectric until breakdown, the size of these defects, and the percentage of occupied defects. From percolation model, Chentir *et al.* [15] have established a direct correlation between the physical properties of defects (voids, interfaces defects, etc.) and the breakdown statistics of PZT capacitors. They show that percolation defects, which appears under electric field, participate in the creation of the breakdown path. Note that, in PZT thin film the main defects take origin either the oxygen-vacancies ( $V_O$ ) or the Pb-vacancies ( $V_{Pb}$ ) [16, 17, 18, 19].

During this thesis, breakdown field (voltage) measurements was carried out using Linear Ramp Voltage Stress (LRVS) [9] test ( $\Delta V=0.5$  V and  $\Delta t=0.5$  s) and Weibull statistical analysis. As shown in Figure 3.4 (a-b), the current as a function of voltage for the PZT10 before and after post metallization annealing were measured by using a Keithley 2400 source meter unit interfaced with a computer to perform the measurement and record data. With an appropriate trigger on the current, the voltage at which the capacitor has shorted can be detected and recorded. Short Circuit is defined for an abrupt current increase, typically greater than a decade in a single voltage step. The criterion of the short Circuit chosen for a capacitor of size  $(80 \times 80)\mu m^2$  is 1 mA. As the breakdown field follows a probability law (Weibull statistical analysis [20, 21, 22, 23]), by cumulating short Circuit data over 90 capacitors tested per wafer, the repartition function can be fitted and breakdown voltage can be extracted.

It is very important to note that the choice of the voltage step and the delay time values used during this thesis is to determine the breakdown voltage (field) values for each sample and not for studying the different leakage current mechanisms in the samples. Indeed, for current-voltage measurements, the voltage step (0.5 V) and the delay time (0.5 s) may be not very appropriate [9]. The voltage step is relatively large which may induce transient currents and the delay time may be not long enough to measure true leakage current, with no parasitic contributions from transient currents. However, a real current-voltage measurement, which requires time dependent current measurement to establish the right delay time and the real leakage current values, is not the main goal of this work.

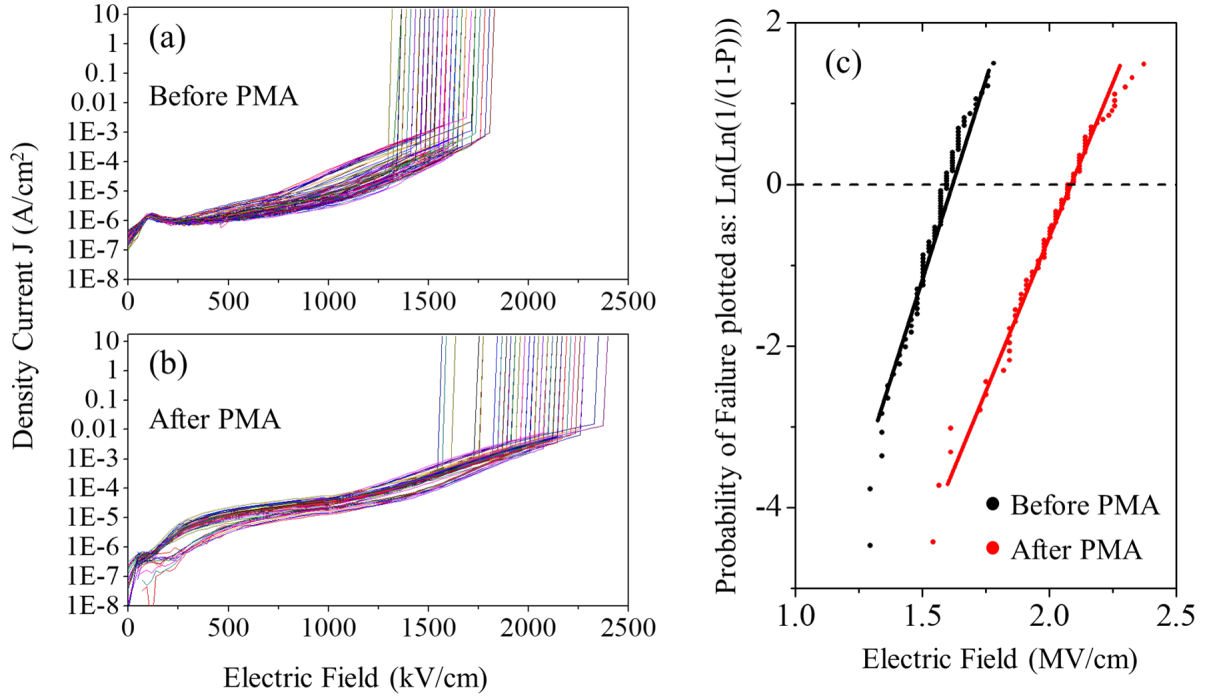


Figure 3.4: The density of current of PZT10 as a function of electric field: (a) before and (b) after post metallization annealing. Electric field (Voltage) was applied to a certain value in a successive voltage step of 0.5 V with delay time of 0.5 s, until the leakage current increased sharply and abruptly, indicating the occurrence of breakdown. (c) Determination of the breakdown field (voltage) before and after post metallization annealing of PZT10 through Weibull distribution [21]. (Note: PZT10 means PZT with 10 % of lead excess)

For breakdown field, experimental data are plotted according to a two-parameter Weibull distribution. The cumulative failure probability is defined as

$$P(E_{BD}) = 1 - \exp \left[ - \left( \frac{E_{BD}}{\alpha} \right)^\beta \right] \quad (3.5)$$

where  $P(E_{BD})$  is the cumulative probability of failure occurring at the electric field lower or equal to  $E_{BD}$ .  $E_{BD}$  is the electric field obtained by dividing the breakdown voltage by the

thickness of the sample. The  $\alpha$  scale parameter of scale factor is the nominal field, i.e. the field corresponding to a 63.2 % breakdown cumulative probability for the sample and, while the shape parameter or shape factor  $\beta$  evaluates the scatter of data. The experimental plot must be a straight line in a coordinate system:

$$\begin{cases} X = E_{BD} \\ Y = Ln \left[ Ln \left( \frac{1}{1-P} \right) \right] \end{cases} \quad (3.6)$$

From Figure 3.4 (c), linear regression was used to determine  $\beta$  which is 13.9 and 17.5 for PZT10 before and after post metallization annealing respectively. According to the percolation theory [24, 25, 26], the  $\beta$  value is related to the critical defect density that is necessary to reach for triggering the breakdown.  $E_{BD}$  is obtain when the  $Y$  reach zero which correspond also to  $\alpha = 63.2$  % of breakdown cumulative probability for the sample.  $E_{BD}$  values are 1.60 and 2.09 MV/cm for PZT10 before and after PMA, respectively.

## 3.2 Pb Excess and Post Metallization Annealing Effects

Studies including eg Wang *et al.* [27], have shown that with below 10 % of Pb excess content in the target, ferroelectric and dielectric properties of PZT thin films fall drastically, whereas with above 30 % of Pb excess content in the target, no dielectric constant responses are obtained. Even though, no lead oxides were detected by XRD analyses for the films fabricated with 30 % and 40 % excess PbO. Wang *et al.* suggested that the residual Pb remains at the grain boundaries of PZT film in the form of small particles of amorphous PbO. These amorphous PbOs seem to be at the origin of the poor properties. These results can be correlated with the data from Yanovskaya *et al.* [6] which show a decrease of the capacitance when the Pb excess is below 10 % and above 30 %.

Furthermore, post metallization annealing shows very crucial importance in the performance of the MIM structures. Kim *et al.* [28] showed a better saturation of the polarization after post metallization annealing. Taylor *et al.* [29] described a possible electro-migration of the Ruthenium from the top electrode down to the film during thermal treatment. Al-Shareef *et al.* [7] observed that annealing the entire capacitor stack after the top electrode deposition improved ferroelectric properties. It described also the possible creation of the  $Pb_2Ru_2O_{7-x}$  conductive layer under annealing ruthenium oxide and PZT interface. The presence of the  $Pb_2Ru_2O_{7-x}$  between the Metal/PZT interface leads to the increase of the leakage current values but enhanced the ferroelectric properties [30, 31, 32, 33].

Based on the various results provided by Wang *et al.* [27], Vorotilov *et al.* [34] and Yanovskaya *et al.* [6] but also on the impact of the thermal treatment of the entire capacitor, we will study the effects of Pb excess and the post metallization annealing in the electrical responses of the Pt/Ru/PZT/Pt capacitors. Figure 3.5 (a) shows the measurement bench.

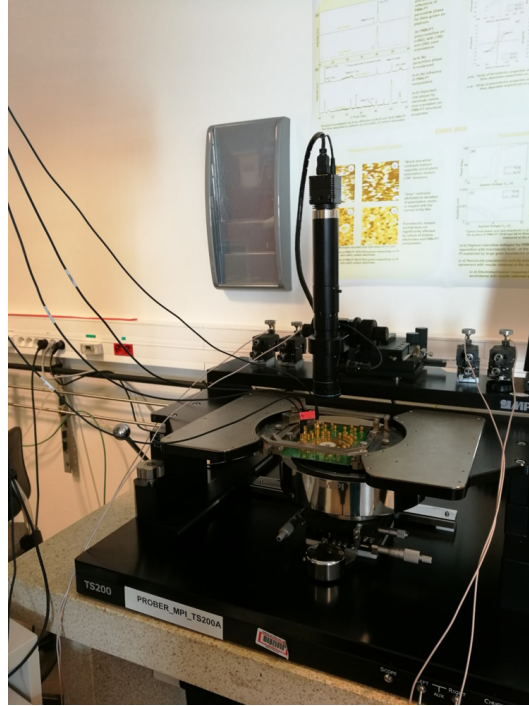


Figure 3.5: Actual electrical measurements bench

### 3.2.1 Dielectric Constant and Loss Tangent

In this section, we will study the value of the capacitance density and Loss tangent as a function of the lead excess content and the post metallization annealing effects.

#### (a) Dielectric Constant and Loss Tangent Before PMA

Using the electrical set up, capacitance measurements were carried out on Pt/Ru/PZT/Pt stacks as shown in Figure 3.6. The experimental data from dielectric constant-voltage curves are presented in Figure 3.6 (a) with an offset for better clarity the presentation of data. Curves show the characteristic butterfly loop of a ferroelectric. Butterfly loop are not symmetric about zero voltage but they display a high asymmetry along voltage axis with a shift toward the positive voltage relatively to the zero bias. This shift is 0.75 V for PZT30 whereas it is at 0.875 V for PZT10, PZT15 and PZT20, indicating a downwards pointing imprint polarization for all grown films. Note that the shift along the negative voltage axis is obtained when the bias is applied on the top electrode and the bottom electrode connected to the ground as we will see in chapter 5 in section 5.5 page 132. Finally, like the dielectric constant, loss tangent curves are shifted towards the positive voltage as seen in Figure 3.6 (b)).

Maximum dielectric constant and maximum loss tangent values obtained on each sample (as a function of the Pb excess used on the first and the fourth layers during the PZT thin film deposition) are recorded and reported in Figure 3.7. Maximum dielectric constant value shows a net increase (9 %) from 1126 to 1225 between PZT with 10 to 20 % lead excess rate. A maximum dielectric constant value of 1195 is registered for PZT with 15 % of Pb excess. Beyond the 20 % of lead excess, the maximum dielectric constant decreases. Indeed,

introduction of 30 % of Pb excess leads to a dielectric constant of 1193. The variations of permittivity values as a function of Pb excess amount are significant as seen in Figure 3.7. These results are consistent with the assertion that, the fine tuning of Pb content in PZT films may participate in the optimization of the capacitance density of capacitors.

Figure 3.7 shows also that the increase of the excess of Pb in the PZT matrix presents a positive aspect on the values of the maximum loss tangent. Indeed, the addition of Pb excess from 10 to 15 % favors the decrease of the maximum dielectric losses from 4.53 to 4.09 %. Another significant drop in losses occurred between 20 and 30 % of Pb, from 4.04 to 3.67 % is also noted. The variation of maximum loss tangent values might be attributed to the energy loss due to the current displacement in the dielectric. This situation can strongly depend on the thin film microstructure such as grain boundaries and also the defects in the thin film. According to the literature, the high amount of traps ( $V_O$  and  $V_{Pb}$ ) under voltage might behave as a conduction channel. In Figure 3.7, the loss tangent decreases when the lead excess rate increases, which re-establish the stoichiometry of PZT by reducing the defects density, vacancies or traps inside the PZT.

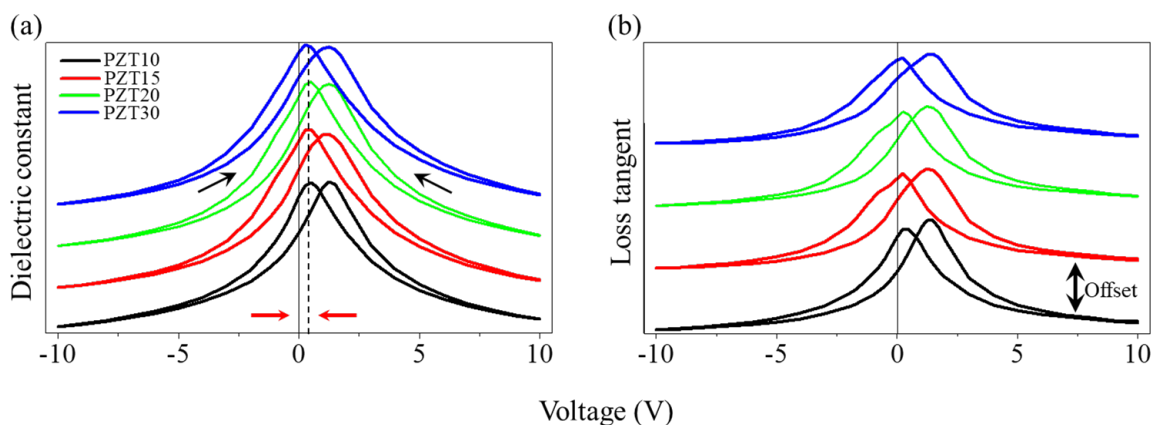


Figure 3.6: Dielectric constant and Loss tangent before post metallization annealing as function of voltage for different Pb excess rate used on the first and the fourth layers during the PZT thin film deposition

According to the data from literature, the Pb evaporation during thermal treatment of sol-gel PZT induces the development of the secondary phase at the surface or in the bulk of PZT film [27, 35, 36]. In fact, secondary or parasitic phases at the surface are often described as a non-FE phase such as pyrochlore [27] with a lower dielectric constant and are usually presumed to be at the origin of dead layers observed at the metal/insulator interface. These dead layers tend therefore to modify the electrical properties of capacitor devices. It is important to underline that the composition of the surface of the samples (mixture of PZT and secondary phase) obtained before deposit of the top electrodes should not change after deposit of the top electrodes, except in the case where a thermal treatment under oxygen of the Metal/PZT interface is performed.

Furthermore, from results presented in Figure 3.7, we conclude that there exist an optimum of Pb excess between 15 % and 20 %. This optimum of Pb excess allows to reach the optimal value of  $\epsilon_r$ . In fact, below the optimum of the Pb excess rate, parasitic phase or dead layer might be created and above this optimum value of Pb content the thin film

might present a residual cluster of PbO because the Pb oxide is often accumulated in the intercrystalline and interface layers of the films. Both situations favor the decrease of the capacitance density of PZT as seen with the PZT in 10 % and 30 % of Pb excess.

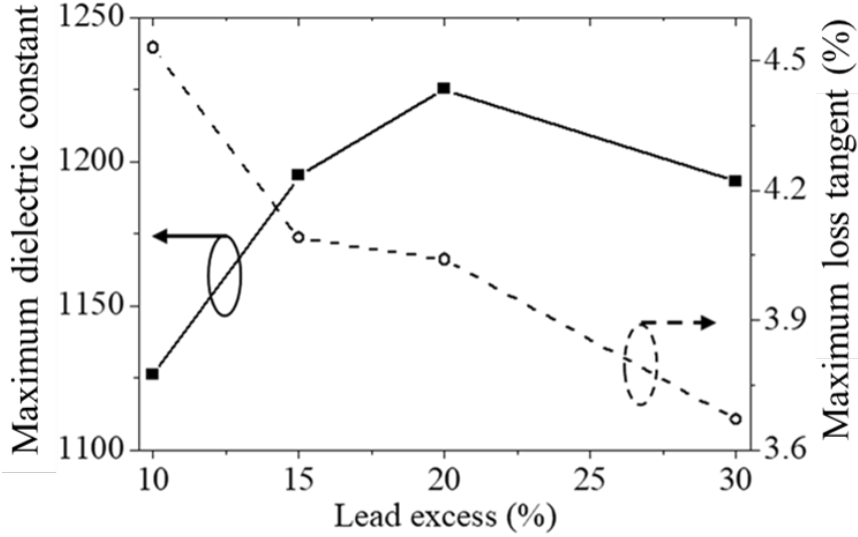


Figure 3.7: Maximum of dielectric constant and maximum loss tangent values before post metallization annealing as function of voltage for different Pb excess rate used on the first and the fourth layers during the PZT thin film deposition

The presence of strongly positive shift of butterfly curve (dielectric constant-voltage and loss tangent-voltage) suggests the presence of the imprint effect [37, 38, 39, 40] in the MFM which is certainly linked to the creation of internal electrical fields. In fact, the internal electric fields can be explained by several mechanisms [41], such as (i) defects domains pinning, which is due to the charge alignment or accumulation of charged defects, (ii) complex vacancies present at domain walls, that can screen the polarization state of PZT, and cause domain pinning, or by interface charge injection. Additionally, the use of different electrode materials for bottom and top contacts, which induces two types of Schottky barrier (asymmetric barrier heights), might participate to the creation of the imprint effect. This internal field (or Imprint) is obtained by making the ratio between the difference potential on thickness of the PZT. However, by considering the large thickness of the PZT (220 nm), it is unlikely that this asymmetry plays an important role on the capacitors. Indeed, the Imprints observed in samples are between 34.0 and 39.8 kV/cm in contrast to the effect due to the asymmetry which is of the order of 10 kV/cm. Furthermore, if the asymmetry effects played an important role on capacitors, the value of the Imprint is expected to remain almost identical for all samples.

Chen *et al.* [42] suggests that the shift of the dielectric constant-voltage curve observed on PZT can be caused by charge injection into defect states (traps), which modifies the local potential of interface and shifts the butterfly loop.

Furthermore, the presence of internal interfaces created inside the PZT sample during the different steps of PZT layer deposition (e.g. between the bulk with 10 % of Pb excess and the interface layers with higher Pb excess (10, 15, 20 and 30 % of Pb excess)) can

contributed to appearance of the internal field and therefore to the imprint of butterfly curves.

Considering PZT as a p-type semiconductor is equivalent to setting up a depletion layer width between the PZT and the electrode, resulting a non-zero internal electrical field. It has been also suggested that a thin layer with low dielectric constant interfacial layer can behave as the dead layer present at the interface, which can induce imprint behavior in the ferroelectric capacitors [43]. Teowee *et al.* [44] showed that defects in PZT films, such as  $V_O$  and  $V_{Pb}$ , play an important role since they are mobile under electrical stress and can migrate to the PZT-electrode interface or grain domain boundaries. This assertion is in agreement with the results of Lee *et al.* [45], which shows the hysteresis ferroelectric curve shifted by the presence of oxygen vacancy at the interface metal/BaTiO<sub>3</sub>.

### (b) Dielectric Constant and Loss Tangent After PMA

Figure 3.8 shows dielectric constant and loss tangent after post metallization annealing (550°C for 30 min at room temperature) of each PZT (with Pb excess rate used on the first and the fourth layers during the PZT thin film deposition) based capacitor. We remark that the characteristics of ferroelectric butterfly loop after post metallization annealing (PMA) showed a symmetric curves relative to 0 V. The fact that the dielectric constant and loss tangent butterfly curves become symmetrical is related to the impact of PMA because the other parameter have not been modified.

Maximum loss tangent values obtained after PMA of PZT10, PZT15, PZT20 and PZT30 capacitors (Figure 3.8 (b)) are 4.51, 4.36, 3.72 and 3.08 %, respectively. These data show reduction of the maximum loss tangent values relative to the samples before PMA. However, these results are keeping the same trend as the function of the lead excess content in the PZT layers.

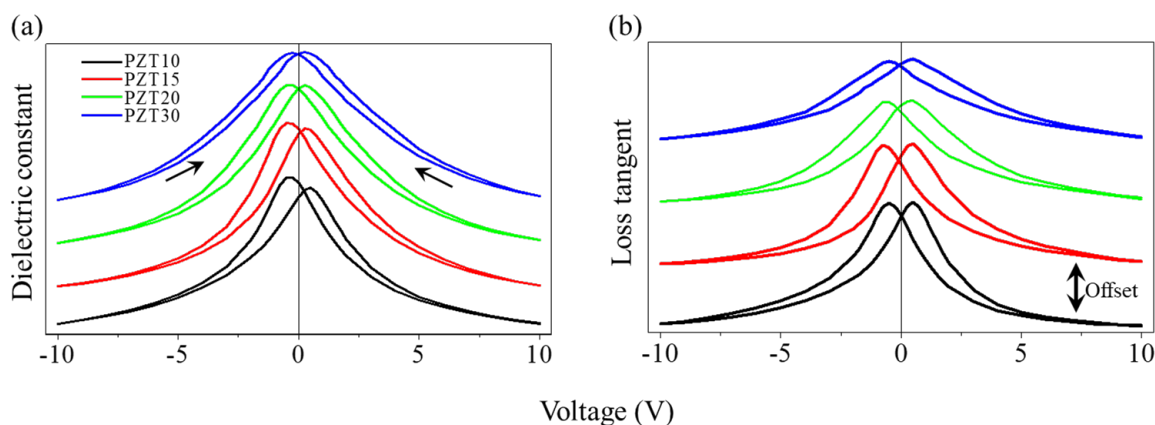


Figure 3.8: Dielectric constant and Loss tangent after post metallization annealing as function of voltage for different Pb excess rate used on the first and the fourth layers during the PZT thin film deposition

Furthermore, after PMA of the Pt/Ru/PZT/Pt stack, maximum dielectric constant of 1198, 1284, 1257 and 1227 have obtained respectively for PZT10, PZT15, PZT20 and PZT30 (results from Figure 3.8 (a)). These values of maximum dielectric constant are compared

with the maximum dielectric constant values obtained before PMA as illustrated in Figure 3.9.

The enhancement of dielectric constant independently of the Pb excess after PMA can be linked to several phenomena [46]. First, the effects of thermal annealing might induce higher densification [47] of the PZT thin film capacitors. Uhlmann [48] shows that the size of the grain increases when the post metallization is performed from 100 to 700°C which tend to decrease the number of grain boundaries. This may favor an enhancement of capacitance (dielectric constant). Furthermore, PMA may favor the migration of the oxygen-vacancies ( $V_O$ ) or the Pb-vacancies ( $V_{Pb}$ ) [16, 17, 18, 19] containing in the PZT thin film towards the top electrode which induces a decrease of defect and therefore improves the performance. PMA might also favor diffusion of residual PbO clusters at the interfaces between the polycrystalline PZT film and the top electrode because up to 350°C the lead oxide tends to evaporate as described by Uhlmann [48]. Bao *et al.* [49] explained that the difference of the electrical performance can be linked by the fact that polarization may penetrate more deeply into an oxide electrode than in the metal electrode. This results in smaller depolarizing fields at the interfaces with oxide electrodes than at the interfaces with metal electrodes. In our case, post metallization annealing might also lead to oxidation of Ru top electrode [50, 51, 52].

Finally, observation of a symmetry of the butterfly after PMA suggest the no-existence of the imprint effect in the capacitors. This situation may be explained by the reduction of the internal electric field either at the level of metal/PZT interfaces or at the level of internal interfaces inside the PZT samples (due to the multiple sol-gel deposition steps). This symmetry of the butterfly may be also associated by the modification of the Schottky barrier heights at the level of metal/PZT interfaces after PMA.

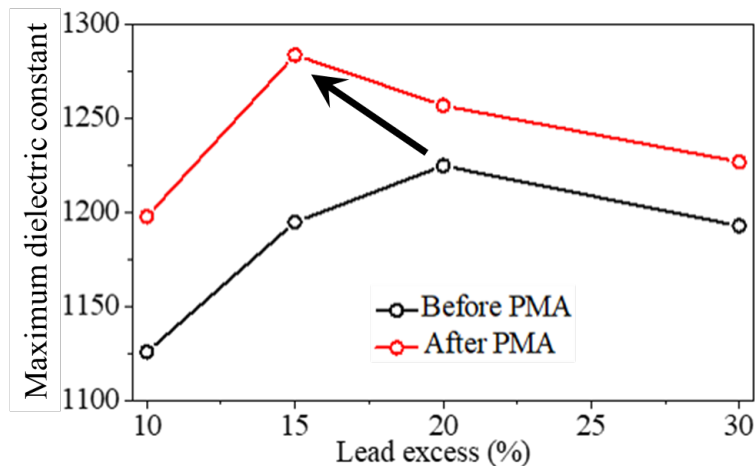


Figure 3.9: Comparison of maximum Dielectric constant values before and after post metallization annealing (PMA) as a function of the Pb excess rate used on the first and the fourth layers during the PZT thin film deposition

### 3.2.2 Breakdown Field

The breakdown fields measured before and after PMA on PZT capacitors samples with different Pb excess rate are shown in Figure 3.10. Regardless the Pb excess content in the

precursor, there is an improvement of the breakdown voltage value after thermal treatment under  $O_2$  during 30 min at  $550^\circ C$  relative to the results obtained before post metallization annealing. Indeed, before post metallization annealing, the increase of the Pb excess content in sol-gel precursors from 10 to 15 % leads to slight increase (from 1.60 to 1.68 MV/cm) of the breakdown field. Then, higher excess of lead (for 20 % and 30 %) induces the decrease of the breakdown field to 1.57 and 1.26 MV/cm respectively. With annealing process (red dash line), there is a decrease of the breakdown field from 2.09 MV/cm to 1.81 MV/cm for 10 % and 30 % respectively. An intermediate value (1.94 MV/cm) is obtained for both 15 and 20 % lead excess.

The results obtain in Figure 3.10, might be in agreement with the percolation theory developed Degraeve *et al.* [14]. Indeed, with a lower rate of Pb excess such as in PZT10 can induce a presence of high number of oxygen-vacancies ( $V_O$ ) or the Pb-vacancies ( $V_{Pb}$ ) which can favor the creation of conduction path. Furthermore, increasing the lead excess content in the precursors solution such as in PZT30, favors the generation of PbO clusters in the bulk at the level of grain boundaries which behaves as conduction way and thus favor the breakdown process [53].

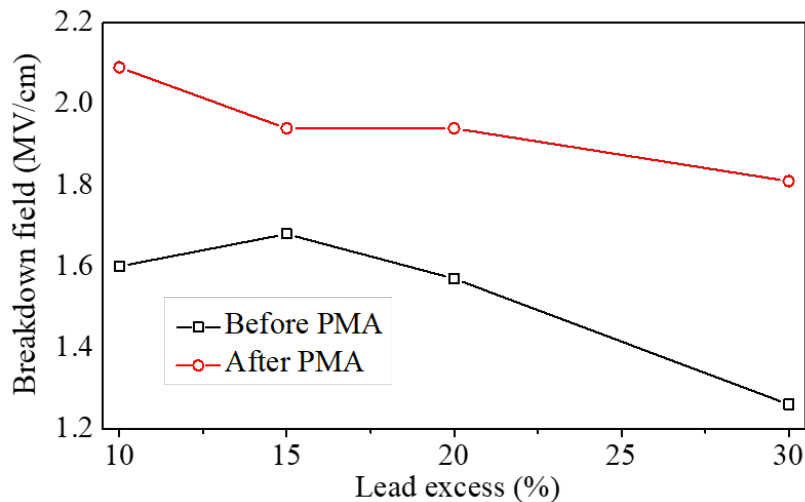


Figure 3.10: Breakdown Field as function of the Pb excess rate used on the first and the fourth layers during the PZT thin film deposition: (Black) before post metallization annealing and (Red) after post metallization annealing

### 3.3 Conclusion

In this chapter, both effects of Pb excess content and post metallization annealing on electrical properties of dielectric constant, loss tangent and breakdown field from the Pt/Ru/PZT/Pt were presented.

Permittivity results show an optimum between 15 and 20 % of Pb depending on both the lead excess and the post metallization annealing. The decrease of the dielectric constant for the PZT10 and PZT30 might be attributed to the presence of the secondary phase both interface metal/PZT and the bulk of PZT thin film. Loss tangent reduction due to the increase of the part of Pb excess in the precursor solution is observed. This might be linked

to the reduction of the defect (vacancies) which can favor the current conduction. With the post metallization annealing, the lost tangent evolution shows the same behavior as the one before thermal treatment whereas the values of the dielectric constant increases. Finally, we have shown that the high content of lead excess leads to the reduction of the breakdown field value. These situation might be linked with the high residual lead excess when the Pb excess is very high.

In the subsequent chapters, we will try to understand how Pb precursor excess and PMA modified the electric results. This is achieved by using primarily photoelectron spectroscopy to probe the PZT surface (XPS), interface (HAXPES) chemistry, and finally by using SEM, TEM and XRD for better understanding the physicochemical, structural and microstructural changes.

## Bibliography

- [1] F. Calame and P. Muralt. Growth and properties of gradient free sol-gel lead zirconate titanate thin films. *Applied Physics Letters*, 90(6):062907, 2007.
- [2] V. PhD Universite Grenoble Alpes Kovacova. Study of correlations between microstructure and piezoelectric properties of PZT thin films. 2015.
- [3] H. D. Chen, K. R. Udayakumar, C. J. Gaskey, and L. E. Cross. Electrical properties maxima in thin films of the lead zirconatelead titanate solid solution system. *Applied Physics Letters*, 67(23):3411–3413, 1995.
- [4] C. B. Carter and M. G. Norton. *Ceramic Materials-Science and Engineering*. 53(9), 2013.
- [5] S. Trolier-McKinstry and P. Muralt. Thin Film Piezoelectrics for MEMS. *Journal of Electroceramics*, 12(1/2):7–17, 2004.
- [6] M. I. Yanovskaya, I. E. Obvintseva, L. I. Solovyova, E. P. Kovsman, K. A. Vorotilov, and V. A. Vasilyev. Alkoxy-derived ferroelectric PZT films: The effect of lead acetate dehydration techniques and lead content in the electrochemically prepared solutions on the properties of the films. *Integrated Ferroelectrics*, 19, 1998.
- [7] H.N. Al-Shareef, K.R. Bellur, O. Auciello, and A.I. Kingon. Phase evolution and annealing effects on the electrical properties of  $\text{Pb}(\text{Zr}_{0.53}\text{Ti}_{0.47})\text{O}_3$  thin films with  $\text{RuO}_2$  electrodes. *Thin Solid Films*, 256(1-2):73–79, 1995.
- [8] D. Henry, F. Jacquet, M. Neyret, X. Baillin, T. Enot, V. Lapras, C. Brunet-Manquat, J. Charbonnier, B. Aventurier, and N. Sillon. Through silicon vias technology for CMOS image sensors packaging. In *2008 58th Electronic Components and Technology Conference*, pages 556–562. IEEE, 2008.
- [9] E. Defay. *Ferroelectric Dielectrics Integrated on Silicon*. 2011.
- [10] Y. A. Gagou. *Etude du changement de phase dans le composé  $\text{PbK}_2\text{LiNb}_5\text{O}_{15}$  de la famille des TTB*. PhD thesis, 2002.
- [11] Ch. Huber. *Synthèse et caractérisation de nouveaux matériaux ferroélectriques accordables pour applications hyperfréquences. (French)*. PhD thesis, 2003.
- [12] J. F. Scott, B. M. Melnick, L. D. McMillan, and C. A. P. De Araujo. Dielectric breakdown in high- $\epsilon$  films for ULSI DRAMs. *Integrated Ferroelectrics*, 3(3):225–243, 1993.
- [13] J. Suñé, I. Placencia, N. Barniol, E. Farrés, F. Martín, and X. Aymerich. On the breakdown statistics of very thin  $\text{SiO}_2$  films. *Thin Solid Films*, 185(2):347–362, 1990.
- [14] R. Degraeve, G. Groeseneken, R. Bellens, J.L. Ogier, M. Depas, P.J. Roussel, and H.E. Maes. New insights in the relation between electron trap generation and the statistical properties of oxide breakdown. *IEEE Transactions on Electron Devices*, 45(4):904–911, 1998.
- [15] M. T. Chentir, J. B. Jullien, B. Valtchanov, E. Bouyssou, L. Ventura, and C. Anceau. Percolation theory applied to PZT thin films capacitors breakdown mechanisms. *Microelectronics Reliability*, 49(9-11):1074–1078, 2009.
- [16] R. Moazzami, C. Hu, and W.H. Shepherd. Electrical characteristics of ferroelectric PZT thin films for DRAM applications. *IEEE Transactions on Electron Devices*, 39(9):2044–2049, 1992.

- 
- [17] J. F. Scott, C. A. Araujo, B. M. Melnick, L. D. McMillan, and R. Zuleeg. Quantitative measurement of spacecharge effects in lead zirconatetitanate memories. *Journal of Applied Physics*, 70(1):382–388, 1991.
- [18] I. K. Yoo and S. B. Desu. Mechanism of Fatigue in Ferroelectric Thin Films. *Physica Status Solidi (a)*, 133(2):565–573, 1992.
- [19] H. M. Duiker, P. D. Beale, J. F. Scott, C. A. Paz de Araujo, B. M. Melnick, J. D. Cuchiaro, and L. D. McMillan. Fatigue and switching in ferroelectric memories: Theory and experiment. *Journal of Applied Physics*, 68(11):5783–5791, 1990.
- [20] R. A. Schlitz, K. Yoon, L. A. Fredin, Y. Ha, M. A. Ratner, T. J. Marks, and L. J. Lauhon. Weibull Analysis of Dielectric Breakdown in a Self-Assembled Nanodielectric for Organic Transistors. *The Journal of Physical Chemistry Letters*, 1(22):3292–3297, 2010.
- [21] V. Tomer, E. Manias, and C. A. Randall. High field properties and energy storage in nanocomposite dielectrics of poly(vinylidene fluoride-hexafluoropropylene). *Journal of Applied Physics*, 110(4):044107, 2011.
- [22] K. Wu, Y. Wang, Y. Cheng, L. A. Dissado, and X. Liu. Statistical behavior of electrical breakdown in insulating polymers. *Journal of Applied Physics*, 107(6):1–5, 2010.
- [23] C. Chauvet and C. Laurent. Weibull Statistics in Short-term Dielectric Breakdown of Thin Polyethylene Films. *IEEE Transactions on Electrical Insulation*, 28(1):18–29, 1993.
- [24] E.Y. Wu and R. P. Vollertsen. On the weibull shape factor of intrinsic breakdown of dielectric films and its accurate experimental determination-part I: theory, methodology, experimental techniques. *IEEE Transactions on Electron Devices*, 49(12):2131–2140, 2002.
- [25] J. H. Stathis. Percolation models for gate oxide breakdown. *Journal of Applied Physics*, 86(10):5757–5766, 1999.
- [26] R. Degraeve, G. Groeseneken, R. Bellens, J.L. Ogier, M. Depas, P.J. Roussel, and H.E. Maes. New insights in the relation between electron trap generation and the statistical properties of oxide breakdown. *IEEE Transactions on Electron Devices*, 45(4):904–911, 1998.
- [27] Z. J. Wang, K. Kikuchi, and R. Maeda. Effect of Pb content in target on electrical properties of laser ablation derived lead zirconate titanate thin films. *Japanese Journal of Applied Physics, Part 1: Regular Papers and Short Notes and Review Papers*, 39(9 B):5413–5417, 2000.
- [28] B. J. Kim, J. Lee, J. B. Yoo, and K. S. No. Pb(Zr,Ti)O<sub>3</sub> films fabrication by sol-gel method for piezoelectric actuated device. *Ferroelectrics*, 232(1):247–252, 1999.
- [29] D.J. Taylor, J. Geerse, and P.K. Larsen. Fatigue of organometallic chemical vapor deposited PbZr<sub>x</sub>Ti<sub>1-x</sub>O<sub>3</sub> thin films with Ru/RuO<sub>2</sub> and Pt/Pt electrodes. *Thin Solid Films*, 263(2):221–230, 1995.
- [30] H.N. Al-Shareef, Y.L. Chen, O. Auciello, and A.I. Kingon. Microstructural and Electrical Properties of Ferroelectric Capacitors with Pt/RuO<sub>2</sub> Hybrid Electrodes. *MRS Proceedings*, 361:229, 1994.
- [31] H. L. Ee and W. L. Ee. Preparation and Characterization of Pb(Zr,Ti)O<sub>3</sub> Films Deposited on Pt/RuO<sub>2</sub> Hybrid Electrode for Ferroelectric Random Access Memory Devices. *Jpn. J. Appl. Phys.*, 40(11):6566–6573, 2001.

- [32] N. J. Seong, K. J. Choi, and S. G. Yoon. Thickness effect of  $\text{Pb}_2\text{Ru}_2\text{O}_{7-x}$  conductive interfacial layers on ferroelectric properties of  $\text{Pt}/\text{Pb}(\text{Zr}_{0.35}\text{Ti}_{0.65})\text{O}_3/\text{Pt}$  capacitors. *Thin Solid Films*, 468(1-2):100–104, 2004.
- [33] S. Ryoo, S. Yoon, and S. Kim. Improvement in ferroelectric properties of  $\text{Pb}(\text{Zr}_{0.35}\text{Ti}_{0.65})\text{O}_3$  thin films using a  $\text{Pb}_2\text{Ru}_2\text{O}_{7-x}$  conductive interfacial layer for ferroelectric random access memory application. *Applied Physics Letters*, 83(14):2880–2882, 2003.
- [34] K.A. Vorotilov, M.I. Yanovskaya, L.I. Solovjeva, A.S. Valeev, V.I. Petrovsky, V.A. Vasiljev, and I.E. Obvinzeva. Ferroelectric capacitors for integrated circuits. *Microelectronic Engineering*, 29(1-4):41–44, 1995.
- [35] J. Wang, J.M. Xue, D.M. Wan, and B.K. Gan. Mechanically Activating Nucleation and Growth of Complex Perovskites. *Journal of Solid State Chemistry*, 154(2):321–328, 2000.
- [36] A. D. Polli, F. F. Lange, and C. G. Levi. Metastability of the Fluorite, Pyrochlore, and Perovskite Structures in the  $\text{PbO-ZrO}_2\text{-TiO}_2$  System. *Journal of the American Ceramic Society*, 83(4):873–881, 2004.
- [37] W. L. Warren, D. Dimos, G. E. Pike, B. A. Tuttle, R. Raymond, M. V. nad Ramesh, and J. T. Evans. *Applied Physics Letters*.
- [38] M. Grossmann, O. Lohse, D. Bolten, U. Boettger, T. Schneller, and R. Waser. The interface screening model as origin of imprint in  $\text{PbZr}_x\text{Ti}_{1-x}\text{O}_3$  thin films. I. Dopant, illumination, and bias dependence. *Journal of Applied Physics*, 92(5):2680–2687, 2002.
- [39] J. J. Lee, C. L. Thio, and S. B. Desu. Retention and imprint properties of ferroelectric thin films. *Physica Status Solidi (a)*, 151(1):171–182, 1995.
- [40] A. Gruverman, B. J. Rodriguez, A. I. Kingon, R. J. Nemanich, A. K. Tagantsev, J. S. Cross, and M. Tsukada. Mechanical stress effect on imprint behavior of integrated ferroelectric capacitors. *Applied Physics Letters*, 83(4):728–730, 2003.
- [41] Y. Zhou, H. K. Chan, C. H. Lam, and F. G. Shin. Mechanisms of imprint effect on ferroelectric thin films. *Journal of Applied Physics*, 98(2):024111, 2005.
- [42] H. Chen and J. Y. Lee. Electron trapping process in ferroelectric leadzirconatetitanate thin-film capacitors. *Applied Physics Letters*, 73(3):309–311, 1998.
- [43] A. K. Tagantsev and G. Gerra. Interface-induced phenomena in polarization response of ferroelectric thin films. *Journal of Applied Physics*, 100(5):051607, 2006.
- [44] G. Teowee, C. D. Baertlein, E. A. Kneer, J. M. Boulton, and D. R. Uhlmann. Effect of top metallization on the fatigue and retention properties of Sol-gel PZT thin films. *Integrated Ferroelectrics*, 7(1-4):149–160, 1995.
- [45] H. Lee, T. H. Kim, J. J. Patzner, H. Lu, J.W. Lee, H. Zhou, W. Chang, M. K. Mahanthappa, E. Y. Tsybal, A. Gruverman, and C. B. Eom. Imprint Control of  $\text{BaTiO}_3$  Thin Films via Chemically Induced Surface Polarization Pinning. *Nano Letters*, 16(4):2400–2406, 2016.
- [46] K. Kushida-Abdelghafar, M. Hiratani, and Y. Fujisaki. Post-annealing effects on antireduction characteristics of  $\text{IrO}_2/\text{Pb}(\text{Zr}_x\text{Ti}_{1-x})\text{O}_3/\text{Pt}$  ferroelectric capacitors. *Journal of Applied Physics*, 85(2):1069–1074, 1999.

- 
- [47] J. L. Cao, A. Solbach, Y. Fang, U. Boettger, P. J. Schorn, R. Waser, and U. Klemradt. Effects of Thermal Annealing on Lead Zirconate Titanate Thin Film Capacitors with Platinum Electrodes. *Journal of The Electrochemical Society*, 154(11):G251, 2007.
- [48] D. R. Professor Uhlmann. Air force office of scientific research by university of arizona. Technical report, 1994.
- [49] P. Bao, T. J. Jackson, X. Wang, and M. J. Lancaster. Barium strontium titanate thin film varactors for room-temperature microwave device applications. *Journal of Physics D: Applied Physics*, 41(6):063001, 2008.
- [50] K.J. Choi and S.G. Yoon. Effect of  $\text{Pb}_2\text{Ru}_2\text{O}_{7-x}$  (PRO) conductive interfacial layers on ferroelectric properties of  $\text{Pt}/\text{Pb}(\text{Zr}_{0.35}\text{Ti}_{0.65})\text{O}_3/\text{Pt}$  capacitors for nonvolatile memory applications. *Applied Physics A*, 81(4):855–859, 2005.
- [51] S. Kim, D. Park, H. Woo, D. Lee, J. Ha, and C. S. Hwang. Effects of  $\text{IrO}_2/\text{Pt}$  Hybrid Electrodes on the Crystallization and Ferroelectric Performances of Sol-gel-derived  $\text{Pb}(\text{Zr,Ti})\text{O}_3$  Thin Film Capacitors. *Journal of Materials Research*, 17(07):1735–1742, 2002.
- [52] K.T. Jacob, V.S. Saji, and Y. Waseda. Standard Gibbs energy of formation of  $\text{Pb}_2\text{Ru}_2\text{O}_{6.5}$ . *Journal of Materials Research*, 22(05):1174–1181, 2007.
- [53] X. Tan and J. K. Shang. In-situ transmission electron microscopy study of electric-field-induced grain-boundary cracking in lead zirconate titanate. *Philosophical Magazine A*, 82(8):1463–1478, 2002.

## Chapter 4

# SURFACE CHEMISTRY IN Pb PRECURSOR-RICH $\text{Pb}(\text{Zr}_{0.52}\text{Ti}_{0.48})\text{O}_3$ SOL-GEL THIN FILMS

### Contents

---

<b>4.1</b>	<b>Pb(<math>\text{Zr}_{0.52}\text{Ti}_{0.48}</math>)<math>\text{O}_3</math> Surface with 30 % Pb Excess . . . . .</b>	<b>97</b>
<b>4.2</b>	<b>X-ray Photoelectron Spectroscopy . . . . .</b>	<b>98</b>
<b>4.3</b>	<b>Investigations of Surface Chemistry . . . . .</b>	<b>100</b>
4.3.1	XPS Measurement at Normal Emission . . . . .	101
4.3.2	Angle dependent XPS investigations . . . . .	103
4.3.3	Depth Profile by Ion Beam Etching . . . . .	104
4.3.4	X-ray Diffraction Analysis . . . . .	107
4.3.5	Discussion . . . . .	108
<b>4.4</b>	<b>Nanostructures as a Function of the Pb Excess . . . . .</b>	<b>112</b>
4.4.1	Scanning Electron Microscopy . . . . .	112
4.4.2	X-ray Photoelectron Spectroscopy . . . . .	113
4.4.3	X-ray Diffraction . . . . .	115
4.4.4	Discussion . . . . .	116
<b>4.5</b>	<b>Conclusion . . . . .</b>	<b>118</b>
	<b>Bibliography . . . . .</b>	<b>119</b>

---

From chapter 3, the electrical responses of Pt/Ru/PZT/Pt capacitors have been strongly modified by the Pb excess content and the post metallization annealing. Breakdown field and loss tangent are decreasing with the increase of the lead excess from 10 to 30 % and the maximum of dielectric constant shows an optimum between 15 % and 20 % as the function of the post metallization annealing. Electric data obtained on both dielectric constant and breakdown field have been enhanced after post metallization annealing.

In addition to the effects induced by the bulk, the electrical responses of Metal-ferroelectric-Metal capacitors can be strongly affected by the chemical composition of the interfaces as described in the literature [1, 2, 3, 4]. In fact, the Metal-ferroelectric can present nonstoichiometric interfacial layer or secondary phase with no ferroelectricity or low dielectric constant [5]. This can prevent the optimal function of Metal-ferroelectric-Metal capacitors. However, for the ferroelectric capacitor based on the PZT thin film, the Pb excess content in the sol-gel solution during the deposition process can be used to control the amount of the secondary (or parasite) phase at the surface of the PZT thin films.

In this context, the main objective of this chapter is to study the chemical composition of the secondary phase and the mechanisms involved in its creation. By exploiting the extreme sensitivity and the relative ability to quantify the elements offered by X-ray photoelectron spectroscopy (as described in Figure 4.1 and chapter 2 section 2.4.1 page 56), the characterization of the PZT have been performed.

In order to achieve this goal, first we will analyze the surface of the deposited PZT bare with 30 % of Pb excess (PZT30) which should be without a secondary phase according to the results published by Grader *et al.* [6]. Then, we will compare the surface states of the PZT thin film bare for different Pb excess content (10 % and 30 %). Finally, we will expand this characterization to the intermediate Pb excess content i.e. with 15 % and 20 % of Pb excess.

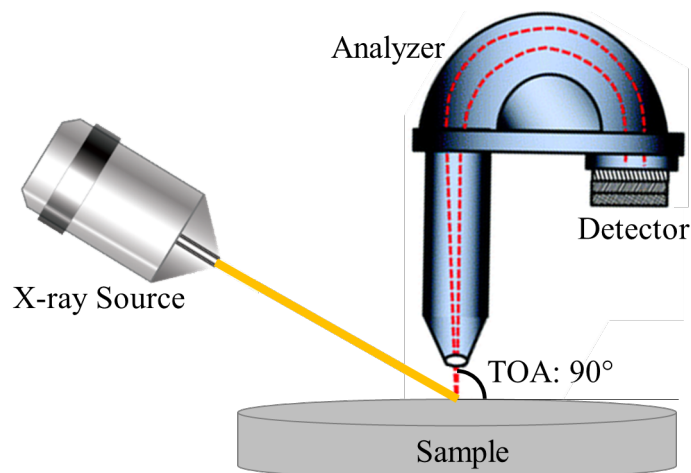


Figure 4.1: Schematic description of the XPS probing with  $90^\circ$  take-off angle (angle between the surface sample and the detector axe).

## 4.1 $Pb(Zr_{0.52}Ti_{0.48})O_3$ Surface with 30 % Pb Excess

The surface of PZT deposited with 30 % of Pb excess and its cross-sectional microstructure were analyzed with a high-resolution scanning electron microscopy (SEM). As already shown by Grader *et al.* [6], our PZT30 sample (deposited at CEA-LETI) presents only large grains, distributed over the whole surface with well-defined grain boundaries as seen in Figure 4.2 (a). The grain size varies from 40 nm to 250 nm. The surface is clean with no other visible

grain types (different to the large PZT grains). Cross-sectional microstructure presented in Figure 4.2 (b) allows to demonstrate a perfect deposition process of the PZT30. We remark also a perfect adhesion of the PZT30 layer on the substrate. The PZT30 film was  $\sim 220$  nm thick and Pt bottom electrode  $\sim 100$  nm thick.

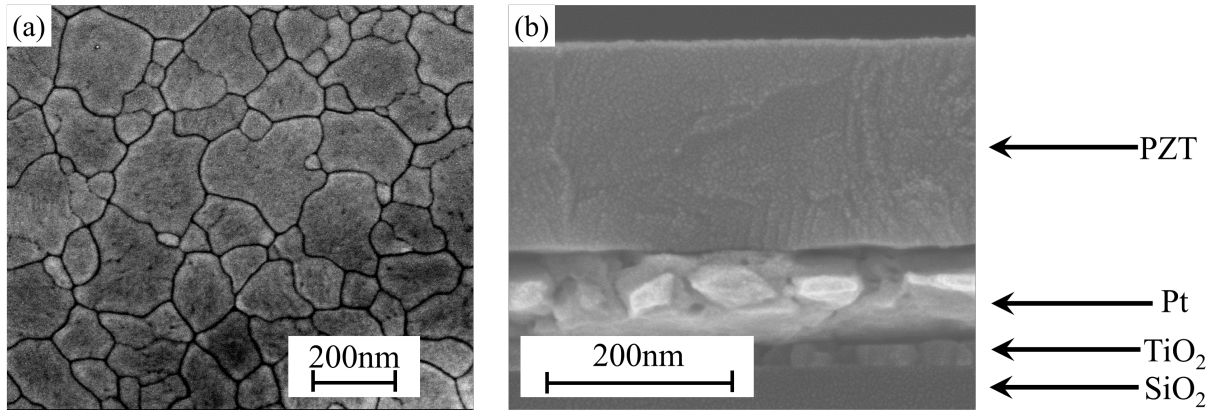


Figure 4.2: SEM images of PZT30 as deposited (or bare) (a) surface microstructure image and (b) cross section image

## 4.2 X-ray Photoelectron Spectroscopy

The survey performed from 0 to 1200 eV in binding energy with energy step of 0.1 eV are shown in Figure 4.3 (a). Constant analyzer energy (CAE) mode is used to collect the electrons. The pass energy of the analyzer is held at a constant value of 30 eV. The energy resolution is 0.37 eV. All of the expected core level peaks for PZT are present. The survey reveals several interesting region with Pb 4f, Zr 3d, Ti  $2p_{3/2}$  and O 1s core levels, which are detected at 137.5, 180.5, 457.2 and 528.7 eV, respectively. These values are in agreement with data found in NIST X-ray Photoelectron Spectroscopy Database.

High resolution core level analysis of Pb 4f, Zr 3d, Ti  $2p_{3/2}$  and O 1s presented in Figure 4.3 (b - e) was carried out with the pass energy at 10 eV and the energy resolution of 0.27 eV. Using the tabulated sensitivity factors of each element, the relative composition of Pb, Zr, Ti and O with a take-off angle of  $90^\circ$  are 21.9, 3.4, 15.6 and 59.1 %, respectively. From these results, we can see a relative difference between the nominal composition (i.e. expected theoretical ratio of  $Pb_{1.3}(Zr_{0.52}Ti_{0.48})O_3$ ) and the real composition as shown in Table 4.1. The amount of Pb and O at 21.9 and 59.1 %, respectively are almost identical to the nominal composition. Contrary to the Pb and O, we have a high decrease of the amount of Ti and increase of the relative concentration of Zr compared to the nominal composition. We have a weak percent of Ti (3.4 rather than 9.6) conversely to the Zirconium which is at 15.6 % rather than 10.4 %.

Shirley background and Gaussian-Lorentzian mixing line-shape functions were used for fitting each core level. Respectively, we have used (30-70), (30-70), (50-50) and (40-60) for Pb, Ti, Zr and O. Full width at half maximum (FWHM) for all spectra are also obtained

with 0.89, 0.73, 0.85 and 0.95 eV for the Pb 4f, Zr 3d, Ti 2p<sub>3/2</sub> and O 1s, respectively.

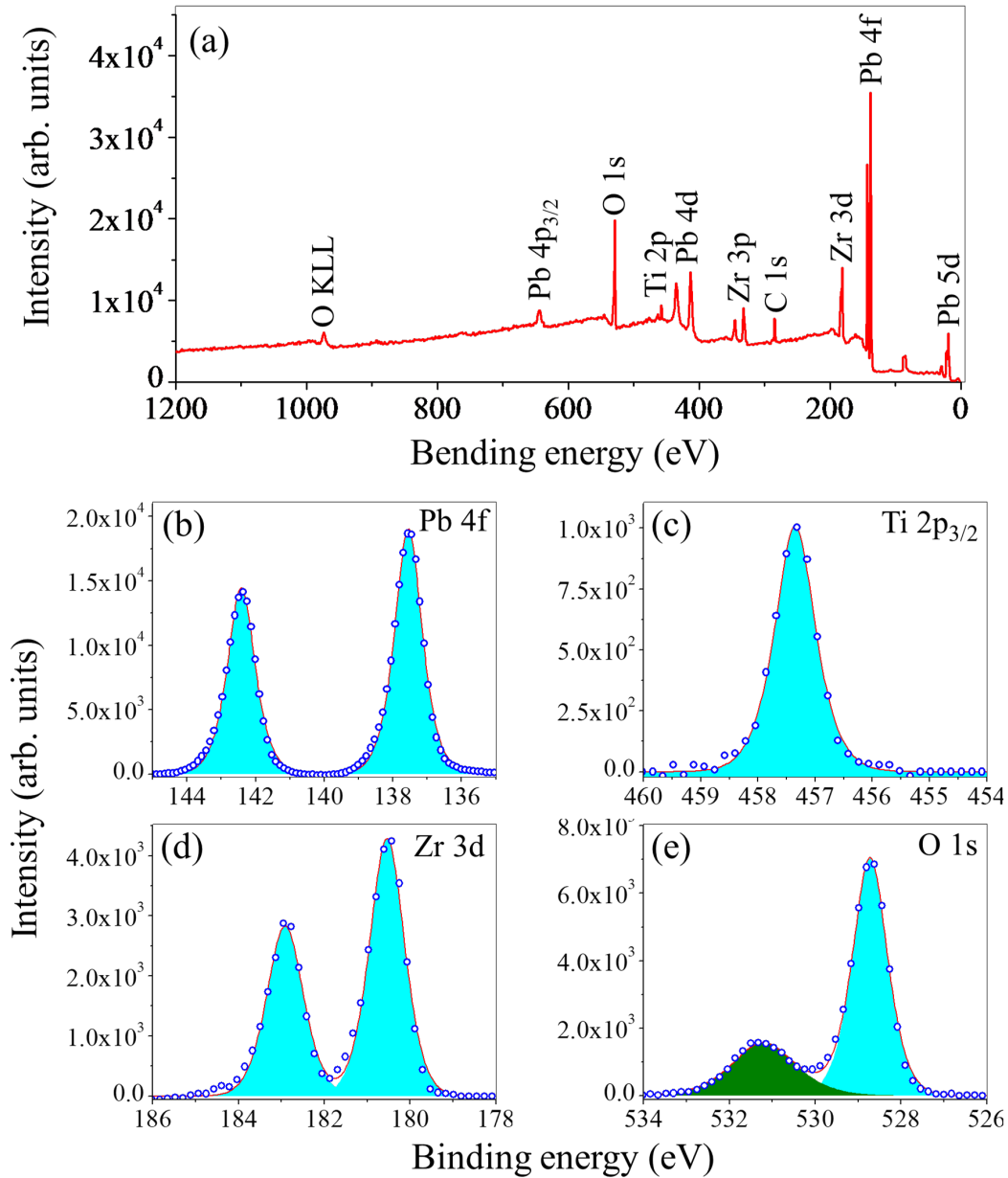


Figure 4.3: XPS measurements of PZT30 (a) survey spectrum and core level spectra for b) Pb 4f; c) Ti 2p<sub>3/2</sub> d) Zr 3d and e) O 1s

Further, except the components from the PZT30 thin film (Pb 4f, Zr 3d, Ti 2p<sub>3/2</sub> and O 1s), we can also observe in Figure 4.3 (a) the presence of carbon (C 1s). The main C 1s peak at 284.4 eV reflects the presence of adventitious surface carbon. In fact, by using the Relative Sensitivity Factors (RSF, provided by ScientaOmicron) and data from the measured peak area with a takeoff angle of 90° and 30° as illustrated in Figure 4.4, we success to estimate the relative concentration of the carbon at the surface of PZT30 sample depending on the takeoff angle. These results are 22.1 and 30.3 % for the takeoff angle of 90° and 30°, respectively. These data support that the carbon is localized at the surface of

the sample rather than into the bulk.

	Elementary composition of PZT30 (%)	
	Nominal composition	Real composition
Lead	20 (+ Pb excess content)	21.9
Zirconium	9.6	3.4
Titanium	10.4	15.6
Oxygen	60	59.1

Table 4.1: Synthetic table of nominal and real composition of the PZT30

Following previous results from the SEM and XPS, for the PZT30 without any secondary phases, in the next section, we will study the impact of Pb excess content on the surface state of samples [6]. For this purpose, we will begin by comparing the microstructures of PZT containing 10 and 30 % of Pb excess.

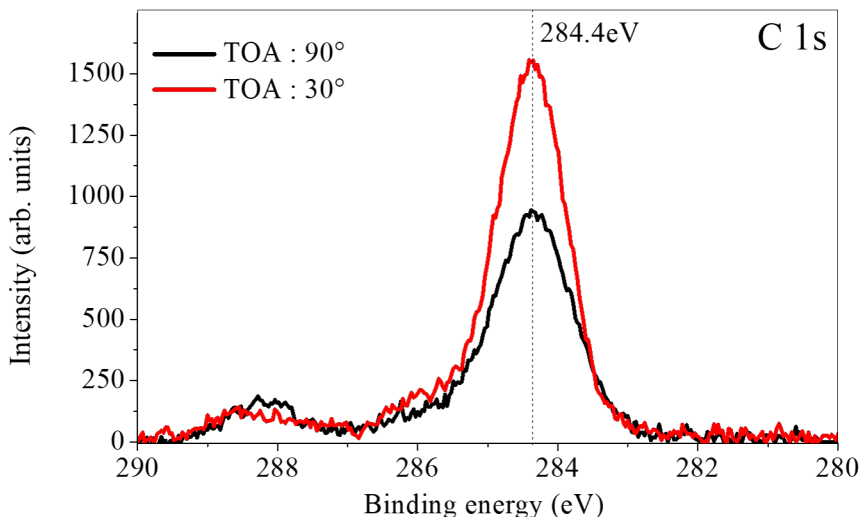


Figure 4.4: XPS measurements of C 1s peak at the surface of the PZT30 as function of the TOA

### 4.3 Investigations of Surface Chemistry

Surface comparison of PZT10 and PZT30 by SEM is illustrated in Figure 4.5 (a - b). The surface of PZT10 has a similar underlying grain structure similar to that of PZT30. In addition, the PZT10 is covered by a large number of nanoparticles. The size of these nanostructures or parasitic phase varies between 5 and 25 nm with an average size around 15 nm. Using Image J, the nanostructures cover around 10 to 20 % of the total surface as the function of the basic threshold chosen. A closer inspection (Zoom of 1/4 of the surface) suggests that the nanostructures tend to be predominantly located along the grain boundaries rather than in the center of the large grains. The XPS chemical analysis might allow to elucidate the composition of the nanostructures.

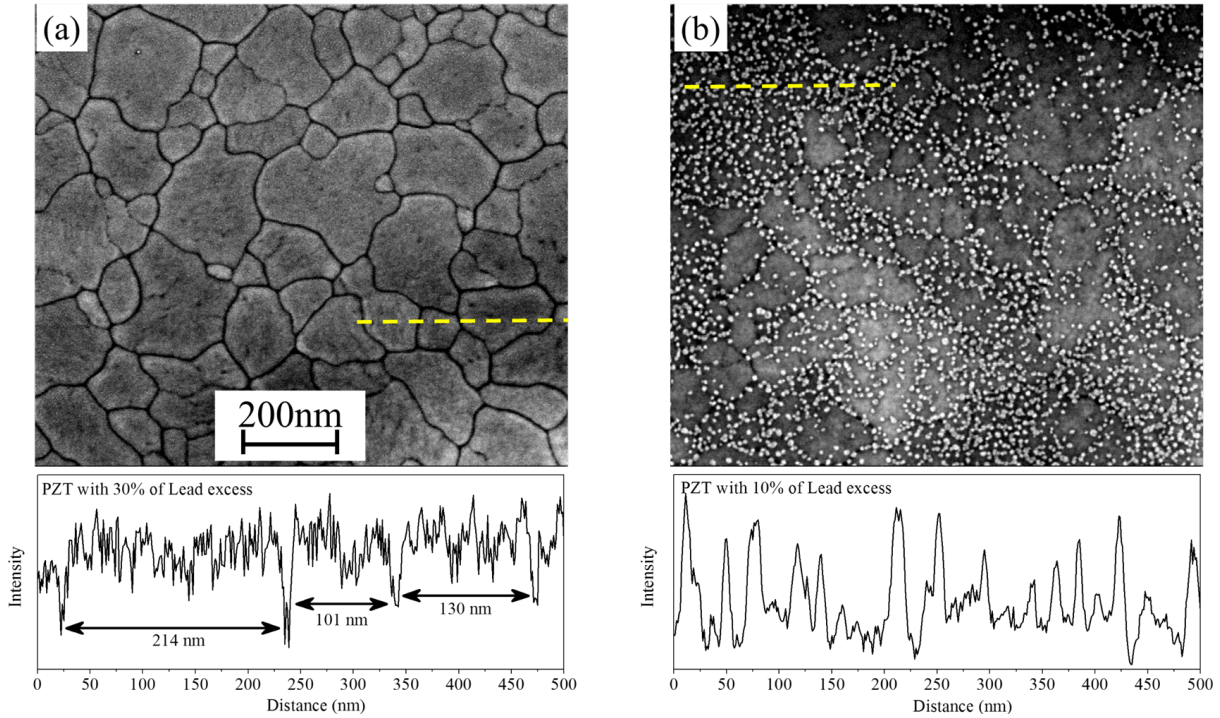


Figure 4.5: SEM images of as deposited (a) PZT30 and (b) PZT10. The scale bar is the same for both images.

### 4.3.1 XPS Measurement at Normal Emission

The Pb 4f, Zr 3d, Ti  $2p_{3/2}$  and O 1s core level spectra recorded at normal emission (TOA =  $90^\circ$ ) on the PZT10 and PZT30 are shown in Figure 4.6 (a - d) and the results of the best fits to the data are given in Table 4.2.

The Pb  $4f_{7/2}$  binding energy (137.5 eV) is identical for both PZT10 and PZT30 as illustrated in Figure 4.6 (a). The single Pb component is attributed to  $Pb^{2+}$  ions in the PZT perovskite structure. No other chemical state of Pb is observed. Similarly, the Ti  $2p_{3/2}$  binding energy (457.2 eV) is unchanged between PZT30 and PZT10 and is attributed to  $Ti^{4+}$  ions in the PZT matrix as seen in Figure 4.6 (b). The FWHM of the Pb  $4f_{7/2}$  and the Ti  $2p_{3/2}$  emission are 0.89 eV and 0.73 eV, respectively.

The Zr 3d core level spectrum, shown in Figure 4.6 (c), changes dramatically between 10 % and 30 % Pb excess. For the PZT30 sample, it shows a single chemical state labelled  $Zr_I$  with a Zr  $3d_{5/2}$  binding energy of 180.5 eV. In contrast, for 10 % Pb excess, there is an additional component denoted  $Zr_{II}$  at 181.5 eV binding energy.  $Zr_I$ , common to both PZT30 and PZT10, is related to  $Zr^{4+}$  ions in the PZT perovskite structure.  $Zr_{II}$ , shifted by 1 eV to higher binding energy, seems to be correlated with the appearance of nanostructures at the surface of PZT10, as seen in Figure 4.5 (b). This suggests a different chemical composition of nanostructures with respect to that of PZT.

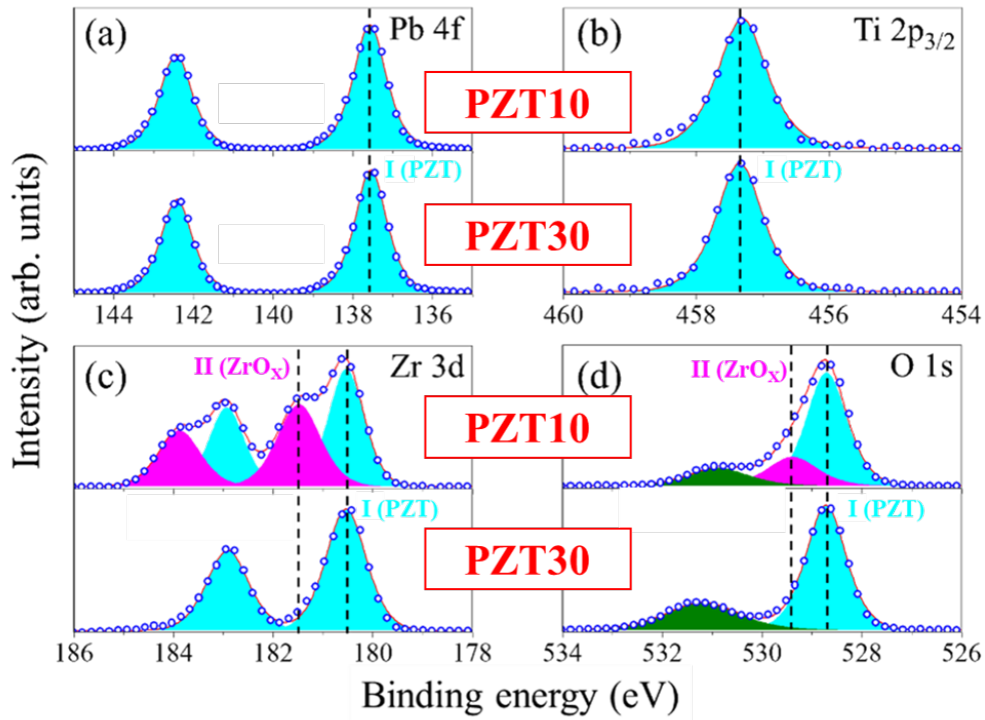


Figure 4.6: XPS core level spectra for a) Pb 4f; b) Ti  $2p_{3/2}$  c) Zr 3d and d) O 1s. Open circles are the experimental points, red lines the best fit, colored peaks the different components. In each panel, the upper (lower) spectrum is that of PZT10 (PZT30). The main peak I (light gray, turquoise online) is the perovskite structure; gray peak II (magenta online) surface phase and low intensity, peaks green surface contaminations.

The O 1s shown in Figure 4.6 (d), has several distinct core level components. The main peak,  $O_I$  at 528.70 eV is attributed to  $O^{2-}$  in the PZT perovskite structure and is common to both PZT10 and PZT30. For PZT10, there is a second peak at 529.40 eV. Finally, the green peak for O is present in both samples with weak shift. The green peaks are attributed to surface contamination [7, 8] which are linked to the presence of the carbon contamination at the surface.

Core-Levels	Gaussian-Lorentzian	PZT30		PZT10	
		BE (eV)	FWHM (eV)	BE (eV)	FWHM (eV)
Pb $4f_{7/2}$	30-70	137.5	0.89	137.5	0.89
Ti $2p_{3/2}$	30-70	457.2	0.73	457.2	0.73
Zr $3d_{5/2}$	50-50	180.5	0.85	180.5	0.85
Zr $3d_{5/2}$		-	-	181.5	1.02
O 1s (I)	40-60	528.7	0.95	528.7	0.95
O 1s (II)		-	-	529.4	1.18

Table 4.2: Pb 4f, Zr 3d, Ti  $2p_{3/2}$  and O 1s line shapes, binding energies and FWHM of the fits shown in Figure 4.6 for PZT30 and PZT10

### 4.3.2 Angle dependent XPS investigations

In order to clarify the assignment of the  $Zr_{II}$  component to a surface secondary phase, a depth profile of elements in near surface layers were performed from Angle Resolved XPS (chapter 2 section 2.4.1 page 56). PZT10 was analyzed at TOA of  $90^\circ$  and  $30^\circ$ .

This Angle Resolved XPS measurement will enable us to highlight the components located at the extreme surface in relatively to the slightly buried elements. Results corresponding to Pb 4f, Zr 3d, Ti  $2p_{3/2}$  and O 1s core level spectra at TOA of  $30^\circ$  are shown in Figure 4.7 (a - d), and compared with the normal emission case.

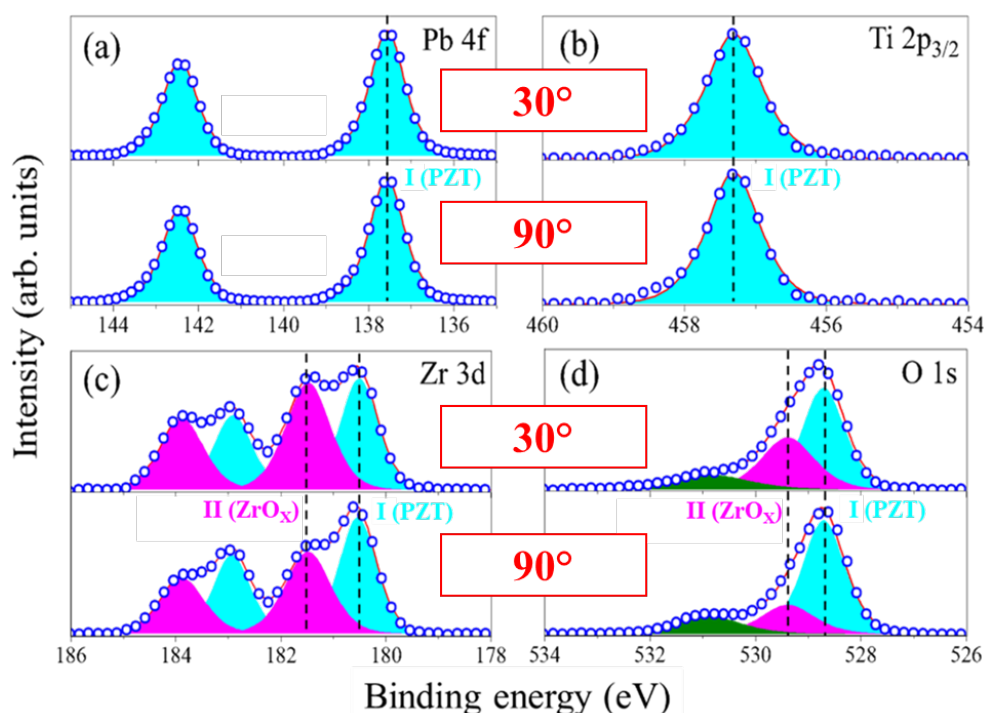


Figure 4.7: XPS core level spectra of PZT10 as a function of take-off angle a) Pb 4f; b) Ti  $2p_{3/2}$  c) Zr 3d and d) O 1s. Symbols and color code as in Figure 4.6

The binding energy does not change as a function of take-off angle. Only a relative variation of intensities of the Zr and O core level components I and II is remarked. At  $30^\circ$  the  $Zr_{II}$  intensities increase significantly relative to the  $Zr_I$  component (by 48 % with respect to normal emission), which is in good agreement with the expected enhanced surface sensitivity at  $30^\circ$  take-off angle (probing depth is halved). The same twofold increase is observed for the  $O_{II}$  peak as presented in Table 4.3. At  $30^\circ$  take-off angle the  $O_{II}$  intensity increases by 49 % with respect to the intensity at normal emission. As the only effect of changing the take-off angle is to change the surface sensitivity, this is clear evidence that both Zr and O are related to a surface specific phase. We can therefore conclude that both  $Zr_{II}$  and  $O_{II}$  are surface-related peaks. These latter are also related with the appearance of nanostructures observed at the surface of PZT10.

	PZT30		PZT10	
	90°	30°	90°	30°
Pb	21.9	25.3	20.9	20.3
Ti	3.4	2.8	4.3	3.6
Zr <sub>I</sub>	15.6	14.8	11.3	7.3
Zr <sub>II</sub>			6.8	8.3
O <sub>I</sub>	59.1	57.1	36.7	34.5
O <sub>II</sub>			12.4	15.7
O (green)			7.6	10.3

Table 4.3: PZT composition based on the XPS intensities at 90° and 30° take-off angles for both as deposited PZT30 and PZT10

### 4.3.3 Depth Profile by Ion Beam Etching

In order to enhance the interpretation of additional Zr<sub>II</sub> and O<sub>II</sub> peaks and to demonstrate the link between the presence of secondary phases (SEM) and Zr<sub>II</sub> and O<sub>II</sub> peaks (XPS), another trick is used. Total etching of the surface of PZT10 has been carried out and all nanostructure phases have been removed. Ion beam etching (IBE) of the PZT10 (with nanostructures at the surface) was performed by utilizing the NEXUS 350A machine during 45s. After the etching process using pure Ar gas, the measurement of thickness shows that it has been removed around 20 nm thick of PZT. Moreover the nano-grains have vanished and the surface has become perfectly smooth as reported in Figure 4.8. The etching damage and nanostructure removal are supported by the XPS results presented below.

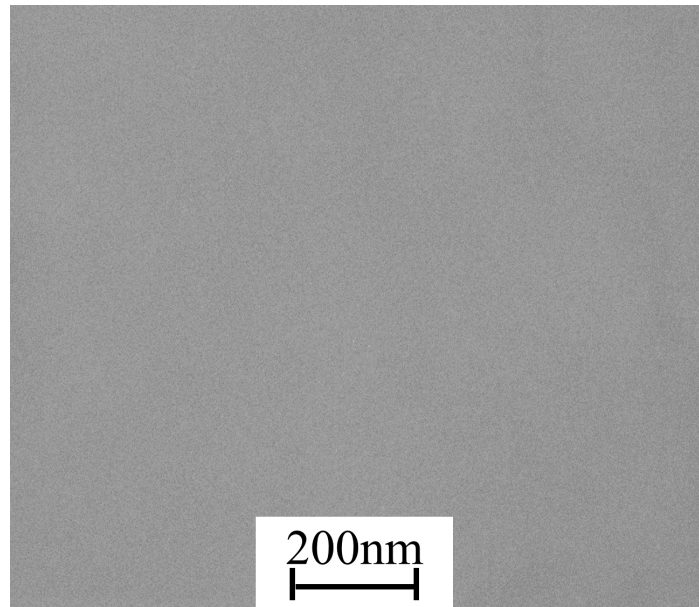


Figure 4.8: SEM image of PZT10 after ion beam etching.

After IBE, the surface is smooth without any detectable nanostructure, as can be seen in Figure 4.8. Therefore the etching treatment has removed the additional surface phase. The

absence of a clear grain structure is due to the amorphization of the surface, well-known in the literature [8, 9, 10, 11]. IBE can also reduce the surface [11, 12] in which case one would expect a shift in the electronic levels similar to that induced by n-type doping of semiconductors. In order to compare the core level spectra before and after IBE, we have to correct the energy scale and aligned the core level spectra by using the VBMs.

Figure 4.9 shows the valence band spectra before and after etching. The position of the valence band maximum (VBM) is determined by a straight line extrapolation [13]. After etching, the VBM shifts from 1.17 to 1.94 eV and the density of states in the band gap appear. The latter is associated with the creation of O vacancies which, schematically, donate 2 free electrons to the PZT lattice, reducing neighboring B-type cations, usually Ti. The resulting n-type doping pins the Fermi level near the bottom of the conduction band. This result in a rigid shift of all electronic levels to higher binding energy.

In Figure 4.10, we compare the Pb 4f, Zr 3d, Ti 2p<sub>3/2</sub> and O 1s core level spectra, before and after IBE. In the Pb 4f spectrum, a new component at lower binding energy appears, and corresponds to reduce Pb at 136.07 eV as described by Lu and Zhu [14]. Similarly, a partial reduction of Ti is evidenced with an additional component to lower binding energy (Ti<sub>II</sub> at 456.64 eV), as also observed previously [12]. Both results provide chemical confirmation of the surface reduction after IBE.

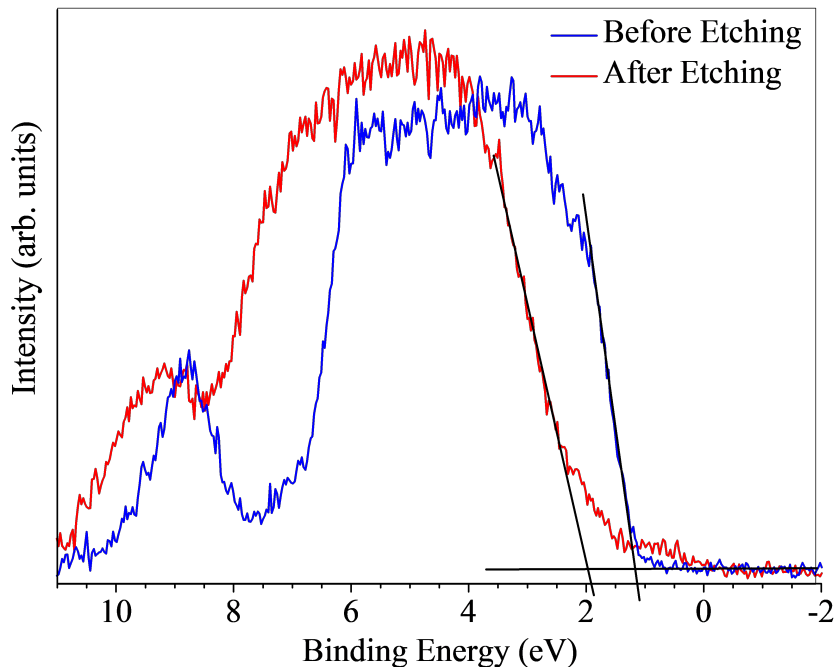


Figure 4.9: Valence band maxima of PZT10 before (blue) and after IBE (red)

More importantly, the surface related to the components Zr<sub>II</sub> and O<sub>II</sub> disappear after etching. IBE removes 20 nm thickness of PZT, i.e., well above the photoelectron escape

depth. We can conclude that the  $Zr_{II}$  and  $O_{II}$  components observed before etching are directly correlated with the surface nanostructures. Finally, we observe a broadening of FWHM of about 0.2 eV for all spectra of PZT after etching as illustrated in Table 4.4.

This is probably due to IBE induced surface amorphization, which is responsible for the absence of the grain as can be observed in Figure 4.8. The broadening induced by the amorphization is mainly due to Ar ion bombardment. A morphology change leads to the crystal damage and displacement of the lattice atoms [11, 15, 16] and thus to the transitions from the crystal phase to the amorphous phases.

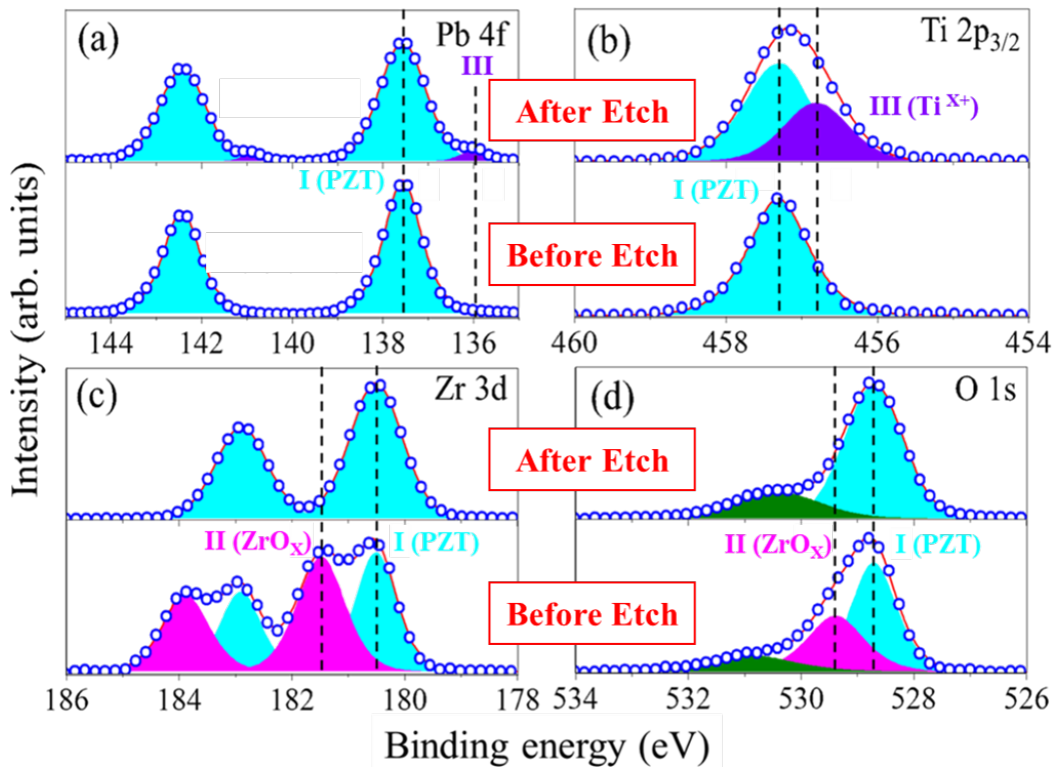


Figure 4.10: PZT10 a) Pb 4f; b) Ti  $2p_{3/2}$  c) Zr 3d and d) O 1s core level spectra before and after ion beam etching. Open circles are the experimental points, continuous (red) lines the best fit. Color coding of the core level components as for Figure 4.6.

Otherwise, with IBE, as can be seen in Table 4.5 a large decrease of the Pb from 20.9 to 8 and an increase of the Zr after etching are observed. The Ti and O increase slightly. This situation is strongly linked with difference collision cross sections between argon ions and target atoms (Pb, Ti, Zr and O) as a function of the target and the energy of the argon atoms. Indeed, using individual metal targets of Pb, Zr and Ti for deposition of PZT thin films, Krupanidhi *et al.* [17] showed that Pb has a higher Sputtering rate under argon bombardment than Zr and Ti, which induce a higher deposition rate on the substrate. These results are in agreement with lower concentration of Pb on the surface of the PZT10 under argon bombardment during the IBE process.

Core Levels	Before Etch		After Etch	
	BE (eV)	FWHM (eV)	BE (eV)	FWHM (eV)
Pb 4f <sub>7/2</sub> (I)	137.5	0.89	137.5	1.11
Pb 4f <sub>7/2</sub> (II)	-	-	136.07	0.89
Ti 2p <sub>3/2</sub> (I)	457.2	0.73	457.2	0.95
Ti 2p <sub>3/2</sub> (II)	-	-	456.64	0.95
Zr 3d <sub>5/2</sub> (I)	180.5	0.85	180.5	1.05
Zr 3d <sub>5/2</sub> (II)	181.5	1.02	-	-
O 1s (I)	528.7	0.95	528.7	1.14
O 1s (II)	529.4	1.18	-	-

Table 4.4: Pb 4f, Zr 3d, Ti 2p<sub>3/2</sub> and O 1s line shapes, binding energies and FWHM of PZT10 before and after ion beam etching

In addition to the angle resolved XPS and IBE experiment, grazing incidence X-ray diffraction (GIXRD) was also carried out to obtain the texture information regarding nanostructures at the surface of PZT10. The link between surface microstructure and crystal orientation of PZT bulk has been studied by using standard X-ray diffraction as will be presented in the next part.

	Pb	Ti	Zr	O
PZT30 before Etch	21.9	3.4	15.6	59.1
PZT10 before Etch	20.9	4.3	18.1	56.7
PZT10 after Etch	8	5.9	27	58.1

Table 4.5: Relative composition of PZT30 before etch, PZT10 before and after ion beam etching as quantified by XPS using the tabulated RSFs

#### 4.3.4 X-ray Diffraction Analysis

The  $\theta/2\theta$  scans in Figure 4.11 (a) show peaks characteristic of PZT (at the level of the first-order reflexion), the Si substrate and the Pt electrode. The X-ray diffraction XRD reveals several structural differences between PZT10 and PZT30. With 10 % Pb excess content during deposition, the sample is almost fully (100) oriented. Increasing the Pb excess from 10 to 30 % leads to a modification of the structure i.e. the PZT film is strongly (111) oriented. Finally, the peak at 31.2° in Figure 4.11 (a) corresponds to the PZT (110) orientation. By taking into account only the area of diffraction peaks and the data provided by the Joint Committee on Powder Diffraction Standards [JCPDS] card for the PZT, the comparison of peaks from PZT10 and PZT30 films showed that the (100), (110) and (111) orientation are 93.2, 2.6 and 4.2 % for PZT10 and 18.4, 21.5 and 60.2 % for PZT30, respectively.

Moreover, electrical performances of PZT based capacitors show a crystallographic orientation dependence. Ehara *et al.* [18] demonstrated that the saturation polarization of PZT can be modified by the simple tilting angle of the polar axis of the perovskite cell which depends on the crystallographic orientation. Furthermore, the variation dielectric

constant values of capacitors as a function of the Pb excess may be partially attributed to the differences of polarization states, including the growth mode of domains, the tilting angle of the polar axis and the degree of polarization inversion of PZT thin films when the orientation passes mainly from (100) to (111) as observed in the  $BaTiO_3$  [19].

In order to highlight the crystallographic composition of the surface of PZT10 and PZT30 layer relative to the bulk, Grazing Incidence XRD (GIXRD) tool is used. GIXRD results are presented in Figure 4.11 (b). Contrary to the  $\theta/2\theta$  scans, the GIXRD is carried out by fixing both the incoming x-ray beam and the detector of diffracted beam at  $0.5^\circ$  relative to the sample surface as already illustrated in chapter 2 section 2.2 page 50. It allows to enhance the sensibility of the surface relative to the bulk and therefore provides better information of the surface texture.

Data from GIXRD show that in addition to the crystallographic orientation of the PZT from the first-order reflexion ((100), (110) and (111)), we also have the the second-order reflexion ((200), (201), (211) and (220)) when increasing the angle. Furthermore, we observe three peaks respectively at  $34^\circ$  (for (200)),  $58^\circ$  (for (-222)) and  $61.5^\circ$  (for (-302)) in PZT10 which will be attributed to the surface phase (or nanostructures based on the  $ZrO_x$ ) [20] [21]. These reflection correspond to monoclinic  $ZrO_x$  crystal phase [JCPDS Card No. 37-1484]. There is also one peak at  $28^\circ$  for both samples which corresponds to the relatively intense  $k_\beta$  stimulated peak of the PZT (110).

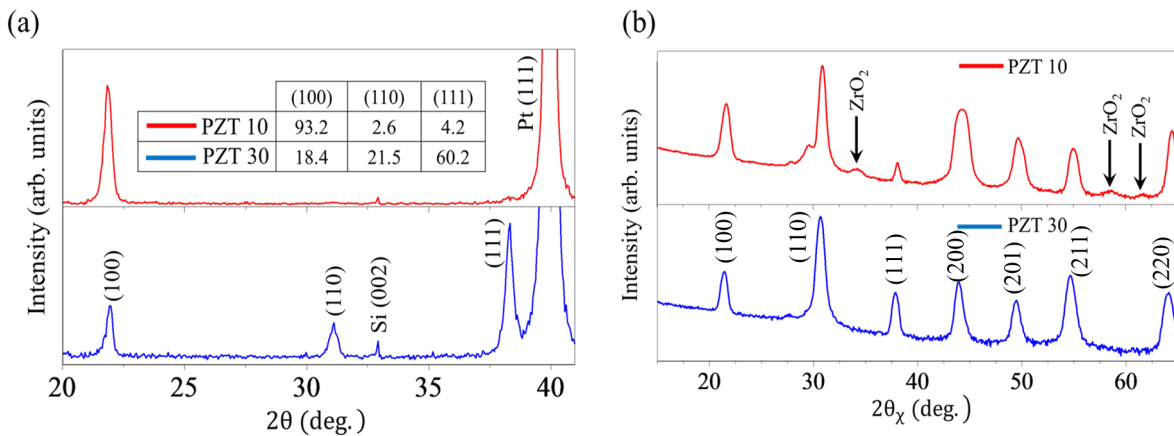


Figure 4.11: XRD scans at (a)  $\theta/2\theta$  geometry of PZT10 (top, red) and PZT30 (bottom, blue) (b) XRD scans at grazing incidence of PZT10 (top, red) and PZT30 (bottom, blue)

### 4.3.5 Discussion

The comparative study between PZT10 and PZT30 reveals several very important aspects. The determination of the composition of nanostructures based on  $ZrO_x$  and the variation of the crystallographic orientation as a function of the Pb level are highlighted. However, the origin of the presence of  $ZrO_x$  on the surface of the PZT as seen in Figure 4.5 (b) is a fairly complex process.

Using RSFs we can quantify the surface stoichiometry measured by XPS. The quantification reveals several important features. First, a slight Pb enrichment at the surface for both PZT10 and PZT30 is observed. This is expected since the excess Pb is used in both cases, which is greater than the stoichiometric value of 20 %. As expected, the surface enrichment is stronger for PZT30. The higher Pb content at PZT30 surface appears, which is correlated with the complete disappearance of the nanostructures. This suggests that the addition of Pb allows completion of the PZT reaction which consumes all of the other precursors and inhibits the formation of the chemically distinct nanostructures. The O content is slightly depleted, possibly as a result of the high annealing temperature for crystallization. As seen in Figure 4.7, both  $Zr_I$  and  $O_I$  decrease at the surface for PZT10 and at the same time the  $Zr_{II}$  and  $O_{II}$  concentrations increase. O (green) is included to show that their weight also increases at the surface, consistent with the assignment to the surface contamination.

The presence of the nanostructures at the grain boundaries can be understood by the fact that, the formation of the perovskite phase starts from a seed and proceeds by outward, lateral growth. It then enlarges by transforming the remaining precursors into the perovskite phase between  $500^\circ C$  and  $700^\circ C$  via three dimensional growth [22]. When the Pb precursor is exhausted, the reaction stops abruptly. Any residual precursors remaining at the grain boundaries become available to form a secondary phase since the  $TiO_2$  precursor is consumed first. Therefore, the resulting secondary phase nanostructures will be Zr-enriched [23, 24].

XRD shows that high Pb excess modifies the preferential (100) orientation to a mixed state dominated by (111), in agreement with previous results [25, 26]. Despite the difference of Pb excess, in both cases the reacted PbO has formed the perovskite which is different from the secondary phase which not includes Pb. Furthermore, the nanostructures appear only at the surface (according to the profilometric analysis carried out by ion beam etching tool). They are presumably formed at the end of the PZT growth and therefore do not influence the crystallographic orientation.

The surface Zr content of PZT10 is 15.6 %, while for PZT30 is 14.8 %. This shows that there is slightly more Zr at the surface of PZT10. As can be seen from Table 4.3, the Zr surface enrichment is due to the  $Zr_{II}$  component. On the basis of the  $Zr_{II}$  and  $O_{II}$  core level intensities, we can estimate the  $ZrO_x$  composition. The  $O_{II}/Zr_{II}$  ratio for TOA at  $90^\circ$  gives  $x = 1.82$  (i.e.  $ZrO_{1.82}$ ), whereas at  $30^\circ$  the  $O_{II}/Zr_{II}$  ratio gives  $x = 1.89$  (i.e.  $ZrO_{1.89}$ ). The formal valence state of Zr in both PZT and  $ZrO_2$  is 4+. It is therefore surprising that a Zr rich surface oxide shows a distinct core level binding energy with respect to that of Zr in PZT.

Furthermore, the XPS data from the literature shows that the Zr binding energy is  $181.4 \pm 0.1$  eV in PZT [10, 22, 27, 28, 29, 30, 31, 32, 33, 34, 35, 36, 37, 38, 39] and  $182.4 \pm 0.3$  eV in  $ZrO_2$  [40, 41, 42, 43, 44, 45, 46, 47, 48, 49]. These results are in excellent agreement with 1 eV shift measured here. Beyond the immediate chemical environment of the Zr emitter, two other effects may influence the BE shift. First, in a simple picture of electron transfer following relative electronegativity, the second neighbor interactions, could modify the electron transfer between ZrO-Ti. The electronegativity of Zr, Ti and O basis of Pauling's

scale are 1.33, 1.54 and 3.44, respectively. For Zr-O, a charge transfer are produced from the outer core level of Zr to the O atom. Thus to compensate this charge transfer, the inner core level of the Zr are attracted towards the nucleus which leads the increase of the binding energy. Secondly, we are considering 15 nm nanostructures, with a much higher surface to volume ratio and probable shorter interatomic distances. These might influence the core level shift. Here some first principles calculations or even tight binding cluster calculations would be useful to confirm this interpretation.

The core level XPS analyses as a function of the precursor composition, emission angle and ion beam etching demonstrate that the nanostructures at the PZT10 surface are a Zirconium oxide,  $ZrO_{1.82-1.89}$ .

The XPS results are confirmed by XRD scans at grazing incidence (Figure 4.11 (b)). The intensities centered on  $34^\circ$ ,  $58^\circ$  and  $61.5^\circ$  on the PZT10 sample are not visible on the PZT30 sample and can be attributed to  $ZrO_2$ -like monoclinic structure [20]. Using a Scherrer fit to the  $61.5^\circ$  peak width, the diameter of grains is in the range of 15 nm, and is in good agreement with the nanograin size estimated from the SEM image shown in Figure 4.5 (b). The Scherrer formula allows to relate the particle sizes or crystallite sizes in a material to the broadening of a peak in a diffraction pattern [50].

Furthermore, the presence of 10 % of Pb excess in PZT leads to the formation of surface nanostructures, preferentially localized at the grain boundaries. This secondary phase has been attributed to the incomplete reaction of  $ZrO_2$  precursor [51] resulting from the opposite slopes in the concentration gradients of Ti and Zr during the growth of sol-gel layers [23, 52]. The major portion of Ti incorporated into each layer is consumed at the beginning of nucleation, consistent with the known crystallization temperatures. This process leads to a dramatic reduction of Ti surface concentration and increase of Zr as seen from the quantitative analysis of the XPS data in Table 4.3. As a consequence of the gradient, the surface of the layer is strongly Zr-enriched. The complete reaction for the growth of lead zirconate titanate can be written in two stages:  $PbO + TiO_2 \rightarrow PbTiO_3$ , followed by  $PbTiO_3 + PbO + ZrO_2 \rightarrow Pb(Zr_{1-x},Ti_x)O_3$ , where the initial precursors are PbO,  $TiO_2$  and  $ZrO_2$  [51].

$ZrO_2$  is a good insulator with a static dielectric constant of 25 [53] and a band gap of 5.8 eV [54]. The presence of  $ZrO_{1.82-1.89}$  at the PZT/electrode interface of a capacitor might influence electrical performance. Given the higher band gap with respect to PZT, a discontinuous or continuous interfacial  $ZrO_{1.82-1.89}$  layer with lower dielectric constant [55] compared to PZT (dielectric constant  $> 1000$ ) [56] will decrease device capacitance.  $ZrO_2$  is not ferroelectric, therefore a surface phase close to  $ZrO_2$  would act like a ferroelectric dead-layer (or paraelectric layer). In fact, with  $ZrO_2$  layer, several effects can take place. Indeed, a strong depolarization field due to the uncompensated PZT surface charge by the top electrode may occur due to the presence of  $ZrO_2$  layer and therefore reduce the ferroelectric polarization. For ideal metal, the polarization charges are perfectly compensated at the interface and therefore no depolarization field emerges in the ferroelectric film. However, in real case, the depolarization field arising from the bound charges on the surface of the film and at the interface with the metal is not fully compensated due to the insufficient screening by the free charges from the electrode and the presence of the non-ferroelectric layer. There-

fore, with the absence of sufficient free charges from the electrode induce by the presence of the paraelectric  $\text{ZrO}_2$  layer, the depolarization field may increase and thus modify the capacitor. Furthermore, according to Lichtensteiger *et al.* [57], the non-ferroelectric layers are also polarized in order to preserve the uniform polarization state and hence eliminate the depolarization fields at the ferroelectric-paraelectric interface level. Thus taking into account these probable impact of  $\text{ZrO}_2$  layer, we decided to analyze the effect of an  $\text{ZrO}_2$  layer at the interface Metal/PZT.

Dielectric constant and loss tangent measurements of PZT10 based capacitor were executed and presented in Figure 4.12. The PZT10 (PZT with 10 % of Pb excess) thickness is 385 nm and top electrodes are 100 nm of Pt or Ru. Depending on the thickness of the interfacial layer of  $\text{ZrO}_2$  between the top electrode and the surface of PZT, electrical performances are modified.

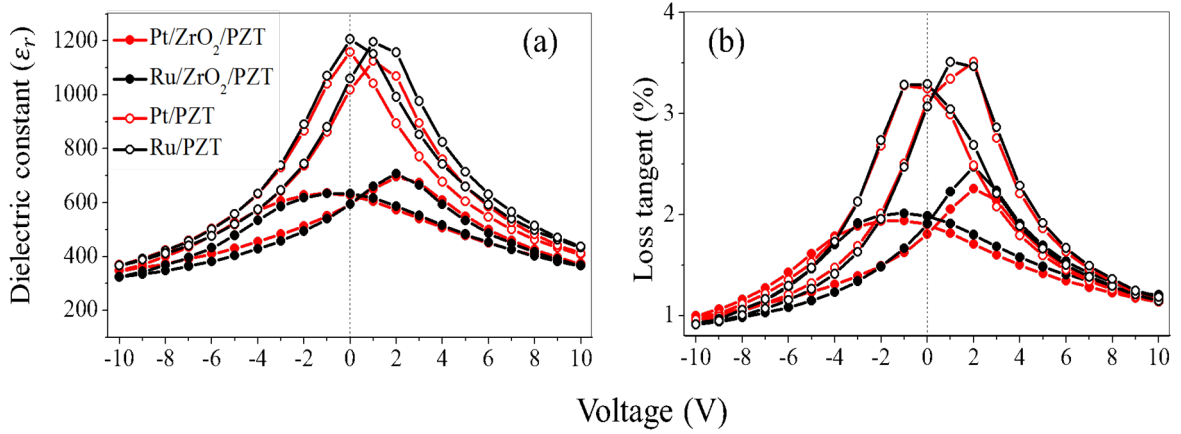


Figure 4.12: Dielectric constant depending on both  $\text{ZrO}_2$  thickness and top electrodes (frequency 10 kHz)

The dielectric constant and loss tangent curves are performed at room temperature between -10 V to +10 V (superposed with a sinusoidal electric signal with amplitude of 100 mV at the frequency of 10 kHz). The evolution of the maximum values of dielectric constant obtained in Figure 4.12 (a) is an interesting result. The Ru top electrode has a higher dielectric constant value than the Pt top electrode. Ru/PZT/Pt and Pt/PZT/Pt provide a dielectric constant values of 1207 and 1159 respectively. The introduction of a 5 nm of  $\text{ZrO}_2$  interfacial layer induces a drop in the capacitance density of about 50 % relatively to the sample without  $\text{ZrO}_2$  interfacial layer. Indeed, there are a decrease of the dielectric constant of Ru/ $\text{ZrO}_2$ /PZT and Pt/ $\text{ZrO}_2$ /PZT up to 708.

However, positive effects are recorded with the presence of interfacial layer of  $\text{ZrO}_2$ . This produces a drastic reduction in the value of tangent of loss, which is a good advantage. Indeed, we observe a decrease from around 3.5 % to 2.5 %, i.e. a reduction of 50 % as can be seen in Figure 4.12 (b).

Figure 4.12 allows to underline three major conclusions. Firstly, the few difference of the value of the dielectric constant between the PZT with Ru (100 nm) or Pt (100 nm) can

be related to the electronic and chemistry bound at interfaces between top electrode-PZT [58, 59, 60].

Secondly, the low values of the constant dielectric of Zirconium oxide at the interface (Figure 4.12) can strongly affect the function of the top electrode-PZT/Pt structure with impacts of almost 50 % of the dielectric constant. These results are in agreement with the existence of a series capacitor model presented in section 1.4 page 37 chapter 1. Finally,  $ZrO_2$  as an interfacial layer can be considered as a barrier which reduces the energy loss (loss tangent) in the capacitor.

Thus, the formation of nanostructures is favored or inhibited by the Pb excess. However, the composition of these nanostructures has a more complex dependence on the process conditions. Systematic experiments as a function of several Pb excess content will be studied in the last part of this chapter.

## 4.4 Nanostructures as a Function of the Pb Excess

The characterization of PZT10 surface chemistry by XPS reveals the presence of a parasitic phase of Zr oxide. Initial characterization of the PZT30 shows no surface nanostructures. However, the results presented in chapter 3 indicate a decrease of the dielectric constant (section 3.2.1 page 85) and breakdown voltage (section 3.2.2 page 89). In this section, we extend the study by varying the Pb excess content in order to manage mainly the surface secondary phase. We will analyze several PZT samples with 10, 15, 20 and 30 % of Pb excess called PZT10, PZT15, PZT20 and PZT30, respectively. These samples with different Pb excess are grown at mophotropic phase boundaries (Zr/Ti: 0.52/0.48) and in the same condition as the PZT10 and PZT30 analyzed previously in this chapter.

### 4.4.1 Scanning Electron Microscopy

Figure 4.13 shows the surface microstructure of PZT depending to the Pb excess in sol-gel precursors. From 10 to 30 % of Pb amount, SEM images show that the secondary phase is strongly linked to the grain sizes and grain boundary numbers of PZT. The analysis of PZT10 and PZT15 thin films in Figure 4.13 (c-d) show the presence of small grains of  $ZrO_x$  which coexist with perovskite PZT grains. They also reveal that the shape of  $ZrO_x$  is almost uniform and circular whereas the big grain sizes of PZT are inhomogeneous with a random form. Diameter of parasitic phase can reached 40 nm caused by their gatherings. The mean crystallite size of secondary phase is always around 15 nm. These results are in agreement with the average size determined by Epifani *et al.* [61]. Using Image J software, we noticed that the proportions of the secondary structures at the surface are around 19.5 % and 15 % for PZT10 and PZT15, respectively.

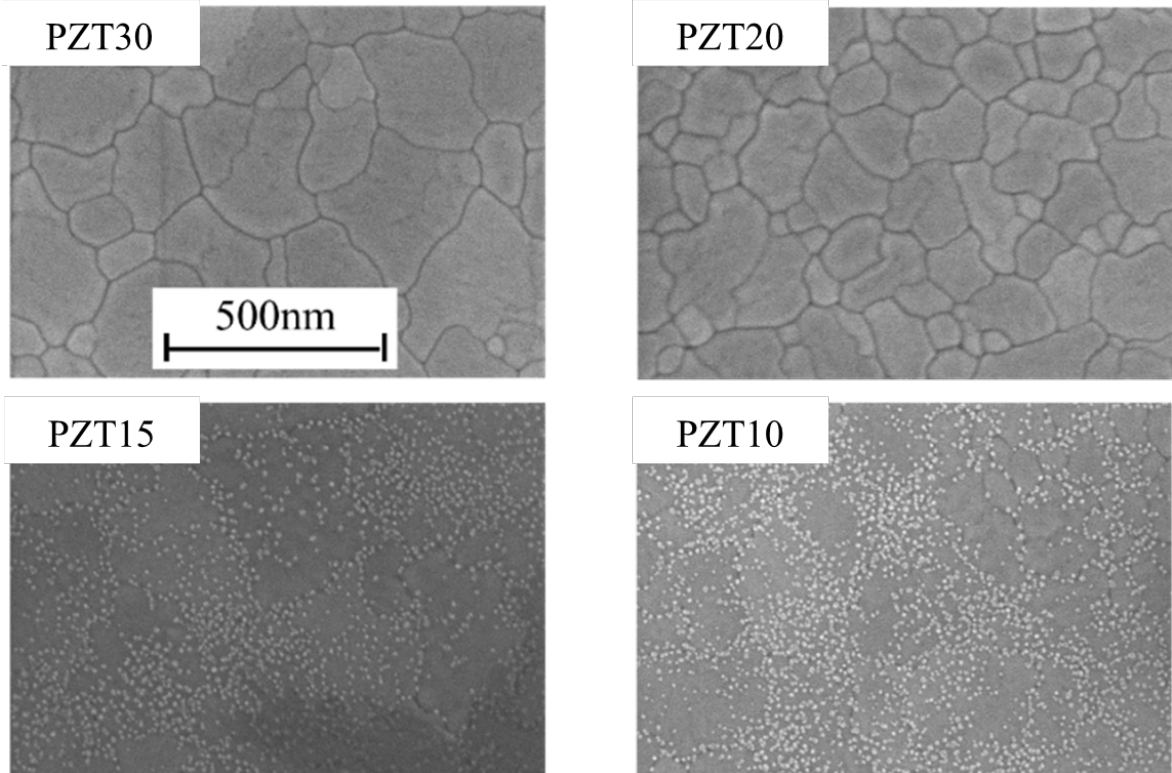


Figure 4.13: SEM images of as deposited (a) PZT30, (b) PZT20, (c) PZT15 and (d) PZT10. The scale bar is the same for all images.

PZT30 and PZT20 (Figure 4.13 (a-b)), show we have practically no Zr oxide at the surface. The size of the large grains also increase with the Pb excess and the number of grain boundaries gradually decrease. Grain size of PZT are ranged from 40 nm to around 350 nm. The average of PZT grains diameter are round 150 and 250 nm for PZT20 and PZT30 respectively. XPS can better quantify both the Zr oxide and PZT at the surface relatively to the Pb excess in the sol-gel solution.

#### 4.4.2 X-ray Photoelectron Spectroscopy

The XPS analysis on PZT thin film with 10, 15, 20 and 30 % Pb excess allows to follow the secondary phase evolution and determine the optimum of the Pb excess, that, we should use to vanish all  $ZrO_x$ . All measurements are carried out with a TOA=70°. Composition of all elements (based on RSFs of each elements) are summarized in Table4.6.

Figure 4.14 (a-b) displays the Pb  $4f_{5/2}$  (at 137.5 eV) and Ti  $2p_{3/2}$  lines (at 457.2 eV) respectively and do not show any binding energy shift. The chemical state of Pb does not change by passing from 10, 15, 20 and even up to 30 % excess of Pb. These data seem to be in good agreement with the previous results from PZT10 and PZT30. From XPS, the relative concentration of Pb varies by 19.6, 24, 25.8 and 24.1 % for PZT10, PZT15, PZT20 and PZT30 %, respectively. Figure 4.14 (b) reveals a low level of Ti at the surface of the PZT layers with 3.4, 2.8, 2.7 and 3.2 % for PZT10, PZT15, PZT20 and PZT30 respectively. The results of relative composition of PZT10 and PZT30 are different to section II of this

chapter due to the modification of the sampling depth (fixing the takeoff angle at  $70^\circ$  instead of  $90^\circ$  or  $30^\circ$ ). In fact, with an IMFP around 2.7 nm obtained with Quases (IMFP TPP2M) with kinetic energy of 1486.6 eV, sampling depth passes to 8.10, 7.61 and 4.05 nm for a TOA of  $90^\circ$ ,  $70^\circ$  and  $30^\circ$ , respectively.

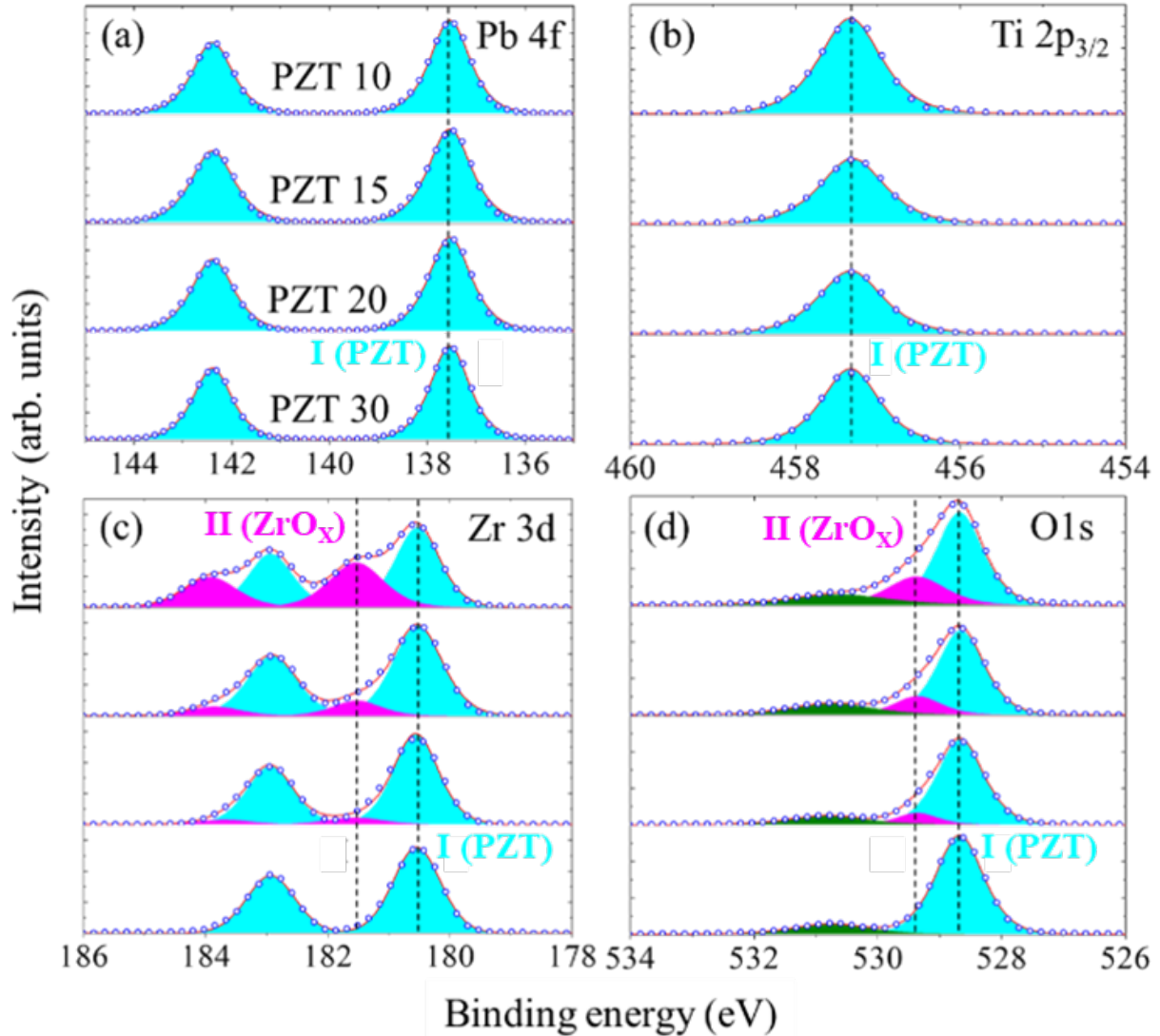


Figure 4.14: XPS core level spectra for PZT30, PZT20, PZT15 and PZT10. a) Pb 4f, b) Ti  $2p_{3/2}$  c) Zr 3d and d) O 1s. Open circles are the experimental points, red lines the best fit, colored peaks the different components. In each panel, the upper (lower) spectrum is that of PZT10 (PZT30). The main peak I (turquoise online) is the perovskite structure; gray peak II (magenta online) surface phase and low intensity, peaks green surface contaminations.

Zr 3d and O 1s spectra shown in Figure 4.14 (c-d) give information on chemical surface states. Binding energy of  $Zr_I$ ,  $Zr_{II}$ ,  $O_I$  and  $O_{II}$  are constant at 180.5, 181.5, 528.7 and 529.4 eV, respectively. In Figure 4.14 (c), the Zr 3d peak corresponding to the  $ZrO_x$  decreases with an increase of the excess of Pb in the precursor solution. The peak intensity of  $O_{II}$

decreases during the variation of Pb excess rate as described in Table 4.6. Regarding to the chemical states labeled  $Zr_I$  and  $O_I$ , any modification of the binding energy was registered. The relative concentration increases when the Pb concentration increases. The increasing intensities of Zr and O labeled  $I$  is correlated with a lowering of the secondary phase labeled II ( $Zr_{II}$  and  $O_{II}$ ) at the surface. Finally, by associating the results on Zr and O shown in Table 4.6 to find the stoichiometry of the Zr oxide with  $TOA = 70^\circ$ , one have respectively  $ZrO_{1.98}$ ,  $ZrO_{1.63}$  and  $ZrO_{1.61}$  for the PZT10, PZT15 and PZT20.

	PZT30	PZT20	PZT15	PZT10
Pb	24.1	25.8	24.0	19.6
Ti	3.2	2.7	2.8	3.4
$Zr_I$	14.2	13.1	11.4	9.4
$Zr_{II}$	-	2.6	5.2	7.1
$O_I$	50.3	43.1	38.7	35.9
$O_{II}$	-	4.2	8.5	14.1
O (green)	8.2	8.5	9.4	10.5

Table 4.6: Composition of the PZT thin films based on the XPS intensities at  $70^\circ$  take-off angle

### 4.4.3 X-ray Diffraction

Even though secondary phase is based on the Zr oxide, the excess Pb content control strongly zircon oxide concentration at the surface and the texturing of the PZT bulk. XRD measurements performed on all PZT thin films reveal a mixed orientation between (100), (110) and (111) localized at  $21.9^\circ$ ,  $31.0^\circ$  and  $38.3^\circ$ , respectively, as presented in Figure 4.15.

	% Average orientation			
	PZT30	PZT20	PZT15	PZT10
(100)	9.4	27.7	41.2	92.4
(110)	3.3	2.2	1.9	0.4
(111)	87.3	70.1	56.9	7.2

Table 4.7: Pb excess effect on the PZT crystallographic orientation

By increasing the Pb excess content from 10 to 30 % a gradual increase of (111) texture and decrease of (100) are observed, which is in contrast with the resultsshowed by Yanovskaya *et al.* [62], Cheng *et al.* [63], Tu *et al.* [64] and Wang *et al.* [65]. Composition ratios calculated according to the formula proposed by Harris [66] are summarized in Table 4.7. From PZT10 to PZT15, an increase of orientation around 50 % (from 7.2 to 56.9 %) of (111) is observed. A decrease of more than 50 % for (100) texture with 92.4 % for PZT10 and 41.2 % for the PZT15 is registered at the same time. The increase in (111) orientation as well as the decrease of (100) orientation are still observed on PZT15 and PZT20. Finally, (110) orientation observed in the MPB phase undergoes a continuous decrease from 3.3 to 0.4 % when the Pb excess is reduced.

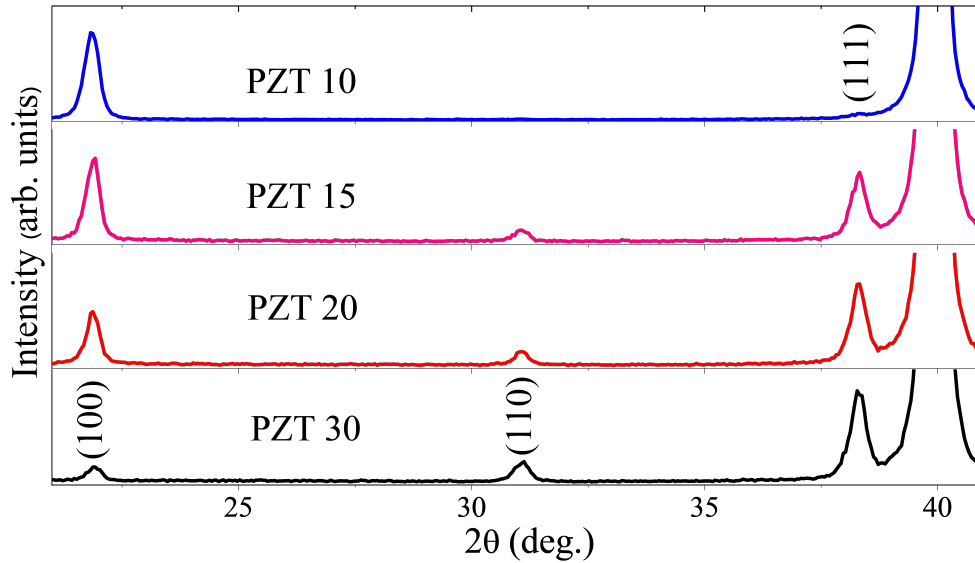


Figure 4.15: XRD scans ( $\theta-2\theta$ ) of PZT thin films with different Pb excess content in sol-gel precursors

#### 4.4.4 Discussion

The large investigation of the Pb excess effect on the chemistry, microstructural surface and texturing characteristics of PZT thin films highlights several crucial points. Indeed, relative to the high proceeding temperatures, Pb desorption remains high as long as sol-gel solution does not crystallize into a compact film of PZT. Therefore, solgel solution must contain Pb excess to compensate its loss. Depending on the level of Pb excess used, PZT samples will exhibit important chemical and structural differences after deposition.

XRD data reveals that the Pb excess influences the nucleation process and determine texture of PZT. This affirmation is based on the fact that the first nanometers of PZT film control the phase and the texture (orientation) during the transition of PZT from amorphous to perovskite phase. As observed by Seung-Hyun Kim *et al.* [67], the use of thin seed layer of  $\text{PbTiO}_3$  allows to have a PZT with a preferred (100) texture.

The sol-gel PZT layer has a concentration of Zr and Ti as described by abergel *et al.* [23] and Calame *et al.* [24]. The highest concentration of Ti is localized near the bottom of the layer and the Zr at the surface of the PZT layer. In others word, the major amount of  $\text{TiO}_2$  precursor reacts to  $\text{PbO}$  at the beginning of the sol-gel deposition (leading the creation of  $\text{PbTiO}_3$ ) contrary to the  $\text{ZrO}_2$  precursor which is at the origin of the  $\text{PbZrO}_3$  perovskite. The phenomenon is linked to the crystallization temperature which increases in the sequence  $\text{PbTiO}_3 < \text{PbZrO}_3 < \text{Pb}(\text{ZrTi})\text{O}_3$  [68]. Furthermore, the favor (100) orientation of PZT10 (PZT with 10 % of lead excess contain) is linked to preferential orientation of the first layer of  $\text{PbTiO}_3$ . These first layers are often described to manage the thin films orientation as shown by Zeng *et al.* [69]. Additionally, for PZT with (100) orientation, the grain nucleation energy is low, therefore, (100) phase was energetically favorable as reported by Trolier-Mckinsty *et al.* [70].

With the high Pb excess compensation in PZT30 presented in Figure 4.12 (a), a  $\text{Pt}_x\text{Pb}$  intermetallic phase may be formed at the bottom interface (PZT/Pt). The  $\text{Pt}_x\text{Pb}$  favors the (111) orientation. According to Wu *et al.* [71], the formation of the transient  $\text{Pt}_x\text{Pb}$  phase is related to the nature of the local thermodynamic conditions in the film. Combustion of the organic groups of solgel precursors during pyrolysis may cause a temporary depletion of O, causing locally reducing conditions. The reduction of  $\text{Pb}^{2+}$  to Pb and the reaction of Pb with Pt to form the  $\text{Pt}_x\text{Pb}$  phase is consequently favored.

Finally, Zhu *et al.* [72] showed that with the increase of Pb concentration, the preferred orientation of PZT films changes from (100) for 0 %, (110) for 10 % and (111) for 20 %. They explain also that with 20 % of Pb excess, Pb–Pt intermetallic phase is easily formed and enhances (111) oriented films. With PZT film with 0 % of Pb excess, the composition changes quickly with the evaporation of (PbO), resulting to the formation (100) orientation. This situation is caused by the fact that with (100) orientation, the grain nucleation energy was energetically favorable as described by Tani *et al.* [73]. For Zhu *et al.* [72], the high percentage of relative intensity of (110) is linked to the presence of moderate Pb excess (10 %) and of annealing treatment near the quantum of PbO volatilization.

The parasite phase has its origin to the lack of Pb atom (PbO) for interacting with  $\text{TiO}_2$  or  $\text{ZrO}_2$  after a high evaporation process. With a gradient of Zr/Ti inside the film, almost of Ti are already transformed at perovskite and the  $\text{ZrO}_2$  is found at the surface in the form of secondary phase. Pb loss process can stop the coalescence of the PZT grains [51]. This is supported by the decreasing of PZT grain size when the Pb excess in precursors pass from 30 % to 10 %. For Hassold *et al.* [74] the decrease of PZT grain size is linked by the inert second-phase particles which is pinning grain boundaries and inhibit grain growth.

The presence of  $\text{ZrO}_2$  at the surface might behave as a lower permittivity dielectric interface layer and induce a reduction of the capacitance density when the Pb excess content is too low like PZT10. However, with PZT30, the decline of the dielectric constant might also be linked with a high amount of Pb excess which is localized inside the PZT sample [62]. In fact, under electrical stress, PbO might behave like the  $\text{ZrO}_2$  and reduce the capacitance value.

The loss tangent compartment can be attributed to the grain boundary which favor the creation of defects or vacancies. The high number of grain boundaries allow to charge carriers to move from one electrode to another. This phenomenon induces dissipation of energy and increases the loss tangent. By increasing the Pb excess content, small grains aggregate reduces the number of grain boundary and decreases the loss tangent.

The decrease of the breakdown voltage of the PZT thin film is linked to the presence of the PbO inside of the bulk as mentioned by Yanovskaya *et al.* [62]. In this context, with increasing the Pb excess, the amount of the PbO increase and favor the generation of Pb cluster inside the ferroelectric which leads an early breakdown voltage. This situation leads the channels path as described by the percolation model and allows the current flowing between one electrodes to another.

Finally, the enhancement of the electric properties observed after PMA (referred chapter 3) can be linked at several effects. The diffusion (or the decrease) both the O/Pb vacancies and residual PbO (often accumulated in the intercrystalline and interface layers of PZT) inside the PZT towards the Ru/PZT interface can allow to improve the electrical responses.

Furthermore, the modification of the internal interfaces inside the PZT samples (due to the multiple solgel deposition steps) occurs at the level of the Ru/PZT interface with the presence of the secondary phase (based on  $ZrO_{2-x}$ ) at the PZT surface under PMA process. This favors the improvement of the electrical performances of capacitors. Indeed, we can hypothesize the creation of alloy between the secondary phase  $ZrO_{2-x}$  and the metal electrode (Ru). This situation would lead to the disappearance of part of nanostructures  $ZrO_{2-x}$  (with lower dielectric constant) at the interface and the creation of new phase which may be conductive. This conductive phase can improve the screening at the interface and the shottky barrier. However, other studies at the level of the interfaces are necessary in order to understand the evolution of the nanostructures and the interface Ru/PZT after PMA process.

## 4.5 Conclusion

This chapter highlights the chemical composition of the PZT surface and the Pb excess dependence on the surface nanostructures. First part focuses on the determination of the parasitic phase composition. The photoemissions spectroscopy measurements of PZT10 and PZT30 are essential for the separation of the perovskite (PZT) and parasitic ( $ZrO_{1.82-1.89}$ ) phases. TOA study performed from 90 to 30° allows to distinguish the parasitic phase at the surface and the PZT in the bulk. These results are supported by the grazing incidence X-ray diffraction data. Ion beam etching study confirms that the  $ZrO_{1.82-1.89}$  is only localized at the surface but not inside the PZT thin films. Scanning electron microscopy increases the size of PZT grain when the rate of Pb excess increase. X-ray diffraction shows a change of the crystallographic orientation from mostly (111) to (100) when passing to 30 at 10 % of Pb excess.

The second part of this chapter is dedicated to the wide study of the evolution of PZT thin film as the function of the Pb excess content. It is observed that with 10, 15, 20 and 30 % of Pb excess, the secondary phase decreases and vanishes at the surface level. From scanning electron microscopy measurements, it is clear that the diminution of the parasitic phase is followed by the increase of the grain size. Finally, the x-ray diffraction shows change of the orientations respectively from (100) to (111) when the Pb excess rate increase.

In the next chapter, we will analyze the behavior of interface Metal-PZT stack during the switching polarization by using Hard x-ray photoelectron spectroscopy (HAXPES). This technique is a well-adaptable non-destructive method for the analysis of the electronic interfaces buried of metal ferroelectric. These *operando* experiments provides important informations of the binding energies of all elements in the ferroelectric under the electrical field.

---

## Bibliography

- [1] C. Zhou and D. M. Newns. Intrinsic dead layer effect and the performance of ferroelectric thin film capacitors. *Journal of Applied Physics*, 82(6):3081–3088, 1997.
- [2] C. K. Wong and F. G. Shin. Modeling of anomalous shift and asymmetric hysteresis behavior of ferroelectric thin films. *Journal of Applied Physics*, 96(11):6648–6656, 2004.
- [3] M. Stengel and N. A. Spaldin. Origin of the dielectric dead layer in nanoscale capacitors. *Nature*, 443(7112):679–682, 2006.
- [4] L. J. Sinnamon, M. M. Saad, R. M. Bowman, and J. M. Gregg. Exploring grain size as a cause for dead-layer effects in thin film capacitors. *Applied Physics Letters*, 81(4):703–705, 2002.
- [5] Q. Y. Xiang, K. Zhang, Y. Wang, X. J. Lou, W. Q. Yao, Y. Bai, D. W. Duan, X. P. Hu, J. Wang, Z. D. Luo, H. H. Wang, L. X. Zhang, U. Klemradt, and J. L. Cao. Insight into Metalized Interfaces in Nano Devices by Surface Analytical Techniques. *ACS Applied Materials & Interfaces*, 7(49):27351–27356, 2015.
- [6] A. Etin, G. E. Shter, G. S. Grader, and G. M. Reisner. Interrelation of Ferroelectricity, Morphology, and Thickness in Sol-Gel-Derived  $\text{PbZr}_x\text{Ti}_{1-x}\text{O}_3$  Films. *Journal of the American Ceramic Society*, 90(1):77–83, 2007.
- [7] J. L. Wang, F. Gaillard, A. Pancotti, B. Gautier, G. Niu, B. Vilquin, V. Pillard, G. L. M. P. Rodrigues, and N. Barrett. Chemistry and Atomic Distortion at the Surface of an Epitaxial  $\text{BaTiO}_3$  Thin Film after Dissociative Adsorption of Water. *The Journal of Physical Chemistry C*, 116(41):21802–21809, 2012.
- [8] J. D. Baniecki, M. Ishii, T. Shioga, K. Kurihara, and S. Miyahara. Surface core-level shifts of strontium observed in photoemission of barium strontium titanate thin films. *Applied Physics Letters*, 89(16):162908, 2006.
- [9] R.H. Liang, D. Rémiens, C. Soyer, N. Sama, X.L. Dong, and G.S. Wang. Etching characteristics and absence of electrical properties damage of PZT thin films etched before crystallization. *Microelectronic Engineering*, 85(4):670–674, 2008.
- [10] J. K. Lee, T. Y. Kim, I. Chung, and S. B. Desu. Characterization and elimination of dry etching damaged layer in  $\text{Pt/Pb}(\text{Zr}_{0.53}\text{Ti}_{0.47})\text{O}_3/\text{Pt}$  ferroelectric capacitor. *Applied Physics Letters*, 75(3):334–336, 1999.
- [11] J. N. Kim, K. S. Shin, D. H. Kim, B. O. Park, N. K. Kim, and S. H. Cho. Changes in chemical behavior of thin film lead zirconate titanate during  $\text{Ar}^+$ -ion bombardment using XPS. *Applied Surface Science*, 206(1-4):119–128, 2003.
- [12] A. Bose and M. Sreemany. Influence of processing conditions on the structure, composition and ferroelectric properties of sputtered PZT thin films on Ti-substrates. *Applied Surface Science*, 289:551–559, 2014.
- [13] S.A. Chambers, T. Droubay, T.C. Kaspar, M. Gutowski, and M. van Schilfgaarde. Accurate valence band maximum determination for  $\text{SrTiO}_3(001)$ . 554(2-3):81–89, 2004.
- [14] T. J. Zhu and L. Lu. X-ray diffraction and photoelectron spectroscopic studies of (001)-oriented  $\text{Pb}(\text{Zr}_{0.52}\text{Ti}_{0.48})\text{O}_3$  thin films prepared by laser ablation. *Journal of Applied Physics*, 95(1):241–247, 2004.

- [15] Y. Sakai, S. Ninomiya, and K. Hiraoka. XPS depth analysis of CuO by electrospray droplet impact. *Surface and Interface Analysis*, 44(8):938–941, 2012.
- [16] A. M. Ektessabi and S. Hakamata. XPS study of ion beam modified polyimide films. *Thin Solid Films*, 377-378:621–625, 2000.
- [17] S. B. Krupanidhi, H. Hu, and V. Kumar. Multiionbeam reactive sputter deposition of ferroelectric  $\text{Pb}(\text{Zr,Ti})\text{O}_3$  thin films. *Journal of Applied Physics*, 71(1):376–388, 1992.
- [18] Yoshitaka Ehara, Satoru Utsugi, Takahiro Oikawa, Tomoaki Yamada, and Hiroshi Funakubo. Crystal orientation dependency of ferroelectric property in rhombohedral  $\text{Pb}(\text{Zr,Ti})\text{O}_3$  films. *Japanese Journal of Applied Physics*, 53, 2014.
- [19] Wei Zhang, Hongbo Cheng, Qian Yang, Fangren Hu, and Jun Ouyang. Crystallographic orientation dependent dielectric properties of epitaxial  $\text{BaTiO}_3$  thin films. *Ceramics International*, 42(3):4400–4405, 2016.
- [20] C. Lin, C. Zhang, and J. Lin. Phase Transformation and Photoluminescence Properties of Nanocrystalline  $\text{ZrO}_2$  Powders Prepared via the Pechini-type SolGel Process. *The Journal of Physical Chemistry C*, 111(8):3300–3307, 2007.
- [21] Patricia María Perillo and Daniel Fabián Rodríguez. Anodization growth of self-organized  $\text{ZrO}_2$  nanotubes on zircaloy-4. Evaluation of the photocatalytic activity. *Matéria (Rio de Janeiro)*, 20(3):627–635, 2015.
- [22] N. Wakiya, K. Kuroyanagi, Y. Xuan, K. Shinozaki, and N. Mizutani. An XPS study of the nucleation and growth behavior of an epitaxial  $\text{Pb}(\text{Zr,Ti})\text{O}_3/\text{MgO}(100)$  thin film prepared by MOCVD. *Thin Solid Films*, 372(1-2):156–162, 2000.
- [23] J. Abergel, M. Allain, H. Michaud, M. Cuffe, T. Ricart, C. Dieppedale, G. Le Rhun, D. Faralli, S. Fanget, and E. Defay. Optimized gradient-free PZT thin films for micro-actuators. In *2012 IEEE International Ultrasonics Symposium*, pages 972–974. IEEE, 2012.
- [24] F. Calame and P. Muralt. Growth and properties of gradient free sol-gel lead zirconate titanate thin films. *Applied Physics Letters*, 90(6):062907, 2007.
- [25] C. Soyer, E. Cattan, and D. Rèmeiens. Ion beam etching of PZT thin films : Influence of grain size on the damages induced. *Journal of the European Ceramic Society*, 25(12):2269–2272, 2005.
- [26] C. S. Park, J. W. Lee, S. M. Lee, S. H. Jun, and H. E. Kim. Effect of excess PbO on microstructure and orientation of PZT(60/40) films. *Journal of Electroceramics*, 25(1):20–25, 2010.
- [27] A. Sachdeva, M. Kumar, V. Luthra, and R. P. Tandon. Phase evolution studies of solgel derived lead zirconate titanate (PZT) nanopowder using X-ray diffraction and X-ray photoelectron spectroscopy. *Applied Physics A*, 104(1):103–108, 2011.
- [28] R. Vaidya, R. J. Simonson, J. Cesarano, D. Dimos, and G. P. López. *Langmuir*.
- [29] N. G. Apostol, L. E. Stoflea, G. A. Lungu, L. C. Tanase, C. Chirila, L. Frunza, L. Pintilie, and C. M. Teodorescu. Band bending in  $\text{Au}/\text{Pb}(\text{Zr,Ti})\text{O}_3$  investigated by X-ray photoelectron spectroscopy: Dependence on the initial state of the film. *Thin Solid Films*, 545:13–21, 2013.

- [30] N. G. Apostol, L. E. Stoflea, G. A. Lungu, C. Chirila, L. Trupina, R. F. Negrea, C. Ghica, L. Pintilie, and C. M. Teodorescu. Charge transfer and band bending at Au/Pb(Zr<sub>0.2</sub>Ti<sub>0.8</sub>)O<sub>3</sub> interfaces investigated by photoelectron spectroscopy. *Applied Surface Science*, 273:415–425, 2013.
- [31] M. M. Zhu, Z. H. Du, and J. Ma. Defect enhanced optic and electro-optic properties of lead zirconate titanate thin films. *AIP Advances*, 1(4):042144, 2011.
- [32] M. H. Tang, J. Zhang, X. L. Xu, H. Funakubo, Y. Sugiyama, H. Ishiwarra, and J. Li. Electrical properties and x-ray photoelectron spectroscopy studies of Bi(Zn<sub>0.5</sub>Ti<sub>0.5</sub>)O<sub>3</sub> doped Pb(Zr<sub>0.4</sub>Ti<sub>0.6</sub>)O<sub>3</sub> thin films. *Journal of Applied Physics*, 108(8):084101, 2010.
- [33] S. W. Lee, S. H. Joo, S. L. Cho, Y. H. Son, K. M. Lee, S. D. Nam, K. S. Park, Y. T. Lee, J. S. Seo, Y. D. Kim, H. G. An, H. J. Kim, Y. J. Jung, J. E. Heo, M. S. Lee, S. O. Park, U. I. Chung, and J. T. Moon. Plasma-Assisted Dry Etching of Ferroelectric Capacitor Modules and Application to a 32M Ferroelectric Random Access Memory Devices with Submicron Feature Sizes. *Japanese Journal of Applied Physics*, 41(Part 1, No. 11B):6749–6753, 2002.
- [34] Shinichiro Takatani, Hiroshi Miki, Keiko Kushida-Abdelghafar, and Kazuyoshi Torii. Pt/PbZr<sub>x</sub>Ti<sub>1-x</sub>O<sub>3</sub> interfacial reaction and Schottky barrier formation studied by x-ray photoelectron spectroscopy: Effect of H<sub>2</sub> and O<sub>2</sub> annealing. *Journal of Applied Physics*, (11):7784–7791.
- [35] M. G. Kang, K. T. Kim, and C. I. Kim. Recovery of plasma-induced damage in PZT thin film with O<sub>2</sub> gas annealing. *Thin Solid Films*, 398-399:448–453, 2001.
- [36] A.C. Galca, V. Stancu, M.A. Husanu, C. Dragoi, N.G. Gheorghe, L. Trupina, M. Enculescu, and E. Vasile. Substratetarget distance dependence of structural and optical properties in case of Pb(Zr,Ti)O<sub>3</sub> films obtained by pulsed laser deposition. *Applied Surface Science*, 257(14):5938–5943, 2011.
- [37] D.W. Zeng, K. Li, K.C. Yung, H.L.W. Chan, C.L. Choy, and C.S. Xie. UV laser micromachining of piezoelectric ceramic using a pulsed Nd:YAG laser. *Applied Physics A*, 78(3):415–421, 2004.
- [38] Y. Y. Lin, Q. Liu, T. A. Tang, and X. Yao. XPS analysis of Pb(Zr<sub>0.52</sub>Ti<sub>0.48</sub>)O<sub>3</sub> thin film after dry-etching by CHF<sub>3</sub> plasma. *Applied Surface Science*, 165(1):34–37, 2000.
- [39] C. Dragoi, N. G. Gheorghe, G. A. Lungu, L. Trupina, A. G. Ibanescu, and C. M. Teodorescu. X-ray photoelectron spectroscopy of pulsed laser deposited Pb(Zr,Ti)O<sub>3-δ</sub>. *physica status solidi (a)*, 209(6):1049–1052, 2012.
- [40] Y. Gao, L. Zhang, Y. Pan, G. Wang, Y. Xu, W. Zhang, and J. Zhu. Epitaxial growth of ultrathin ZrO<sub>2</sub>(111) films on Pt(111). *Chinese Science Bulletin*, 56(6):502–507, 2011.
- [41] H. S. Kim, J. Woo, Y. Joo, and C. Kim. The Use of Inductively Coupled CF<sub>4</sub> / Ar Plasma to Improve the Etch Rate of ZrO<sub>2</sub> Thin Films. *Transactions on Electrical and Electronic Materials*, 14(1):12–15, 2013.
- [42] G. I. Cubillos, J. J. Olaya, M. Bethencourt, G. Cifredo, and G. Blanco. Structural changes in ZrO<sub>x</sub> N<sub>y</sub> / ZrO<sub>2</sub> coatings deposited through spray pyrolysis-nitriding. *Revista Mexicana de Física*, 60:233–242, 2014.

- [43] G.I. Cubillos, M. Bethencourt, J.J. Olaya, J.E. Alfonso, and J.F. Marco. The influence of deposition temperature on microstructure and corrosion resistance of  $ZrO_xN_y/ZrO_2$  coatings deposited using RF sputtering. *Applied Surface Science*, 309:181–187, 2014.
- [44] R. Brenier, J. Mugnier, and E. Mirica. XPS study of amorphous zirconium oxide films prepared by solgel. *Applied Surface Science*, 143(1-4):85–91, 1999.
- [45] Y. Pan, Y. Gao, D. Kong, G. Wang, J. Hou, S. Hu, H. Pan, and J. Zhu. Interaction of Au with Thin  $ZrO_2$  Films: Influence of  $ZrO_2$  Morphology on the Adsorption and Thermal Stability of Au Nanoparticles. *Langmuir*, 28(14):6045–6051, 2012.
- [46] V. R. Chinchamatpure, S. M. Chore, S. S. Patil, and G. N. Chaudhari. Synthesis and Electrical Characterization of  $ZrO_2$  Thin Films on Si(100). *Journal of Modern Physics*, 03(01):69–73, 2012.
- [47] J. C. Woo, S. G. Kim, J. G. Koo, G. H. Kim, D. P. Kim, C. H. Yu, J. Y. Kang, and C. I. Kim. A study on dry etching for profile and selectivity of  $ZrO_2$  thin films over Si by using high density plasma. *Thin Solid Films*, 517(14):4246–4250, 2009.
- [48] L. M. Eshelman, A. M. de Jong, and J. W. Niemantsverdriet. Preparation of  $ZrO_2$  on flat, conducting  $SiO_2/Si(100)$  model supports by wet chemical techniques; X-ray photoelectron spectroscopy and Auger depth profiling. *Catalysis Letters*, 10(3-4):201–209, 1991.
- [49] J. C. Woo, C. A. Choi, W. S. Yang, Y. S. Chun, and C.I. Kim. Surface properties of  $ZrO_2$  thin film under  $Cl_2 / Ar$  plasma using angle-resolved X-ray photoelectron spectroscopy. *Japanese Journal of Applied Physics*, 53(8S3):08NB05, 2014.
- [50] B. M. Melnick, J. D. Cuchiaro, L. D. Mcmillian, C. A. P. de Araujo, and J. F. Scott. Process optimization and characterization of device worthy sol-gel based PZT for ferroelectric memories. *Ferroelectrics*, 112(1):329–351, 1990.
- [51] A. Zomorrodian, A. Mesarwi, N.J. Wu, and A. Ignatiev. XPS oxygen line broadening in lead zirconium titanate and related materials. *Applied Surface Science*, 90(3):343–348, 1995.
- [52] S. A. Impey, Z. Huang, A. Patel, R. Beanland, N. M. Shorrocks, R. Watton, and R. W. Whatmore. Microstructural characterization of solgel leadzirconatetitanate thin films. *Journal of Applied Physics*, 83(4):2202–2208, 1998.
- [53] J. Robertson. High dielectric constant oxides. *The European Physical Journal Applied Physics*, 28(3):265–291, 2004.
- [54] P. W. Peacock and J. Robertson. Band offsets and Schottky barrier heights of high dielectric constant oxides. *Journal of Applied Physics*, 92(8):4712–4721, 2002.
- [55] C. Soyer, E. Cattan, D. Rèmes, and M. Guilloux-Viry. Ion beam etching of leadzirconatetitanate thin films: Correlation between etching parameters and electrical properties evolution. *Journal of Applied Physics*, 92(2):1048–1055, 2002.
- [56] R. Moazzami, C. Hu, and W.H. Shepherd. Electrical characteristics of ferroelectric PZT thin films for DRAM applications. *IEEE Transactions on Electron Devices*, 39(9):2044–2049, 1992.
- [57] Céline Lichtensteiger, Pavlo Zubko, Massimiliano Stengel, Pablo Aguado-Puente, Jean-Marc Triscone, Philippe Ghosez, and Javier Junquera. Ferroelectricity in ultrathin film capacitors. Ch. 12 in *Oxide Ultrathin Films, Science and Technology*, Wiley (2011).

- [58] L. A. Bursill, I. M. Reaney, D. P. Vijay, and S. B. Desu. Comparison of lead zirconate titanate thin films on ruthenium oxide and platinum electrodes. *Journal of Applied Physics*, 75(3):1521–1525, 1994.
- [59] Z. Jia, T. L. Ren, T. Z. Liu, H. Hu, Z. G. Zhang, D. Xie, and L. T. Liu. Study on oxidization of Ru and its application as electrode of PZT capacitor for FeRAM. *Materials Science and Engineering: B*, 138(3):219–223, 2007.
- [60] J. Ze, R. Tian-Ling, L. Tian-Zhi, H. Hong, Z. Zhi-Gang, X. Dan, and L. Li-Tian. Comparison of Properties of Pt/PZT/Pt and Ru/PZT/Pt Ferroelectric Capacitors. *Chinese Physics Letters*, 23(4):1042–1045, 2006.
- [61] M. Epifani, C. Giannini, L. Tapfer, and L. Vasanelli. Sol-Gel Synthesis and Characterization of Ag and Au Nanoparticles in SiO<sub>2</sub>, TiO<sub>2</sub>, and ZrO<sub>2</sub> Thin Films. *Journal of the American Ceramic Society*, 83(10):2385–2393, 2004.
- [62] M. I. Yanovskaya, I. E. Obvintseva, L. I. Solovyova, E. P. Kovsman, K. A. Vorotilov, and V. A. Vasilyev. Alkoxy-derived ferroelectric PZT films: The effect of lead acetate dehydration techniques and lead content in the electrochemically prepared solutions on the properties of the films. *Integrated Ferroelectrics*, 19(1-4):193–209, 1998.
- [63] J. Cheng and Z. Meng. Orientation controlling of PZT thin films derived from sol-gel techniques. *Journal of Materials Science Letters*, 19(21):1945–1949, 2000.
- [64] Y. L. Tu and S. J. Milne. A study of the effects of process variables on the properties of PZT films produced by a single-layer sol-gel technique. *Journal of Materials Science*, 30(10):2507–2516, 1995.
- [65] Z. J. Wang, K. Kikuchi, and R. Maeda. Effect of Pb content in target on electrical properties of laser ablation derived lead zirconate titanate thin films. *Japanese Journal of Applied Physics, Part 1: Regular Papers and Short Notes and Review Papers*, 39(9 B):5413–5417, 2000.
- [66] G.B. Harris. X. Quantitative measurement of preferred orientation in rolled uranium bars. *The London, Edinburgh, and Dublin Philosophical Magazine and Journal of Science*, 43(336):113–123, 1952.
- [67] S. H. Kim, Y. S. Choi, C. E. Kim, and D. Y. Yang. The effects of PbTiO<sub>3</sub> thin template layer and Pt/RuO<sub>2</sub> hybrid electrode on the ferroelectric properties of sol-gel derived PZT thin film. *Thin Solid Films*, 325(1-2):72–78, 1998.
- [68] A. P. Wilkinson, J. S. Speck, A. K. Cheetham, S. Natarajan, and J. M. Thomas. In situ x-ray diffraction study of crystallization kinetics in PbZr<sub>1-x</sub>Ti<sub>x</sub>O<sub>3</sub>, (PZT, x = 0.0, 0.55, 1.0). *Chemistry of Materials*, 6(6):750–754, 1994.
- [69] J. Zeng, M. Zhang, L. Wang, and C. Lin. Influence of lead titanate seed layer on orientation behaviour and ferroelectric characteristics of sol-gel derived PZT thin films. *Journal of Physics: Condensed Matter*, 11(4):1139–1146, 1999.
- [70] S. Trolier-McKinstry and P. Muralt. Thin Film Piezoelectrics for MEMS. *Journal of Electroceramics*, 12(1/2):7–17, 2004.
- [71] A. Wu, P. M. Vilarinho, I. M. M. Salvado, J. L. Baptista, Z. Zhou, I. M. Reaney, A. R. Ramos, and M. F. Silva. Effect of Lead Zirconate Titanate Seeds on Pt<sub>x</sub>Pb Formation during the Pyrolysis of Lead Zirconate Titanate Thin Films. *Journal of the American Ceramic Society*, 85(3):641–646, 2004.

- [72] C. Zhu, Y. Chentao, L. Bo, and Y. Bangchao. Investigation on the effects of PbO content and seeding layers of  $\text{TiO}_2$  and  $\text{ZrO}_2$  on the orientation and microstructure of  $\text{Pb}(\text{Zr}_{0.52}\text{Ti}_{0.48})\text{O}_3$  ferroelectric films grown by reverse dip-coating method of solgel. *Materials Letters*, 60(13-14):1559–1564, 2006.
- [73] T. Tani, Z. Xu, and D. A Payne. Preferred Orientations for Sol-Gel Derived Plzt Thin Layers. *MRS Proceedings*, 310(100):269, 1993.
- [74] G.N. Hassold, E.A. Holm, and D.J. Srolovitz. Effects of particle size on inhibited grain growth. *Scripta Metallurgica et Materialia*, 24(1):101–106, 1990.

# Chapter 5

## Pt/Ru/PbZr<sub>0.52</sub>Ti<sub>0.48</sub>O<sub>3</sub> INTERFACES

### Contents

<b>5.1</b>	<b>Hard X-ray Photoelectron Spectroscopy . . . . .</b>	<b>126</b>
<b>5.2</b>	<b>PZT Bare with 10 % of Pb Excess . . . . .</b>	<b>126</b>
<b>5.3</b>	<b>Investigations of Pt/Ru/PZT10 Interfaces . . . . .</b>	<b>130</b>
5.3.1	Survey of Buried Interface of Pt/Ru/PZT10 . . . . .	130
5.3.2	Dielectric Constant and Polarization of Pt/Ru/PZT/Pt . . . . .	131
5.3.3	Bias Correction After HAXPES Measurements . . . . .	134
5.3.4	Background Subtraction . . . . .	135
5.3.5	Analysis on <i>Operando</i> HAXPES Data Based on PZT10 . . . . .	136
<b>5.4</b>	<b>Interface Analysis of Pb Excess Content in PZT . . . . .</b>	<b>140</b>
5.4.1	Pt/Ru/PZT30/Pt Electrical Measurements . . . . .	140
5.4.2	Analysis on <i>Operando</i> HAXPES Data Based on PZT30 . . . . .	142
<b>5.5</b>	<b>Post Metallization Annealing of Pt/Ru/PZT10 Interface . . . . .</b>	<b>144</b>
5.5.1	Electrical Characterization After PMA . . . . .	145
5.5.2	Ru and Pt Chemical State Before and After PMA . . . . .	145
5.5.3	Analysis on <i>Operando</i> HAXPES Data Based on PZT10 After PMA	147
<b>5.6</b>	<b>Conclusion . . . . .</b>	<b>150</b>
	<b>Bibliography . . . . .</b>	<b>152</b>

Electrical performances of PZT-based capacitors as a function of the Pb excess content in precursor and the post metallization annealing (PMA) raise important questions. By far, the understanding on how these parameters can modify the properties of Pt/Ru/PZT/Pt capacitors is not clear yet.

The results presented in chapter 4 have pointed out the importance of Pb excess on the texture (XRD), microstructure (TEM) and surface chemistry by using mainly laboratory-based photoelectron spectroscopy. The XPS results (with low Inelastic Mean Free Path (IMFP) of electrons) were

crucial to understand the intrinsic chemistry and electronic at the surface of PZT layer.

Furthermore, Zircon oxide nanostructures formed at the surface of the PZT layer might lead to the creation of undesired interfacial layer with a lower dielectric constant. This affects the performances of capacitors as already presented in chapter 4, section 4.3.5 (page 111).

In fact, the electrode/PZT interface plays a major role in polarization switching, permittivity, breakdown voltage, fatigue and reliability [1, 2, 3]. The Schottky barrier height (SBH) at the metal/PZT interface has an important influence on leakage current [4] and depends on the polarization [3, 5, 6, 7] at the interface. On a microscopic scale the electrode/PZT interface is determined by the local chemistry [7, 8]. The resulting interfacial layer has been described in terms of an additional capacitor in series [9] with specific bias dependent chemistry and screening of the depolarizing field [10]. However, XPS is a surface sensitive tool. Since a probing depth of XPS is between  $\sim 3$  and 6 nm, this technique cannot give us any information on the evolution of nanostructures or the interactions at the electrode/PZT interface.

In order to overcome this limitation, the synchrotron radiation source was used. The higher photon energy provided by synchrotron source, helps to balance out the effect of low IMFP electron observed with XPS, yielding adequate counting rates [11].

In this chapter, we used Hard X-ray Photoelectron Spectroscopy (HAXPES) to probe the buried Pt/Ru/PbZr<sub>0.52</sub>Ti<sub>0.48</sub>O<sub>3</sub> interface in a Pt(5 nm)/Ru(5 nm)/PZT(220 nm)/Pt/TiO<sub>2</sub>/SiO<sub>2</sub>/Si stack. A customized sample-holder allows in-situ photoemission analysis while applying bias to the capacitor. Thus, *operando* HAXPES measurements of the Pt/Ru/PbZr<sub>0.52</sub>Ti<sub>0.48</sub>O<sub>3</sub> interface will allow to better understand both, the Pb excess effect and post metallization annealing effects at the interface region.

## 5.1 Hard X-ray Photoelectron Spectroscopy

X-ray photoelectron spectroscopy (XPS) is an ideal tool to probe the chemical changes and the electronic structure at the surface. However, the investigations of the actual behavior of dielectric under bias with X-ray photoelectron spectroscopy is very difficult due to the low IMFP and the presence of metal electrode. Chen and Klein used XPS with in-situ bias to probe the interface between single crystal BTO and Pt or RuO<sub>2</sub> electrodes [6]. Rault *et al.* measured the Pt/BTO/n-doped STO interface band line-up as a function of the polarization [5]. However, standard XPS is very surface sensitive, and requires ultra-thin electrodes which may be discontinuous [12] or poorly metallic [13].

HAXPES allows to access more deeply the buried interfaces [11] making the study of more realistic device architectures possible. Zenkevich *et al.* [14] measured the barrier-height at the top interface of a Pt/BTO/Cr tunnel junction after ex situ switching. Interestingly, it recently showed that the applied bias gives rise to an additional core level shift due to the strain generated in a relaxor ferroelectric [7]. Such effect is absent under zero field, underlining the importance of *operando* experiments for a comprehensive understanding of the prototypical device operation.

## 5.2 PZT Bare with 10 % of Pb Excess

Photoionization cross sections of Pb, Zr, Ti and O elements are significantly affected when photon energies pass from 1486.6 eV (*Alk $\alpha$* ) energy used in the laboratory) to 6893.6 eV used in the

synchrotron. From a new NIST database for quantitative photoelectron spectroscopy Simulation of Electron Spectra for Surface Analysis (SESSA) based on the formula given by Cooper [15], the values of photoionization cross sections are obtained as shown in Table 5.1. A photoionization cross section is a physical quantity, corresponding to the probability of interaction between electron (in the specific core level) in the material and the incident photon. The cross section has the dimension of a surface.

We observe that, by using a photon with energy of 6893.6 eV, the Photoionization cross section of Pb 4d<sub>5/2</sub> become higher than the one of the Pb 4f<sub>7/2</sub>. For the zirconium, the photoionization cross section of Zr 3p<sub>3/2</sub> is more intense that that Zr 3d<sub>5/2</sub> when a synchrotron radiation is employed. These variations of the photoionization cross section might induce several modifications in the survey of the PZT with photon energies of 1486.6 and 6893.6 eV.

	Cross section (Barn: 1 b = 10 <sup>-28</sup> m <sup>2</sup> )	
	1486.6 eV	6893.6 eV
Pb 4f <sub>7/2</sub>	1.901 10 <sup>-3</sup>	8.284 10 <sup>-6</sup>
Pb 4d <sub>5/2</sub>	1.839 10 <sup>-3</sup>	4.928 10 <sup>-5</sup>
Zr 3d <sub>5/2</sub>	5.799 10 <sup>-4</sup>	2.502 10 <sup>-6</sup>
Zr 3p <sub>3/2</sub>	7.004 10 <sup>-4</sup>	1.560 10 <sup>-5</sup>
Zr 3s	2.942 10 <sup>-4</sup>	1.501 10 <sup>-5</sup>
Ti 2p <sub>3/2</sub>	7.132 10 <sup>-4</sup>	5.322 10 <sup>-6</sup>
O 1s	4.003 10 <sup>-4</sup>	4.482 10 <sup>-6</sup>

Table 5.1: Photoionization cross section of electrons depending on the photon energy.

The survey of PZT bare with 10 % of Pb excess content (called as deposited PZT10) have been carried out and presented in Figure 5.1. By comparing the survey of PZT10 bare depending on the energy source, we observe several differences. Relative intensity of all PZT emission lines change when energy is modified from laboratory to synchrotron as already seen with the cross section data presented in Table 5.1. The survey from HAXPES and XPS provide all the expected emission lines from Pb, Zr, Ti and O. With 6893.6 eV, the relative intensity of Pb 4f decreases, contrary to the Pb 4d and Pb 4p which become very intense for the same peak line at 1486.6 eV. Further, it is more interesting to measure on the Zr 3p peak instead of the Zr 3d peak when the energy is at 6893.6 eV. All these experimental results are in agreement with the tendency of the photoionization cross section calculated with SESSA.

Furthermore, by using IMFP (QUASES-IMFP-TPP2M) calculated by Tanuma *et al.* [16], the as deposited PZT10 with a film density  $\rho = 8g/cm^3$  provides a inelastic mean free path electron inside the PZT layer of 8.8 nm for 6896.3 eV and 2.7 nm for 1486.6 eV.

Beside the variation of the photoionization cross section of electrons depending on the photon energy, the prolonged exposures of the sample at high energy of photon source can induce a reduction of element like the formation of metallic (reduced) Pb nanoparticle as described by Popescu *et al.* [17] on the PZT thin film.

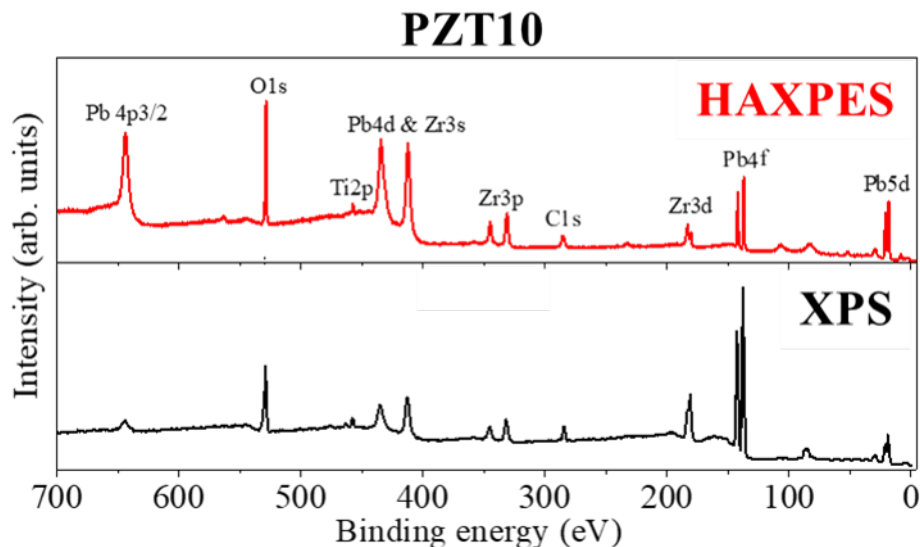


Figure 5.1: PZT10 as deposited survey depending on the photon energy: Top (HAXPES: 6893.6 eV) and Bottom (XPS: 1486.6 eV)

Otherwise, the surface charge which is due to the emission of electrons when X-ray photons strike a sample, can also affect the photoelectron spectrum of elements. Indeed, when the surface is electrically insulating, the emission of electrons causes a positive charge accumulation at the surface. When a non-monochromated source is used for XPS or HAXPES analysis, there are sufficient number of electrons in the region of the sample to limit the effect of the charging. However, when using a monochromated X-ray source for XPS (or HAXPES) measurements, there are too few stray electrons to control the charging and the resulting positive charge severely affects the photoelectron spectrum. It causes the shift of the peaks in the spectrum into high binding energies and becomes distorted. However, during all experiences at synchrotron SOLEIL, any surface charge effect is observed with the PZT as deposited analysis.

In Figure 5.2(a-b), the Pb 4f and Zr 3p<sub>3/2</sub> core level spectra from as deposited PZT10 are shown. The results of the fits are given in Table 5.2.

In Figure 5.2(a), the main component of Pb 4f (peak I at 137.5 eV) corresponds to Pb<sup>2+</sup> in PZT. A spin-orbit (S-O) splitting of 4.8 eV and branching ratio of 1.33 were used and the FWHM was kept constant at 0.89 eV as described in chapter 4 in section 4.3.1 page 102. The Gaussian-Lorentzian line-shapes are 30/70. The low binding energy (LBE) component (peak II), shifted by 1.3 eV with respect to the main peak. The peak II represents for 5 % of the total intensity. The long exposure to X-rays is a possible source of the reduction of Pb. However, we exclude this effect since no evolution was observed on the spectra during the analysis (It occurs very rapidly at the beginning of photon exposure). In other word this peak does not come from the measurements, but already present in the film before the measurement. Therefore, the small proportion of reduced Pb may be intrinsic to the sol-gel layer.

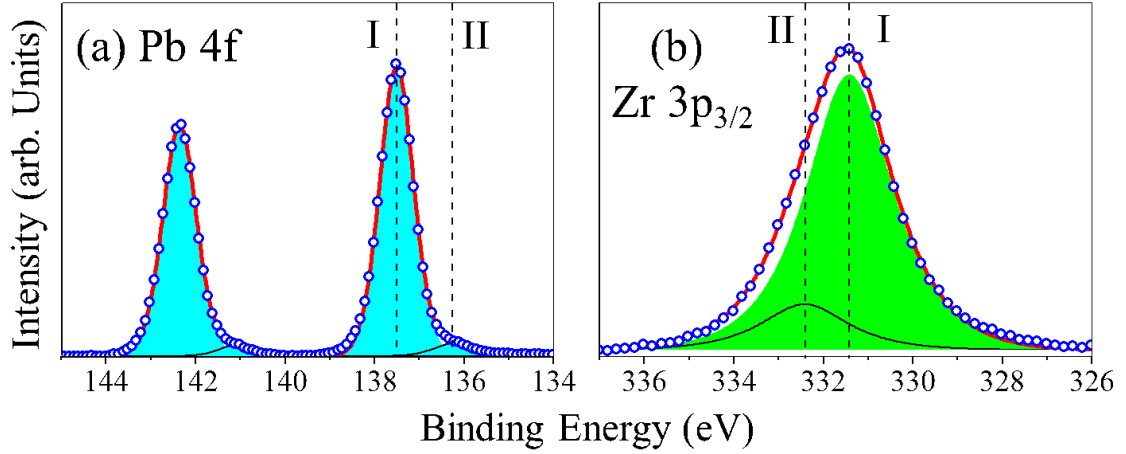


Figure 5.2: (a) Pb 4f and (b) Zr 3p<sub>3/2</sub> spectra. The Pb components are in cyan and the Zr components are in green. The label I represents Pb/Zr in PZT, whereas label II identifies reduced Pb or Zr in surface nanostructures, respectively.

The Zr 3p<sub>3/2</sub> spectrum has also two components as illustrated in Figure 5.2(b). Both FWHM peaks were kept constant at 2.3 eV and the Gaussian-Lorentzian line-shapes was 80/20. The nanostructure contribution peak (II) accounts for 17 % of the total signal of Zr 3p spectrum. The main peak (I) at 331.5 eV is the Zr emission from the PZT. The peak (II), shifted 1.0 eV to higher binding energy (HBE) due to the ZrO<sub>1.82–1.89</sub> nanostructures at the PZT surface has already been identified, see the discussion in chapter 4 in section 4.3 page 100. As shown in chapter 4 in section 4.3.5 page 109, the binding energy shift of the Zr in the ZrO<sub>1.82–1.89</sub> nanostructures consistent with the electronegativity of next nearest neighbour species. As already mentioned, the electronegativity of the Zr, Ti and O basis of Pauling’s scale are 1.33, 1.54 and 3.44, respectively. In the PZT layer, the presence of the Ti in ZrO-Ti tends to modify the electron transfer between Zr-O while in the ZrO<sub>1.82–1.89</sub> nanostructures the charge transfer is produced from the outer core level of Zr to the O atom without any others neighbor interactions.

In the following, the Pb and Zr core level shifts and intensity ratios of the as deposited PZT10 film will be transposed to the spectra obtained by *operando* analysis of the Pt/Ru/PZT10/Pt stack.

Core level	I		II		FWHM (eV)	GL (%)
	BE (eV)	RI (%)	BE (eV)	RI (%)		
Pb 4f <sub>7/2</sub>	137.5	95	136.2	5	0.89	30
Zr 3p <sub>3/2</sub>	331.4	83	332.4	17	2.3	80

Table 5.2: Core level binding energy (BE), Relative intensity (RI), Full width at half maximum (FWHM) and percentage of Gaussian peak in the Gaussian-Lorentzian (GL) peak shapes of the PZT10 as deposited spectra.

### 5.3 Investigations of Pt/Ru/PZT10 Interfaces

Figure 5.3(a) shows the high resolution bright field Transmission Electron Microscopy (TEM) cross section of Pt/Ru/PZT stack. An abrupt interface between PZT layer and Pt/Ru is observed in the TEM cross section. No diffusion between layers is observed and the Pt-Ru electrode follows their topography. The crystalline Zr oxide based nanostructures already observed at the surface of bare PZT shown in Figure 4.5 chapter 4 in section 4.3 page 100, are clearly present at the interface (bump of ZrO<sub>1.89</sub>). The typical nanostructure diameter in Figure 5.3(a) is around 10 nm. We can emphasize the presence of a very thin bright layer at the interface Ru/PZT.

Figure 5.3(b) shows the energy dispersive X-ray analysis cross-sections on Pt, Ru, Pb, Zr and O elements. At the level of very thin bright layer at the interface Ru/PZT, we can observe the presence of the Zirconium and higher amounts of oxygen (Zr<sub>x</sub>O<sub>y</sub>) [18, 19]. Finally, the nanostructure (bump of ZrO<sub>1.89</sub>) composition shows no evidence of Pb particles.

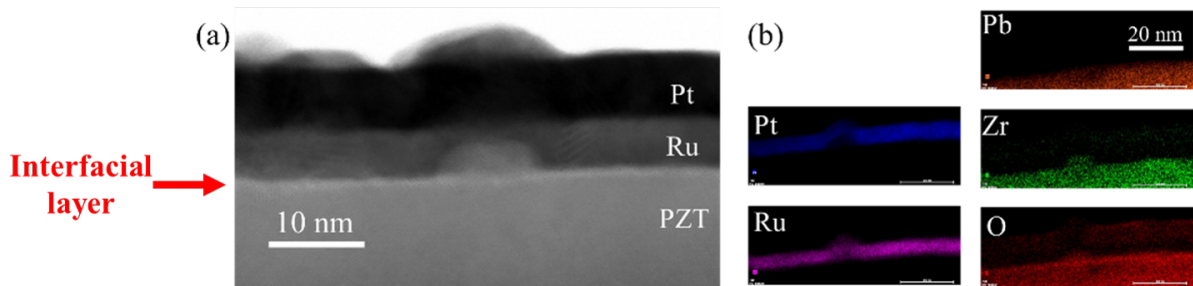


Figure 5.3: Cross section of the as-grown Pt/Ru/PZT10 interface: (a) High-resolution bright TEM and (b) Energy dispersive X-rays analysis of Pt, Ru, Pb, Zr, and O elements

#### 5.3.1 Survey of Buried Interface of Pt/Ru/PZT10

HAXPES survey of the PZT10 bare and PZT10 with 10 nm Pt/Ru top electrode are presented in Figure 5.4. Intensity of Pb, Zr, Ti and O peaks from PZT10 layer are strongly attenuated in Figure 5.4 (bottom) with respect to the as deposited PZT10 thin film observed in Figure 5.4 (top).

According to the position of Pb 4f<sub>7/2</sub> and Zr 3p<sub>3/2</sub> from Table 5.2 and the offset in binding energies between photoelectron lines collected from the literature database, the binding energy expected for Zr 3s and Pb 4d<sub>3/2</sub> are 431.9 eV and 412.8 eV, respectively.

These results are consistent with the top electrodes attenuation effects for Pb 4d and Zr 3s electrons excited by 6.8936 keV photon energy. According to the data provide by Tanuma *et al.*, IMFP are around 5.9 and 5.5 nm in Ru and Pt, respectively [20]. We will use Pb 4d/Zr 3s to understand chemical and electronic interfacial effects under electrical field. We will also record the Ru 3p<sub>3/2</sub> and Pt 4f to check all chemical and electronic modifications which can affect the interface properties like the Schottky barrier height.

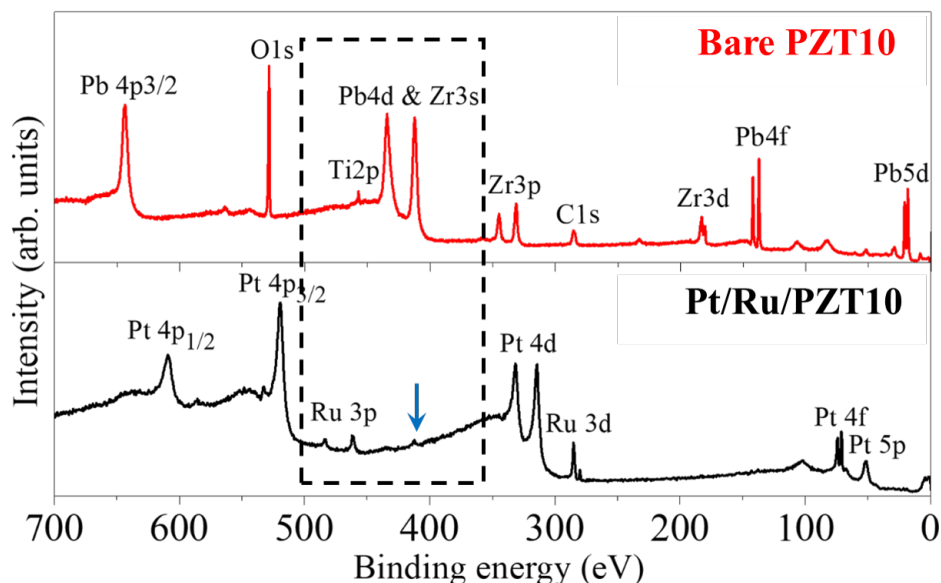


Figure 5.4: Comparison of HAXPES Survey of as deposited PZT10 and Pt/Ru/PZT10 stack

### 5.3.2 Dielectric Constant and Polarization of Pt/Ru/PZT/Pt

During the HAXPES measurements, the Pt/Ru/PZT/Pt structure was biased using an Agilent E4980A capacitor/voltage generator [21]. All dielectric constant-voltage and polarization-voltage curves presented in this chapter are performed on the capacitor with 10 nm thick of top electrode (Pt 5 nm /Ru 5nm) contrary to what have already presented in chapter 3 (Pt 100 nm /Ru 5nm). However, this Pt (5 nm) and Ru (5 nm) thickness cannot induce any change on the electric responses. In fact, as observed in Figure 5.3(a), the thicknesses of Pt [22] and Ru [23] metals are higher than the coalescence threshold which is defined as the thickness where the first conducting link forms across the surface. This situation induces a rapid decrease of the resistivity of metal and favors the conductivity.

The maximum value of dielectric constant for the Pt(5 nm)/Ru(5 nm)/PZT10/Pt is 1221.6. This value is different with the one of Pt(100 nm)/Ru(5 nm)/PZT10/Pt which is 1126.6 (see Figure 3.7 chapter 3 in the section 3.2.1 page 85). Thickness difference of the top electrode could potentially be at the origin of this difference. This difference might also be partly related to the increase of the capacitor area respectively to  $(80 \times 80) \mu\text{m}^2$  and  $(1 \times 1) \text{mm}^2$ . Butterfly dielectric constant characteristic performed at 1 kHz is offset by -1.55 V and the coercive voltages are -2.0 and -1.2 V (Figure 5.5(a)). At zero applied field there is a strong, downwards pointing polarization, which we will call a  $P^-$  imprint. The imprint in Figure 5.5(a) is much higher, more than double, than the one observed in Figure 3.6(a) chapter 3 in the section 3.2.1 page 85 which can be explained by the fact that more voltage was applied in the sample with 100 nm of Platinum (-10 V; +10 V) than the sample with 5 nm of platinum (-7 V; +3 V). Thus, the high voltage tends to decrease the imprint and reduce the offset value. The *operando* analysis was carried out at -7 V (negative voltage on top electrode,  $P^+$  polarization) and +3 V (positive voltage on

top electrode, P<sup>-</sup> polarization), i.e. symmetrically with respect to the center of the butterfly loop of Figure 5.5(a). Remanence measurements are expected to show a similar result to +3 V since the imprint is P<sup>-</sup>. The high voltages relative to the coercive values ensure true saturation conditions whilst remaining below breakdown voltage which is 34.6 V (1.60 MV/cm). Capacitance values at -7 and +3V do not change during the long exposure to high energy X-rays (6893.6 eV).

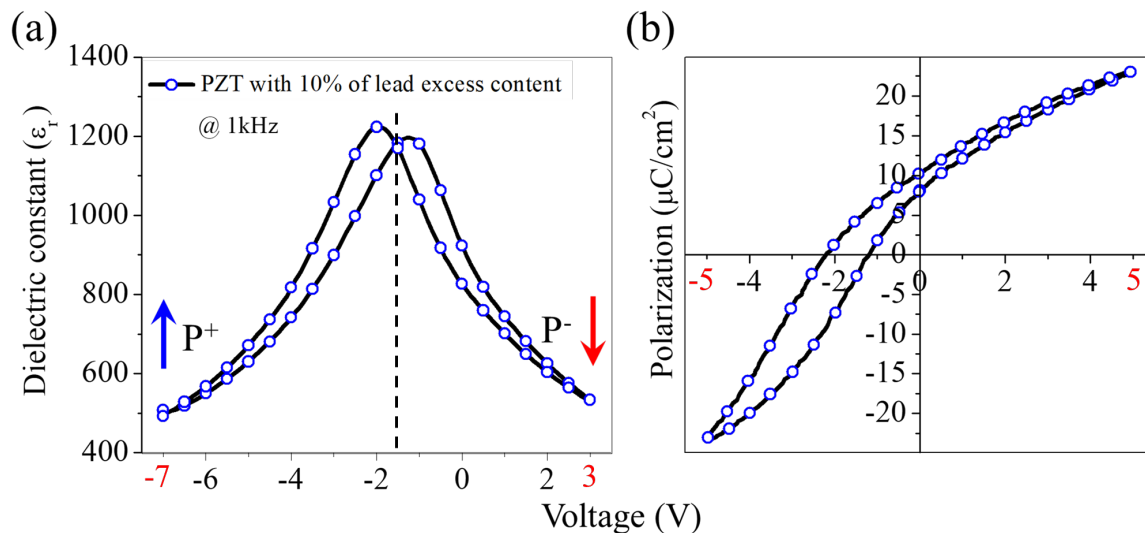


Figure 5.5: Electrical measurements Pt/Ru/PZT10/Pt stack: (a) Dielectric constant and (b) Polarization characteristic

Dynamic hysteresis loop measurement (DHM) at 1 kHz performed by using an Aixacct TF2000 ferroelectric tester [24]. In this case, a succession of four triangular voltages of a few volts of amplitude is applied across the ferroelectric capacitor according to the timing diagram presented in Figure 5.6. There are a prepol pulse and three bipolar excitation signals (three pulses). Each signal is resaw by a relaxation time pause of 1 second. The measurement of the switching currents is carried out during pulses first and third (in red). The prepol pulse and the second pulse (in black) of the excitation signal establish defined polarization states. The prepol pulse has a negative state of relaxed remanent polarization. The second pulse ends in the positive state of relaxed remanent polarization. In this case, only the electrical response due to the switching of the ferroelectric domains is available. However, the measurement gives access to a great deal of information such as the positive and negative coercive fields and the remanent, relaxed, and maximum positive and negative polarizations.

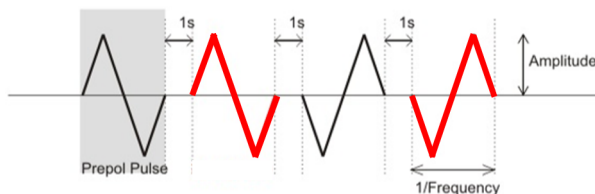


Figure 5.6: Advanced DHM parameter with excitation signal

However, the hysteresis loop in Figure 5.5(b)) reveals a saturation polarization equal to  $23 \mu\text{C}/\text{cm}^2$ . The ferroelectric hysteresis is also offset by 1.7 V towards the negative voltage and the coercive voltages are -2.2 for negative voltage on top electrode and -1.2 V for positive voltage on top electrode (Figure 5.5(b)). Remanent polarization ( $P_r$ ) are 10.4 and  $7.9 \mu\text{C}/\text{cm}^2$  for respectively  $P_r^-$  and  $P_r^+$ . Zhou *et al.* [25] showed the same behavior of hysteresis with both the horizontal shifting towards the negative and voltage and the presence of long tail at positive voltage. They explained that imprint phenomena may originate from :(i) stress induced by film/electrode lattice mismatch or clamping, (ii) domain pinning induced by, e.g., oxygen vacancies, or (iii) degradation of ferroelectric properties in film/electrode surface layers. Additionally, Zhou *et al.* [25] argued that the long tail of shape hysteresis loop for ferroelectric thin films has been induced by the presence of the pseudo-non-switching layer. In fact, the hysteresis loop of the ferroelectric layer is completely cycled, while the polarization of the nonswitching layer only stays in the upper part of the P-E loop so that polarization switching cannot occur.

The use of different metals between the bottom and top electrodes which induces two types of Schottky barrier (asymmetric barrier heights) might participate to the creation of the offset P-E curve. However, as we have already stated in the chapter 3 in section 3.2.1 page 87, the effect of the asymmetry of the electrodes remains rather small compared to the shift observed on the different samples. Furthermore, the interface metal electrode/PZT can be at the origin of the hysteresis offset. In fact, when a metal electrode is placed in contact with a semiconductor material, there may be a flow of charge carriers from the semiconductor to the metal, depending on the work function of the metal. An accumulation of charge carriers results at the electrode/semiconductor interface, inducing an electrostatic potential that depletes these carriers in adjacent regions. This space charge region or depletion layer is typically formed near interfaces such as grain boundaries and interfaces between heterophases [26]. With ferroelectric materials such as PZT, the presence of space charge region or depletion layer can affect the properties. It suppresses ferroelectricity in the space charge regions. Furthermore, the domain pattern that is formed under the influence of space charge can substantially differ from those without. Consequently when such a sample is switched, the hysteresis loop constricts with a lowering of the coercive field, and depending on the extent of the depletion layer, the remnant polarization as well. If the distribution of charges in the sample is asymmetric, the resulting internal electric field leads to a preferred polarization direction, thereby shifting the hysteresis loop along the electric field axis; this phenomena is called imprint. In our Pt/Ru/PZT/Pt a preference orientation of the polarization along the  $P^-$  direction might be obtained. Finally, the presence of the very thin bright layer at the top interface Ru/PZT observed in the Figure 5.3(a), can induce an offset characteristic of the hysteresis and butterfly.

Figure 5.5(b) also shows that the hysteresis curve presents an asymmetric shape relative to zero voltage bias. This variation of slim shape of the hysteresis at positive voltage might be attributed by a poor switching ferroelectric domains. In fact with the presence of the imprint, major of domains are orientated on the same direction as the electric field when the bias is positive. Otherwise, when the voltage is negative, a large switching of ferroelectric domains will be observed, which is accompanied by the restoration of the character ferroelectric of the hysteresis shape. These assertions are supported by a supplementary

measure performed on the same sample but with a higher voltage as illustrated in the Figure 5.7. In fact, when strong electric field (voltage) is applied in the ferroelectric, the locked ferroelectric domains become more switchable that when the electric field is low.

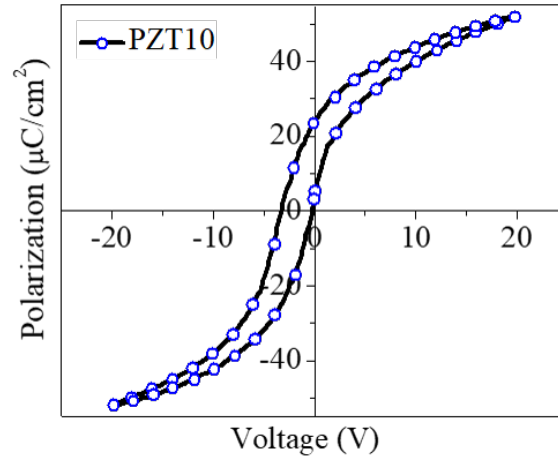


Figure 5.7: Polarization characteristic measurement Pt/Ru/PZT10/Pt stack at 1 kHz

### 5.3.3 Bias Correction After HAXPES Measurements

The raw Ru 3p, Pb 4d and Zr 3s spectral regions from the capacitor structure with -7 V (red curve) and +3 V (blue) on the top electrode are shown in Figure 5.8(a). The advantage of the Pb 4d/Zr 3s energy window is that the similar kinetic energies guarantee the same depth sensitivity, despite the additional difficulty that the Zr 3s peak partially overlaps the Pb 4d<sub>3/2</sub>, making deconvolution more difficult.

The Ru 3p peak in the two bias states (with an absolute value of 10 V) is separated by 10 eV, showing that there is very little parasitic resistance in the circuit as seen in Figure 5.8( (a)top). Now, once corrected for bias, the spectra of Ru 3p<sub>3/2</sub> are similar (see in Figure 5.8((a)bottom)). The Ru 3p<sub>3/2</sub> spectrum has only a single component at 461.5 eV (component I corresponding to the Ru<sup>0</sup>) for both bias states as shown in Figure 5.8(b). These results are in agreement with the observation of the Figure 5.3 which show an unoxidized electrode layers.

Component (II) observed in Figure 5.8(b) is linked by the presence of the Ti 2p<sub>3/2</sub>. Shift of the Ti 2p<sub>3/2</sub> under voltage is equal at 1.4 eV with respectively 457.3 eV for +3V and 458.7 eV for -7V. The residual differences observed with Pb 4d & Zr 3s in Figure 5.8(a) and the shift of the Ti 2p<sub>3/2</sub> in 6(b) are attributed to polarization-dependent changes.

Furthermore, correction of the bias states after operando HAXPES process, demonstrated also the presence of residual binding energy shift at the Pb 4d & Zr 3s core levels between +3 V and -7 V. This residual shift is linked to the intrinsic polarization of PZT under voltage bias and allows to the chemistry and electronic behaviors of sample.

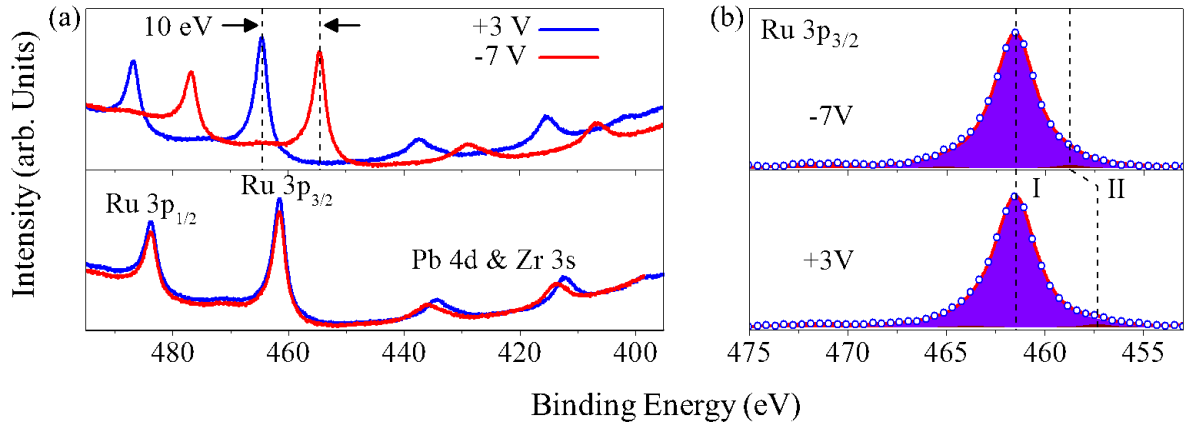


Figure 5.8: (a) *operando* Ru 3p, Pb 4d and Zr 3s spectra with -7 (red curve) and +3 (blue curve) on top electrode before (top) and after (bottom) correction for bias and (b) Ru 3p<sub>3/2</sub>/Ti 2p<sub>3/2</sub> depending on the bias.

### 5.3.4 Background Subtraction

Due to the energy loss tail of the Pt 4d emission from the Pt at top electrode, the background increases with kinetic energy of photoelectron in the Pb 4d/Zr 3s region. Therefore, standard background subtraction like Shirley or Tougaard [27] cannot be used. We have tested polynomial and linear backgrounds and found that the latter gives better results as illustrated in Figure 5.9.

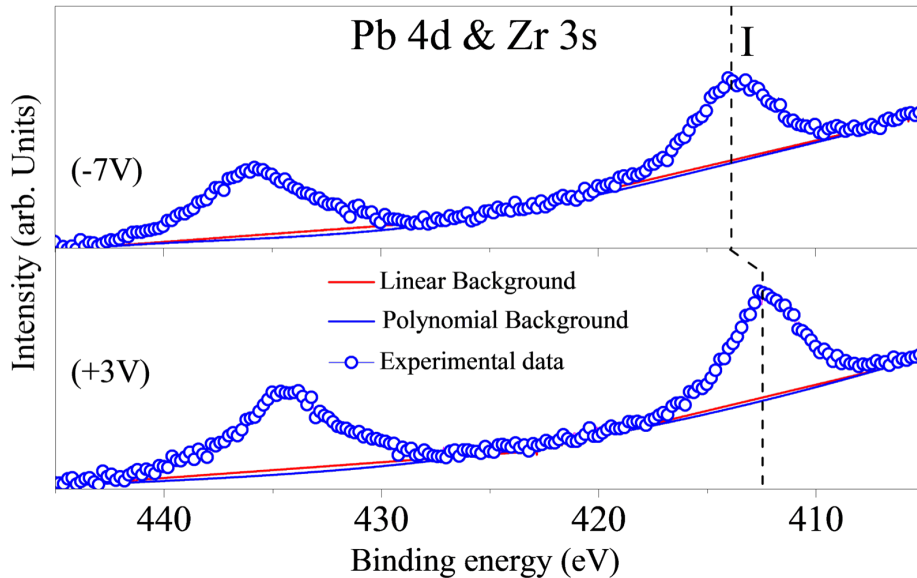


Figure 5.9: Comparison of the linear and polynomial background used for data treatments depending on the bias: Top (-7V) and Bottom (+3V)

Table 5.3 shows the different areas for each component depending to the background

model. Following that, the value of the relative error of each area peak is calculated by the relation: % Relative error = (difference/Area peak) \* 100. Thus, by using the linear background model at +3 and -7 V, relative errors are between 16.1 and 12.2 % for the Pb 4d and 7.6 and 8.2 % for the Zr 3s. Otherwise, the use of polynomial background favors an overestimation of the area of the various components. Indeed, the relative error values are between 20.6 and 25.9 % for the Pb 4d and 25.6 and 34.5 % for the Zr 3s. Therefore, we use the linear background subtraction.

		Area of peaks		
		Pb 4d <sub>5/2</sub>	Pb 4d <sub>3/2</sub>	Zr 3s
Linear	V= +3V	442618	296554	166117
	V= -7V	371167	248682	179747
	Difference	71451	47872	-13630
<hr/>				
Polynomial	V= +3V	513106	343781	255491
	V= -7V	407288	272883	190016
	Difference	105818	70898	65475

Table 5.3: Comparison of the Linear (at +3 and -7V) and polynomial (at +3 and -7V) area of peaks

### 5.3.5 Analysis on *Operando* HAXPES Data Based on PZT10

Pb and Zr core level shifts and intensity ratios found in the PZT10 bare have been directly transposed to the Pb 4d & Zr 3s spectra obtained during the *operando* measurements. The free parameters during the deconvolution of the spectra are the absolute binding energy, the intensity and any additional, interface-specific component. Figure 5.10 shows the best fits to the Pb 4d/Zr 3s spectrum for (a) the PZT10 bare and (b-d) the *operando* spectra of PZT10 with the top electrode under bias. The binding energies and line-shape parameters are given in Table 5.4.

The PZT10 bare spectrum (Figure 5.10(a)) has a high signal to noise ratio which is to be expected in the absence of attenuation by the 10 nm Pt/Ru top electrode observed on the capacitor structures. For the spectra with top electrode under bias, once the PZT Pb 4d, PZT Zr 3s, reduced Pb and Zr oxide nanostructure components have been included, there are two important differences with respect to the as deposited PZT10.

First, there is a 1.4 eV systematic shift of both Pb and Zr emission to higher BE going from +3 V (P<sup>-</sup>) to -7 V (P<sup>+</sup>) whereas the Ru core level does not shift (as shown in Figure 5.8). This suggests a change in electrostatic boundary conditions rather than the chemical environment since the latter would also affect the first layer or layers of the Ru electrode (except a change of local chemistry effect of PZT that would not affect the photoemission signals of Ru). However, the assumptions of a change in electrostatic boundary conditions is supported by results from Figure 5.3 which suggests any interdiffusion between the Ru and PZT layers. The core level shift between +3.0 and 0.0 V is smaller than between 0 V and

-7.0 V consistent with the  $P^-$  imprint measured electrically. Assuming that the polarization-dependent core level shift is equal to the potential drop across the film. The residual internal field is 65 kV/cm, approximately three times the coercive field. This demonstrates that the polarization charge is poorly screened. The Zr 3s component due to the nanostructures is fixed since the nanostructures are above the PZT layer. They should be independent of the polarization. However, the nanostructures might also show polarization due to the stray fields, and this remains an open question.

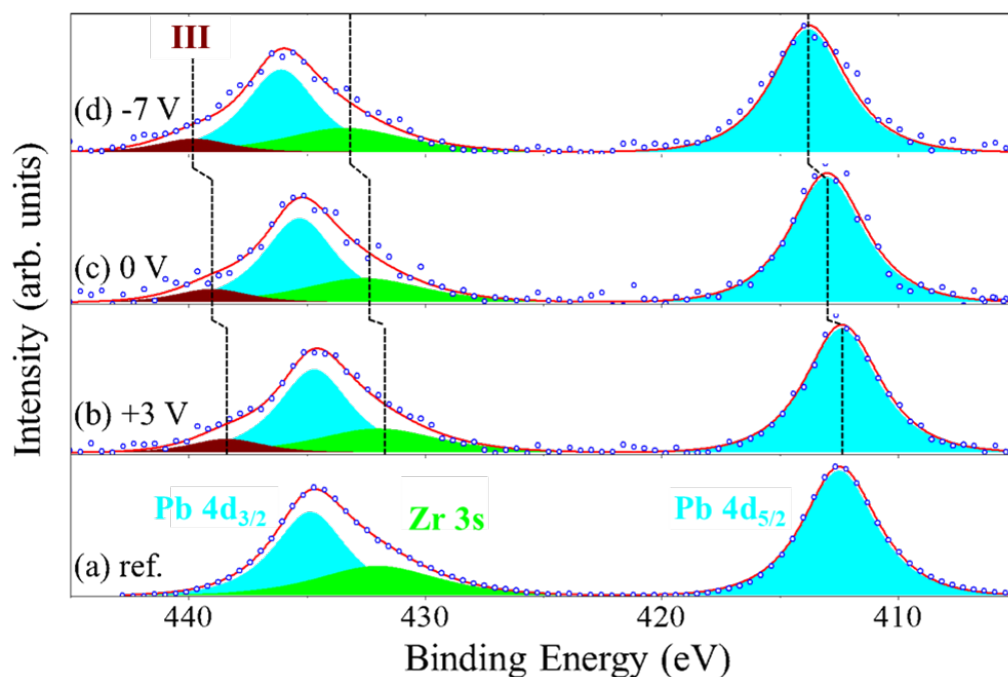


Figure 5.10: Pb 4d and Zr 3s spectra and best fits for (a) PZT10 as deposited film compared with electrode under (b) +3 (c) 0 and (d) -7 V applied bias. The Pb and Zr components have been transposed from the as deposited PZT10 spectra and the color code is the same as in Figure 5.2. Label III identifies the interface related peak discussed in the text

Secondly, there is an additional component, labelled peak III at high binding energy as shown in Figure 5.10(b-d). This interface-related component shifts from 439.8 eV at -7 V to 438.4 eV at +3 V bias, i.e. 1.4 eV like the other core levels. It is also possible to fix the binding energy at 439 eV, which corresponds to an interface contribution, distinct from the PZT as illustrated in Figure 5.11. The single component suggests that it is due to Zr 3s. However, 5-6 eV is too high to be a simple chemical shift of Zr which is already in  $Zr^{4+}$  valence state in PZT. The absence of such component in the reference spectrum and in the XPS analysis of the bare PZT layer proves that it is related to the capacitor structure. The exact origin of this component is therefore not clear. However given that it was not observed on the as deposited PZT10, it probably come from the interface formed with the top electrode (thin bright layer at the interface Ru/PZT reported in Figure 5.3(a)). Furthermore, we can notice that the peak III is not due to the bias voltage because the peak III is present when 0 V is applied on the capacitor as seen in Figure 5.10(c).

The existence of this interface component can be linked to the interface rumpling. The relative intensity of peak III is 4.7 % of the total intensity of Pb 4d and Zr 3s spectra. Assuming an IMFP of 5.7 nm (average of values in Ru and Pt), the intensity corresponds to that expected from some unit cell layer of PZT. First principles calculations have shown that rumpling at electrode interface changes significantly with polarization [9]. This explanation is in good agreement for the Pt-PbTiO<sub>3</sub> interface of 0.11 Å [9, 28]. The rumpling variation would induce a change in the local chemistry and might be responsible for an additional Zr component. This has to be confirmed by further experiments with higher statistics and by acquiring the Pb 4f and Zr 3p.

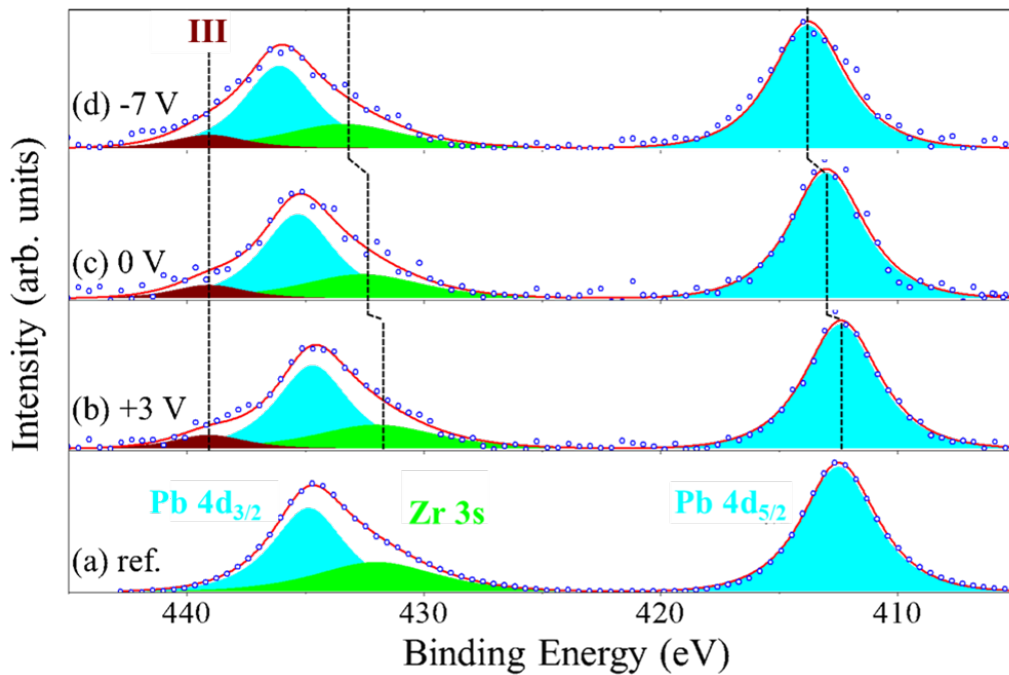


Figure 5.11: Pb 4d and Zr 3s spectra and best fits for (a) reference film without electrode compared with electrode under (b) +3 (c) 0 and (d) -7 V applied bias. The Pb and Zr components have been transposed from the as deposited PZT10 and the color code is the same as in Figure 5.2. Label III identifies the interface related peak is fixed at 439 eV

Furthermore, Figure 5.12 illustrates a schematic of the localization of interface layer (based on the  $Zr_xO_y$  as seen in Figure 5.3) at the level of interface Ru/PZT. In fact, with the presence of high rate of  $O_2$  at the interface, the Zr tends to oxidize at  $Zr_2O_5$ ,  $ZrO_3$ ,  $ZrO_4$  [18, 19]. The presence of these zircon oxide phase (interfacial layer) can be probably at the origin of the interface component (III) observed in Figure 5.10 and Figure 5.11.

The valence band offset at the interface is calculated using the expression of binding energies:  $Ru\ 3p_{3/2} - (Ru\ 3p_{3/2} - Pb\ 4d_{5/2}) - (Pb\ 4d_{5/2} - VBM)$  [29], where  $Ru\ 3p_{3/2}$  is the binding energy measured from the Pt/Ru/PZT10 stack.  $Pb\ 4d_{5/2}$  in the  $(Ru\ 3p_{3/2} - Pb\ 4d_{5/2})$  term represents the binding energy measured from the Pt/Ru/PZT10 stack.  $Pb\ 4d_{5/2}$  and VBM (valence band maximum) in the  $(Pb\ 4d_{5/2} - VBM)$  term are the binding energy measured on the as deposited PZT10. The resulting offset obtained by switching the voltage from +3 to

-7V are  $0.7$  and  $2.1 \pm 0.1$  eV, respectively. Assuming a  $3.4$  eV band gap, this gives a SBH for electrons of  $1.3(2.7) \pm 0.1$  eV, consistent with the capacitive behavior in Figure 5.5(a).

From the difference in Schottky barrier height  $\Delta\Phi$ , we can estimate the effective screening length  $\lambda_{eff}$  in the metal/ferroelectric interface. The effective screening length takes into account all microscopic details of the interface dipole response to the polarization (including electronic and chemical bonding effects). This is in contrast to the Thomas-Fermi model of screening [30] used on the metal/semiconductor interface.

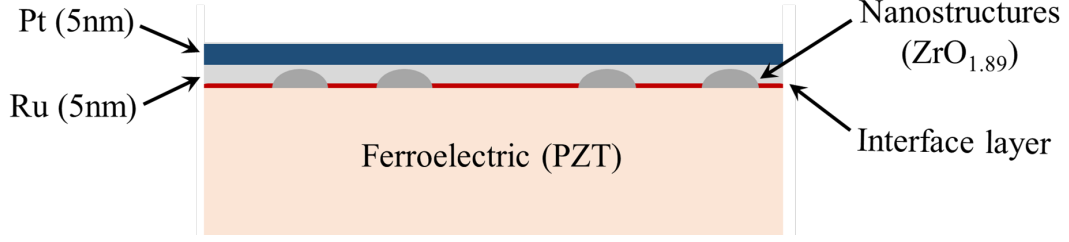


Figure 5.12: Schematic cross section of Pt/Ru/PZT with interface phase ( $Zr_xO_y$ ) and nanostructures ( $ZrO_{1.89}$ )

In fact, with metal/semiconductor interface all the compensating (distribution of the screening charges (Thomas-Fermi screening length  $\delta$ )) reside in the electrodes. With the schematic model considering ideal insulator presented in Figure 5.13(a), we assume that the metal 1 (top electrode) and the metal 2 (bottom electrode) have different screening length, which leads to the asymmetric potential profile. Thus, the spatial distribution of the compensation charge induced by the presence of dissimilar electrodes materials can produce different electric field at each electrodes. This situation may be caused by the shift observed in both permittivity-voltage and polarization-voltage curves presented in Figure 5.5.

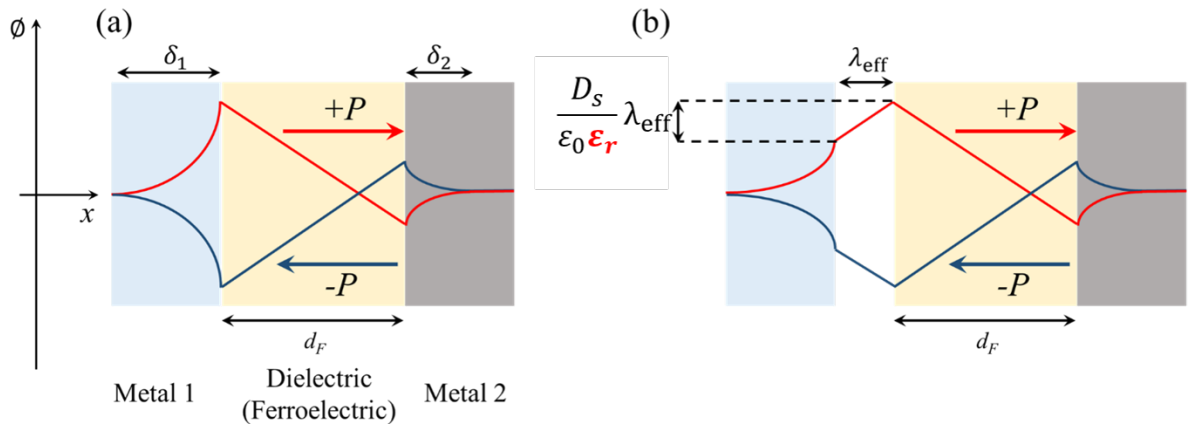


Figure 5.13: Schematic distribution of the electrostatic potential  $\Phi$  in the MFM structure with  $\pm P$  polarization direction,  $d_F$  thickness of ferroelectric (a) Thomas-Fermi model of screening,  $\delta_{1,2}$  screening length in the metal and (b) Effective screening length model ( $\lambda_{eff}$ ),  $D_S$  is the spontaneous polarization

However, Stengel *et al.* [9] explained that the imperfect screening is a property of the interface (the metal, the ferroelectric and the specific interfacial layer), which requires consideration of an effective screening length  $\lambda_{eff}$ , rather than the Thomas-Fermi model of screening one. These imperfections are described by assuming that the screening charges separated from the bound charges by an empty layer of thickness  $\lambda_{eff}$  as illustrated in Figure 5.13(b).

This thickness  $\lambda_{eff}$  acts like a capacitor in series and induces a potential drop of  $\Phi = \lambda_{eff} \cdot D_S / (\epsilon_0 \epsilon_r)$  where  $D_S$  is the spontaneous polarization of the ferroelectric [28]. Thus, using the difference Schottky barrier height  $\Delta\Phi = 2\lambda_{eff} \cdot D_S / (\epsilon_0 \epsilon_r)$  and the value of  $\epsilon_r$  for the interfacial layer Zr<sub>x</sub>O<sub>y</sub> (25 - 40), we can obtain the effective screening length which is 0.575 - 0.920 nm. These results are in quite good agreement with the thickness of the interfacial layer observed in Figure 5.3(a).

		Binding energy (eV)				FWHM (eV)	GL (%)
		PZT reference	Bias on top electrode (V)				
			+3.0	0.0	-7.0		
Cyan	Pb 4d <sub>5/2</sub> (PZT)	412.5	412.4	413.0	413.8	3.6	82
	Pb 4d <sub>5/2</sub> (Reduced)	411.2	411.1	411.7	412.5		
Green	Zr 3s (PZT)	432.0	432.0	432.6	433.4	6.0	70
	Zr 3s (ZrO <sub>1.89</sub> )	433.0	433.0	433.6	434.4		
Wine	III	-	438.4	439.0	439.8	3.6	70

Table 5.4: Pb 4d<sub>5/2</sub> and Zr 3s core level binding energies (eV), FWHM and percentage of Gaussian peak in the Gaussian-Lorentzian peak shapes as a function of applied bias on top electrode of PZT reference capacitor

## 5.4 Interface Analysis of Pb Excess Content in PZT

According to the results in chapter 4, high proportion of Pb induces the disappearance of nanostructures (ZrO<sub>1.89</sub>) at the surface. Considering the ZrO<sub>1.89</sub> as a dead interface layer, their disappearance should enhance the dielectric properties. However, we observed in chapter 3, the dielectric constant and the breakdown field decrease when the Pb excess reaches 30 % (PZT30). Yanovskaya *et al.* [31, 32] show a decrease of the breakdown voltage from 18.2 to 11.2V for PZT10 and PZT30, respectively. In this context, we will investigate the effect of high amounts of Pb excess content on the chemical and electronic configuration of the interface Pt/Ru/PZT.

### 5.4.1 Pt/Ru/PZT30/Pt Electrical Measurements

Figure 5.14(a), shows that the dielectric constant-voltage of Pt/Ru/PZT30/Pt is shifted 1.24 V towards the negative voltage. It also has a dissymmetric butterfly shape. Values of a dielectric constant at -5 and 1V are 670.3 and 899.3, respectively. The maximum value of the dielectric constant is 1181.7. Coercive voltages are -1.48 and -1V for polarization along to the P<sup>+</sup> and P<sup>-</sup>, respectively. According to this fact, the capacitor based on the PZT30

exhibits a low dielectric constant relative to the Pt/Ru/PZT10/Pt capacitor.

From Figure 5.14(b), the maximum value of polarization obtained is  $16.5 \mu\text{C}/\text{cm}^2$  with remanent polarization of  $2.2 \mu\text{C}/\text{cm}^2$  for  $P_r^-$  and  $1.5 \mu\text{C}/\text{cm}^2$  for  $P_r^+$ . It presents an offset of 0.58 V towards the negative voltage with coercive voltages of -0.74 and -0.42 at  $E_C^-$  and  $E_C^+$ , respectively. The changes in the electrical properties might be correlated with the high amount of Pb excess content in the PZT film.

Figure 5.14(b) shows a slim hysteresis shape compared to the result obtained Pt/Ru/PZT10/Pt capacitor. The curve is almost linear which can be probably linked to the ferroelectric relaxor [33] behavior caused by high Pb excess residual. Furthermore, this behavior is observed in the PLZT film when a high concentration of  $\text{La}^{3+}$  (La is used to substitute Pb atom) is incorporated in the PZT film. Leclerc *et al.* [34], Park *et al.* [35] and Podgornyi *et al.* [36] showed the deterioration of the polarization properties of the samples. These can be linked either to the relaxor properties observed on the highly doped PZT thin films or to the transformation of the PZT from ferroelectric state to paraelectric state with the increase of La concentration. It is important to notice that even though the degradation of polarization is observed, Park *et al.* [35] reported that the dielectric was enhanced with the introduction of a high amount of La dopant.

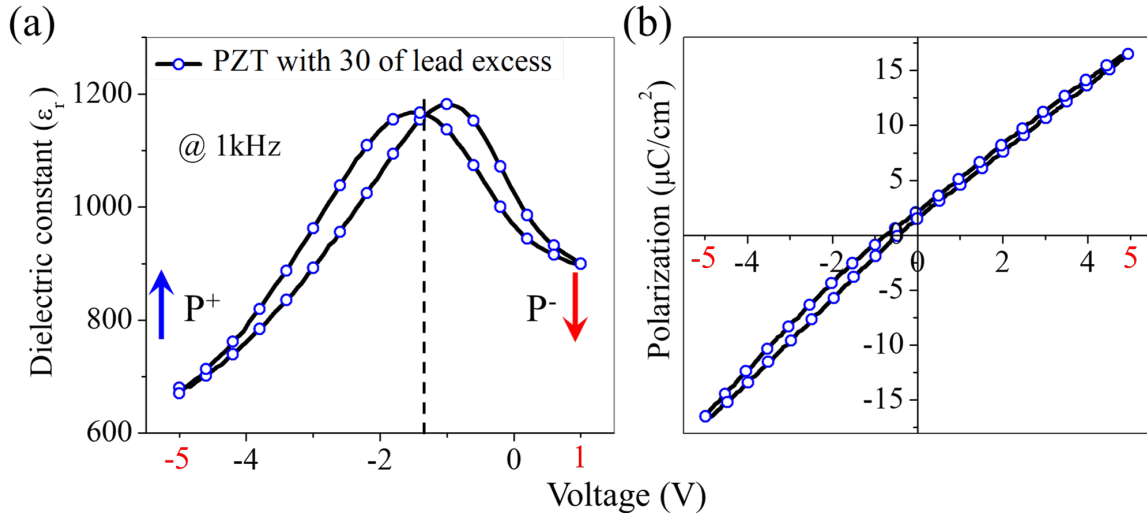


Figure 5.14: Electrical measurements Pt/Ru/PZT30/Pt stack: (a) Dielectric constant and (b) Polarization characteristic

Jin *et al.* [37] explained that the existence of the slim hysteresis loop can be induced by the presence of the pseudocubic phase structure of relaxor ferroelectrics, micro-domains or polar nano-grains. These lead to nonlinear (dielectric) responses under external field while the ferroelectric domains switching give rise a hysteresis. In fact, the current from the conductivity of material can modify the shape of the hysteresis. Indeed, following Dawber *et al.* [38]:  $Q = 2P_r A + \sigma E A t$  (where  $\sigma$  is the electrical conductivity,  $t$  is the measuring time,  $A$  is electrode area of a parallel plate capacitor,  $E$  is the applied field and the switched charge  $Q$  which can allow to get the remanent polarization value  $P_r$ ). This relation shows that, the ferroelectric response can present two types of contribution: the currents from switching

domains and the current from loss (leakage current). According to Jin and Dawber, we can suppose that, under electric field, the response of these micro-domains may be much faster than macroscopic ferroelectric domains and therefore modify the shape of the hysteresis.

This assertion seems to be consistent, when we compare the hysteresis results of the Pt/Ru/PZT30/Pt capacitor performed at 5 V (Figure 5.14(b)) and 20 V (Figure 5.15). These data show that the ferroelectric character of PZT30 seems to be recovered, when the voltage become high (20 V) contrary to the linear response at low voltage (5 V). It is due to the fast response of the micro-domains under polarization electric relative to the ferroelectric domains. However more investigations like the analysis of the dielectric constant as the function of frequency and temperature will be necessary to make more definitive statements on the effect of high rate (30 %) of Pb excess.

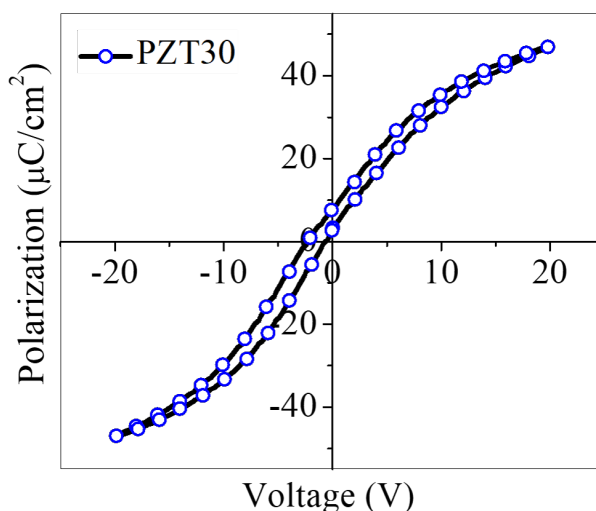


Figure 5.15: Polarization characteristic measurement Pt/Ru/PZT30/Pt stack at 1 kHz

#### 5.4.2 Analysis on *Operando* HAXPES Data Based on PZT30

*Operando* HAXPES measurement are carried out at -5V and +1V. Figure 5.16 shows the Pb 4d/Zr 3s core level spectra (relative to the Pt/Ru/PZT30 stacks) as the function of the voltage applied on the top electrode. The binding energy of the Pb<sup>2+</sup> (cyan color) and the Zr<sup>4+</sup> (green color) from the PZT30 layer depending on the voltage are similar that obtained with a Pt/Ru/PZT10 in Figure 5.10 or Figure 5.11. In fact, we observe a global shift of 1.4 eV of the Zr and Pb relative to the PZT30 perovskite. All binding energy results are summarized in Table 5.5.

Figure 5.16 demonstrates once again the presence of the interface component (peak (III)). For PZT10, peak III shifts from 439.8 eV at -5 V bias to 438.4 eV at +1 V bias. Even though, it was also possible to fix the binding energy at 439 eV. With uncertainty about the position of the interface component, it is very difficult to determine the exact origin of this component.

Furthermore, Figure 5.16 shows an additional chemical state of lead  $Pb^{x+}$  with  $2 < x < 4$  (blue color) between +1V and -5V. This additional chemical state can be attributed by the residual lead oxide due to the high amount of lead excess content in PZT30. However, the exact formula of  $PbO_x$  is not determined [33, 39, 40, 41]. Further, this latter component undergoes a shift of 4.4 eV during the switch. It is important to remark that this phase was not observed with laboratory XPS and XRD. In fact, the  $PbO_x$  seems to be localized in the bulk of PZT and therefore undetectable with the XPS tool. According to the X ray diffraction patterns of PZT films prepared from solutions with different Pb excess content published by Yanovskaya *et al.* [31, 32], the component linked to the PbO appears only with 50 % of Pb excess content but not at 30 % (as that is observed in chapter 4) even though that act the electrical responses of PZT capacitors. However, it is easier and appropriated to highlight the  $PbO_x$  phase with *Operando* HAXPES measurement under bias.

Thus, the presence of the new component of lead oxide observed in HAXPES spectra can be correlated with the decrease of the dielectric constant value and the lowering of the breakdown voltage (Figure 3.10 chapter 3 in the section 3.2.2 page 89). The presence of this lead oxide component is also in agreement with the hypothesis of the existence of microdomains which leads to the slimming of the ferroelectric hysteresis curve as explained by Jin *et al.* [37].

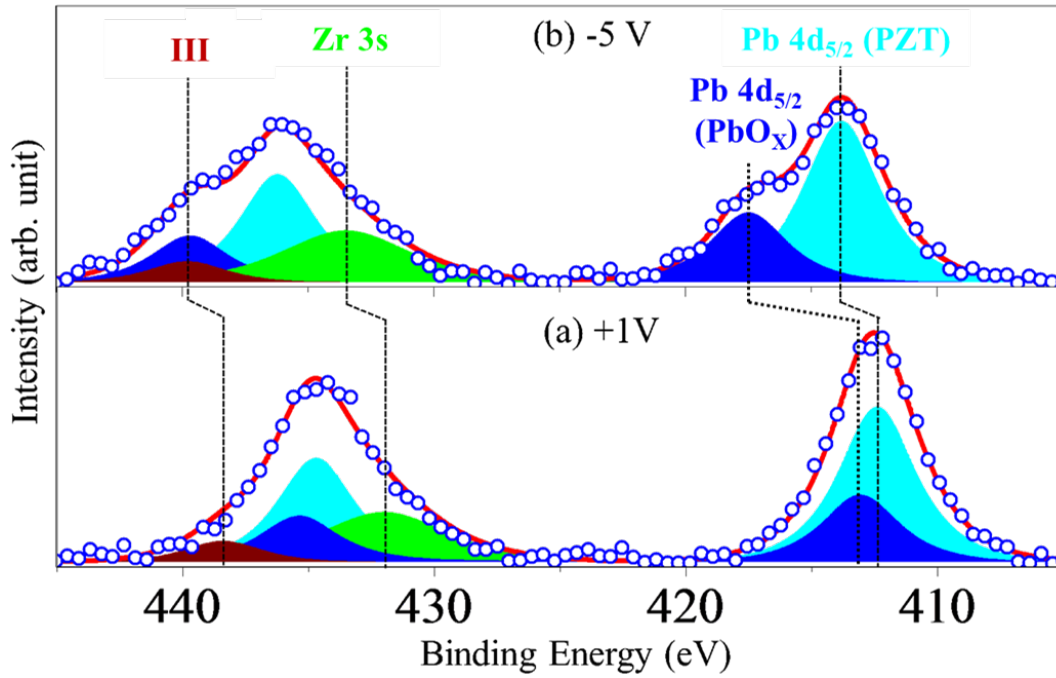


Figure 5.16: Pb 4d and Zr 3s spectra and best fits for Pt/Ru/PZT30 (a) +1 (b) -5 V applied bias. The color code for cyan, green and wine peaks are the same as in Figure 5.10. Blue peak corresponds to the additional lead component.

Furthermore, lead oxide presents low dielectric constant (25.9-35) [42] compared to PZT. It shows a high electronic polarizability (between 3.311 and 3.450) relatively to the  $ZrO_2$  (between 1.897 and 2.054)[43]. This high electronic polarizability can be explained by

the high shift observed during the switching polarization. The PbO can behave like Zr oxide and reduce the capacitance density of MIM capacitors. When the PbO is at the interface, it will behave as a dielectric layer in series with the PZT and induce a lower total capacitance density. Mukhin *et al.* [44] explained that the series layers of lead oxide deposited between the PZT and the bottom electrode (Pt/PZT/PbO/Pt/Ti/SiO<sub>2</sub>/Si) affect the electrical response by reducing the effective dielectric constant from 760 to 410 and the residual polarization from 13 to 11  $\mu\text{C}/\text{cm}^2$ . However, Mukhin also reported an increase of the coercive field from 110 to 185 kV/cm. Yanovskaya *et al.* [32], Maria *et al.* [45] and Afanasev *et al.* [46] have studied the presence of PbO inside the PZT thin films. They showed a reduction of the polarization and the coercive field with increasing Pb excess.

	Binding energy (eV)		Relative intensity (%)	FWHM (eV)	GL (%)
	Bias on top electrode (V)				
	+1	-5			
Pb 4d <sub>5/2</sub> (Pb <sup>2+</sup> )	412.4	413.8	57.9	3.6	82
Pb 4d <sub>5/2</sub> (PbO <sub>x</sub> )	413.1	417.5	22.4		
Zr 3s (Zr <sup>4+</sup> )	432.0	433.4	19.9	6.0	70
III	438.4	439.8	3.9	3.6	70

Table 5.5: Pb 4d<sub>5/2</sub> and Zr 3s core level binding energies (eV), relative intensity, FWHM and percentage of Gaussian peak in the Gaussian-Lorentzian peak shapes as a function of applied bias on top electrode of Pt/Ru/PZT30/Pt capacitor.

In summary, PbO observed during the *operando* measurement can be at the origin of the creation of microdomains inside the PZT30 layer and induce the modification of the hysteresis shape as described by Jin *et al.* [37]. Further, the Pb excess can be localized at the grain boundaries [47] and favor the flow of charge carriers consistent with the premature breakdown field (voltage).

## 5.5 Post Metallization Annealing of Pt/Ru/PZT10 Interface

According to the results from the literature, the Post Metallization Annealing (PMA) under the oxygen enhances the electric responses of MIM capacitors. Kushida-Abdelghafar *et al.* [47] showed an increase of the spontaneous polarization of IrO<sub>2</sub>/PZT/Pt capacitor after PMA. PMA makes the hysteresis curve symmetric and increases the polarization. The improved electrical properties have been also observed in other perovskites like Ba<sub>0.5</sub>Sr<sub>0.5</sub>TiO<sub>3</sub> under PMA with O<sub>2</sub> and N<sub>2</sub> [48] such as an increase of the maximum of capacitance and a reduction of the leakage current values. These data are in agreement with the improvement of the maximum dielectric constant and breakdown voltage after PMA presented in the chapter 3 in section 3.8 page 88 and section 3.2.2 page 89. However, the origins and the physico-chemical impact of PMA were not really explored. Using *operando* HAXPES, we have studied the interface chemistry as a function of the applied bias (switching polarization).

### 5.5.1 Electrical Characterization After PMA

The dielectric constant and polarization data under voltage are presented in Figure 5.17. In contrast to PZT10 before PMA (Figure 5.5(a)), after PMA we observe an increase of the maximum dielectric constant from 1221.6 to 1234.9 and a saturation of the polarization from 23 to 33  $\mu\text{C}/\text{cm}^2$ . In Figure 5.17(b), remanent polarization  $P_r^-$  are 11.2  $\mu\text{C}/\text{cm}^2$  ( $P_r^+ = -8.7 \mu\text{C}/\text{cm}^2$ ). The coercive voltages of -0.83 V and 0.76 V are register for  $E_C^-$  and  $E_C^+$ , respectively. The dielectric-voltage butterfly and polarization-voltage hysteresis curves are symmetric relative to zero voltage. The symmetric hysteresis loop might be attributed at the thermal treatment of the top electrode. In fact, the two metal electrodes are different. The bottom electrode is annealed during the crystallization of the PZT layer while the top electrode is unannealed (Figure 5.17(b)). After PMA a rectifying barrier at the top interface favors the symmetric hysteresis loop as presented in Figure 5.17(b).

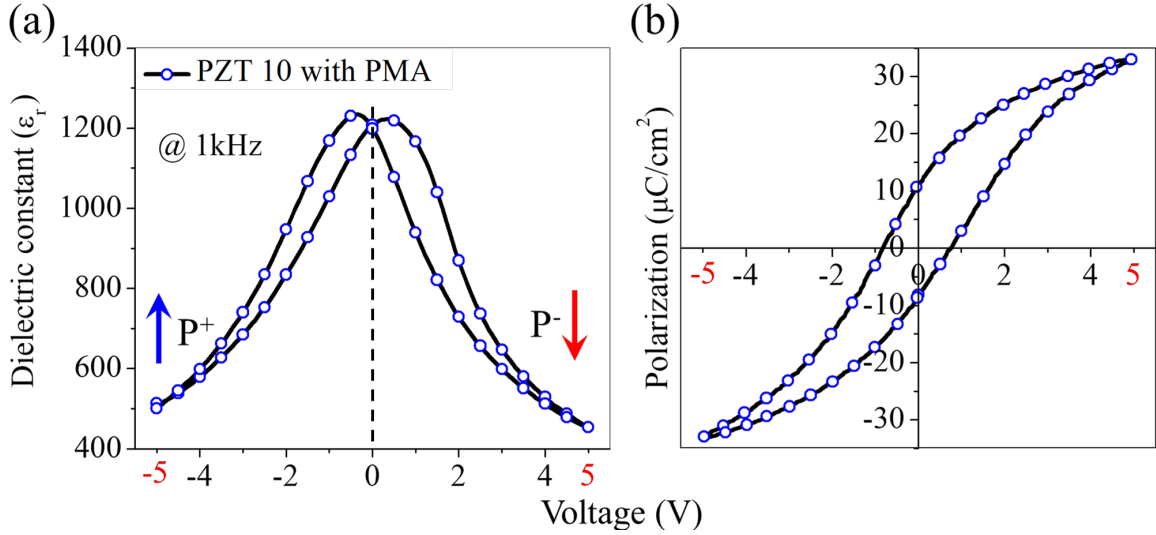


Figure 5.17: Electrical measurements Pt/Ru/PZT reference with PMA/Pt stack: (a) Dielectric constant and (b) Polarization characteristic

### 5.5.2 Ru and Pt Chemical State Before and After PMA

The Ru  $3p_{3/2}$ /Ti 2p and Pt 4f/Ru 4s core level spectra are presented in Figure 5.18(a-b), respectively. Standard Shirley-type background subtraction is used for Ru  $3p_{3/2}$  and Pt 4f spectra. Asymmetric peak-shapes based on the Lorentzian functional form convoluted with a Gaussian are used for fitting the metallic  $\text{Pt}^0$  [49] and  $\text{Ru}^0$  components [50] as observed in Table 5.6. Asymmetric line-shapes describe well the intrinsic energy losses due to the interaction between the photoelectron and the conduction band of the metal [51]. During this interaction, a certain part of the kinetic energy of photoelectron is lost. This leads to a trailing higher intensity at high binding energies.

In Figure 5.18(a) (bottom), Ru is only present in metallic form ( $\text{Ru}^0$ ) localized at 461.5 eV [50, 52, 53] as already presented in Figure 5.8(b). After PMA, the oxidation of the Ru layer is illustrated in Figure 5.18(a) (top). Finally, Table 5.7 shows a drastic decrease of

the Ru<sup>0</sup> which is lower 10 % after PMA, in contrast to what was observed before PMA. This situation is induced by the large oxidation (higher 90 %) of the Ru under the form of RuO<sub>2</sub> and RuO<sub>x</sub> with  $x > 4$ . Ru metallic is only at 8.1 % after PMA. Majority of Ru is transformed (green component at 462.5 eV represents 48.3 % of Ru 3p<sub>3/2</sub>/Ti 2p area) in the form of RuO<sub>2</sub> corresponding to the Ru<sup>4+</sup>. Part of the Ru shows a higher oxidation state (6 and/or 8) as suggested by the (orange) component at 464.8 eV. This HBE component represents 41.8 % of the total Ru 3p<sub>3/2</sub>/Ti 2p intensity. Thus, PMA induces strong changes at the interface and modify the MIM capacitor behaviour.

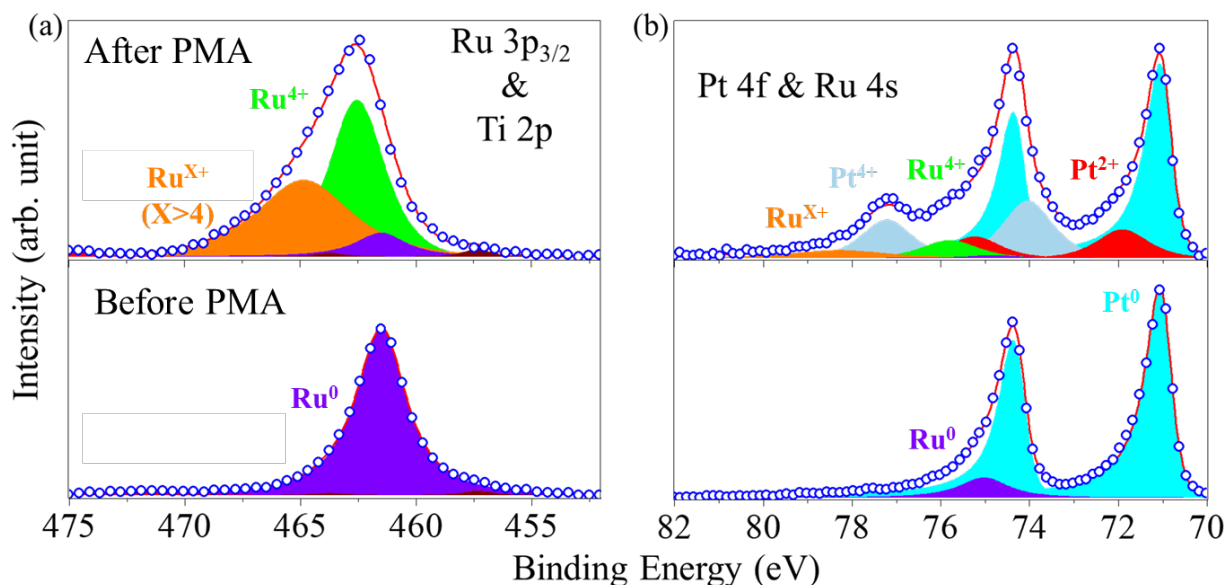


Figure 5.18: Ru 3p<sub>3/2</sub>/Ti 2p and Pt 4f/Ru 4s core level spectra and best fits for Pt/Ru/PZT10/Pt (bottom) before and (top) after post metallization annealing

Zhu *et al.* [54] highlighted the possibility to prepare an amorphous Ru<sub>0.48</sub>Zr<sub>0.52</sub>O<sub>2</sub> film in solid solution by thermal decomposition at 563 K. Under the thermal effect, the Pt/Ru/PZT can undergo a strong change which can lead the appearance of the Ruthenium oxide. The Ti 2p<sub>3/2</sub> (wine peak) is at 457.3 eV for before and after PMA.

Figure 5.18 shows the Pt 4f and Ru 4s core level spectra from the Pt/Ru/PZT10 before and after PMA. After deposition of Pt/Ru top electrode without annealing, only Pt<sup>0</sup> is recorded at 71 eV [55, 56] as illustrated by the cyan color in Figure 5.18. Similarly, the presence of the Ru 4s at 74.8 eV is in agreement with the Ru<sup>0</sup> binding energy according to the NIST database and Handbook of X-ray Photoelectron Spectroscopy [57]. After annealing, a large part of the Ru is oxidized as illustrated in Table 5.7. Once again, oxidation of the Ru is evidenced by the presence of two new components of Ru 4s at high binding energy.

After the PMA process, 33.3 % of Pt is oxidized as Pt<sup>+2</sup> (red) and Pt<sup>+4</sup> (azure) at 71.9 and 74 eV, respectively, [55, 56] as observed in the Table 5.6). Thus, Pt oxidation can come from either the oxygen of the annealing chamber or diffusion of oxygen from the PZT.

In summary, we can assume that the presence of oxygen (from the annealing chamber or the PZT layer) leads to the oxidation of Ru (RuO<sub>x</sub>) and Pt (PtO<sub>x</sub>).

	Oxidation state	Binding Energy (eV)	FWHM	Line shape
Figure 5.18(a)	Ru <sup>0</sup>	461.5	2.5	LF(1.1,1.2,25,5)
	Ru <sup>4+</sup>	462.5	2.8	GL(70)
	Ru <sup>x+</sup> (x > 4)	464.8	4.8	GL(80)
	Ti <sup>4+</sup>	457.3	1.5	GL(30)
Figure 5.18(b)	Pt <sup>0</sup>	71.0	0.6	LA(0.8,2,60)
	Pt <sup>+2</sup>	71.9	1.2	GL(70)
	Pt <sup>+4</sup>	74.0	1.2	GL(70)
	Ru <sup>0</sup>	74.8	1.8	LF(1.1,1.2,25,5)
	Ru <sup>4+</sup>	75.8	2.0	GL(70)
	Ru <sup>x+</sup> (x > 4)	78.2	3.4	GL(80)

Table 5.6: Ru 3p<sub>3/2</sub>/Ti 2p and Pt 4f/Ru 4s core level binding energies (eV), FWHM and symmetric Gaussian-Lorentzian and asymmetric  $LA(\alpha, \beta, m)$  and  $LF(\alpha, \beta, w, m)$  peak shapes (where  $LA$  is Lorentzian Asymmetric lineshape,  $LF$  is Lorentzian Asymmetric lineshape with Tail Damping). The implementation of asymmetric parameters  $\alpha$  and  $\beta$  enables the spread of the Lorentzian tail to be different either side of the Lorentzian component. The integer  $m$  is responsible for the control of the width of a Gaussian which allows to perform a convolution between the Lorentzian Asymmetric lineshape and a Gaussian to adjust the actual shape of the photoemission peak. Finally, the damping parameter  $w$  which allows to limit the range of the asymmetric tail by suppressing the extended tail.

	Oxidation state	Concentration (%)	
		Before PMA	After PMA (%)
Figure 5.18(a)	Ru <sup>0</sup>	98.2	8.1
	Ru <sup>4+</sup>	-	48.3
	Ru <sup>x+</sup> (x > 4)	-	41.8
	Ti <sup>4+</sup>	1.8	1.8
Figure 5.18(b)	Pt <sup>0</sup>	91.3	58.0
	Pt <sup>+2</sup>	-	11.4
	Pt <sup>+4</sup>	-	21.9
	Ru <sup>0</sup>	8.7	0.7
	Ru <sup>4+</sup>	-	4.3
	Ru <sup>x+</sup> (x > 4)	-	3.7

Table 5.7: Relative composition of the Pt 4f/Ru 4s and Ru 3p<sub>3/2</sub>/Ti 2p before and after PMA

### 5.5.3 Analysis on *Operando* HAXPES Data Based on PZT10 After PMA

The Pb 4d/Zr 3s core level spectra presented in Figure 5.19 provide a crucial information on the HBE component (peak III). The fit parameters and the Pb 4d and Zr 3s binding energies as a function of the bias are reported in Table 5.8. The binding energy of peak III

remains fix at 439 eV independently of the applied bias. The difference of binding energy between Zr<sup>4+</sup> (from the PZT thin film (cyan peak) at 432.0 eV for +5V (or 433.4 eV for -5V)) and the position of the peak III is too high (between 5.6 and 7 eV respectively). A new Pb<sup>2+</sup> component (red component) in Figure 5.19 is highlighted. This Pb<sup>2+</sup> component (red) is to be fixed at 412.1 eV and insensitive to the value of the applied electric field. Two possible assumptions can be used to discuss these results: the partial decomposition of the PZT film or the creation of alloys at the interface level.

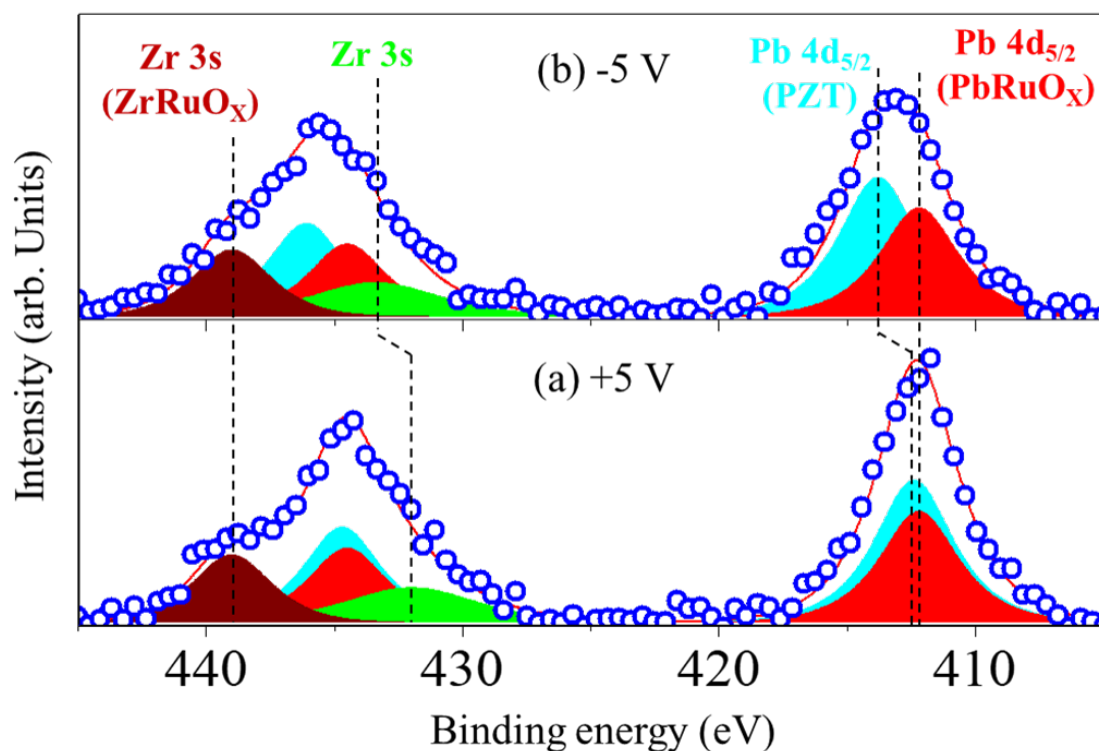


Figure 5.19: Pb 4d and Zr 3s spectra and best fits for Pt/Ru/PZT10 after PMA (a) +5 (b) -5 V applied bias. The color code for cyan and green peaks are the same as in Figure 5.10. Wine peak is linked to oxidation of the interface. Red peak corresponds to the additional lead component after PMA.

Results in Figure 5.19 can be explained by the alloys formation at the interface level. In fact, the creation of this red peak can be explained by a diffusion of the lead oxide (during the PMA) to the ruthenium layer and the formation of alloy based on the lead-ruthenium oxide (PbRuO<sub>x</sub>) as already observed by Prakash *et al.* [58]. Hrovat *et al.* [59] demonstrated an incompatibility reaction between RuO<sub>2</sub> based electrodes and PZT ceramics at low temperature. However, at high firing temperature, a reaction between PZT layer and RuO<sub>2</sub> is possible and can lead to the creation of Pb<sub>2</sub>Ru<sub>2</sub>O<sub>6.5</sub> at the interface level (which is a good conductor layer as described by Bobnar *et al.* [60]). Kushida-Abdelghafar *et al.* [47] showed that under annealing (O<sub>2</sub> at 600°C), the Pb excess diffuse through the grain boundaries and reaches the top electrodes. These results are in agreement with the study of Kennedy [61] which described the creation of deficient oxygen structure (Pb<sub>2</sub>Ir<sub>2</sub>O<sub>6.5</sub>) after the diffusion of Pb.

However, with the migration of Pb inside the Ruthenium layer, the presence of  $ZrO_x$  at the interface might also induce the creation of alloys based on the  $ZrRuO_X$ . During the PMA process, zirconium can get a higher degree of oxidation ( $Zr_2O_5$ ,  $ZrO_3$ ,  $ZrO_4$  [18, 19]), which leads to the increase of binding energy up to 439 eV. Thus, with the presence of the ruthenium layer shown in Figure 5.18(a), we can assume a possibility of the creation of alloy between the  $RuO_x$  and  $ZrO_x$ . These assumption are in agreement with the data from Zhu *et al.* [54], which showed a successful preparation of an amorphous  $Ru_{0.48}Zr_{0.52}O_2$  film of a solid solution phase by a thermal decomposition at a low temperature (563K). Even though, they did not show the XPS result on this  $Ru_{0.48}Zr_{0.52}O_2$  film. Additionally, Weizhen Li *et al.* [62] described that the  $RuO_4$  can be found in the form of  $Zr(RuO_4)_2$  after interaction with the  $ZrO_2$ . Further, Yang *et al.* [63] mixed  $RuO_2$  with inert metal oxides  $ZrO_2$ , in order to maintain a high catalytic activity and stability of  $RuO_2$  during anodic polarization. These results demonstrate a possible reaction between the Zirconium oxide at the interface and the Ruthenium oxide during the PMA process. Depending to the concentration of the  $ZrO_2$  and  $RuO_2$ , Kristof *et al.* [64] and Burke *et al.* [65] also investigated the alloys  $ZrO_X-RuO_Y$ . Finally, we can say that an eventual formation of  $ZrRuO_X$  at the interface can explain the fact that the peak III remains fix at 439 eV during the voltage bias switching.

In summary, beside the potential reduction of the oxygen-vacancies ( $V_O$ ) and the Pb-vacancies ( $V_{Pb}$ ) inside the PZT bulk under high temperature annealing which can improve the electrical performances, the modification of the interface chemistry also act to the electrical responses. In fact, the presence of the news  $Pb^{2+}$  (reb) and  $Zr^{x+}$  (wine) components shown in Figure 5.19 and Ruthenium ( $Ru^{2+}$  and  $Ru^{x+}$   $2 < x < 4$ ) components illustrated in Figure 5.18 might induce a possible creation of interface  $PbRuO_X$  and  $ZrRuO_X$  alloys under thermal treatment. These oxides alloys at the interface lead to the enhancement of electric performances (dielectric constant, breakdown voltage and ferroelectricity) of Pt/Ru/PZT10/Pt after PMA. In fact, the oxide phases observed at the interface before PMA which present a low dielectric constant and lead a formation of the ferroelectric/paraelectric interface can potentially induce a detrimental screening with a higher depolarizing field. Conversely, the formation of the interfacial  $PbRuO_X$  and  $ZrRuO_X$  alloys between the PZT and the top electrode leads to the better screening of bounds charge from the surface of PZT due to the good conductivity of alloys and the absence of oxide phases at the interface.

Conversely to the supposition of the formation of interface alloys and according to the results from Popescu *et al.* [17] which highlighted the progressive increase of intensity for a low binding energy component of Pb core levels (for both 5d and 4f) during the photoemission process with intense synchrotron radiation beam, we can also suppose that the origin of the new  $Pb^{2+}$  component at 412.1 eV (red component) in Figure 5.19 may be attributed with the formation of metallic (reduced) Pb nanoparticles. This situation would be due to a partial decomposition of the PZT film at the interface which promotes the presence of metallic  $Pb^0$ . This nanoscopic separation of PZT structure is also in agreement with the apparition of the peak III. In fact, we can say that with high intensity of source, the decomposition of the perovskite can lead both the reduction of the  $Pb^{2+}$  into  $Pb^0$  and the  $ZrO_3$  matrix [19]). Thus, the  $ZrO_3$  matrix with higher oxidation degree than the  $ZrO_2$  (in PZT) can explain the presence of the peak III at very high binding energy.

However, the assumption based on the partial decomposition of the PZT film can not explain why the red component is not observed with the Pt/Ru/PZT10 before PMA process. Even though these two samples are exposed to the same X-ray source during the same time. The fact that the peak III is fix at 439 eV is not explained by the decomposition possess of PZT under photon source because under bias voltage the Zr component from ZrO<sub>3</sub> (dielectric) should change a binding energy when the polarization switch from +5 V to -5 V. Additionally, the shoulder of the peak III was already remarked at the first swept (first minutes) not after all scans (several hours under synchrotron radiation). According to these information and questions, we suppose that the possible creation upon annealing (PMA) of interface alloys PbRuO<sub>x</sub> and ZrRuO<sub>x</sub> seems more relevant to explain our observations than the partial decomposition of the PZT even though more experiments have to be performed in order to clear and understand the interface interaction under PMA process.

	Binding energy (eV)		Relative intensity (%)	FWHM (eV)	GL (%)
	Bias on top electrode (V)				
	+5	-5			
Pb 4d <sub>5/2</sub> (Pb <sup>2+</sup> )	412.4	413.8	46.12	3.6	82
Pb 4d <sub>5/2</sub> (Interface)	412.1	412.1	30.46		
Zr 3s (Zr <sup>4+</sup> )	432.0	433.4	10.58	6.0	70
Zr 3s (ZrO <sub>1.89</sub> )	433.0	434.4	1.8		
III	439.0	439.0	11.04	3.6	70

Table 5.8: Pb 4d<sub>5/2</sub> and Zr 3s core level binding energies (eV), relative intensity, FWHM and percentage of Gaussian peak in the Gaussian-Lorentzian peak shapes as a function of applied bias on top electrode of Pt/Ru/PZT10/Pt capacitor after PMA

## 5.6 Conclusion

In this chapter, we have carried out *operando* hard X-ray photoelectron spectroscopy of the top interface in a Pt/Ru/PZT/Pt/TiO<sub>2</sub>/SiO<sub>2</sub>/Si capacitors.

The presence of ZrO<sub>1.89</sub> nanostructures at the surface of the bare sol-gel film can act as a dead layer in the dielectric structure and reduce screening of the surface polarization charge in Pt/Ru/PZT10/Pt capacitor. The Schottky barrier height for electrons is 1.3 and 2.7 eV for upwards and downwards pointing polarization, respectively, which is consistent with the electrical characteristics and the effective screening length. However, further studies are necessary to find the real binding energy of the interface layer situated at the Ru/PZT10 interface.

The impact of excess Pb in the precursor is studied by using the PZT with 30 % Pb excess. Sample exhibits a new (PbO<sub>x</sub>) component. The presence of high Pb excess induces a reduction of the capacitance due to the low dielectric constant of (PbO<sub>x</sub>) and a linear hysteresis loop linked to the micro-domains based on the creation of lead oxide clusters. It seems that the addition of PbO<sub>x</sub> induces a decrease of breakdown voltage observed with capacitor base on PZT30. These results show that the optimization of PZT via the elimina-

tion of parasitic  $\text{ZrO}_{1.89}$  and  $(\text{PbO}_x)$  phases are needed to improve the dielectric responses and breakdown voltage performance in view of an optimal use in FE capacitor application. Moreover, regarding the lead excess effect, other investigations are required to find the degree of oxidation of the  $\text{PbO}_x$ .

Finally, post metallization annealing on the PZT10 highlights a modification of the interface by the creation of  $\text{ZrRuO}_x$  and  $\text{PbRuO}_x$  during the annealing process. However, more work is required to fully confirm the origin of the interface related to the signals manifest in the Pb 4d and Zr 3s spectra and to understand if these alloy are responsible for the enhancement of the dielectric constant, the breakdown voltage and the imprint effect on the Pt/Ru/PZT/Pt capacitors.

## Bibliography

- [1] J. F. Scott. *Ferroelectric Memories*, volume 3 of *Springer Series in Advanced Microelectronics*. Springer Berlin Heidelberg, 2000.
- [2] X. J. Lou. Polarization fatigue in ferroelectric thin films and related materials. *Journal of Applied Physics*, 105(2):024101, 2009.
- [3] F. Chen, R. Schafrank, A. Wachau, S. Zhukov, J. Glaum, T. Granzow, H. von Seggern, and A. Klein. Barrier heights, polarization switching, and electrical fatigue in Pb(Zr,Ti)O<sub>3</sub> ceramics with different electrodes. *Journal of Applied Physics*, 108(10):104106, 2010.
- [4] L. Pintilie and M. Alexe. Metal-ferroelectric-metal heterostructures with Schottky contacts. I. Influence of the ferroelectric properties. *Journal of Applied Physics*, 98(12), 2005.
- [5] J. E. Rault, G. Agnus, T. Maroutian, V. Pillard, P. Lecoer, G. Niu, B. Vilquin, M. G. Silly, A. Bendounan, F. Sirotti, and N. Barrett. Interface electronic structure in a metal/ferroelectric heterostructure under applied bias. *Physical Review B - Condensed Matter and Materials Physics*, 87(15):1–9, 2013.
- [6] F. Chen and A. Klein. Polarization dependence of Schottky barrier heights at interfaces of ferroelectrics determined by photoelectron spectroscopy. *Physical Review B - Condensed Matter and Materials Physics*, 86(9):1–7, 2012.
- [7] E. Kroger, A. Petraru, A. Quer, R. Soni, M. Kallane, N. A. Pertsev, H. Kohlstedt, and K. Rossnagel. In situ hard x-ray photoemission spectroscopy of barrier-height control at metal/PMN-PT interfaces. *Physical Review B*, 93(23):235415, 2016.
- [8] I. Pintilie, C. M. Teodorescu, C. Ghica, C. Chirila, A. G. Boni, L. Hrib, I. Pasuk, R. Negrea, N. Apostol, and L. Pintilie. Polarization-control of the potential barrier at the electrode interfaces in epitaxial ferroelectric thin films. *ACS Applied Materials and Interfaces*, 6(4):2929–2939, 2014.
- [9] M. Stengel, D. Vanderbilt, and N. A. Spaldin. Enhancement of ferroelectricity at metaloxide interfaces. *Nature Materials*, 8(5):392–397, 2009.
- [10] P. Zubko, J. C. Wojde, M. Hadjimichael, S. Fernandez-Pena, A. Sené, I. Lukyanchuk, J. M. Triscone, and J. Íñiguez. Negative capacitance in multidomain ferroelectric superlattices. *Nature*, 534(7608):524–528, 2016.
- [11] C.S. Fadley. X-ray photoelectron spectroscopy: Progress and perspectives. *Journal of Electron Spectroscopy and Related Phenomena*, 178-179(C):2–32, 2010.
- [12] G. Kaune, M. A. Ruderer, E. Metwalli, W. Wang, S. Couet, K. Schlage, R. Rohlsberger, S. V. Roth, and P. Muller-Buschbaum. In Situ GISAXS Study of Gold Film Growth on Conducting Polymer Films. *ACS Applied Materials & Interfaces*, 1(2):353–360, 2009.
- [13] A. Utkin and A. Yushkanov. The Model of the Thin Metal Layer Electrical Conductivity in the Case of Different Reflection Coefficients of its Surfaces. *Universal Journal of Applied Mathematics*, 1(2):127–130, 2013.
- [14] A. Zenkevich, Y. Matveyev, M. Minnekaev, Y. Lebedinskii, S. Thiess, and W. Drube. Electronic and electrical properties of functional interfaces studied by hard X-ray photoemission. *Journal of Electron Spectroscopy and Related Phenomena*, 190(PART B):302–308, 2013.

- 
- [15] J. W. Cooper. Photoelectron-angular-distribution parameters for rare-gas subshells. *Physical Review A*, 47(3):1841–1851, 1993.
- [16] S. Tanurna and D. R. Penn. Calculations of Electron Inelastic Mean Free Paths. *Surface and Interface Analysis*, 17:927–939, 1991.
- [17] Dana Georgeta Popescu, Marius Adrian Huanu, Lucian Trupin, Luminia Hrib, Lucian Pintilie, Alexei Barinov, Silvano Lizzit, Paolo Lacovig, and Cristian Mihail Teodorescu. *Physical Chemistry Chemical Physics*, (1):509–520.
- [18] L. A. Simpson, M. Thomsen, B. J. Alloway, and A. Parker. A dynamic reaction cell (DRC) solution to oxide-based interferences in inductively coupled plasma mass spectrometry (ICP-MS) analysis of the noble metals. *Journal of Analytical Atomic Spectrometry*, 16(12):1375–1380, 2001.
- [19] J. Kristóf, S. Daolio, A. De Battisti, C. Piccirillo, J. Mihály, and E. Horváth. Investigations on the Formation of RuO<sub>2</sub> / ZrO<sub>2</sub> - Based Electrocatalytic Thin Films by Surface Analysis Techniques. *Langmuir*, 15(4):1498–1502, 1999.
- [20] H. Shinotsuka, S. Tanuma, C. J. Powell, and D. R. Penn. Calculations of electron inelastic mean free paths. X. Data for 41 elemental solids over the 50eV to 200keV range with the relativistic full Penn algorithm. *Surface and Interface Analysis*, 47(9):871–888, 2015.
- [21] Data Sheet. Agilent E4980A Precision LCR Meter How to Use Tables.
- [22] J. S. Agustsson, U. B. Arnalds, A. S. Ingason, K. B. Gylfason, K. Johnsen, S. Olafsson, and J. T. Gudmundsson. Electrical resistivity and morphology of ultra thin Pt films grown by dc magnetron sputtering on SiO<sub>2</sub>. *Journal of Physics: Conference Series*, 100(8):082006, 2008.
- [23] K. Roodenko, S. K. Park, J. Kwon, L. Wielunski, and Y. J. Chabal. Characterization of Ru thin-film conductivity upon atomic layer deposition on H-passivated Si(111). *Journal of Applied Physics*, 112(11):113517, 2012.
- [24] T F Analyzer. aixPlover Software. *aixACCT Systems GmbH*, (aixPlover Software Manual):Version 3.0.20.0 M1.
- [25] Y. Zhou, H. K. Chan, C. H. Lam, and F. G. Shin. Mechanisms of imprint effect on ferroelectric thin films. *Journal of Applied Physics*, 98(2):0–9, 2005.
- [26] Wei Li Cheah, Nathaniel Ng, and Rajeev Ahluwalia. Influence of space charge on domain patterns and susceptibility in a rhombohedral ferroelectric film. *Acta Materialia*, 100:323–332, 2015.
- [27] M. Aronniemi, J. Sainio, and J. Lahtinen. Chemical state quantification of iron and chromium oxides using XPS: the effect of the background subtraction method. *Surface Science*, 578(1-3):108–123, 2005.
- [28] M. Stengel, P. Aguado-Puente, N. A. Spaldin, and J. Junquera. Band alignment at metal/ferroelectric interfaces: Insights and artifacts from first principles. *Physical Review B - Condensed Matter and Materials Physics*, 83(23), 2011.
- [29] E. A. Kraut, R. W. Grant, J. R. Waldrop, and S. P. Kowalczyk. Precise determination of the valence-band edge in X-Ray photoemission spectra: Application to measurement of semiconductor interface potentials. *Physical Review Letters*, 44(24):1620–1623, 1980.

- [30] N. W. Ashcroft and N. D. Mermin. Solid State Physics. *W.B. Saunders Company, Philadelphia*, 1976.
- [31] K.A. Vorotilov, M.I. Yanovskaya, L.I. Solovjeva, A.S. Valeev, V.I. Petrovsky, V.A. Vasiljev, and I.E. Obvinzeva. Ferroelectric capacitors for integrated circuits. *Microelectronic Engineering*, 29(1-4):41–44, 1995.
- [32] M. I. Yanovskaya, I. E. Obvintseva, L. I. Solovyova, E. P. Kovsman, K. A. Vorotilov, and V. A. Vasilyev. Alkoxy-derived ferroelectric PZT films: The effect of lead acetate dehydration techniques and lead content in the electrochemically prepared solutions on the properties of the films. *Integrated Ferroelectrics*, 19(1-4):193–209, 1998.
- [33] J. M. Thomas and M. J. Tricker. Electronic structure of the oxides of lead. Part 2. An XPS study of bulk rhombic PbO, tetragonal PbO,  $\beta$  PbO<sub>2</sub> and Pb<sub>3</sub>O<sub>4</sub>. *J. Chem. Soc., Faraday Trans. 2*, 71:329–336, 1975.
- [34] G. Leclerc, G. Poullain, C. Yaicle, R. Bouregba, and A. Pautrat. Substrate and orientation influence on electrical properties of sputtered La-doped PZT thin films. *Applied Surface Science*, 254(13):3867–3872, 2008.
- [35] Hyeong Ho Park, Woo Sik Kim, Jun Kyu Yang, Hyung Ho Park, and Ross H. Hill. Characterization of PLZT thin film prepared by photochemical deposition using photosensitive metal-organic precursors. *Microelectronic Engineering*, 71(2):215–220, 2004.
- [36] Yu. V. Podgornyi, A. S. Vishnevskii, K. A. Vorotilov, P. P. Lavrov, and A. N. Lantsev. Electrophysical properties of lead zirconate titanate films doped with lanthanum. *Russian Microelectronics*, 43(6):438–444, 2014.
- [37] L. Jin, F. Li, and S. Zhang. Decoding the Fingerprint of Ferroelectric Loops: Comprehension of the Material Properties and Structures. *Journal of the American Ceramic Society*, 97(1):1–27, 2014.
- [38] M. Dawber, K. M. Rabe, and J. F. Scott. Physics of thin- film ferroelectric oxides. 77:1083–1130, 2005.
- [39] S. Rondon and P. M. A. Sherwood. Core Level and Valence Band Spectra of PbO<sub>2</sub> by XPS. *Surface Science Spectra*, 5(2):104–110, 1998.
- [40] S. Rondon and P. M. A. Sherwood. Core Level and Valence Band Spectra of Pb<sub>3</sub>O<sub>4</sub> by XPS. *Surface Science Spectra*, 5(2):90–96, 1998.
- [41] S. Rondon and P. M. A. Sherwood. Core Level and Valence Band Spectra of Lead by XPS. *Surface Science Spectra*, 5(2):83–89, 1998.
- [42] 2 Mar 1972 New Change Limitation; AFSC USAF ltr. Lead oxide. 1972.
- [43] V. Dimitrov and T. Komatsu. An Interpretation of Optical Properties of Oxides and Oxide Glasses in Terms of the Electronic Ion Polarizability and Average Single Bond Strength. *Journal of the University of Chemical Technology and Metallurgy*, 45(3):219–250, 2010.
- [44] N. V. Mukhin and D. A. Chigirev. Effect of the lead oxide content on the microstructure and properties of PZT films obtained by RF magnetron sputtering. *Journal of Physics: Conference Series*, 872:012045, 2017.

- [45] J. P. Maria, W. Hackenberger, and S. Trolrier-McKinstry. Phase development and electrical property analysis of pulsed laser deposited  $\text{Pb}(\text{Mg}_{1/3}\text{Nb}_{2/3})\text{O}_3$   $\text{PbTiO}_3$  (70/30) epitaxial thin films. *Journal of Applied Physics*, 84(9):5147–5154, 1998.
- [46] V. P. Afanasev, G. N. Mosina, A. A. Petrov, I. P. Pronin, L. M. Sorokin, and E. A. Tarakanov. Specific properties of the PZT-based thin-film capacitor structures with excess lead oxide. *Technical Physics Letters*, 27(6):467–469, 2001.
- [47] K. Kushida-Abdelghafar, M. Hiratani, and Y. Fujisaki. Post-annealing effects on antireduction characteristics of  $\text{IrO}_2/\text{Pb}(\text{Zr}_x\text{Ti}_{1-x})\text{O}_3/\text{Pt}$  ferroelectric capacitors. *Journal of Applied Physics*, 85(2):1069–1074, 1999.
- [48] P. C. Chen, H. Miki, Y. Shimamoto, Y. Matsui, M. Hiratani, and Y. Fujisaki. Effects of Post-Annealing Temperatures and Ambient Atmospheres on the Electrical Properties of Ultrathin  $(\text{Ba},\text{Sr})\text{TiO}_3$  Capacitors. *Japanese Journal of Applied Physics*, 37(Part 1, No. 9B):5112–5117, 1998.
- [49] E. Skrzyska, A. Wondowska-Grabowska, M. Capron, and F. Dumeignil. Crude glycerol as a raw material for the liquid phase oxidation reaction. *Applied Catalysis A: General*, 482:245–257, 2014.
- [50] D. J. Morgan. Resolving ruthenium: XPS studies of common ruthenium materials. *Surface and Interface Analysis*, 47(11):1072–1079, 2015.
- [51] S. Doniach and M. Sunjic. Many-electron singularity in X-ray photoemission and X-ray line spectra from metals. *Journal of Physics C: Solid State Physics*, 3(2):285–291, 1970.
- [52] K. Qadir, S. H. Joo, B. S. Mun, D. R. Butcher, F. Renzas, J. R. Aksoy, G. A. Liu, Z. Somorjai, and J. Y. Park. Intrinsic Relation between Catalytic Activity of CO Oxidation on Ru Nanoparticles and Ru Oxides Uncovered with Ambient Pressure XPS. *Nano Letters*, 12(11):5761–5768, 2012.
- [53] S. Kezilebieke, M. Ali, B. Shadeke, and R. Gunnella. Magnetic properties of ultrathin  $\text{Ni}_{81}\text{Fe}_{19}$  films with Ta and Ru capping layers. *Journal of Physics: Condensed Matter*, 25(47):476003, 2013.
- [54] J. Zhu, X. Wang, Z. Yi, Z. Tang, B. Wu, D. Tang, and W. Lin. Stability of solid-solution phase and the nature of phase separation in Ru-Zr-O ternary oxide. *Journal of Physical Chemistry C*, 116(49):25832–25839, 2012.
- [55] S. Axnanda, E. J. Crumlin, B. Mao, S. Rani, R. Chang, P. G. Karlsson, M. O. M. Edwards, M. Lundqvist, R. Moberg, P. Ross, Z. Hussain, and Z. Liu. Using Tender X-ray Ambient Pressure X-Ray Photoelectron Spectroscopy as A Direct Probe of Solid-Liquid Interface. *Scientific Reports*, 5(1):9788, 2015.
- [56] L. K. Ono and B. Roldan Cuenya.
- [57] J. F. Moulder, W. F. Stickle, P. E. Sobol, and K. D. Bomben. *Handbook of X-ray Photoelectron Spectroscopy (1st Edition)*. Perkin-Elmer Corp. Physical Electronics Division, Eden Prairie, Minnesota, USA, 1992.
- [58] J. Prakash, D. A. Tryk, and E. B. Yeager. Kinetic Investigations of Oxygen Reduction and Evolution Reactions on Lead Ruthenate Catalysts. *Journal of The Electrochemical Society*, 146(11):4145, 1999.

- [59] M. Hrovat, A. Benan, J. Holc, and M. Kosec. Subsolidus phase equilibria in the RuO<sub>2</sub> - TiO<sub>2</sub> - ZrO<sub>2</sub> system. *Journal of Materials Science Letters*, 20(22):2005–2008, 2001.
- [60] V. Bobnar, M. Hrovat, J. Holc, and M. Kosec. All-Ceramic Percolative Composites with a Colossal Dielectric Response. In *Ferroelectrics - Characterization and Modeling*. InTech, 2011.
- [61] Brendan J. K. Oxygen Vacancies in Pyrochlore Oxides: Powder Neutron Diffraction Study of Pb<sub>2</sub>Ir<sub>2</sub>O<sub>6.5</sub> and Bi<sub>2</sub>Ir<sub>2</sub>O<sub>7-y</sub>. *Journal of Solid State Chemistry*, 123(1):14–20, 1996.
- [62] W. Li, H. Liu, and E. Iglesia. Structures and properties of zirconia-supported ruthenium oxide catalysts for the selective oxidation of methanol to methyl formate. *The journal of physical chemistry. B*, 110(46):23337–42, 2006.
- [63] C.H. Yang, C. C. Lee, and T. C. Wen. Hypochlorite generation on RuPt binary oxide for treatment of dye wastewater. *Journal of Applied Electrochemistry*, 30(9):1043–1051, 2000.
- [64] J. Kristóf, S. Daolio, A. De Battisti, C. Piccirillo, J. Mihály, and E. Horváth. Investigations on the Formation of RuO<sub>2</sub> / ZrO<sub>2</sub> Based Electrocatalytic Thin Films by Surface Analysis Techniques. *Langmuir*, 15(4):1498–1502, 1999.
- [65] L.D. Burke and M. McCarthy. Oxygen gas evolution at, and deterioration of, RuO<sub>2</sub> / ZrO<sub>2</sub>-coated titanium anodes at elevated temperature in strong base. *Electrochimica Acta*, 29(2):211–216, 1984.

---

# SUMMARY AND OUTLOOK

This thesis mainly aims at identifying and explaining certain physicochemical phenomena that could inhibit the integration of Metal-Insulator-Metal (MIM) structures based on the Lead Zirconate Titanate (PZT) thin films. In particular, we correlate the electronic and chemical structures at the surface level of PZT and at the top interfaces of Pt/Ru/PZT with the electrical results (dielectric constant-voltage, loss tangent and breakdown field) from Pt/Ru/PZT/Pt capacitors.

In this context, this work focused on both the importance of lead excess in the PZT layers and the effect of the post metallization annealing (PMA) at the metal/PZT interface. This study allows us to extend our knowledge about MIM structures and to overcome certain technological obstacles so that the performances of the thin films can approach to those of the bulk material in Multi-MIM architectures in microelectronics. This work has given rise to specific contributions in different areas, which are now summarized.

Chapter 1 is dedicated to better understand the MIM structures. We have presented the fundamental properties of Metal-Insulator-Metal structure by introducing the capacitance, loss tangent and breakdown field. The origin of the texture of Lead Zirconium Titanium (PZT for  $\text{Pb}(\text{Zr}_{0.52}\text{Ti}_{0.48})\text{O}_3$ ), its ferroelectric and its dielectric properties have been largely discussed. Further, this chapter have pointed out the importance of the surface and interface which play a central role in the performance of MIM structures.

Chapter 2 begins by the description of the deposition process used during this thesis work. The main steps for manufacturing our Pt/Ru/PZT/Pt structures are explained. An important place is dedicated to the description of the sol-gel technique, which was used to deposit the PZT layers. Besides that, the goal of this chapter is also to relate all necessary tools used to understand the impact of the structural, microstructural, electronical and physicochemical properties of Metal-PZT-Metal based on the PZT thin films. We have described the microstructural (X-ray diffraction such as XRD and GIXRD) and structural (electronic microscopies such as SEM, TEM, STEM) tools used for studying the PZT layers. We have also developed and explained the work principal of photoemission spectroscopy, which is an effective technique to study the physico-chemical and the electronic properties of materials. Finally, the most important details of XPS setup is presented and work principle of the synchrotron beamline and the protocol used to perform the *operando* HAXPES are provided.

Chapter 3 provides results of the electrical measurements (dielectric constant-voltage, loss tangent and breakdown field) performed on Pt/Ru/PZT/Pt capacitors depending on both the lead excess and the post metallization annealing. The first part of the chapter is devoted to present all characteristics of the electrical measurement setup. The permittivity results show the presence of the optimum between 15 and 20 % of lead excess content depending on both the lead excess and the post metallization annealing. The decrease of the permittivity for PZT10 and PZT30 could be attributed to the presence of the secondary phase respectively at the interface metal/PZT and the bulk of PZT thin film as shown in chapter 4 and 5. Finally, we have shown that the higher the lead excess content in the PZT thin film, the lower the breakdown field response of Pt/Ru/PZT/Pt capacitors. This seems to be linked to the high residual lead excess in PZT as demonstrated in chapter 5.

Chapter 4 is dedicated to show all intrinsic contributions from the surface of PZT film, which is responsible for the variation in electrical performances as a function of the lead excess. In the first

part, we focus on the determination of the parasitic phase composition. The comparative studies made between the as deposited PZT10 and PZT30 through the use of photoemissions spectroscopy are found to be essential for the separation of the perovskite (PZT) and parasitic ( $\text{ZrO}_{1.82-1.89}$ ) phases. Takeoff angle study performed from  $90$  to  $30^\circ$  are essential to distinguish the parasitic phase at the surface and at the bulk of the PZT. These results are supported by the grazing incidence X-ray diffraction data. Ion beam etching study confirms that the  $\text{ZrO}_{1.82-1.89}$  is only localized at the surface of PZT thin films. Further, scanning electron microscopy shows the increase of size of PZT grain when the rate of Pb excess increases. X-rays diffraction shows a change of crystallographic orientation from mostly (111) to (100) when we pass to 30 % at 10 % of Pb excess content. The transformation of the crystallographic orientation is linked to the competition between the  $\text{PbTiO}_3$  and the  $\text{Pt}_x\text{Pb}$  during the first stage of the growth of the first PZT layer. The second part of this chapter is dedicated to the investigation of the evolution of PZT thin film as a function of the lead excess content. It is observed that with 10, 15, 20 and 30 % of lead excess the secondary phase decreases and vanishes at the surface level. From scanning electron microscopy results, it is clear that the diminution of the parasitic phase is correlated with the increase of the grain size.

In the last chapter of this thesis, we analyze the behavior of interface of Pt/Ru/PZT stack during the switching polarization using Hard X-ray photoelectron spectroscopy (HAXPES). This technique is a well-suited non-destructive method for the analysis of electronic interfaces buried of Pt/Ru/PZT/Pt/TiO<sub>2</sub>/SiO<sub>2</sub>/Si capacitor. It also provides important information of the chemical states from the Pt/Ru/PZT interface under the electric field.

With HAXPES, as deposited PZT10 have been analyzed.  $\text{ZrO}_{1.82-1.89}$  nanostructures, which present at the surface of the bare sol-gel film act as a dead layer in the capacitance structure and reduce the screening for PZT10. The Schottky barrier height for electrons is 1.3 and 2.7 eV for upwards and downwards pointing polarization, respectively, consistent with the electrical characteristics and the effective screening length.

The impact of the excess Pb in the precursor is also studied by using the PZT with 30 % of lead excess. The sample exhibits a new component based on the lead oxide ( $\text{PbO}_x$ ) as shown by the photoelectron spectroscopy. The presence of high lead excess in the capacitor induce the reduction of the capacitance due to the low dielectric constant of the lead oxide and the slimming of the hysteresis loop which is linked to the micro-domains based on the  $\text{PbO}_x$ . We assume that the addition of  $\text{PbO}_x$  peak can induce the decrease of the breakdown field observed with capacitor base on PZT30, as seen in chapter 3. The results show that the optimization of PZT via elimination of parasitic  $\text{ZrO}_{1.82-1.89}$  and lead oxide residual phase is needed to improve the dielectric response and the breakdown field performance which are important for the ferroelectric capacitor application.

Finally, The post metallization annealing on the PZT10 bare highlights an interface modification. According to the results, the interface seems to be linked to the creation of  $\text{ZrRuO}_x$  and  $\text{PbRuO}_x$  during the annealing process. However, more work is required to fully characterize the origin of the HBE peak in the Pb 4d and Zr 3s spectra, their creation process and the real consequences in terms of the interface dielectric responses.

To conclude, this study has enabled us to highlight several aspects such as the presence and the composition of nanostructures, the variation in the texture and in the morphology of the PZT layers depending on the lead excess and the presence of interface phases and residual Pb oxide in some Pt/Ru/PZT/Pt capacitors. However, additional characterizations are required to understand the impact of the presence of interface phase layers as well as the different phase of manufactur-

---

ing processes. Additional TEM/EDX measurements at the Pt/Ru/PZT interface are necessary to complete the results obtained on the PZT with 30 % of lead excess and the PZT10 sample with post metallization annealing.

Finally, *operando* HAXPES analysis methodology which allows to highlight several important results could be adapted to *operando* studies of active devices, for example, gate/channel interfaces in transistors based on the functional oxides in future.

